



**HAL**  
open science

# Basculement de polarisation, contrôle et synchronisation de lasers à cavité verticale émettant par la surface (VCSELs) soumis à injection optique

Ignace Gatare Gahangara

► **To cite this version:**

Ignace Gatare Gahangara. Basculement de polarisation, contrôle et synchronisation de lasers à cavité verticale émettant par la surface (VCSELs) soumis à injection optique. Autre. Université Paul Verlaine - Metz, 2008. Français. NNT : 2008METZ004S . tel-01752565

**HAL Id: tel-01752565**

**<https://hal.univ-lorraine.fr/tel-01752565>**

Submitted on 29 Mar 2018

**HAL** is a multi-disciplinary open access archive for the deposit and dissemination of scientific research documents, whether they are published or not. The documents may come from teaching and research institutions in France or abroad, or from public or private research centers.

L'archive ouverte pluridisciplinaire **HAL**, est destinée au dépôt et à la diffusion de documents scientifiques de niveau recherche, publiés ou non, émanant des établissements d'enseignement et de recherche français ou étrangers, des laboratoires publics ou privés.



## AVERTISSEMENT

Ce document est le fruit d'un long travail approuvé par le jury de soutenance et mis à disposition de l'ensemble de la communauté universitaire élargie.

Il est soumis à la propriété intellectuelle de l'auteur. Ceci implique une obligation de citation et de référencement lors de l'utilisation de ce document.

D'autre part, toute contrefaçon, plagiat, reproduction illicite encourt une poursuite pénale.

Contact : [ddoc-theses-contact@univ-lorraine.fr](mailto:ddoc-theses-contact@univ-lorraine.fr)

## LIENS

Code de la Propriété Intellectuelle. articles L 122. 4

Code de la Propriété Intellectuelle. articles L 335.2- L 335.10

[http://www.cfcopies.com/V2/leg/leg\\_droi.php](http://www.cfcopies.com/V2/leg/leg_droi.php)

<http://www.culture.gouv.fr/culture/infos-pratiques/droits/protection.htm>



Vrije Universiteit Brussel



# Polarization Switching, Locking and Synchronization in VCSELs with Optical Injection

PhD dissertation by:

**GATARE GAHANGARA Ignace**



Metz, 8 February 2008







Vrije Universiteit Brussel



# Polarization Switching, Locking and Synchronization in VCSELs with Optical Injection

PhD dissertation by:

**GATARE GAHANGARA Ignace**

## Members of the Jury

Prof. Dr. K. A. Shore - *Bangor University, Bangor, United Kingdom*.....Reviewer  
 Prof. Dr. J. G. McInerney - *University College Cork, Cork, Ireland*.....Reviewer  
 Prof. Dr. A. Valle - *Universidad de Cantabria, Santander, Spain*.....President  
 Dr. E. Lacot - *Université Joseph-Fourier, Grenoble, France*.....Examiner  
 Prof. Dr. Ir. J. Stiens - *Vrije Universiteit Brussel, Brussels, Belgium*.....Examiner  
 Prof. Dr. Ir. J. Tiberghien - *Vrije Universiteit Brussel, Brussels, Belgium*.....Examiner  
 Prof. Dr. Ir. H. Thienpont - *Vrije Universiteit Brussel, Brussels, Belgium*.....Director  
 Prof. Dr. Sc. K. Panajotov - *Vrije Universiteit Brussel, Brussels, Belgium*..... Co-Director  
 Prof. Ir. J. Maufooy - *Supélec, LMOPS, Metz, France*.....Director  
 Dr. Ir. M. Sciamanna - *Supélec, LMOPS, Metz, France*.....Co-Director



Metz, 8 February 2008





# Acknowledgements

The present PhD work has been prepared in the framework of collaboration between the Ecole Supérieure d'Electricité (SUPELEC), the Université Paul Verlaine Metz, in France, and the Vrije Universiteit Brussel (VUB), in Belgium. I would like to thank my promoters Hugo Thienpont (VUB) and Jean Maufoiy (SUPELEC) for having supported my PhD project. It was a great opportunity to work alternately between Metz and Brussels.

I would like to express my sincere thanks to Marc Sciamanna who supervised my research work at SUPELEC in Metz. I am grateful to him for all his precious advice which constantly stimulated my research activities. I benefited a lot not only from his skills as a passionate researcher but also from his organizational abilities.

I owe thanks to Krassimir Panajotov, my supervisor at VUB, Department of Applied Physics and Photonics (TONA). I am mostly grateful to him for training me how to “navigate” between theory and experiments. I also thank him for always facilitating fruitful interactions between students working in the TONA lab.

During the period of my PhD work, I had the opportunity to meet and collaborate with scientists from different research groups:

Here, I would first express my thanks to Angel Valle (Universidad de Cantabria) for the fruitful collaboration on transverse mode competition in VCSELs. I greatly learned from his long experience on the modelling of polarization switching and transverse mode behavior in VCSELs. I am also grateful to Michel Nizette (Université Libre de Bruxelles) for our collaboration on bifurcation and nonlinear dynamics and also for having taught me the “secrets” of AUTO continuation tool. I thank also Alexandre Locquet (Georgia Tech Lorraine) for our collaboration on chaos synchronization.

I had also the opportunity to work and discuss with motivated students. I would like to thank J. Buesa and M. Triginer, two ERASMUS students at TONA, for their collaboration in performing some of the experiments, Mikel and Xavier for their precious advice and for creating a wonderful working environment in the lab.

Working between Metz and Brussels allowed me to meet many people who provided me with their encouragement and support. Though I will not be able to acknowledge all those people, I would like just to mention D. Wolfersberger for her encouragements, G. Berlin, P. and C. Mercier for their very professional technical assistance.

I am also thankful to all the jury members for their active involvement in the examination process of my PhD work, in spite of their numerous duties. In particular, I appreciate their constructive remarks, suggestions and questions I received during both my private and public PhD defenses.

I would like to acknowledge the Vrije Universiteit Brussel, SUPELEC and the Conseil Régional de Lorraine for their financial and technical supports. I am extremely grateful for all the opportunities I had to attend several international and national scientific meetings and conferences from which I benefited a lot. I also acknowledge the Université Paul Verlaine Metz and the CNRS Laboratoire des Matériaux Optiques, Photonique et Systèmes (LMOPS) for their implication in the cotutelle PhD program.

Let me thank other people outside my professional sphere. I am grateful to Dr. C. Muligande for his advice and support; Mr. and Mrs. Rudahunga; Mr. and Mrs. Rusera, and D. Dusabe for their warm encouragements and care. I can not forget my best friend L. Bora who was always ready to drive me during my several shifts between Metz and Brussels.

Finally, I would like to thank all my family in Rwanda for their particular care. In spite of the distance, I regularly received a warm support from you. In particular, I thank my brother Félix Sesonga for his permanent advice.



# Contents

<b>1</b>	<b>General Introduction</b>	<b>1</b>
<b>2</b>	<b>Edge-emitting and surface-emitting semiconductor lasers</b>	<b>7</b>
2.1	Edge-emitting semiconductor lasers . . . . .	7
2.2	Vertical-Cavity Surface-Emitting Lasers (VCSEL) . . . . .	11
<b>3</b>	<b>Polarization properties of VCSELs</b>	<b>17</b>
3.1	Polarization switching . . . . .	17
3.2	Modelling of polarization switching using the Spin-Flip Model (SFM) . . . . .	21
3.2.1	The four-level energy system . . . . .	21
3.2.2	The Spin-Flip Model (SFM) . . . . .	22
3.2.3	Linearly-Polarized steady state solutions of the SFM model . . . . .	25
3.3	Type I and type II polarization switching in the framework of the SFM . . . . .	27
3.3.1	Experimental polarization switching scenarios . . . . .	27
3.3.2	Numerical simulations of type II PS using the SFM model . . . . .	30
3.4	VCSELs subject to external perturbation . . . . .	33
3.4.1	Semiconductor lasers with external optical injection . . . . .	38
3.4.2	External optical injection in VCSELs . . . . .	39
3.5	Conclusions . . . . .	42
<b>4</b>	<b>Polarization control and bistability in VCSEL subject to or-</b>	

<b>thogonal Optical Injection</b>	<b>45</b>
4.1 Introduction . . . . .	46
4.2 Intensity-induced polarization bistability and switching: <i>experiments</i> . . . . .	48
4.2.1 Experimental setup . . . . .	48
4.2.2 Polarization-resolved light-current characteristics of the solitary VCSEL . . . . .	49
4.2.3 Intensity-induced polarization switching bistability . .	50
4.3 Modelling of the VCSEL subject to orthogonal optical injection	53
4.4 Intensity-induced polarization bistability in VCSEL under orthogonal optical injection: <i>theory</i> . . . . .	56
4.5 Frequency-induced polarization bistability in VCSEL with orthogonal optical injection . . . . .	58
4.5.1 Polarization bistability . . . . .	60
4.5.2 Polarization dynamics accompanying polarization switching . . . . .	62
4.5.3 Dependency of hysteresis width on injected power . . .	64
4.5.4 Tunability of the hysteresis width . . . . .	66
4.6 Conclusions . . . . .	70
<b>5 Experimental study of nonlinear dynamics accompanying polarization switching in VCSELs with orthogonal optical injection</b>	<b>73</b>
5.1 Introduction . . . . .	74
5.2 Mapping of polarization dynamics . . . . .	75
5.3 Complex nonlinear dynamics . . . . .	81
5.3.1 Subharmonic resonances . . . . .	81
5.3.2 Period doubling route to chaos . . . . .	82
5.4 Periodic dynamics on the route to polarization switching . . .	86
5.5 Conclusions . . . . .	92
<b>6 Bifurcation to polarization switching and locking in VCSELs with optical injection: <i>Theory</i></b>	<b>95</b>
6.1 Introduction . . . . .	96

6.2	Bifurcation study of nonlinear dynamics in a VCSEL with optical injection . . . . .	98
6.2.1	Polarization switching scenarios . . . . .	98
6.2.2	Bifurcation and polarization switching boundaries . . .	107
6.2.3	Influence of the $\alpha$ factor on the injected VCSEL dynamics . . . . .	111
6.3	Bifurcation study using a two-mode model for VCSELs with orthogonal injection . . . . .	115
6.3.1	The two-mode model . . . . .	116
6.3.2	Bifurcation study . . . . .	118
6.4	Discussions and conclusions . . . . .	123
<b>7</b>	<b>Transverse mode switching and locking in VCSEL subject to orthogonal optical injection</b>	<b>127</b>
7.1	Introduction . . . . .	128
7.2	Theoretical study of optical injection-induced transverse mode competition . . . . .	129
7.2.1	The Model . . . . .	129
7.2.2	Theoretical results . . . . .	133
7.3	Experimental study of optical injection-induced transverse mode competition . . . . .	141
7.3.1	Experimental mapping . . . . .	141
7.3.2	Polarization-resolved switching scenarios . . . . .	143
7.4	Comparison between theory and experiments . . . . .	146
7.5	Conclusions . . . . .	148
<b>8</b>	<b>Polarization-resolved dynamics and chaos synchronization of unidirectionally coupled VCSELs</b>	<b>151</b>
8.1	Introduction . . . . .	152
8.2	Influence of polarization mode competition on the synchronization of two unidirectionally coupled VCSELs . . . . .	157
8.2.1	The Model . . . . .	157
8.2.2	Polarization mode competition and its effect on chaos synchronization . . . . .	159

8.3	Polarization synchronization in unidirectionally coupled VC-SELs with orthogonal optical injection . . . . .	163
8.3.1	Rate equation model . . . . .	164
8.3.2	Polarization switching and polarization synchronization	165
8.3.3	Mapping of correlation coefficient . . . . .	173
8.3.4	Influence of $\gamma_s$ on the two regions of synchronization .	176
8.4	Conclusions . . . . .	179
<b>9</b>	<b>Conclusions</b>	<b>183</b>
9.1	Summary of our main results . . . . .	183
9.2	Perspectives . . . . .	188
<b>A</b>	<b>Modelling optical injection by a travelling wave approach</b>	<b>189</b>
<b>B</b>	<b>Basculement de polarisation, contrôle et synchronisation de lasers à cavité verticale émettant par la surface (VCSELs) soumis à injection optique. <i>Resume de thèse en Français</i></b>	<b>195</b>
B.1	Introduction et contexte de notre thèse . . . . .	197
B.2	Propriétés de polarisation du VCSEL . . . . .	202
B.2.1	Basculement de polarisation dans un VCSEL: <i>mécanismes physiques</i> . . . . .	202
B.2.2	Basculement de polarisation de type I et de type II: <i>observation expérimentale</i> . . . . .	203
B.2.3	Basculement de polarisation de type II: <i>mise en évidence théorique</i> . . . . .	205
B.3	Contrôle du basculement et bistabilité de polarisation d'un VCSEL soumis à injection optique orthogonale . . . . .	207
B.3.1	Bistabilité de polarisation induite par variation de la puissance injectée: <i>résultats expérimentaux</i> . . . . .	208
B.3.1.1	Description du banc expérimental . . . . .	208
B.3.1.2	Résultats expérimentaux . . . . .	209
B.3.2	Bistabilité de polarisation induite par variation la de puissance injectée: <i>résultats théoriques</i> . . . . .	211
B.3.3	Bistabilité de polarisation induite par variation du de-tuning: <i>résultats théoriques</i> . . . . .	213

B.4	Etude expérimentale de dynamiques non-linéaires qui accompagnent le basculement de polarisation d'un VCSEL soumis à injection optique orthogonale . . . . .	214
B.5	Etude théorique du VCSEL soumis à injection optique orthogonale: analyse des bifurcations associées à la dynamique de basculement . . . . .	222
B.5.1	Dynamiques non-linéaires accompagnant le basculement de polarisation: <i>scénarios</i> . . . . .	223
B.5.1.1	Dynamiques nonlinéaires accompagnant le basculement de polarisation: modèle SFM . . . . .	223
B.5.1.2	Cartographie théorique de bifurcations associées à la dynamique de basculement de polarisation . . . . .	226
B.6	Analyse de la compétition des modes transverses dans un VCSEL soumis à injection optique orthogonale . . . . .	228
B.7	Influence de la dynamique de polarisation sur la synchronisation du chaos optique dans les VCSELs en couplage unidirectionnel . . . . .	230
B.7.1	Effet de la dynamique de compétition de modes sur la synchronisation de deux VCSEL couplés: <i>injection unidirectionnelle isotrope</i> . . . . .	231
B.7.2	Effet de la dynamique de compétition de modes sur la synchronisation de deux VCSEL couplés: <i>injection unidirectionnelle orthogonale</i> . . . . .	233
B.8	Conclusions . . . . .	236
	<b>Bibliography</b>	<b>239</b>
	<b>List of publications</b>	<b>257</b>
	<b>Curriculum Vitae</b>	<b>261</b>



# Chapter 1

## General Introduction

Semiconductor lasers have witnessed a rapid development since stimulated emission of light was demonstrated in semiconductor materials in 1962 [1]. The concept of stimulated emission of light was first presented by Einstein at the beginning of the last century [2]. A growing interest in light-matter interaction phenomena took place following the world war II and led to a better physical understanding of stimulated emission in gas and solid state lasers [3, 4]. In the mean time, the development of the semiconductor industry allowed the fabrication of devices with tailored properties. The milestone in the development of semiconductor lasers was the fabrication of heterostructures composed of layers of different direct bandgap, lattice-matched, semiconductor materials. As a result, a better optical confinement was achieved, leading to enhancement of stimulated emission. This major advancement made available semiconductor laser devices operating at room temperature with relatively high power-conversion efficiency.

The development of semiconductor lasers was primarily boosted by their application in optical fiber-based telecommunication industry in 1970's. The motivation laid in the fact that fiber-optic communication could allow to achieve THz bandwidth communication links and yet semiconductor lasers (SL) emerged as suitable light for such applications. If compared to their counterpart gas lasers, SL are low-cost, compact, small in size and long-life devices with a very good efficiency. Moreover, they allow high, GHz modulation speeds which are appropriate in the growing data communication market. The widespread use of internet and related applications, like voice and/or video over internet, are now pushing the thirst for bandwidth to higher limits where optical technologies are expected to compete with the traditional dominating electronics. Nowadays, the concept of all-optical handling is progressively making its own pace and may possibly lead to a paradigm shift in the telecommunication industry. A number of fundamental and applied research activities are increasingly carried out in order to

achieve, for example, all-optical switching and other signal processing functionalities which support such a trend, and for which semiconductor lasers are expected to play an important role.

Apart from their application in the telecommunications sector, semiconductor lasers are also present in several applications which can be found in our daily life, e.g., CD-ROM, DVD players, printers, code bar readers and other data storage and readout technologies. They are also very useful in a range of more specialized applications like optical spectroscopy [5, 6], optical sensing [7], optical metrology [8] and optical computing [9].

In terms of emission and geometrical structure, semiconductor laser technology has been dominated by the so-called Edge-Emitting Lasers (EELs) in which a linearly polarized beam, parallel to the active medium plane, is emitted through a partially reflecting output facet. More recently, the concept of surface emission has captured much attention and has led to the emergence of Vertical-Cavity Surface Emitting Lasers (VCSELs) which are expected to play a key role in the semiconductor market owing to their competitive advantages with respect to EELs [10]. By contrast to EELs, VCSELs emission is achieved along a direction which is perpendicular to the active medium plane. VCSELs are also characterized by particular polarization properties which are interesting on both the fundamental and application viewpoints. In fact VCSELs usually emit a linearly polarized light oriented along one of two orthogonal preferential axes. However this polarization is not fixed and a change in operating conditions may lead to polarization switching between the two linearly polarized modes.

Regardless of their geometrical structure (EELs or VCSELs), semiconductor lasers are sensible to external perturbations. When part of the emitted light is reflected back into the laser cavity, the laser is said to be subject to optical feedback. A semiconductor laser may be injected by another laser, in which case it is said to be subject to external optical injection. Another perturbation may also derive from the modulation of the injection current. Instead of a steady-state dynamics typical for a free-running laser, the output characteristic of a semiconductor laser subject to either one of external perturbations can exhibit a wide range of nonlinear instabilities. For example, when a specific parameter control associated to a given perturbation is adequately swept, the laser may undergo periodic dynamics, self-pulsating or even more complex chaotic dynamics [11]. Usually, the onset of such nonlinear dynamics occurs at a bifurcation point where a qualitative change in the laser output is observed.

Nonlinear dynamics commonly observed in semiconductor lasers are found to be generic features of diverse nonlinear systems encountered in physics, biology, chemistry and engineering sciences. There has been a growing interest in studying nonlinear dynamics induced by external perturbations in



---

semiconductor lasers. On the fundamental viewpoint, because its control and operating parameters can be easily tuned, the externally perturbed semiconductor laser system provides a high level of flexibility for investigating complex nonlinear dynamics. Furthermore, the advancement in theoretical laser modelling, together with affordable computation tools, has contributed to a better understanding of how qualitatively different nonlinear dynamics and their underlying bifurcations are organized [12]. This achievement is very attractive for the control of nonlinear dynamics in semiconductor laser systems.

While externally induced laser instabilities can intuitively be viewed as undesirable phenomena, it turns out that they can also be very useful for applications. For example, one can use optical injection-induced nonlinear dynamics to achieve frequency conversion in radio-over-fiber (ROF) applications [13], or to realize the selection and amplification of modes of an optical frequency comb which is useful in high-precision spectroscopy [14]. Optical chaos has also attracted much attention due to its attractive application in secure chaos-based communication schemes. The underlying operating principle is based on synchronization of two coupled chaotic semiconductor lasers. A first field experimental implementation of chaos communication has been demonstrated in Athens on a commercial fiber-optics communication link [15].

This thesis is mainly devoted to the study of external optical injection in Vertical-Cavity Surface-Emitting Lasers (VCSEL). The study of SL subject to external optical injection has been widely investigated in the case of EEL and a detailed picture of the underlying nonlinear dynamics has been provided [16]. In the case of VCSELs, the intrinsic polarization degree of freedom is expected to play a key role in the dynamical response of the VCSEL subject to optical injection. Therefore, a comprehensive understanding of the interplay between polarization and nonlinear dynamics induced by optical injection is needed. The motivation is twofold. On the one hand, such a study *contributes to the control of the polarization* which is important in VCSEL-based polarization sensitive applications. On the other hand, we believe that a better understanding of *nonlinear polarization dynamics* is indispensable considering the growing interest in VCSELs as suitable devices for fast all-optical switching and signal processing. In addition, a VCSEL under optical injection may exhibit chaos simultaneously in both orthogonal polarization modes. This can contribute to the study of multimode chaotic systems which have been little investigated so far.

The present work is organized as follows. In chapter 2, the basics of semiconductor lasers are presented. We briefly expose the main mechanisms underlying the operation of the free-running semiconductor laser as a nonlinear device. We begin by first describing the edge-emitting laser (EEL)

before presenting the vertical-cavity surface emitting laser which constitutes the device under study throughout this thesis.

In chapter 3, we focus on the polarization properties of VCSELs which are quite different from the ones in EELs. We review different physical mechanisms that have been proposed to explain VCSEL's intriguing polarization switching properties. The so-called spin-flip model (SFM), used to model the free-running VCSEL polarization properties, is described. Two types of polarization switching commonly observed in the VCSEL light-versus-current characteristics are experimentally analyzed and theoretically discussed using the SFM model. The issue of semiconductor laser subject to external perturbations is reviewed. We particularly focus on external optical injection as a way to control the VCSEL polarization properties.

Orthogonal optical injection in VCSELs is introduced in Chapter 4. Optical injection intensity-induced bistable polarization switching (PS) is experimentally and theoretically investigated. The switching is obtained by varying the intensity of the injected signal for a fixed frequency detuning between the master laser and the free-running VCSEL. The dependency of the switching power on the frequency detuning is analyzed. We show that the VCSEL birefringence determines not only the minimum power for which PS is achieved but also whether PS is achieved with or without injection-locking of the VCSEL to the master laser frequency. We furthermore show that the VCSEL bias current is a key parameter for controlling the evolution of the hysteresis loop width associated to the optical injection intensity-induced bistable PS. Furthermore, pure-frequency induced polarization bistability in a VCSEL subject to orthogonal optical injection is theoretically investigated. In this case, the frequency detuning is scanned for a fixed injection power. We show two successive polarization switching points when sweeping the detuning and investigate the associated bistability properties, in particular the impact of injection strength on the width of the hysteresis loop. In qualitative agreement with a previous experimental result, we show that the hysteresis loop width associated with one of the frequency-induced PS point exhibits a maximum for a specific value of injection strength. We also show that the width of the bistable region depends on device parameters such as the linewidth enhancement factor.

Under orthogonal optical injection, the coupling between the injected field and the VCSEL polarization modes may lead to nonlinear dynamics when the optical injection parameters are tuned. In Chapter 5 we provide a detailed experimental investigation of polarization switching and locking mechanisms in a VCSEL subject to orthogonal optical injection. Depending on the injection parameters, i.e., injected power and frequency detuning between the master laser and the injected VCSEL, we observe qualitatively different scenarios of PS and locking. We report on rich dynamics including

---

limit cycle, wave mixing and period doubling route to chaos and we analyze their strong interplay with PS mechanisms.

In Chapter 6 we theoretically analyze the bifurcations underlying polarization switching (PS) and locking mechanisms in a VCSEL subject to orthogonal optical injection. We unveil the interplay between PS and nonlinear polarization dynamics using both standard numerical integration methods as well as modern continuation techniques. We carry out a detailed mapping of different bifurcations in the optical injection parameter plane, thus providing a detailed dynamical picture of the switching and locking mechanisms. Furthermore, we show that, in addition to the so-called saddle-node and Hopf bifurcations previously reported in the case of optically injected edge emitting lasers, two new bifurcations (namely a second Hopf and a torus bifurcations) play a key role in the switching and locking dynamics. We show that the dynamics associated to the onset of the torus bifurcation are in good qualitative agreement with our experiments in Chapter 5.

Throughout this thesis, the free-running VCSEL is mainly operated in the fundamental transverse-mode regime. This is achieved by setting the bias current at a value which is much lower than the higher-order transverse mode threshold. In chapter 7, transverse mode switching and locking in VCSELs subject to orthogonal optical injection is theoretically and experimentally investigated. We show that the switching power is minimal at two different frequency detuning values. The first minimum is resolved for a detuning close to the frequency splitting between the two linearly polarized fundamental transverse modes. On the other hand, the second minimum is achieved for a much larger positive detuning close to the frequency offset between the first order and the fundamental transverse modes of the free-running VCSEL. For a relatively large detuning range, both our experimental and theoretical results unveil that the first order transverse mode appears locked to the master laser frequency and is accompanied by a strong suppression of the fundamental transverse mode.

In chapter 8 we analyze chaos synchronization of two unidirectionally coupled VCSELs. In the preceding injection schemes, investigated from chapter 4 to 7, the slave VCSEL was injected by a linearly-polarized continuous-wave (CW) master laser. In this chapter, the master VCSEL is subject to a delayed optical feedback and may exhibit a chaotic regime. We consider an open-loop configuration, i.e., the slave laser is without feedback and is only submitted to optical injection from the master laser. The master laser is subjected to an isotropic feedback and, depending on the feedback strength, may exhibit chaos in the two orthogonal linearly polarized (LP) modes. Synchronization is studied in both isotropic and polarized orthogonal injection schemes. In the case of isotropic injection coupling, we show that the synchronization quality between the two VCSELs can be significantly enhanced when the

feedback-induced chaos in the master laser involves both fundamental orthogonal LP modes. However, a strong degradation of the synchronization quality is found when the master VCSEL operates in a single mode chaotic regime. In the orthogonal injection scheme, the master laser LP mode which is parallel to the dominant LP mode of the free-running VCSEL is first selected and rotated to an orthogonal polarization direction before being injected into the slave VCSEL. In this configuration we study the synchronization when the injection parameters, i.e., injection strength and frequency detuning between master and slave VCSEL are tuned. We unveil two qualitatively different synchronization regions in the injection parameters plane: the first one (named region I), which corresponds to an injection-locking synchronization mechanism, involves only the injected mode and the second one (named region II) involves both orthogonal LP modes. In region II we find that, for all the injection rate range, the injected mode is almost perfectly synchronized to the master laser mode, a result which agrees qualitatively well with a recent experimental result. We analyze the effect of the spin flip relaxation rate on the synchronization behavior and show the robustness of our results to parameter mismatch, which is inevitable in realistic configurations using coupled semiconductor lasers.

Finally, in chapter 9 we conclude with a summary of our PhD work and present the perspectives related to our present achievements.

## Chapter 2

# Edge-emitting and surface-emitting semiconductor lasers

In this chapter, the basic physical concepts underlying the semiconductor laser operation are presented. The conditions for achieving stimulated emission are briefly introduced and some technological aspects of semiconductor laser structures, which aim at optimizing its operation, are explained. We first present the conventional edge-emitting laser (EEL) before studying the Vertical-Cavity Surface-Emitting Laser (VCSEL) structure. We highlight the numerous advantages of VCSEL with respect to EELs and also compare the two devices on the basis of their optical properties. Of particular interest are the VCSEL polarization properties.

### 2.1 Edge-emitting semiconductor lasers

As in most laser systems, to achieve light amplification by stimulated emission of radiation in a semiconductor laser, two basic ingredients are needed. The first one is a gain medium in which light amplification can be realized. The second one is a positive feedback mechanism which allows both the regeneration of part of the light (thus enhancing the amplification) and the wavelength selection. A schematic view of a semiconductor edge-emitting laser (EEL) is plotted in Fig. 2.1.1. The commonly used configuration is a double-heterostructure in which a thin active region (which serves as gain medium) is sandwiched between two claddings layers. The active region is a narrow direct band-gap semiconductor which can be either intrinsic, n- or p-doped semiconductor while the cladding layers are respectively p-

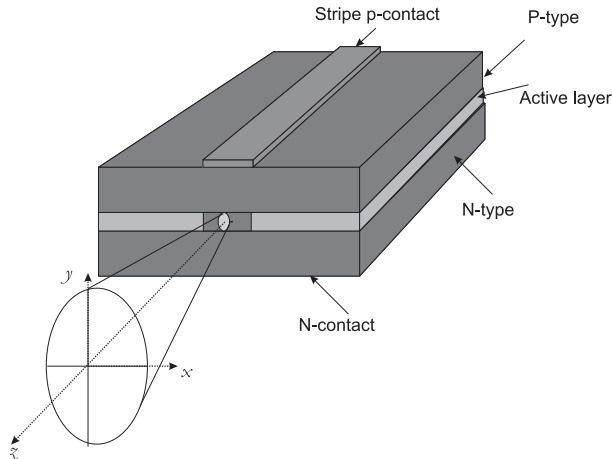


**Figure 2.1.1:** Schematic view of an edge-emitting laser.

and n-doped direct bandgap semiconductors. Typically, the active layer and the claddings are made from lattice-matched semiconductor materials. The band-gap of the active region is usually smaller than that of the claddings.

The basic mechanisms underlying the lasing operation in the double-heterostructure are shown in Fig. 2.1.2 when the device is forward biased as shown in Fig. 2.1.2(a). The corresponding energy band diagram is sketched in Fig. 2.1.2(b) where the evolution of the lowest energy level of the conduction band ( $E_c$ ) and that of the highest level of the valence band ( $E_v$ ) are shown. Under forward bias voltage, the Fermi-level splits into quasi-Fermi level of the conduction band ( $E_{F_c}$ ) and quasi-Fermi level of the valence band ( $E_{F_v}$ ) [17]. Electrons flow from the n-doped cladding to the active layer while holes flow from the p-doped cladding to the active medium. Since the band-gap in the claddings layer is larger than that of the active medium, the resulting potential barriers confine the injected carriers in the active layers and therefore large concentration of electron-hole pairs can be reached. In the active region, both radiative and non-radiative electron-hole recombination processes are possible. In a radiative electron-hole recombination process, a photon is generated when an electron from the conduction band relaxes and recombines with a hole in the valence band. Two radiative recombination processes coexist: the spontaneous and stimulated emission. Spontaneous emissions correspond to photons which are emitted in different direction with uncorrelated phase, leading to incoherent radiation. On the other hand, in the case of stimulated emission (on which the laser operation is based) a photon may stimulate an electron-hole recombination which coherently generates another photon with the same frequency  $\nu$  (or equivalently with the same energy  $h\nu$ ), phase and direction as the incoming one [Fig. 2.1.2(c)]. In a non-radiative electron-hole recombination, the process

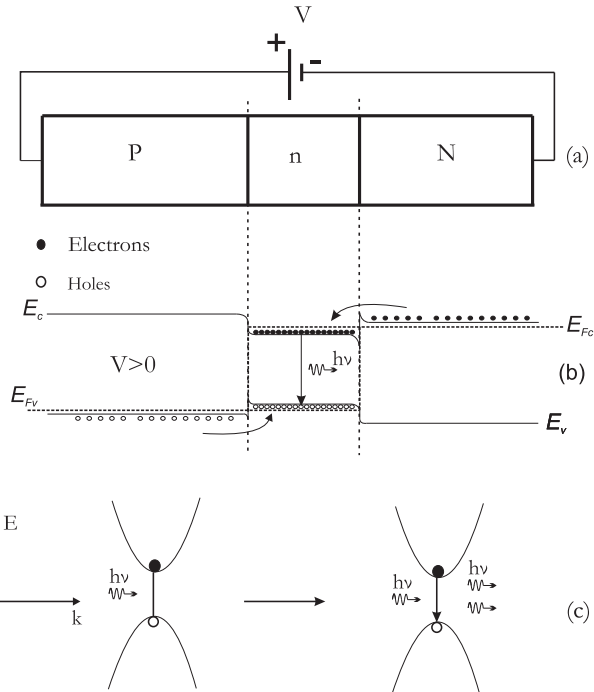


**Figure 2.1.2:** Schematic representation of the energy level diagram of a double heterostructure semiconductor laser. (a) Cross-sectional view of a P-n-N heterostructure for which an n-doped narrow band-gap active semiconductor layer ( $n$ ) is sandwiched between wide band-gap cladding layers which are, respectively, p-doped (P) and n-doped (N) semiconductors. (b) The lowest energy level of the conduction band,  $E_c$ , and the highest level of the valence band,  $E_v$ , are represented when the device is forward biased such that population inversion is achieved. (c) The mechanism of stimulated emission is also sketched in the  $E - k$  plane using the parabolic approximation of the energy band structure.

is not accompanied by any electromagnetic radiation. For example, the released energy in a non-radiative recombination can be converted into thermal energy which may result from lattice vibrations [17].

Because stimulated emission competes with other mechanisms (spontaneous emission, non-radiative recombination processes), a positive net rate of the stimulated emission is required to achieve the lasing action. This is the case when population inversion is achieved, i.e., the electron and hole concentrations in the active layer lead to a positive optical gain. This condition is reached when the separation of the quasi-Fermi levels of the conduction and valence bands is larger than the photon energy at the frequency  $\nu$ :  $\Delta E_F = E_{F_c} - E_{F_v} > h\nu > E_g$  [17], where  $E_g$  is the Energy band-gap of the active layer. The laser reaches the so-called transparency operating point

when the stimulated emission rate is equal to zero.

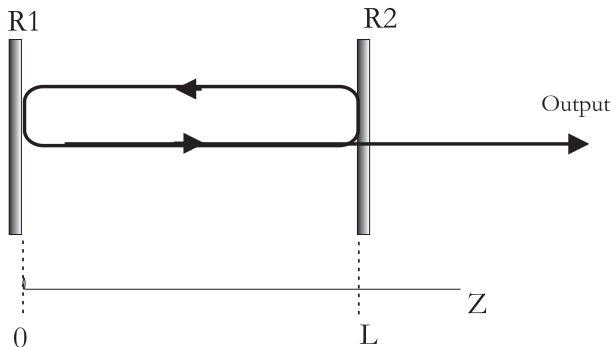


**Figure 2.1.3:** *Schematic view of a Fabry-Perot resonator.*

As aforementioned, for a sustained regenerative amplification of light to take place in a semiconductor laser, a positive feedback mechanism is achieved by placing the the gain medium (the active layer) in a Fabry-Perot optical resonator formed by two cleaved edge facets which delimit the device. In such a configuration the lasing action is achieved along the waveguide axis parallel to the active layer plane. In Fig. 2.1.3, a sketch of the Fabry-Perot resonator is provided. The two mirrors can be associated with the cleaved edge facets of the semiconductor laser. There is a difference in refractive index between the active semiconductor medium and the environment (air) which gives a Fresnel reflectivity of about 30% of the light, thus about 70% escapes outside the cavity [18]. The facet reflectivity is sufficient to maintain the lasing in the cavity, thanks to the high optical gain in the active layer. The cavity defines the boundary conditions and hence the wavelength of lasing optical modes. Due to the relatively long cavity length typical for EEL (a few hundreds of  $\mu\text{m}$ ), they are usually characterized by a longitudinal multimode emission. Moreover, the strongly asymmetric geometrical structure of EELs implies that they emit a linearly polarized light.

In order to satisfy the lasing operation, one needs sufficient gain to overcome optical losses. The threshold gain can be derived from the so-called unity round-trip condition, a situation in which there is a balance between gain and losses [18]. The condition writes:

$$G_{th} = \frac{1}{\Gamma} \left[ \alpha_{abs} - \frac{\ln(R_1 R_2)}{2L} \right] \quad (2.1.1)$$

Where  $R_1$  and  $R_2$  are the edge facet reflectivities,  $\Gamma$  is the confinement factor (which defines the overlap of the cavity mode with respect to the active region cross section).  $L$  is the laser length while  $\alpha_{abs}$  represents the optical losses. The gain threshold determines the threshold bias current which depends strongly on the cavity layer thickness. If one assumes that the confinement



factor is approximately constant, by reducing the active layer thickness, one may significantly reduce threshold current [18]. It is worthy noting that above threshold, the increase of the pump current usually leads to an almost linear increase of the intensity of the lasing mode in the cavity. Moreover, the operating conditions above threshold are such that the gain becomes saturated by the laser intensity in the cavity.

Since the refractive index of the active region is larger than that of the cladding, there is a waveguiding effect which efficiently confines the stimulated emission within the active region. In order to improve laser performances, several techniques are used to enhance optical and/or carrier confinements. For example, lateral optical confinement is obtained by restricting the carrier injection to a small region along the active region length. This is the case when a stripe contact geometry is adopted. However there is a difference in the size of vertical ( $y$  axis) and lateral ( $x$  axis) confinement regions which leads to elliptical profile in transverse cross-section of the light beam (see Fig. 2.1.1). Other methods for lateral optical confinement are based on index-guiding techniques, in which the lateral carrier distribution is defined by the width of the index-guiding stripe. To this end, several structures, such as buried or channelled-substrate heterostructures have been proposed [17].

The semiconductor technology is now dominated by quantum-well (QW) devices in which quantum confinement for the carriers is achieved by significantly reducing the active layer thickness. This results in the splitting of both the conduction and valence bands into discrete levels. Due to the strong reduction of the active layer thickness, QW semiconductor lasers with relatively low threshold currents are available.

## 2.2 Vertical-Cavity Surface-Emitting Lasers (VCSEL)

### Historical overview

The development of Vertical-Cavity Surface-Emitting Lasers (VCSEL) is an important achievement in the semiconductor laser industry. The difference between VCSELs and edge-emitting lasers (EEL) resides substantially in their geometrical and design structure. In a VCSEL, the resonant cavity is engineered in a way that stimulated emission is achieved in the direction perpendicular to the p-n junction plane and the substrate. The concept of vertical-cavity surface emitting laser was first demonstrated by Iga's group at the Tokyo Institute of Technology in 1979 [19]. At that time, the proposed VCSEL was a GaInAsP/InP device operating at a wavelength of 1.3  $\mu\text{m}$ . However, the poorly reflective cavity mirrors combined with the large

cavity size implied that the device operated only in a pulsed mode, with very high threshold currents (900 mA) and at low temperature (77 K). A GaAlAs/GaAs-based VCSEL emitting around 874 nm and operating in a pulsed mode regime at room temperature was demonstrated in 1983 [20]. After, the same group developed a GaAlAs/GaAs-based VCSEL with 6 mA threshold and operating at room temperature but still in pulsed regime [21]. The crucial milestone in the development of VCSELs was reached with the use of epitaxially grown distributed Bragg reflectors as highly reflective cavity mirrors ( $\approx 99\%$  of reflectivity). Using this technique, in 1989 Jewel *et al.* demonstrated a quantum-well VCSEL based on InGaAs material with 1 to 2 mA threshold and operating in pulsed regime at room temperature [22]. The same year, Lee *et al.* [23] demonstrated the first VCSEL working at room temperature, in a continuous wave operating regime, with a relatively low threshold current ( $\approx 1.5$  mA). Following this development, an intensive research activities took place aiming at optimizing the VCSEL performances [24, 25, 26]. As a result, reliable VCSELs are now commercially available for a relatively large range of applications.

### VCSEL's structure

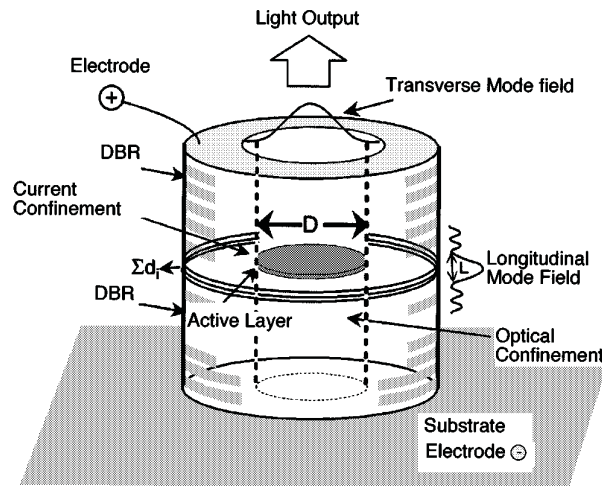


**Figure 2.2.1:** Schematic view of a Vertical-Cavity Surface-Emitting Laser (VCSEL), after [27].

The typical structure of a VCSEL is schematically represented in Fig. 2.2.1. The active region is a very thin multi-quantum well (MQW) semiconductor layer (the thickness of a quantum-well is typically 5-10 nm) which is arranged between two distributed Bragg reflectors (DBR) with high, but slightly different, reflectivities (higher than 99%). To adapt to the output coupling of light from the output mirror, the output DBR has a lower reflectivity than that of the second DBR. The quantum-well structure was adopted to improve the

gain efficiency of the inherently thin active region. The two DBRs are stacks of thin, quarter-wavelength thick, layers with alternating refractive indices which hence constitute index-modulation gratings [17]. Since carriers are injected into the active region vertically through the DBRs, the top and the bottom DBRs are respectively p- and n-doped in order to increase their conductivity and hence decrease ohmic losses which may otherwise dramatically affect the VCSEL performance.

To improve the VCSEL performances, further refinements in the design were made in order to obtain devices which operate at low threshold currents and in which both optical and carrier confinements are achieved. To decrease the threshold current the lateral dimension of the active layer was substantially reduced [10]. A better carrier confinement could be achieved by using several techniques [27]: e.g., 1) a ring-type electrode contact which limits the injection to a selected area of the VCSEL output facet; 2) a proton-bombardment which creates an insulating areas that limit current spreading; 3) a buried heterostructure-type for which a mesa with a wide band gap semiconductor is used to limit the current. Other configurations are 4) air-post; 5) selective oxidation using AlAs and 6) oxidized DBR type.

Interestingly, some structures can allow achieving both carrier and optical confinements. For example, in the mesa air-post structure an index-guiding effect is obtained as a result of the refractive index step at the mesa interface. On the other hand, the proton-implanted configuration as well as buried heterostructures can be seen as gain-guiding devices since the field is limited to the region where the gain exists, resulting in a lateral optical confinement.

Both current and optical confinements can be efficiently achieved in the so-called oxide-confined structure. Oxidized apertures with lower refractive index material are properly designed in the VCSEL structure such that an index guiding effect for optical confinement is obtained. The highly resistive oxidized layer allows also efficient carrier confinement.

### **VCSEL emission properties.**

The emission properties of VCSELs are dictated by the cavity geometry, the bandwidth of the DBRs and the gain profile of the amplifying medium in the active region. The geometrical structure plays a key role in that it determines the allowed resonant cavity modes. The bandwidths of the DBRs and the material gain profile act as optical filters since they contribute to the selection of the lasing modes. Longitudinal and transverse optical mode patterns of VCSELs are schematically presented in Fig. 2.2.1. The resonance frequencies of the longitudinal modes and their frequency mode spacing are mainly determined by both the thickness of the active region and the optical characteristics of the DBRs, e.g., the Bragg effective phase length. However the total effective phase length of the cavity remains relatively short ( $\approx 1$

to 2  $\mu\text{m}$ ), leading to a relatively large longitudinal frequency mode spacing [17]. Due to their relatively short cavity, VCSELs are usually characterized by a single longitudinal mode emission.

The geometry and the size of the cross-sectional plane perpendicular to the emission axis determine the spatial distribution as well as the number of VCSEL's transverse cavity modes. Typically, in addition to the fundamental transverse mode, VCSELs are also characterized by the existence of higher order transverse modes. Depending on the operating conditions, e.g., the injection current and/or the temperature of the device, it has been demonstrated that both the fundamental and higher order transverse modes may compete for the gain [28, 29, 30, 31, 32]. Using proton-implanted gain guided devices, Hasnain *et al.* [29] experimentally showed that near threshold VCSELs emit only in fundamental transverse mode while for higher currents the onset of higher order transverse mode was also observed. A comprehensive understanding of transverse mode behaviors has been achieved [31] by taking into account both the spatial mode field distribution and the spatial distribution of the carriers in the active region. In particular, it was demonstrated that the interplay between carrier injection/diffusion and modal field distribution, giving rise to spatial hole burning, dictates the VCSEL emission characteristics, i.e., single- or multi-transverse steady state operation.

In some applications, a single transverse mode operation is highly needed. Several design improvements have been proposed in order to obtain single transverse mode devices. By reducing the transverse size of the active medium, monomode VCSELs can be achieved but this may seriously hamper the device power performance. Other solutions consist of using a metallic disk contact layer which acts as spatial optical filter [33]; an etched surface relief which spatially modifies the effective index and cavity losses [34] or buried heterostructures in oxide-confined VCSELs [35].

VCSEL are typically characterized by a symmetric transverse geometry which allows for a circular, symmetrically divergent, output beam. Unlike EELs which exhibit a fixed linear polarization due to their strongly asymmetric geometry, the symmetric transverse structure of VCSELs may lead to polarization instabilities since there is no any *a priori* polarization discrimination. However, despite their symmetrical geometry, a small unintentional structural anisotropy introduced in the crystal during the fabrication process leads to the existence of two preferential orthogonal polarization axes. Typically, VCSELs emit a linearly polarized light beam oriented along one among the orthogonal polarization axes. For example, it has been found that the polarization of a device grown on a (100)-oriented substrate is preferentially oriented along [110] or  $[1\bar{1}1]$  [10]. Unless special precautions are taken to stabilize the polarization, VCSEL can exhibit polarization instabilities when changing its operating conditions such as bias current or temperature.

Those instabilities manifest as switchings between orthogonal polarization axes [36]. The issue of polarization switching and its underlying mechanisms will be discussed in the subsequent chapters.

### **Applications.**

VCSELs are now used in a wide range of applications in the optoelectronic and telecommunication industries, because of their competitive advantages with respect to EELs. In fact, due to their symmetrical structure, VCSELs emit a circular beam which allows easy coupling to optical fibers. Very low threshold currents ( $< 1$  mA) can be achieved due to small cavity volume, hence increasing VCSEL's modulation capabilities [10]. Most interestingly, the vertical emission from the substrate allows fabricating dense two-dimensional (2D) VCSEL arrays which are very attractive in a number of applications including parallel high speed optical communication links, optical interconnects, optical computing, optical switching and signal processing. In addition, an on-wafer testing can be performed on 2D VCSEL arrays before they are separated into discrete devices, hence substantially reducing the production cost [10].

An extensive research has been undertaken to fabricate VCSELs for dedicated applications in the long and mid-wavelength windows to infra-red, visible or even ultra-violet ranges [10]. Long-wavelength VCSELs emitting in the 1.2-1.5  $\mu\text{m}$  window are very promising for single-mode-fiber metropolitan and even wide area networks [37]. VCSELs emitting around 0.85  $\mu\text{m}$  are currently key devices in the short distance local area networks (LAN) using multimode silica-based fibers [38]. There is a growing interest in fabricating multiwavelength VCSEL arrays operating around 0.85  $\mu\text{m}$  due to their potential in high bit rates ( $> 10$  Gb/s) wavelength division multiplexing (DWM) technologies [39]. On the other hand, red-color VCSELs emitting at around 0.65 $\mu\text{m}$  are very attractive for the short-distance Gigabit, low cost, data links using plastic optical fibers [40]. Red-color VCSEL emitting in the range of 0.63 $\mu\text{m}$ -0.67 $\mu\text{m}$  are interesting for the video disk system. In the green-to-UV window, VCSEL may be useful for high density optical memories.

There are interesting application areas where VCSELs are also expected to play a major role. For instance for wavelength-tunable lasers, a 2D continuous tunable VCSEL using a microelectromechanical system [41] or an electrothermal system [41] have been demonstrated. For signal processing, VCSEL-based all-optical format conversion using polarization switching techniques has been demonstrated. However the system requires a complex configuration system for polarization control [42].

Despite the fact that VCSELs are expected to play a key role in the growing photonics market, the issue of polarization instabilities has still to be addressed. This is mostly the case in photonics integrated systems in which VCSELs may be subject to external perturbation. In the following chapter, polarization properties of a free-running VCSEL are presented before investigating the situation in which an external perturbation is considered. As mentioned in our introduction, we will mostly focus on the case of a VCSEL subject to external optical injection.

## Chapter 3

# Polarization properties of VCSELs

In Chapter 2, we focussed on the difference between VCSEL and the conventional EEL in terms of their geometrical structure and emission properties. In particular, we mentioned that, due to their symmetrical structure, VCSELs exhibit intriguing polarization properties which may strongly affect their operation. In this chapter, we first investigate polarization switching (PS) properties of a free-running VCSEL. By free-running, we mean a standing alone, direct-current (DC)-biased VCSEL, exempt of any external perturbation. We first review the physics underlying the PS mechanism and then present a theoretical model which supports PS. We study the VCSEL polarization switching behavior by analyzing the numerically computed as well as experimental polarization-resolved light-current characteristics. We then introduce the issue of semiconductor lasers under external perturbations in general, i.e., when the laser is subject to current modulation, to optical feedback from an external mirror or to optical injection from another laser. Previous results reporting the possible effect of these perturbations on the VCSEL polarization properties are reviewed. We pay a particular attention to optical injection which mostly concerns our thesis.

### 3.1 Polarization switching

While describing the emission properties of VCSELs in chapter 2, we mentioned that despite their geometrical symmetry, a small unintentional anisotropy, introduced during the manufacturing process, explains the existence of two preferential linear orthogonal states [43, 44]. The two eigen polarization states are characterized by slightly different refractive indices [43, 44]. Indeed, the existence of this birefringence plays a key role in the VCSEL's

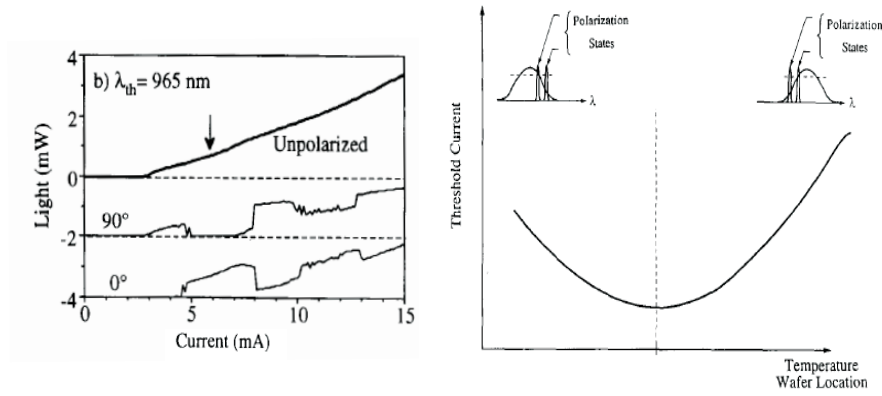


**Figure 3.1.1:** Polarization switching in VCSEL as an effect of current heating (left). Illustration of the redshift in both the material and polarization-resolved modal gain (right).  $0^\circ$  and  $90^\circ$  denotes the two orthogonal polarization states, after [36].

polarization properties. Choquette *et al.* [36] experimentally demonstrated that near threshold, VCSELS emit in the fundamental transverse mode along one of the two orthogonal polarization states (denoted  $90^\circ$  in Fig. 3.1.1, left panel). At such injection current levels, this is mostly attributed to a better overlap between the fundamental cavity modes and the material gain [31]. As the injection is increased, a polarization switching to the orthogonally polarized, frequency-shifted, fundamental mode can be observed. For higher currents, as also reported by Hasnain *et al.*, higher order transverse modes may also be excited, typically with a polarization orthogonal to that of the fundamental mode [29]. Here, we focus our attention on the physical mechanisms which underly the switching between fundamental transverse modes. We review the state of the art of experimental as well as theoretical studies which have been carried out by several research groups in order to elucidate polarization switching in VCSELS.

In their attempt to explain what they observed experimentally, Choquette *et al.* [36] attributed the polarization switching (PS) mechanism to the spectral shift of the material gain maximum relative to the cavity resonance modes, due to current heating. As illustrated in the right panel of Fig. 3.1.1, the conditions for a minimum threshold current are reached at a temperature where the cavity mode resonances match well with the material gain maximum. Outside this optimal temperature, the gain maximum is either red-shifted (see the right inset in right panel in Fig. 3.1.1) or blue-shifted (see the left inset in the right panel in Fig. 3.1.1) with respect to the cavity mode resonances. As a result, in each case, after crossing the threshold, the mode with higher gain is expected to lase first and the second



mode is depressed. However by increasing the current, both the gain and the resonances are red-shifted, i.e., they are moved towards longer wavelengths (or, equivalently, to smaller frequencies). However, the gain curve is shifted faster than the cavities modes. According to Choquette *et al.*, PS is expected if the laser starts lasing on the longer wavelength side of the gain maximum (see the left inset of the right panel in Fig. 3.1.1). In this particular case, PS occurs from the shorter-wavelength mode to the longer-wavelength one after crossing the maximum gain, i.e., after cavities modes are shifted to the shorter-wavelength side of the maximum gain.

The physical interpretation of the switching from the shorter-wavelength to the longer-wavelength mode (type I PS), based solely on the current heating-induced gain spectral shift, revealed insufficient to explain other intriguing VCSEL polarization behaviors. In fact, it was found that some VCSELs could also exhibit a switching from the longer-wavelength mode to the shorter-wavelength one (type II PS) or, for other devices, one could even successively observe both type I and type II PS as the current is increased. To address this particular switching behavior, another complementary model suggested to include also the photon energy and temperature dependence of the total losses, in addition to that of the gain [45].

Polarization switching was also experimentally reported for another interesting situation in which the cavity resonance modes were located on the shorter-wavelength side of the gain maximum. In order to understand such a switching scenario, another physical interpretation based on thermal lensing effects was proposed by Panajotov *et al.* [46]. They demonstrated that an increase in the current heating enhances a thermal waveguiding mechanisms which may, in turn, decrease the difference in the modal gains of the two orthogonally polarized modes. Due to this effect, at low dissipated power (low injection levels), the mode with the shorter wavelength may exhibit a larger modal gain though the VCSEL is working on the shorter-wavelength side of the material gain maximum. As the current is increased, enhancement of the thermal waveguiding may then reverse the sign of the difference in the modal gains in such a way that PS from the shorter wavelength to the longer wavelength can be achieved.

Switching between the fundamental transverse modes can also be explained as a result of the modification in the carrier density profile due to spatial hole burning. Typically, this phenomenon is expected in weakly index-guided VCSELs for which the difference in the refractive index between the core and the cladding is relatively small [47]. Due to birefringence, the fundamental orthogonal modes are not equally confined, i.e., they exhibit different modal gains such that the gain difference between them is positive close to the core of the device and negative near the edge of the device. For low currents, the carrier density is larger at the center of the device where the

fundamental modes, with gaussian intensity profiles, are well confined. The lasing mode is the one oriented along the high index polarization direction due to a better confinement. However, increasing the injection current will change the carrier distribution profile due to spatial hole burning. In fact, increasing the current enhances stimulated emission near the core where the field is more confined, hence leading to a decrease in the carrier density in that region. As a result, an accumulation of carriers near the edge of the device is observed. Since the orthogonal fundamental mode exhibits larger modal gain near the edge, the increase of carrier density in this region may lead to PS.

So far, the polarization switching mechanism was explained as a result of the effect of the injection current on the difference of material or modal gains between the orthogonal polarization states. Another approach is based on a four-level model as proposed by San Miguel, Feng and Moloney [48]. Two sublevels of the conduction and the valence bands are associated to transitions of carriers with opposite spins. Spin-flip relaxations, a mechanism which tends to homogenize the spins, are phenomenologically introduced. The switching between two linearly polarized modes is achieved as a dynamical phenomenon which manifests as nonlinear instabilities. In the next section, we summarize the fundamentals of the Spin-Flip Model (SFM) and present numerical simulations which qualitatively support a polarization switching scenario we experimentally observe.

Polarization switching may constitute a major VCSEL's drawback in polarization sensitive applications. Several methods have been proposed to produce VCSELS with a fixed dominant polarization by breaking the symmetry in the device structure at the fabrication level. For example, one may introduce anisotropic gain by designing an asymmetric active region [49, 50, 51]. Polarization can also be fixed by introducing anisotropic stress from an elliptic etched substrate hole; by utilizing a birefringent Bragg reflector [52]; a tilted pillar structure [53] or a rectangular post [54]. Though these methods may efficiently fix the polarization, they may however introduce additional design complexities which may impact the fabrication costs. An alternative approach consists of controlling the polarization by breaking the symmetry from outside, i.e., by introducing an external degree of freedom. It has been recently demonstrated that using an extremely short external cavity one may successfully achieve VCSEL polarization control by optical feedback [55, 56, 57, 58]. As it will be shown in Chapter 4, using a master-slave configuration, external optical injection can also realize polarization control and/or stabilization.

## 3.2 Modelling of polarization switching using the Spin-Flip Model (SFM)

### 3.2.1 The four-level energy system

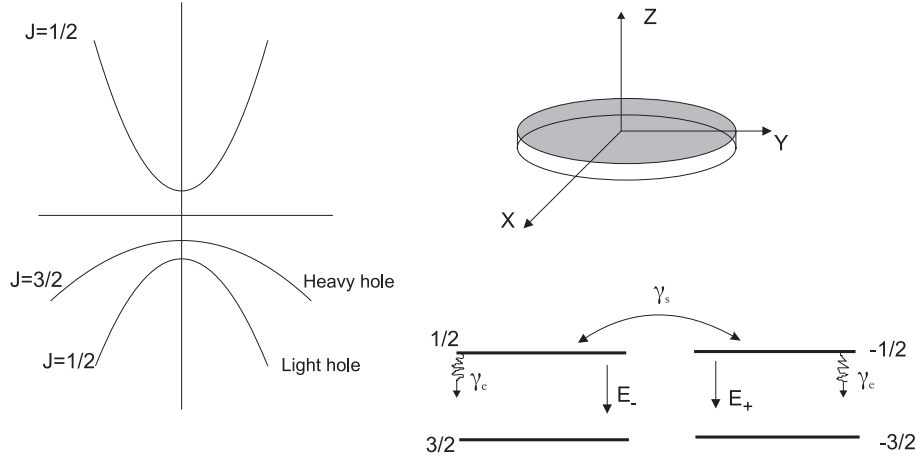


**Figure 3.2.1:** Band structure of a quantum well (left) and four-level model for radiative transitions (bottom right). The surface emission and transverse eigen axes are shown (top right). After [48].

The Spin-Flip Model (SFM) has been extensively used to explain polarization switching mechanism in VCSELs [48, 59, 60, 61]. Here, we present the main physical concepts underlying the four-level model in which the light polarization is taken into account. As usual for the modelling of semiconductor lasers, a semiclassical approach has been adopted, i.e., the gain medium and its related dipolar polarization are treated quantum-mechanically while the laser field is introduced classically. From the resulting Maxwell-Bloch equations one obtains the rate equations used to describe the dynamics.

In the framework of the SFM model, the polarization of light is accounted for by considering the angular momentum of the quantum states which are involved in the transitions for emission and absorption within the semiconductor material. Typically, the VCSEL active medium is a quantum-well structure in which light emission is achieved perpendicularly to the transverse plane (see the  $z$  axis in Fig. 3.2.1). The band structure of such a quantum-well is illustrated in Fig. 3.2.1 where only the conduction band and two valence bands are represented. The valence bands with high and low energies are respectively known as heavy- and light-hole bands. Near the band gap, unlike for bulk materials, the two valence bands are not degenerated due to quantum confinement effect present in quantum well structures. Furthermore, due to the lower energy of the light-hole band, one can neglect

the corresponding transitions in the radiative recombination process [48]. The conduction band has a total angular momentum quantum number of  $J = 1/2$  while  $J = 3/2$  for the heavy-hole band. With such a structure, the allowed quantum transitions are those for which the projection of the total quantum momentum on the propagation direction ( $z$  axis) changes by  $\pm 1$  ( $\Delta J_z = \pm 1$ ) in units of  $\hbar$ . Consequently, only two transitions are allowed between the conduction and heavy-hole bands, leading to two sub-channels as depicted in Fig. 3.2.1. The transition from  $J_z = 1/2$  to  $J_z = 3/2$  (spin-up electron transition) corresponds to left-hand circular polarization while the transition from  $J_z = -1/2$  to  $J_z = -3/2$  (spin-down electron transition) is associated to the right-hand circular polarization of the electric field in the transverse plane.

### 3.2.2 The Spin-Flip Model (SFM)

Applying the semiclassical approach to the four-level system, one obtains the Maxwell-Bloch equations from which, after a number of assumptions, a simplified SFM model can be derived [60, 61]. Specifically, if only the fundamental transverse polarization modes are considered, the effect of the carrier diffusion process and the diffraction of the electric field may be neglected. The resulting rate equations, written in a reference frame such that the laser frequency at threshold is close to zero, are<sup>1</sup>:

$$\frac{d\tilde{E}_\pm}{dt} = -\kappa(1 + i\alpha)\tilde{E}_\pm + \tilde{P}_\pm, \quad (3.2.1)$$

$$\frac{d\tilde{P}_\pm}{dt} = -\gamma_\perp(1 - i\alpha)\tilde{P}_\pm + \gamma_\perp a(1 + \alpha^2)(N - N_t \pm M)\tilde{E}_\pm, \quad (3.2.2)$$

$$\frac{dN}{dt} = C - \gamma_e N - \left(\tilde{E}_+ \tilde{P}_+^* + \tilde{E}_- \tilde{P}_-^* + c.c.\right), \quad (3.2.3)$$

$$\frac{dM}{dt} = -\gamma_s M - \left(\tilde{E}_+ \tilde{P}_+^* - \tilde{E}_- \tilde{P}_-^* + c.c.\right). \quad (3.2.4)$$

The system variables are defined as follows.  $\tilde{E}_\pm$  and  $\tilde{P}_\pm$  are respectively the slowly-varying amplitudes of the left ( $-$ ) and right ( $+$ ) circularly-polarized components of the electric field and the dipole polarization.  $N$  and  $M$  are the carrier variables and can be defined as follows:

$$N = N_+ + N_-, \quad (3.2.5)$$

$$M = N_+ - N_-, \quad (3.2.6)$$

Where  $N_+$  ( $N_-$ ) is the carrier density variable associated to the transition channel for which  $\Delta J_z = +1$  ( $\Delta J_z = -1$ ). Therefore  $N$  is the total carrier

<sup>1</sup>A detailed study of the semiclassical approach leading to the Maxwell-Bloch equations associated the four-level energy system can be found in ref. [61]

inversion variable and corresponds to the sum of the population inversions in the two radiation channels, while  $M$  is the difference between the population inversion associated to the channels with opposite spins (see Fig. 3.2.1).  $N_t$  is the total carrier inversion at laser transparency.

The phase-amplitude couplings of field and polarization, typical for semiconductor lasers, is represented by  $\alpha$ , also named linewidth enhancement factor.  $a$  is the differential gain at the laser frequency [61] while  $C$  accounts for the contribution of the injection current to the total inversion population.

Several relaxations mechanisms are taken into account in the model:  $\kappa$  and  $\gamma_\perp$  are the relaxation rates of the amplitudes of the electric field and the polarization respectively.  $\gamma_e$  and  $\gamma_s$  are respectively the relaxation rates of  $N$  and  $M$ . It is worthy mentioning that  $\gamma_s$  is a relaxation mechanism specific to the four-level energy system. In the framework of the SFM model,  $\gamma_s$  can be considered as a phenomenological parameter accounting for the spin-flip relaxation mechanisms, i.e., different microscopic mechanisms which tend to homogenize the spin orientation of carriers with opposite spins [48].

The complexity of eqs. (3.2.1) to (3.2.4) can be substantially reduced if one takes into account that the polarization relaxes much faster than the other system variables. We consider  $\gamma_\perp \gg \kappa_e > \gamma_s > \gamma_e$ . Consequently, the polarization can be adiabatically eliminated by setting the left-hand side of eq. (3.2.2) equal to zero. Therefore:

$$\tilde{P}_\pm = (1 + i\alpha) a (N - N_t \pm M) \tilde{E}_\pm. \quad (3.2.7)$$

One can normalize the rate equations such that the field and carrier variables become dimensionless. To this end, the following variable change is performed:

$$E_\pm = \sqrt{\frac{2a}{\gamma_e}} \tilde{E}_\pm, \quad (3.2.8)$$

$$D = a \frac{N - N_t}{\kappa}, \quad (3.2.9)$$

$$d = a \frac{M}{\kappa}. \quad (3.2.10)$$

After the polarization variable is adiabatically eliminated from eqs. (3.2.1)-(3.2.4) and using the dimensionless new variables  $E_\pm$ ,  $D$ , and  $d$ , the SFM model writes:

$$\frac{dE_\pm}{dt} = \kappa (1 + i\alpha) (D \pm d - 1) E_\pm, \quad (3.2.11)$$

$$\frac{dD}{dt} = \gamma_e \mu - \gamma_e D (1 + |E_+|^2 + |E_-|^2) - \gamma_e d (|E_+|^2 - |E_-|^2), \quad (3.2.12)$$

$$\frac{dd}{dt} = -\gamma_s d - \gamma_e d (|E_+|^2 + |E_-|^2) - \gamma_e D (|E_+|^2 - |E_-|^2), \quad (3.2.13)$$

where  $\mu$  is the normalized injection current which takes a unit value at the lasing threshold.

The SFM model as described by eqs. (3.2.11)-(3.2.13) does not take into account cavity anisotropies which are usually found in a VCSEL device. By including both linear phase and amplitude anisotropies, the two linearly polarized eigen states exhibit different phases and losses. As it has been theoretically reported by Martin-Regalado [60], such anisotropies contribute to the selection of two preferential orthogonal linearly polarized states in the transverse plane and affect also the stability as well as the polarization switching mechanism [59, 60].

Assuming that the eigen axes of linear phase and amplitude anisotropies are parallel to the VCSEL polarization eigen axes, their contribution can be included in the SFM model as follows:

$$\frac{dE_{\pm}}{dt} = \kappa(1 + i\alpha)(D \pm d - 1)E_{\pm} - (\gamma_a + i\gamma_p)E_{\mp}, \quad (3.2.14)$$

$$\frac{dD}{dt} = \gamma_e\mu - \gamma_e D \left(1 + |E_+|^2 + |E_-|^2\right) - \gamma_e d \left(|E_+|^2 - |E_-|^2\right), \quad (3.2.15)$$

$$\frac{dd}{dt} = -\gamma_s d - \gamma_e d \left(|E_+|^2 + |E_-|^2\right) - \gamma_e D \left(|E_+|^2 - |E_-|^2\right), \quad (3.2.16)$$

The effect of the linear phase anisotropy (also named linear birefringence) is accounted for through  $\gamma_p$ . The linear amplitude anisotropy (also named linear dichroism) is included through  $\gamma_a$ .

Equations (3.2.14)-(3.2.16) can be written in a linear basis using the commonly used transformation relations between circular and linear bases:

$$E_+ = \frac{E_x + iE_y}{\sqrt{2}}, \quad (3.2.17)$$

$$E_- = \frac{E_x - iE_y}{\sqrt{2}}, \quad (3.2.18)$$

which leads to the following formulation of the SFM model:

$$\frac{dE_x}{dt} = -(\kappa + \gamma_a)E_x - i(\kappa\alpha + \gamma_p)E_x + \kappa(1 + i\alpha)(DE_x + idE_y), \quad (3.2.19)$$

$$\frac{dE_y}{dt} = -(\kappa - \gamma_a)E_y - i(\kappa\alpha - \gamma_p)E_y + \kappa(1 + i\alpha)(DE_y - idE_x), \quad (3.2.20)$$

$$\frac{dD}{dt} = -\gamma_e \left[ D \left(1 + |E_x|^2 + |E_y|^2\right) - \mu + id(E_y E_x^* - E_x E_y^*) \right], \quad (3.2.21)$$

$$\frac{dd}{dt} = -\gamma_s d - \gamma_e \left[ d \left(|E_x|^2 + |E_y|^2\right) + iD(E_y E_x^* - E_x E_y^*) \right]. \quad (3.2.22)$$

### 3.2.3 Linearly-Polarized steady state solutions of the SFM model

A comprehensive linear stability analysis of the four-level energy system described by eqs. (3.2.14)-(3.2.16) or (3.2.19)-(3.2.22), for which both phase and amplitude anisotropies have been considered, can be found in ref. [60]. Here, we show the linearly polarized steady-state solutions which can be obtained by assuming that both carrier densities and field amplitudes are constant:

$$E_{\pm} = Q_{\pm} \exp [i(\omega_{\pm}t \pm \Psi) + i\Upsilon], \quad (3.2.23)$$

$$D = D_0, \quad (3.2.24)$$

$$d = d_0. \quad (3.2.25)$$

The arbitrary steady state solutions for the field contain two phases  $\Psi$  and  $\Upsilon$ .  $\Psi$  determines the orientation of the linear polarization in the transverse plane while  $\Upsilon$  defines the global phase and can be ignored without loss of generality.

Two orthogonal linearly polarized (LP) solutions are obtained by setting the time derivatives in eqs. (3.2.14)-(3.2.16) to zero. Using the expressions for the steady states solutions in eqs. (3.2.23)-(3.2.25), the obtained LP solutions for the  $x$ - and  $y$ - polarized states are:

For the  $x$  linearly polarized steady state:

$$Q_{\pm}^2 = \frac{1}{2} \frac{\mu - D_0}{D_0}, \quad (3.2.26)$$

$$\omega_{\pm} = -\gamma_p + \gamma_a \alpha, \quad (3.2.27)$$

$$D_0 = 1 + \frac{\gamma_a}{\kappa}, \quad (3.2.28)$$

$$d_0 = 0, \quad (3.2.29)$$

$$\Psi = 0. \quad (3.2.30)$$

For the  $y$  linearly polarized steady state:

$$Q_{\pm}^2 = \frac{1}{2} \frac{\mu - D_0}{D_0}, \quad (3.2.31)$$

$$\omega_{\pm} = \gamma_p - \gamma_a \alpha, \quad (3.2.32)$$

$$D_0 = 1 - \frac{\gamma_a}{\kappa}, \quad (3.2.33)$$

$$d_0 = 0, \quad (3.2.34)$$

$$\Psi = \frac{\pi}{2}. \quad (3.2.35)$$

The effect of including linear phase and amplitude anisotropies in the SFM model can be readily deduced from the analysis of the steady-states solutions described in eqs. (3.2.26)-(3.2.35). The two LP steady state solutions have an angular frequency detuning of  $2\gamma_p - 2\gamma_a\alpha$ . In addition to the detuning due to birefringence ( $\gamma_p$ ), there is a frequency shift which is induced by a combined effect of linear amplitude anisotropy ( $\gamma_a$ ) and the  $\alpha$ -factor (also known as saturable dispersion). Assuming a positive  $\alpha$ -factor, the magnitude and sign of  $\gamma_p$  and  $\gamma_a$  dictate the stability, the threshold and the selection rules for the two-LP modes but also play a key role in the switching dynamics when varying the injection current [59, 60]. Interestingly, depending on the injection current, a change in  $\gamma_p$  and  $\gamma_a$  may even lead to a regime of bistability for which both  $x$ - and  $y$ -LP modes are stable. In such a situation, the lasing mode will depend on other driving mechanisms such as the effect of spontaneous emission noise or any external perturbation source like current noise, optical feedback [58] or optical injection from another laser [60].

Apart from the linearly polarized (LP) steady-state solutions, a stability analysis has also revealed the existence of an elliptically polarized steady-state (EPSS) in which  $x$  and  $y$  modes are lasing at the same frequency but with different amplitudes. The existence of such a elliptical polarization state has been experimentally reported for some VCSELS operating close but still below the injection current for which the switching from the low to high frequency mode (type II PS) is achieved [62].

In the framework of the SFM model the switching (PS) between the fundamental orthogonal LP modes can be interpreted in terms of polarization instabilities driven by the spin-flip mechanism which is represented in the model by a finite value of  $\gamma_s$ . Several works have been carried out to experimentally quantify the contribution of the spin-flip mechanism by estimating  $\gamma_s$ . It turns out that the magnitude of  $\gamma_s$  can span from few  $\text{ns}^{-1}$  to even  $> 1000 \text{ ns}^{-1}$ , depending on the VCSEL under investigation [63, 64]. As one increases the injection current,  $\gamma_s$  may determine whether the switching occurs from the high- to the low-frequency LP mode (type I PS) or from the low- to the high-frequency mode (type II PS), depending on the magnitude of linear anisotropy. For instance, a type II PS is typically predicted by the SFM model for VCSELS with large  $\gamma_s$  but with a relatively small birefringence, while type I PS is found in the opposite situation (small  $\gamma_s$  and large  $\gamma_p$ ) [61].



### 3.3 Type I and type II polarization switching in the framework of the SFM

In this section both type I PS (from the high-frequency mode to the low-frequency mode) and type II PS (from the low-frequency mode to the high-frequency mode) are numerically and experimentally analyzed. By scanning the injection current, we focus on the elliptically polarized steady state which accompanies type II PS. We provide experimental polarization-resolved light current characteristics of two different VCSELs which qualitatively support the onset of elliptically polarized state associated with type II PS. One of the available VCSELs exhibits also a Type I PS. In this particular case and in agreement with previous observations, we show that type I PS is achieved almost abruptly. Finally using the SFM model, we provide a numerical result which supports the type II switching scenario.

As already mentioned in section 3.1, previous experimental investigations have shown that both type I and type II PS can be simultaneously observed in the same VCSEL [45, 62]. A theoretical explanation for such a switching scenario has been provided by taking into account the temperature dependence of the material gain and losses of the orthogonal fundamental modes [45]. However, the simultaneous occurrence of type I and type II can not be predicted by the basic SFM model as described by eqs. (3.2.19)-(3.2.22), unless one include gain saturation mechanisms as it has been proposed by Prati *et al.* [65].

#### 3.3.1 Experimental polarization switching scenarios

In Figures 3.3.1 and 3.3.2, we show the polarization-resolved power vs. injection current characteristics (L-I curve) of two different VCSELs (respectively VCSEL<sub>1</sub> and VCSEL<sub>2</sub>) which, in fact, belong to the same 2D VCSEL array. When one of the VCSEL is selected, its bias current and temperature are controlled using a low-noise laser driver. Optical power is measured using a power meter. A half-wave plate is used to select the polarization axis in which the measurements are performed. In our setup, the horizontal polarization axis coincides with the low-frequency (LF) linearly polarized mode while the high-frequency (HF) mode is oriented along the vertical axis. Light emitted by the VCSEL is collimated by an antireflection-coated lens. An optical isolator with 40 dB attenuation is used to prevent the VCSEL against optical feedback-induced instabilities from the detection apparatus. For both VCSELs, the injection current is scanned up to a limit value which is always set below the threshold of the first order transverse mode, thus assuring that we operate only in the fundamental mode regime.

The switching scenario depicted in Fig. 3.3.1 describes the polarization-

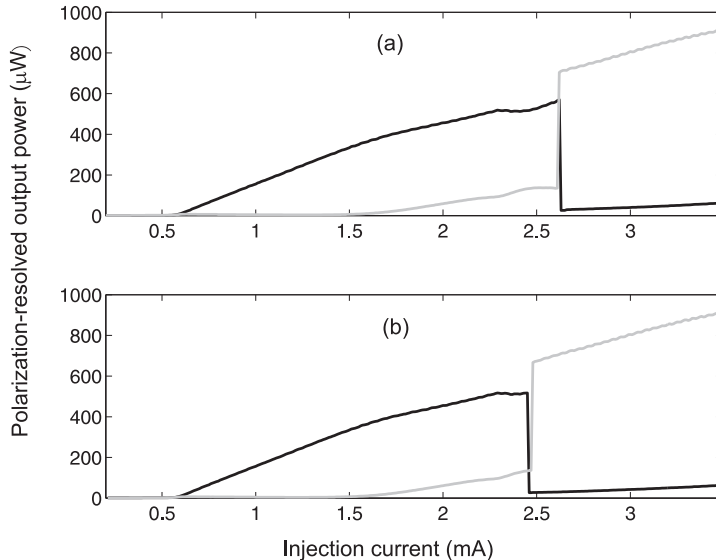


**Figure 3.3.1:** *Experimental polarization-resolved averaged Light-Current characteristic of VCSEL<sub>1</sub> when the injection current is first increased (a) and then decreased (b). Black (gray) represents the averaged power for low- (high-) frequency mode. The temperature has been stabilized at 20° C.*

resolved L-I curves of VCSEL<sub>1</sub>. The black (gray) curve represent the low- (high-) frequency LP mode. If the injection current is increased [see Fig. 3.3.1-(a)], the low-frequency LP mode is first excited with a threshold current of 0.6 mA. As we still increase the injection current, a switching from the low-frequency (LF) mode to the high-frequency (HF) mode (type II PS) is observed for a bias current of 2.66 mA. However, before type II PS is achieved, we observe an elliptically polarized state during which both orthogonal LP modes are emitted. Such a regime corresponds to the bump present in the L-I curve of the high-frequency vertically-polarized mode [see the bump in the gray curve of Fig. 3.3.1(a)]. Indeed, over an injection current range from 1.56 to 2.29 mA, an elliptically polarized state appears but the horizontal LP mode has more power than the vertical one. For injection currents higher than 2.29 mA (but still below the value for which type II PS is achieved), one observes a slightly broadened spectrum with a dominant peak located at the low-frequency mode. This behavior is very similar to what has been previously reported and may be related to the destabilization of the elliptically polarized state through the onset of nonlinear dynamics accompanying type II PS [62, 65, 66]. By still increasing the bias current, type II PS is finally achieved at 2.66 mA. For higher currents VCSEL<sub>1</sub> emits a vertically polarized high-frequency fundamental mode; the horizontal low-frequency mode being strongly depressed. If the injection current is then decreased

[see Fig. 3.3.1(b)], VCSEL<sub>1</sub> switches back to the low-frequency mode at a bias current of 2.46 mA, which is smaller than the current for which type II PS has been achieved. We observe that the switching back point is achieved through a two-mode regime which, as the injection is further decreased, follows the previously resolved elliptically polarized state. The observed hysteresis zone corresponds to bistability between the high-frequency LP mode and the elliptically polarized state.

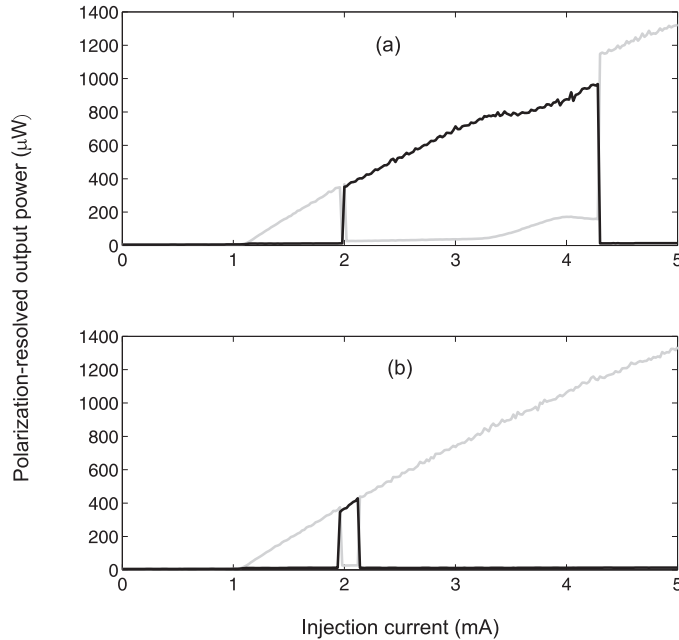


**Figure 3.3.2:** *Experimental polarization-resolved averaged Light-Current characteristic of VCSEL<sub>2</sub> when the injection current is first increased (a) and then decreased (b). Black (gray) represents the averaged power for low- (high) frequency mode. The temperature has been stabilized at 20° C.*

The switching behavior of VCSEL<sub>2</sub> is presented in Fig. 3.3.2. Figure 3.3.2(a) shows polarization-resolved L-I curves in both the vertical and the horizontal polarization directions when the injection current is progressively increased. Unlike VCSEL<sub>1</sub>, if biased just above the threshold current, VCSEL<sub>2</sub> starts lasing in the vertically-polarized high-frequency mode. As the injection is further increased, a polarization switching to the low-frequency mode (type I PS) is detected at 1.97 mA. By increasing the injection further, a type II switching mechanism is resolved for a bias current of 4.3 mA. During the upward scan of the current, type II PS is roughly achieved in the same way as for VCSEL<sub>1</sub>, i.e., it is accompanied by the onset of elliptically-polarized state. If the bias current is then decreased, VCSEL<sub>2</sub> switches back

from the high-frequency mode to the low-frequency mode and exhibits a relatively large hysteresis zone [Fig. 3.3.2(b)]. It is worthy mentioning that, type II PS is now achieved between two orthogonal linearly polarized states and not between the LP and an elliptically polarized one as it has been observed for VCSEL<sub>1</sub>. By further decreasing the injection current, the laser switches back to the high-frequency polarization mode almost without hysteresis.

### 3.3.2 Numerical simulations of type II PS using the SFM model

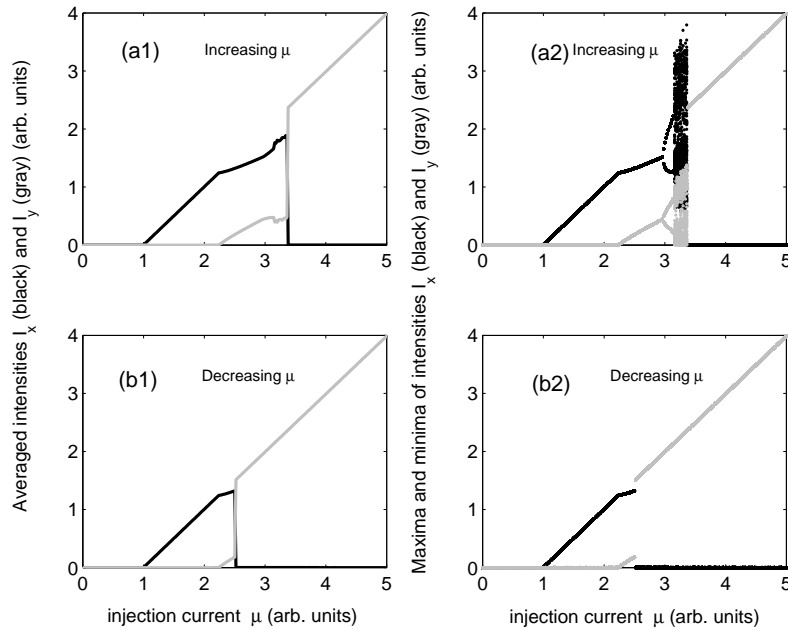


**Figure 3.3.3:** Theoretical polarization-resolved time-averaged intensities of the low-frequency mode ( $x$  in black) and the high-frequency ( $y$  in gray) for increasing (a1) and decreasing (b1) injection currents. Polarization-resolved bifurcation diagram showing the evolution of minima and maxima of intensities of the low-frequency mode ( $x$  in black) and the high-frequency ( $y$  in gray) for increasing (a2) and decreasing (b2) injection currents. The following parameters have been used in the simulations:  $\kappa = 300 \text{ ns}^{-1}$ ,  $\gamma_p = 6.3 \text{ rad/ns}$ ,  $\gamma_a = -0.81 \text{ ns}^{-1}$ ,  $\gamma_s = 91 \text{ ns}^{-1}$ ,  $\gamma_e = 0.55 \text{ ns}^{-1}$ ,  $\alpha = 3$ .

We are interested in numerically analyzing the elliptically polarized state accompanying the type II switching. Fig. 3.3.3 shows numerical simulations which qualitatively reproduce a type II PS scenario as it has been observed experimentally in the case of VCSEL<sub>1</sub> (see Fig. 3.3.1). To this end, we

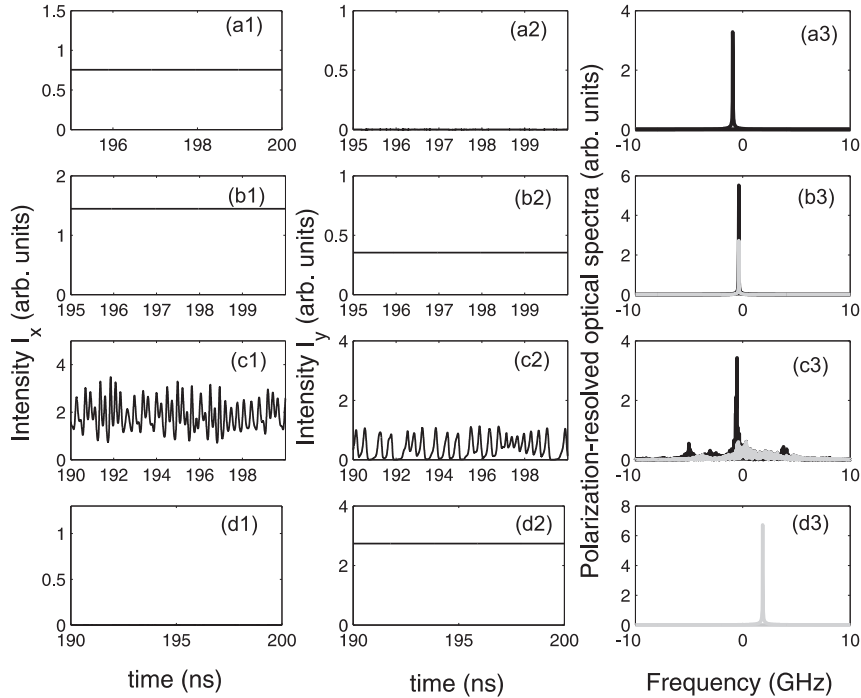


**Figure 3.3.4:** Polarization-resolved intensities and optical spectra showing type II polarization switching scenario when increasing the injection current  $\mu$  of the free-running VCSEL as shown in Fig. 3.3.3(a1)-(a2): (a)  $\mu = 1.75$ , steady state emission in  $x$ -LP mode; (b)  $\mu = 2.8$ , Elliptically polarized steady state; (c)  $\mu = 3.265$ , complex nonlinear dynamics in both  $x$ - and  $y$ -LP modes before PS is achieved; (d)  $\mu = 3.75$ , emission in  $y$ -LP mode after PS is achieved. In the spectra black (grey) corresponds  $x$ -LP ( $y$ -LP) low-frequency (high-frequency) mode.

have performed numerical simulations using eqs. (3.2.19)-(3.2.22) with the following parameters:  $\kappa = 300 \text{ ns}^{-1}$ ,  $\gamma_p = 6.3 \text{ rad/ns}$ ,  $\gamma_a = -0.81 \text{ ns}^{-1}$ ,  $\gamma_s = 91 \text{ ns}^{-1}$ ,  $\gamma_e = 0.55 \text{ ns}^{-1}$ ,  $\alpha = 3$ . Figure 3.3.3(a1) and Fig. 3.3.3(b1) depict the evolution of the polarization-resolved time-averaged intensities when the normalized injection current  $\mu$  is respectively increased and then decreased. In order to mimic the photodetector present in the experiment, the averaged intensities for the  $x$ -polarized mode ( $\langle I_x \rangle = |E_x|^2$ ) and for the  $y$ -polarized mode ( $\langle I_y \rangle = |E_y|^2$ ) are computed by averaging (for each value of  $\mu$ ), the last 50 ns of a 200 ns long, transient-free, time series with an integration step of 1 ps. By increasing the injection current  $\mu$  [Fig. 3.3.3(a1)], the low-frequency mode ( $x$ -LP) is first excited. If the injection  $\mu$  is progressively increased, an elliptically polarized state followed by nonlinear dynamics which involve both  $x$ - and  $y$ -LP mode are observed. Then the VCSEL switches to the high-

frequency  $y$ -LP. In qualitative agreement with what has been experimentally shown in Fig. 3.3.1(a), the elliptically polarized state destabilizes through nonlinear dynamics that precedes type II PS. If  $\mu$  is then decreased after type II PS has been achieved [Fig. 3.3.3(b1)], a hysteresis region is found, showing a possible bistability between the high-frequency LP steady-state and the elliptically polarized state.

The onset of elliptically polarized state and its destabilization through nonlinear dynamics preceding the type II PS as shown in Fig. 3.3.3(a1) is described in details in Fig. 3.3.3(a2) and Fig. 3.3.4. Figure 3.3.3(a2) is a bifurcation diagram displaying the evolution of the maxima and minima of the intensity time-traces. This allows following any qualitative change in the VCSEL dynamics as  $\mu$  is scanned. For a relatively low injection level above threshold, the VCSEL emits a steady-state in the low-frequency  $x$ -LP fundamental mode [see Figs. 3.3.4(a1)-(a3) for  $\mu = 1.75$ ]. For larger injection current, the elliptically polarized state is excited as shown in Figs. 3.3.4(b1)-(b3) for  $\mu = 2.8$ . In fact, the corresponding spectrum in Fig. 3.3.4(b3) shows that both  $x$  (black) and  $y$  (gray) orthogonal LP fundamental transverse modes are emitted with the same frequency. In Fig. 3.3.3(a2) we show that, by further increasing  $\mu$ , the elliptically-polarized state (EP) is destabilized through a Hopf bifurcation mechanism that appears on the EP state. Basically, a nonlinear system undergoes a Hopf bifurcation when a steady-state solution is destabilized to a periodic solution, namely a limit cycle, when changing a system bifurcation parameter. In our case, we notice that, as  $\mu$  is increased close but still before type II PS, the limit cycle undergoes a period-doubling leading to excitation of complex nonlinear dynamics. A sample of such complex nonlinear dynamics is described in Figs. 3.3.4(c1)-(c3) for  $\mu = 3.265$ . By still increasing the injection current  $\mu$ , a type II PS is achieved, i.e., the VCSEL switches to a steady state regime in only the  $y$ -LP mode. We show that if  $\mu$  is decreased after type II PS has been achieved [see Fig. 3.3.3(b2)], the above-mentioned nonlinear dynamics are no longer observed, thus denoting the existence of an injection current region of bistability between two-polarization mode complex nonlinear dynamics and a steady-state regime in the  $y$ -LP mode. Similar polarization-mode dynamics have been also reported by Ackermann and Sondermann [67] in a solitary VCSEL operating close to type II PS, though the authors report the existence of side peaks with a relatively higher amplitude than what the SFM model predicts.

It is well known that conventional semiconductors, which belong to the so-called class B lasers, cannot exhibit chaotic dynamics without external perturbations (e.g., current modulation, optical feedback or optical injection, see Section 3.4). In solitary class B laser systems, the only expected dynamics are damped relaxation oscillations which derive from periodic exchange of energy between the inversion and the electric field inside the cavity. But

we show that the SFM model for a solitary VCSEL supports the existence of complex, possibly chaotic, dynamics close to type II PS. This striking behavior results from an additional degree of freedom provided by the spin-flip relaxation mechanisms which are modelled by  $\gamma_s$ .

### 3.4 VCSELS subject to external perturbation

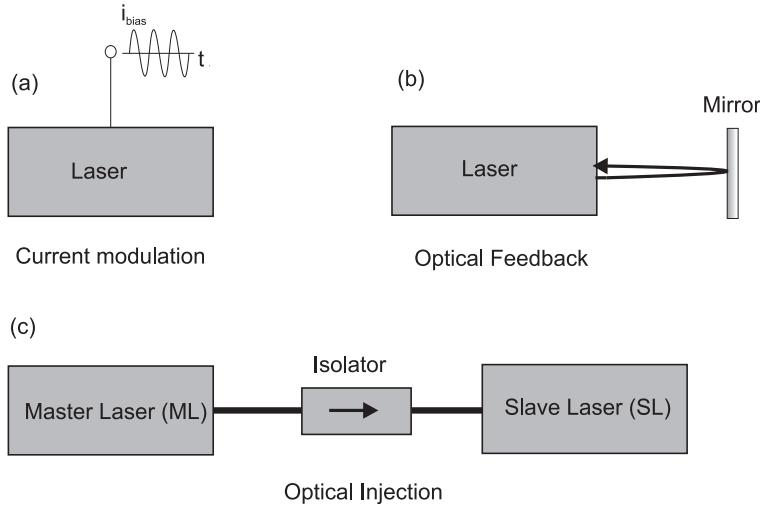


**Figure 3.4.1:** *Semiconductor laser under external perturbations: (a) Current modulation; (b) External Optical feedback; (c) External Optical injection.*

In the previous sections, we have discussed the emission properties of a free-running VCSEL. Semiconductor lasers are however sensitive to external perturbations regardless of their geometrical structure [edge-emitting lasers (EELs) or vertical-cavity surface-emitting lasers (VCSELs)]. In Fig. 3.4.1, we show a schematic representation of three basic external perturbations: direct current modulation, optical feedback, and external optical injection. In the case of current modulation [Fig. 3.4.1(a)], usually the perturbation consists of adding a time-varying modulation signal which oscillates around the DC bias current level. External optical feedback [Fig. 3.4.1(b)] is achieved when the emitted light is partly reflected back into the laser cavity using an external mirror, which thus forms an external cavity. External optical injection is shown in Fig. 3.4.1(c). In that case, a semiconductor laser, commonly named slave laser (SL), is injected by a master laser (ML). The injection is rendered unidirectional by the use of an optical isolator to avoid mutual coupling. Optical injection has been found to be very attractive for controlling laser characteristics and performance since it adds, externally controllable, additional degrees of freedom to the laser system. In fact, one can change

the power of the injected light beam, hence modifying the coupling inside the slave cavity or control the frequency offset between the master laser and the free-running laser (the frequency offset is usually named frequency detuning). In the following, we briefly review some of previous results obtained in the case of semiconductor lasers under current modulation and optical feedback. We then present a more detailed review of the main achievements concerning the issue of optical injection in semiconductor lasers in general, before analyzing the case of VCSEL under optical injection.

### **Semiconductor lasers under current modulation**

Semiconductor lasers subject to direct current modulation have been theoretically [68, 69, 70] and experimentally [71] investigated, mostly EELs. Direct current modulation is attractive from the application viewpoint due to its simplicity as a way to obtain an information-carrying modulated light for high bit-rate analog or digital fiber optics communications. Usually, the laser is biased above threshold and a modulation signal is added to the injection current. Furthermore, when biased close to its threshold current, the directly current-modulated laser may be suitable for the generation of pulses with high repetition rates [72]. It has been demonstrated that the directly modulated laser diodes may also exhibit a wide range of nonlinear dynamics [68, 71, 73]. In fact, depending on the modulation parameters, i.e., the modulation depth and the modulation frequency, several regimes have been theoretically reported: a continuous-wave operation, a pulsating regime, and a period doubling cascade leading to deterministic chaos [73]. In particular, the strongly pulsating regime, which is found for a large modulation depth, is due to a gain switching mechanism [73]. The route to chaos through period-doubling has been experimentally demonstrated by Liu *et al.* in a directly modulated distributed feedback (DFB) laser [71]. It has been found that these nonlinear instabilities are more likely to occur when the laser is biased near threshold and modulated at high frequencies with high modulation depth.

Although current modulation has been extensively investigated in the case of EELs, there is a growing interest in studying directly current-modulated VCSELS [74, 75, 76, 77]. The results show mainly that the inherent VCSEL multi-transverse mode characteristics play a key role in the type of dynamics induced by direct current modulation. It has been experimentally demonstrated that when a short pulse is superimposed to the DC bias current of a VCSEL, transient multimode dynamics are excited as a result of strong multitransverse mode competition [74]. When the VCSEL is subject to high-frequency current modulation, Valle *et al.* [76] have numerically demonstrated that a multimode chaotic regime may be excited due to multitransverse mode competition. In a subsequent theoretical study, polarization-resolved nonlinear dynamics have been reported in a directly



modulated VCSEL operating only in the fundamental transverse mode [78]. In this particular case, time-periodic as well as chaotic dynamics which involve both orthogonal linearly-polarized (LP) fundamental modes have been shown, even for small modulation amplitude and slow modulation frequency [78]. A more recent study has however suggested that, when multitransverse spatial effects are accounted for, the polarization-resolved dynamics induced by current modulation may be modified [77]. This effect on the fundamental LP mode dynamics becomes more important when the modulation amplitude is increased [77]. Furthermore, polarization dynamics induced by current modulation VCSELS have been numerically studied by Masoller *et al.* [79] when the VCSEL is biased close to its polarization switching (PS) points. For instance, the results show that if the VCSEL is biased close to type II PS (PS from the low-frequency to the high-frequency LP fundamental mode), complex dynamics are excited in both LP fundamental transverse modes for relatively large modulation amplitudes. This behavior is attributed to polarization dynamics that are intrinsically observed near type II PS.

### Semiconductor lasers subject to optical feedback

When compared to conventional gas lasers, semiconductor lasers are characterized by a much higher efficiency of light that is coupled out of the cavity. As already mentioned in Section 2.1, due to the difference in refractive index between the active medium and the environment, about 70% of the total light intensity escape from the cavity. Thus semiconductor lasers are “open” to the outside. Furthermore, due to intrinsic characteristics such as high gain active medium and self-phase modulation, laser diodes are affected by the coupling of external light from optical feedback or optical injection. The seemingly simple configuration of a laser diode with optical feedback is a delay system which may exhibit complex nonlinear instabilities [80, 81, 82]. The study of such a system is vital, for instance, for optical communications in which back reflections from an optical fiber may severely affect laser emission properties. Basically, the laser response to optical feedback depends on how the intracavity laser field is coupled to the delayed field which reaches the laser cavity after an external round-trip time  $\tau_{ext} = 2L/c$  ( $L$  is the external cavity length, i.e., the distance between the laser output facet and the external reflector, while  $c$  is the light speed in the external cavity medium). The delay  $\tau_{ext}$  and the feedback strength are external key parameters which drive the feedback-induced laser dynamics [82]. Interestingly, by adequately controlling the external cavity length and the feedback strength, it has been demonstrated that optical feedback can be used to achieve laser linewidth narrowing [83], which is advantageous for optical communication and interferometric fiber sensor systems. It is worth noting that other intrinsic laser characteristics such as the intracavity round-trip time  $\tau_{in}$ , the relaxation oscillation frequency  $f_{RO}$  and the phase-amplitude coupling (usu-

ally accounted for by the so-called  $\alpha$ -factor) plays a determinant role in the response to optical feedback [80].

Depending on the feedback strength and the distance to the external reflector, five qualitatively different regimes (I-V) have been clearly identified [82]. The so-called regime I is observed for relatively low feedback strength and is characterized by either spectral narrowing or broadening, depending on the phase of the feedback. In the so-called regime II and depending on the feedback strength level, the laser may undergo mode hopping or spectral broadening. Over a small range of moderately higher feedback strength, the laser exhibits the so-called regime III for which a single-mode operation, characterized by narrow line emission and suppression of mode hopping, is observed. In Regime IV, which occurs for relatively larger feedback strengths, there is a substantial broadening of the laser linewidth (typically from hundreds of MHz to about tens of GHz) and the laser exhibits the so-called coherence collapse, i.e., the emission is characterized by a dramatic reduction of the coherence length [81]. In the coherence collapse regime, the laser exhibits a dramatic linewidth broadening (by a factor of more than 1000) [81] and may undergo undamped relaxation oscillation dynamics [82]. For much higher feedback strengths, the laser dynamics is dominated by a narrow linewidth emission and operates mainly in the external cavity mode (regime V). The feedback-induced laser dynamics can be harnessed by controlling the optical characteristics of light in the external cavity. This can be achieved by using optical devices such as a half-wave plate for polarization-rotated feedback [84], a phase-conjugating mirror [85] for phase-conjugate feedback, or even by inserting an optical filter in the external cavity to realize filtered optical feedback [86]. When the external mirror is replaced by a movable grating element, stable single-mode compound external laser with a tunable wavelength can be achieved.

In the coherence collapse regime, the feedback-induced instabilities may consist of low frequency fluctuations (LFF) [87, 88], in comparison to the underlying relaxation oscillation frequency. LFF are denoted by low-frequency time-averaged intensity dropouts followed by relatively rapid recoveries. They are typically observed for sufficiently long external cavities (typically  $> 1$  cm) and with moderate feedback strength. For shorter external cavities (for which the external cavity length is such that  $f_{RO}\tau_{ext} \ll 1$ ), feedback-induced high-frequency self-oscillations (in the range of tens of GHz) have been reported as a result of a self-locking mechanism of two compound-cavity modes which have almost equal cavity losses [89]. Another intriguing nonlinear dynamics different from the LFF and which has been observed in the short external cavity configuration is the so-called regular pulse package (RPP): the light intensity exhibits a fast regime of high-frequency pulses in the GHz range intensity which are modulated by a relatively low-frequency signal (of hundreds of MHz) [90, 91, 92].

An extensive research activity has been devoted to investigating external optical feedback in VCSELS [58], [55], [93]-[99]. As aforementioned (see chapter 2), the VCSEL output mirror is made of highly reflective distributed Bragg reflectors (the reflectivity is about 99%) which intuitively should prevent VCSELS from feedback-induced instabilities. Nevertheless, this is not the case since VCSELS have a relatively short internal cavity length (a few  $\mu\text{m}$  thick) which implies a shorter internal round-trip time  $\tau_{in}$  which, in turn, favors the coupling of smaller amount of light. As a result, similarly to EELs, VCSEL are sensitive to optical feedback. However, unlike EELs, the intrinsic polarization properties of VCSELS may strongly affect their response to optical feedback [93, 94, 95, 96, 97]. Using a polarized optical feedback, Besnard *et al.* [93] have numerically shown that periodic modulation of the external cavity phase may lead to alternative switchings between the orthogonal linearly-polarized (LP) VCSEL modes. In the case of a polarization-rotated optical feedback using a quarter-wave plate in the external cavity, the VCSEL may exhibit polarization self-modulation (PSM) dynamics with antiphase periodic oscillations in the intensities of both orthogonal LP fundamental modes [97]. Furthermore, LFF with possible excitation of antiphase dynamics in the time-averaged intensities of both VCSEL orthogonal LP modes have been numerically predicted [94, 95] and experimentally demonstrated for the polarization-maintaining feedback scheme [96]. Similarly to what has been observed in EELs [90], a VCSEL subject to optical feedback from a short external cavity may undergo regular pulse package (RPP) dynamics. These RPP exhibit polarization mode competition which may affect the overall dynamic response [98].

Optical feedback also allows achieving control and stabilization of the VCSEL polarization state [55, 58]. In the preceding section, we have commented on the fact that, typically, VCSEL exhibit polarization instabilities when changing the operating conditions, e.g., bias current or temperature. By selecting specific wavelengths that are reflected back into the VCSEL from an external cavity, one can control the output polarization state [55]. Using a polarization-selective feedback scheme, Hong *et al.* have experimentally demonstrated that, by increasing the feedback strength, polarization switching can be completely suppressed regardless the level of the bias current [99]. Polarization selection and stabilization has also been achieved for an isotropic feedback scheme with an extremely short external cavity (the external cavity length is less than 20  $\mu\text{m}$ ). In such a configuration, the polarization switching current is proportional to the external mirror reflectivity. Thus, polarization control or stabilization can be realized by adequately changing the external mirror reflectivity [58].

### 3.4.1 Semiconductor lasers with external optical injection

Optical injection in semiconductor laser has been a subject of intensive research since 1980, due to its potential application to achieve injection-locking, i.e., the locking of the slave laser to the master laser frequency. Although the issue of locking between two oscillators can be traced back to the historical observation of the locking between two pendulums by Christian Huygens in 1665 [100], its development and application was enhanced by Addler's work on locking phenomena in electric oscillators [101]. Later on, frequency locking induced by optical injection has been demonstrated in gas lasers [102, 103]. Following the development of semiconductor lasers as suitable light sources for fiber optics communications, experiments aiming at using optical injection to improve the output performances of a directly modulated laser diode was undertaken. Nishizawa and Ishida demonstrated that the waveform of the output of the directly modulated laser diode could be significantly improved using optical injection [104]. After, it was demonstrated that frequency stabilization of a directly modulated slave laser could be achieved under injection locking to a master laser [105, 106].

The first theoretical approach to explain injection-locking phenomena in semiconductor lasers has been proposed by Kobayashi and Kimura using a model based on the Van der Pol equation [107]. In a subsequent study, Lang demonstrated that the injected carrier dependence of the refractive index (usually accounted for through the so-called  $\alpha$ -factor) strongly affects the injection locking regime and explains the presence of dynamical instabilities outside the injection-locking state [108]. For instance, the effect of the dependence of the active region refractive index on the injection explains the asymmetry of the locking zone usually found in the frequency detuning vs. optical injection power map. Injection locking is achieved through a change in the gain profile caused by the injected signal and results in a peak at the master laser frequency. In fact, injection locking is a complex mechanism which involves a competition between the amplified spontaneous emission field, the amplified injected field as well as the beating between the two fields [109].

Injection locking has been extensively used to address a number of applications aiming at either improving semiconductor laser performances or generating new functionalities:

- Single mode operation can be achieved by injection locking of a multi-mode Fabry-Perot to a stable master laser [110]. Using injection locking techniques, it has been demonstrated that one can substantially reduce the frequency chirp [111], suppress the mode partition noise [112] or achieve a modulation bandwidth enhancement [113, 114, 115] of directly modulated laser diodes. In particular, an optical injection-

induced modulation bandwidth enhancement of four times the relaxation oscillation frequency has been demonstrated in a distributed feedback laser [116].

- On the other hand, several functionalities based on injection-locking have been realized. In coherent optical communications, injection locking has been used to synchronize several laser diode sources to a unique highly coherent master laser [117]. By combining phase locking techniques with optical injection locking, one can achieve an optical injection phase-locked loop (OIPLL) for application in optical communication system. Injection locking of mode-locked lasers can be used to generate an optical frequency comb for the channelization of a wide-band radio-frequency signal into several subbands [118]. Furthermore, injection locking techniques have proved useful for achieving all-optical signal processing such as wavelength add-drop in optical networks [119] or modulation conversion in Radio-over-Fiber (RoF) applications [13].

From the fundamental viewpoint, apart from injection locking, a semiconductor laser subject to external optical injection can also exhibit a wide range of interesting nonlinear dynamics including wave mixing, subharmonic resonance, a period doubling route to chaos [16]. Nonlinear dynamics induced by external optical injection has been extensively investigated in the case of edge-emitting lasers (EEL). However, concerning optical injection in VCSELS, the problem becomes much more complex than for EEL due to polarization instabilities and the underlying nonlinear dynamics are still not fully investigated. Nonlinear dynamics in VCSEL subject to external optical injection will be analyzed in subsequent chapters.

### 3.4.2 External optical injection in VCSELS

We provide here a summary of the main research achievements about optical injection in VCSELS. In addition to the injection power and the frequency detuning between the master and the slave laser as injection control parameters, the polarization of the injected beam with respect to that of the free running VCSEL plays also a key role. If one assume that the free-running VCSEL operates in the fundamental mode regime, two main injection schemes are usually considered: the so-called parallel and orthogonal optical injection configurations. In the *parallel injection* scheme, the polarization of injected field is parallel to that of the free-running laser while in the *orthogonal injection* case the injected field polarization is orthogonal to that of the free-running VCSEL.

Optical injection in VCSEL was investigated for the first time by Pan *et al.* using an orthogonal optical injection scheme [120]. In this pioneer-

ing work, the VCSEL was biased such that it emitted a single transverse mode, linearly polarized along the [011] crystal axis (horizontal). For the adopted bias current, the offset between the lasing horizontal low-frequency (LF) mode and the strongly depressed, high-frequency (HF), vertical transverse mode was of ( $\nu_{\text{HF}} - \nu_{\text{LF}} = 9$  GHz). The VCSEL was then injected by a tunable external cavity master laser, emitting along the vertical polarization axis. Optically induced polarization switching was observed when scanning the injection power for a wide range of frequency detuning between the master laser and the horizontal free-running VCSEL mode. The obtained results showed that the minimum switching power was achieved when the frequency of the master laser corresponds to the frequency of the vertically polarized cavity mode ( $\nu_{\text{HF}}$ ), i.e., when the frequency detuning coincides with the VCSEL birefringence (9 GHz). It was observed that the VCSEL birefringence influence qualitatively how optical injection-induced polarization switching (PS) is achieved. In fact, it was observed that if the injection power is scanned when the master laser frequency was set to the low-frequency side of  $\nu_{\text{HF}}$ , a bistable switching from horizontal to vertical polarization is achieved abruptly. On the other hand, when the master laser frequency was set to the high-frequency side of  $\nu_{\text{HF}}$ , the switching is achieved in a rather gradual manner, i.e., with a progressive decrease of the power in the VCSEL low-frequency transverse mode. Moreover, in the later case, PS was achieved without hysteresis. Nevertheless, for all the detuning range, it was observed that PS was always followed by injection locking of the VCSEL to the master laser frequency.

Polarization-resolved instabilities have been investigated for a VCSEL operating in the fundamental mode [121] and subject to a parallel optical injection. The dynamics of the injected VCSEL were analyzed in both orthogonally polarized modes by scanning the injected power for a relatively wide frequency detuning range. An injection-locking zone was observed mainly in the negative detuning range (See the mapping in Fig. 3.4.2). Two optical injection-induced chaotic regimes were observed for both positive and negative detuning from the injection locking regime as shown in Fig. 3.4.2(b) and Fig. 3.4.2(f). Interestingly, it was found that chaos was associated with antiphase polarization-resolved instabilities. As a result, chaos was observed in both VCSEL polarization modes while the total intensity remained constant. Apart from injection locking and chaos, several nonlinear dynamics including wave mixing [Fig. 3.4.2(a)] as well as time periodic dynamics [Fig. 3.4.2(c) and Fig. 3.4.2(d)] were also reported. It is worthy mentioning that no polarization switching phenomena was observed in this injection configuration. Time periodic dynamics was also observed in a previous study by Li *et al.* using a parallel optical injection scheme [122]. In particular, it was found that outside injection locking state a resonant regime could be excited when the detuning coincides with the VCSEL relaxation oscillation or its harmon-

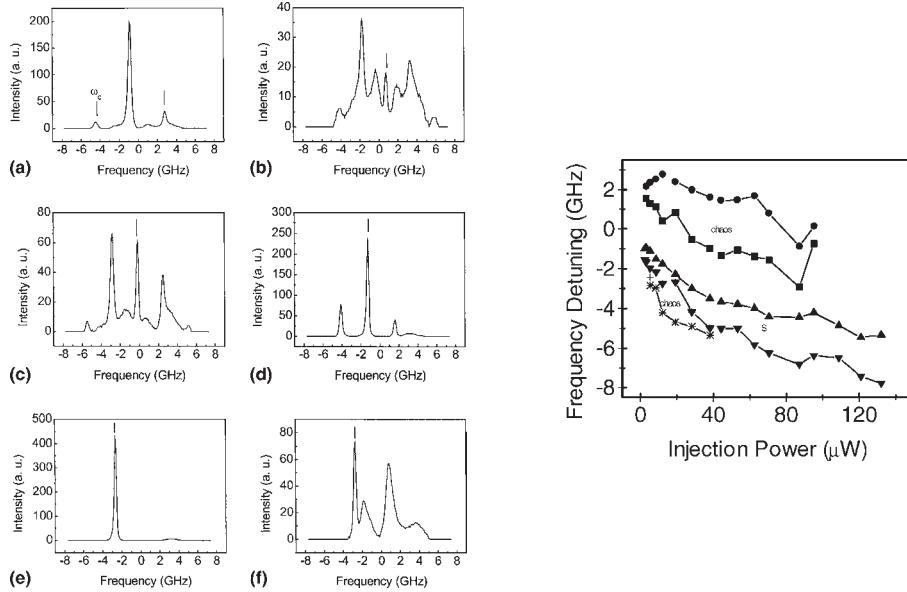


**Figure 3.4.2:** Mapping of nonlinear dynamics induced in a VCSEL subject to parallel optical injection in the plane detuning vs. injection power (right-most figure).  $S$  refers to stable injection locking. Optical spectra show qualitatively different dynamics when the VCSEL is subject to about  $19 \mu\text{W}$  injection power for different frequency detunings: (a)  $2.72 \text{ GHz}$ , wave-mixing; (b)  $0.77 \text{ GHz}$ , Chaotic dynamics; (c)  $0.17 \text{ GHz}$ , Period doubling dynamics; (d)  $1.26 \text{ GHz}$ , period-one limit cycle; (e)  $2.66 \text{ GHz}$ , injection-locking; (f)  $2.71 \text{ GHz}$ , chaotic dynamics. The arrows indicates the master laser frequency position. After reference [121].

ics. In contrast to what was reported in ref. [121], injection locking was observed when the master laser frequency was tuned at both low- and high-frequency side of the free-running VCSEL frequency.

Besides its effect on fundamental mode polarization dynamics, optical injection was investigated for a VCSEL operating in the multi-transverse mode regime [120, 122, 123, 124]. It was found that if the VCSEL is biased such that higher order transverse modes are excited, the polarization of the transverse modes can be independently switched by optical injection if the frequency of the injected field is tuned close to the individual transverse mode [120]. It was also experimentally demonstrated that the dynamical response of a multi-transverse mode VCSEL to external optical injection depends strongly on both the polarization of the injected light and that of the individual transverse mode [124]. For instance, external optical injection can be used to achieve single-mode operation in a VCSEL that exhibits two orthogonally-polarized transverse modes in its free running regime [124]. The

issue of transverse mode switching and locking in a VCSEL under orthogonal optical injection will be discussed in details in chapter 7.

### 3.5 Conclusions

In this chapter, we have discussed polarization properties which mainly distinguish VCSEL from their counterpart edge-emitting lasers. We have surveyed possible mechanisms which underly different experimentally observed VCSEL polarization switching (PS) scenarios, i.e., from the high-frequency mode to the low-frequency mode (type I) or from the low-frequency mode to the high frequency mode (type II PS). Whether the VCSEL should exhibit a type I PS, a type II, or both type I and type II depends strongly on the device under investigation and its operating conditions such as the bias current, temperature or mechanical stress. Strong efforts have been previously undertaken to explain the unique VCSEL polarization dynamics. To the best of our knowledge, a unified model which explains all the observed polarization properties is not yet available. One possible way consists of explaining PS on the basis of the temperature dependence of the gain and losses of the two linearly polarization states. Another way is to model the VCSEL polarization properties by including the carriers spin dynamics (spin-flip model). There is no a priori reason to choose one or the other model since both have been extensively used in the literature to explain particular switching properties. A comparison between the two modelling approaches is beyond the scope of this thesis. Nevertheless we have presented the SFM model which has proved useful for illustrating the elliptically polarized state accompanying the type II PS, in qualitative agreement with our experimental observations.

In Section 3.4, we have reviewed the main results on external perturbations in semiconductor lasers. Yet, these previous results clearly indicate that the polarization degree of freedom plays a key role in the VCSEL response to external perturbations. However, concerning nonlinear dynamics induced by optical injection in VCSELS, previous studies have been mainly carried out in the so-called parallel injection scheme for which the polarization of the injected beam and that of the free-running VCSEL are parallel. Although nonlinear dynamics such as injection-locking, wave-mixing, period-doubling route to chaos have been reported, the parallel injection does not allow to capture the role played by the VCSEL polarization switching and its possible interplay with injection-induced nonlinear dynamics. In the following chapter we discuss the issue of polarization bistability in the so-called orthogonal optical injection configuration for which the injection field is orthogonally polarized with respect to the free-running VCSEL. Interestingly, in subsequent chapters we show that orthogonal optical injection allows to address the issue of possible interplay between the polarization switching mechanism



and nonlinear dynamics induced by optical injection in VCSEL.



## Chapter 4

# Polarization control and bistability in VCSEL subject to orthogonal Optical Injection

In this chapter, we investigate polarization switching (PS) in a vertical-cavity surface-emitting laser (VCSEL) subject to orthogonal optical injection. Intensity-induced polarization switching (PS) and the associated bistability are experimentally and theoretically studied. The VCSEL is injected by a continuous-wave single mode master laser whose polarization is orthogonal to that of the free-running VCSEL. We unveil qualitatively different switching scenarios depending on the injection parameters, i.e., injected power and frequency detuning between the master laser and the free-running VCSEL. Intensity-induced polarization switching bistability is studied by scanning the injected power for a fixed detuning. We show that, depending on the detuning, bistable switching can lead to injection-locking of the VCSEL to the master laser frequency and polarization or simply switching to an unlocked state. For sufficiently large positive detunings, we experimentally observe the injection locking of the first order transverse mode which is associated with a strong suppression of the fundamental transverse mode.

Furthermore, we provide a theoretical investigation of a pure frequency-induced polarization bistability in a VCSEL subject to orthogonal optical injection, i.e., polarization bistability is analyzed when the frequency detuning is scanned for a fixed injection power. As the frequency detuning is scanned from negative to positive values and for a fixed injected power, the VCSEL exhibits two successive and possibly bistable polarization switchings. The first switching (from the slave laser polarization to the injected light polarization) exhibits a bistable region whose width is maximum for a given value of the injected power. Such a dependency of hysteresis width

on the injected power is similar to that found experimentally by Hong *et al.* [Electron. Lett. 36, 2019 (2000)]. The bistability accompanying the second switching (from the injected light polarization back to the slave laser free-running polarization) exhibits, however, significantly different features related to the occurrence of optical chaos. Interestingly, the width of the bistable region can be tuned over a large range not only by modifying the injection parameters but also by modifying the device parameters, in particular the linewidth enhancement factor ( $\alpha$ -factor).

This chapter is based on the following publications:

- I. Gatare, K. Panajotov, and M. Sciamanna, “*Frequency-induced bistability in vertical-cavity surface-emitting lasers with optical injection,*” Phys. Rev. A **75**, 023804 (2007).
- I. Gatare, J. Buesa, H. Thienpont, K. Panajotov, and M. Sciamanna, “*Polarization switching bistability and dynamics in vertical-cavity surface-emitting laser under orthogonal optical injection,*” Opt. and Quantum Electron. **42**, 429 (2006).
- I. Gatare, M. Trigriner, H. Thienpont, M. Sciamanna, and K. Panajotov, “*Experimental study of polarization switching and polarization mode hopping induced by optical injection in VCSELs,*” Proc. of the Symposium IEEE/LEOS Benelux Chapter, pp.143-146, December 2004, Gent, Belgium.

## 4.1 Introduction

Optical bistability in semiconductor lasers has attracted much attention due to its promising applications in various areas such as optical switching, optical memory, and optical signal processing [125, 126]. Optical bistability refers to the situation in which two stable optical output states are associated with a single optical input state, depending on the switching history. The use of bistable semiconductor lasers was justified by their competitive advantages such as optical gain, low optical switching power with high-speed switching. Moreover, unlike nonlinear Fabry-Perot cavity-based devices, bistable semiconductor lasers do not require any holding optical power, in addition to the switching optical power [127]. Extensive theoretical and experimental studies have been conducted on bistability in edge-emitting lasers subject to external optical injection from a master laser [127, 128, 129, 130]. The bistable behavior has been attributed to nonlinear gain saturation mechanisms resulting from the effect of the injected field on the cavity refraction index [127]. Two different approaches to achieve optical bistability in EEL

have been proposed. The first one is a bistability occurring on an injection-locking regime as the injection current of the slave laser is swept or when scanning the frequency detuning between the master laser and the slave laser [127, 129]. On the other hand, bistability can be achieved in so-called polarization-bistable laser diodes. Here, optical injection induced bistability occurs between transverse-electric (TE) and transverse magnetic (TM) polarization states through nonlinear gain saturation mechanisms [128]. A TE-TM bistable switching requires, however, two orthogonally polarized input pulses, each of which should respectively be parallel to the slave TE and TM polarization directions. Particular attention was later focused on optical injection-induced bistability in vertical-cavity surface-emitting lasers (VCSELs) [120, 125, 131]. As aforementioned, VCSELs offer many advantages with respect to edge-emitting lasers such as the possibility to fabricate large two-dimensional laser arrays for optical network interconnects [27]. By contrast to conventional edge-emitting lasers, the VCSEL light polarization suffers from instabilities and switching between two linearly polarized orthogonal states. Polarization bistability can be induced either electrically when modifying the injection current (as shown in Chapter 3) or when the VCSEL is optically driven (by optical injection [120] or optical feedback [99]).

Polarization bistability in VCSELs can indeed be induced as a result of orthogonal optical injection, i.e., the VCSEL is subject to the injection of external light with polarization linear and orthogonal to that of the free-running VCSEL [120, 132, 133, 134, 135, 136]. It was found that the sweep of the injected power for a fixed frequency detuning between the master laser (ML) and the VCSEL leads to polarization bistability switching of the VCSEL polarization to the master polarization, i.e., an intensity-induced polarization bistability [120, 133, 134]. On the other hand, Hong *et al.* reported experimentally on a different bistability behavior, called pure frequency-induced polarization switching bistability [132, 135, 136]. This type of polarization bistability occurs when sweeping the frequency detuning for a fixed injection strength. It was observed that hysteresis loop width increases with injection power at lower fixed injection levels and saturates as higher injection levels are reached.

Here, optical injection intensity-induced polarization bistability is first experimentally and theoretically investigated. The experiments are carried out for a large detuning range and unveil a switching mechanism which is associated with injection-locking of the first-order transverse mode. The effect of the bias current on polarization bistability is also analyzed. We then perform a theoretical investigation of pure frequency-induced bistability and discuss our results in light of experimental results reported by Hong *et al.* [132]. Our theoretical studies are carried out using a rate equation model that accounts for competition between fundamental transverse, orthogonal linearly polarized, modes. To this end, we use the spin-flip model (SFM)

extended to orthogonal optical injection.

## 4.2 Intensity-induced polarization bistability and switching: *experiments*

In this section, polarization switching bistability is experimentally investigated in the orthogonal optical injection configuration and for a wide frequency detuning range. We show that, depending on the frequency detuning, PS can be achieved with or without injection locking of the VCSEL to the master laser frequency. The key role played by the VCSEL's birefringence in the injection-locking mechanism is analyzed. We also show that polarization bistability mechanisms depend on VCSEL bias current.

### 4.2.1 Experimental setup

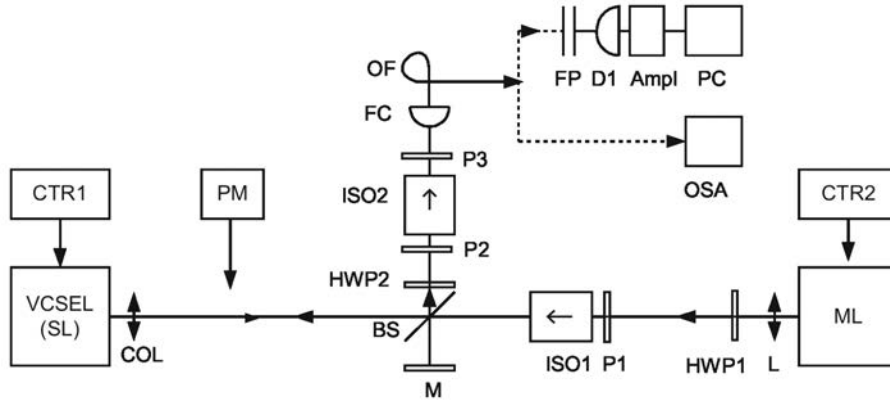


**Figure 4.2.1:** *Experimental setup of orthogonal optical injection in VCSEL. SL: slave laser, ML: master laser, COL: collimator, BS: beam splitter, HWP1-HWP2: half wave plate, ISO1, ISO2: optical isolators, L: lens, P1-P3: polarizers, M: mirror, FC: fiber coupling unit, OF: optical fiber, FP: Fabry-Perot interferometer, D1: photodiode, Ampl: amplifier, PC: computer, OSA: optical spectrum analyzer, PM: power meter, CTR1 (CTR2): current driver and temperature controller of SL (ML). The VCSEL temperature was fixed at 20°C.*

The experimental setup which implements orthogonal optical injection is presented in Fig. 4.2.1. A quantum-well VCSEL that emits around 845 nm is used as a slave-laser (SL). The VCSEL was selected from a 2D VCSEL array which is mounted on a heat sink with a Peltier element for temperature control. Its bias current and temperature are controlled by a low-noise

laser driver (CTR1). An external-cavity laser diode is used as master laser (ML). The wavelength of the light emitted by the ML can be tuned within the range of 845 -855 nm by another low-noise laser driver (CTR2). The injection beam from the ML is then focused on the SL using a lens (L) while the light emitted by the SL is collimated by another lens (COL). An isolator (ISO1) with 36-40 dB of attenuation achieves a unidirectional coupling between the ML and the SL. The strength of the injected beam is varied using a polarizer P1. A half-wave plate (HWP1) fixes the polarization of the injected light to be orthogonal to the polarization direction of the free-running VCSEL. A non-polarizing 50/50 beam-splitter and a mirror M are used to align the SL and the ML with the detection branch. The polarization in which the measurements are performed is selected by a half wave plate HWP2. The second isolator ISO2 with 36-40 dB of attenuation together with two polarizers P2 and P3 prevent the VCSEL from feedback-induced instabilities that may be generated by the light reflected by the fiber-coupling device FC. A power meter PM is used to measure the power emitted by the ML or the SL whereas spectral measurements are performed using either an optical spectrum analyzer (OSA) or a Fabry-Perot spectrometer (Free Spectral Range of 30 GHz and finesse of 150) associated with a photodetector D1 and amplifier (Ampl) coupled to a computer (PC).

#### 4.2.2 Polarization-resolved light-current characteristics of the solitary VCSEL

The experimental polarization-resolved Light-Current ( $L-I$ ) curve of the solitary VCSEL is plotted in Fig. 4.2.2. A power meter is used to measure the light emitted by the free-running VCSEL which is detected just in front of the collimating lens COL (see Fig. 4.2.1). A polarizer is also used to select the desired polarization direction. The fundamental transverse mode with vertical polarization (higher frequency mode  $\nu_{\text{HF}}$ ) starts to lase at around 1 mA. When the injection current is increased, a PS of type I [from  $\nu_{\text{HF}}$  to the lower frequency mode ( $\nu_{\text{LF}}$ )] occurs through mode hopping at a current of 1.6 mA. Then, the horizontal polarization mode prevails until a current of 4.6 mA where an abrupt PS is observed. This PS is of type II, i.e., from low-frequency mode  $\nu_{\text{LF}}$  to the high-frequency mode  $\nu_{\text{HF}}$ . It is worth noting that just before the type II PS, we observe emission in an elliptical polarization and an increase of the power emitted in the vertical polarization, but only in the right-hand scan, i.e., when increasing the injection current. The PS of type I occurs at the same current value if the current is increased or decreased, while the type II PS takes place for different values of current depending on the direction we change the current. As a result, a hysteresis is observed. The  $L-I$  curves are only represented until 5 mA injection current is reached. For higher currents higher-order transverse modes are excited.

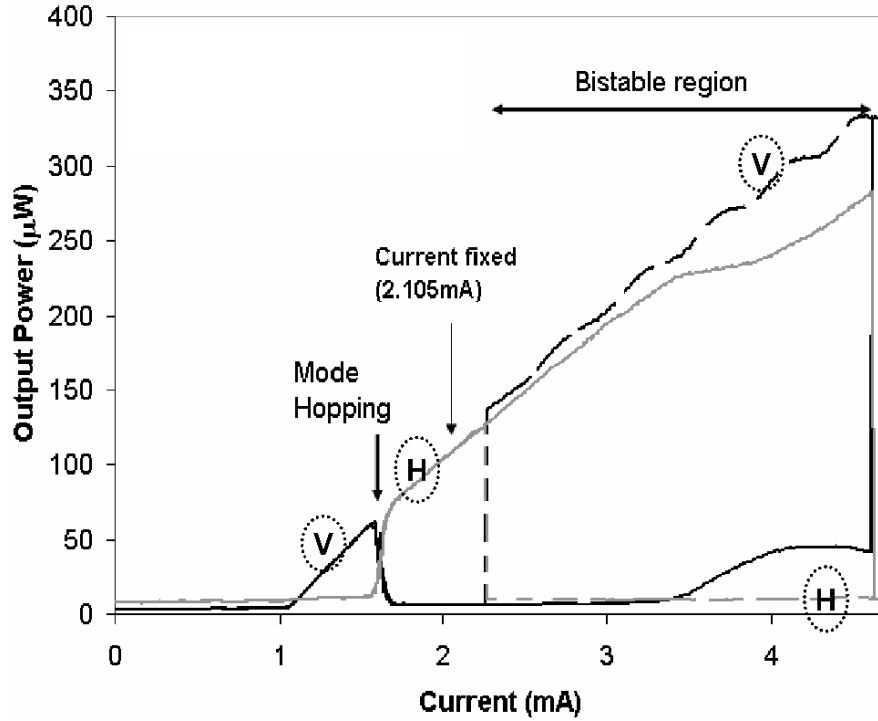


**Figure 4.2.2:** Polarization-resolved optical power versus injection current curve of the solitary VCSEL for a substrate temperature of 20°C. The lines corresponding to the vertical and horizontal polarization are indicated by V and H, respectively. The continuous (dashed) line represents the upward (downward) scan.

In Fig. 4.2.2, the values of the VCSEL polarization resolved output power are relative, for optimized optical alignment we measure total output power of  $P_{inj} = 1.28$  mW at a fixed VCSEL current of 2.105 mA.

### 4.2.3 Intensity-induced polarization switching bistability

Intensity induced polarization switching (PS) is analyzed by scanning the injection power for fixed detuning values. The bias current is always chosen such that the free-running VCSEL emits in the low-frequency fundamental transverse mode (which is horizontally polarized). Injection-induced PS and its associated hysteresis are investigated for different biasing conditions. For a fixed injection current, we explore how the polarization switches when scanning the injection power for a very wide detuning range. We focus on the role of the VCSEL birefringence in the optically induced bistable PS.

Polarization switching of the VCSEL submitted to orthogonal optical in-



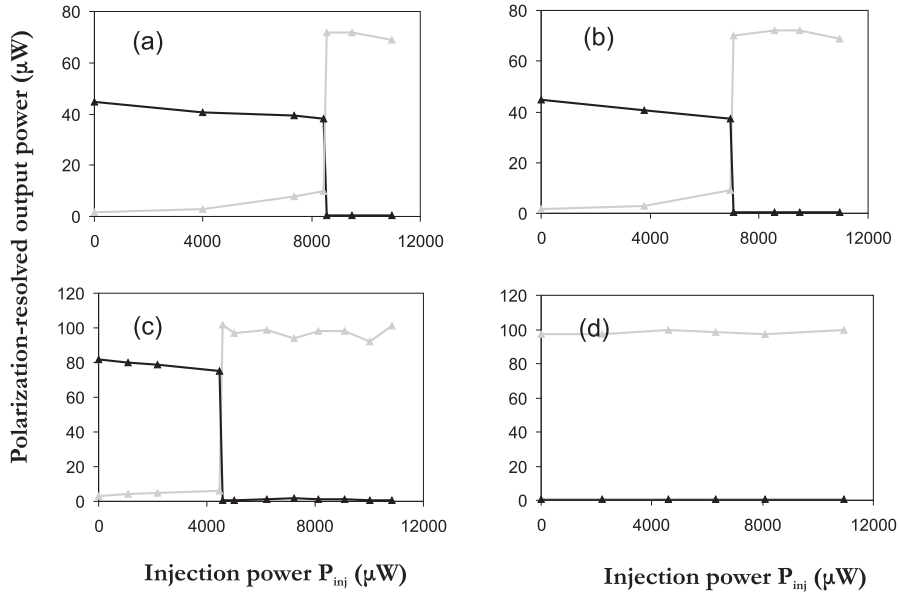


**Figure 4.2.3:** *Hysteresis in the polarization resolved optical power of the VCSEL when the injected power  $P_{inj}$  is first increased and then decreased for two values of the bias current  $I_{SL}$ . The black (gray) line represents the horizontal (vertical) polarization.  $I_{SL} = 1.9$  mA and for  $\Delta\nu = -36$  GHz: (a) Increasing  $P_{inj}$ , (b) Decreasing  $P_{inj}$ ;  $I_{SL} = 2.603$  mA and for  $\Delta\nu = -20$  GHz: (c) Increasing  $P_{inj}$ , (d) decreasing  $P_{inj}$ .*

jection is experimentally analyzed when the injected power is first increased and then decreased in the conditions where both the bias current and temperature of the VCSEL are fixed. If we also keep the wavelength of ML constant, the frequency splitting between ML and the solitary VCSEL is also constant. Figure 4.2.3 shows the evolution of the power emitted by the VCSEL when the injected power is varied using polarizer P1 (see the setup in Fig. 4.2.1). Figures 4.2.3(a) and 4.2.3(b) represent the situation in which, with no injection power, the VCSEL emits in horizontal polarization with a bias current fixed at 1.9 mA (which is less than the lower limit of the bistable region of the LI curve, see Fig. 4.2.2). If the injected power is increased [Fig. 4.2.3(a)], a PS from horizontal (black line) to vertical (gray line) LP fundamental mode is observed. The SL keeps emitting in the vertical polarization direction until the maximum power limit of the ML is reached. From this maximum point, we then decrease the injected power [Fig. 4.2.3(b)]. The VCSEL switches back to the horizontal polarization direction for an injection strength level that is lower than the power at which we observed PS during the upwards scan, thus showing a hysteresis associated to PS [120]. When

the VCSEL is biased at 2.6 mA, i.e., within the bistable zone of the LI curve (see Fig. 4.2.2), PS from horizontal to vertical direction is also observed during the upwards scan of the injected power [Fig. 4.2.3(c)]. However, when the injected power is then decreased, the VCSEL keeps emitting in the vertical polarization direction even if the injection power is suppressed [Fig. 4.2.3(d)].

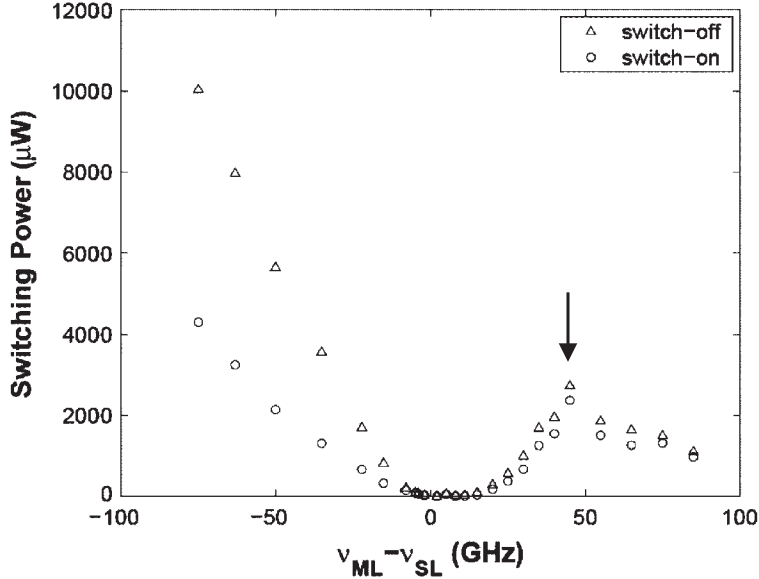


**Figure 4.2.4:** Evolution of the switching off (triangle) and switching on (circle) power when the injected power is increased and decreased respectively and this for different frequency detunings between master and slave lasers,  $\Delta\nu = \nu_{ML} - \nu_{SL}$ . The arrow indicates the onset of the locking of the VCSEL first order transverse mode to the master laser which is associated with a strong depression of the fundamental transverse mode

We have analyzed the dependency of the width of the hysteresis zone on the frequency detuning between ML and the free running VCSEL for a fixed bias current of 2.105 mA. The measurements are performed after the coupling between ML and SL is optimized. We plot in Fig. 4.2.4 the evolution of the injected power required for polarization-switching (PS) from horizontal to vertical (switch off) and from vertical to horizontal (switch on), and for different detuning values. We recall that the low-frequency mode ( $\nu_{LF}$ ) corresponds to horizontal polarization while high-frequency mode  $\nu_{HF}$  is vertically polarized. The minimum switching power is obtained for a detuning of about 2 GHz which corresponds to the frequency splitting between the two LP orthogonal modes of our VCSEL. This is consistent with what has been previously reported by Pan *et al.* [120]. In fact the minimum power needed to achieve PS is reached when the master laser frequency coincides with that of the vertically polarized VCSEL mode (which has the same polarization as

the ML). Beyond 2 GHz detuning, PS is achieved for larger injection power. Furthermore, we find that the width of the hysteresis zone associated to PS increases when evolving toward larger negative detunings from the minimum switching power point. Interestingly, over this detuning range PS is always accompanied by injection locking to the ML frequency. On the other hand, for positive detunings larger than 2 GHz the hysteresis loop width remains almost constant with increasing detuning. By contrast to what has been reported in ref. [120], for detuning values larger than 2 GHz, PS is not accompanied by injection locking. In fact over that detuning range, as the injection power is progressively increased from the free-running regime, the SL horizontal mode is progressively frequency-pushed with respect to the ML. As the injection power is still increased, PS to the fundamental vertical mode is achieved but the VCSEL remains unlocked. However, for large positive detuning more than 50 GHz, injection locking of the first-order transverse mode to the ML frequency is observed and is accompanied by a strong suppression of the VCSEL fundamental mode. Transverse mode competition and locking of the first order transverse mode are theoretically and experimentally investigated in chapter 8.

The results presented so far are obtained by analyzing the evolution of the polarization-resolved output power of the injected VCSEL. However polarization switching and locking induced by orthogonal optical injection may involve interesting nonlinear dynamics which deserve further investigations. The interplays between PS and nonlinear dynamics will be addressed in subsequent chapters (see chapters 5 and 6).

### 4.3 Modelling of the VCSEL subject to orthogonal optical injection

We introduce the theoretical study of optical injection in VCSELs. The orthogonal optical injection is modelled in the framework of the spin-flip model (SFM). To this end, the model presented in section. 3.2 for the free-running VCSEL is appropriately modified to account for the effect of external optical injection.

A semiconductor laser subject to external optical injection can be easily modelled by analogy to a Fabry-Perot cavity. The injected beam is transmitted into the cavity through one of the partially reflecting mirrors as sketched in Fig. 4.3.1. If we assume that only the propagation effects along the lasing direction  $z$  are considered, the injected beam can be written as follows:

$$E_{\text{inj}}(t, z) = E_{\text{inj}}^0 \exp[i(\omega_{\text{inj}}t + k_{\text{inj}}z)]. \quad (4.3.1)$$

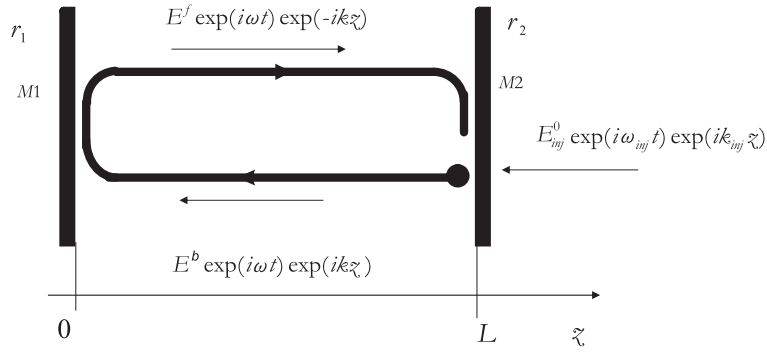


**Figure 4.3.1:** Schematic of a Fabry-Perot cavity for the modelling of a semiconductor laser under optical injection. The superscripts *f* and *b* denote the forward and backward internal travelling field waves.

Where  $E_{inj}^0$  is the constant amplitude of the injected field, and  $\omega_{inj}$  and  $k_{inj}$  are respectively the frequency and the propagation constant of the injected field.

Optical injection can be accounted for by using the so-called travelling wave phenomenological approach for the modelling of semiconductor lasers. The boundary conditions at the internal facet of mirror *M2* imposes the matching between the electric field at time *t* and that after the internal cavity round-trip time ( $\tau_{in}$ ):

$$E^b(t, L) \exp(-ikL) r_1 \exp(-ikL) r_2 + t_2 E_{inj}(t + \tau_{in}, L) = E^b(t + \tau_{in}, L). \quad (4.3.2)$$

Let us assume that the operating conditions are chosen such that the free-running VCSEL emits in the fundamental mode, linearly polarized along the *x* eigen axis. In the framework of the SFM model [see eqs. (3.2.19)-(3.2.22)] and by analogy to the travelling wave approach as described by eq. (4.3.2), orthogonal optical injection can be implemented by adequately modifying the rate equation related to the *y*-LP mode. The procedure is quite similar to the case of an edge-emitting laser subject to external optical injection<sup>1</sup>. As a result, one obtains the following modified SFM rate equations:

---

<sup>1</sup>For details, see the Appendix A

$$\frac{dE_x}{dt} = -(\kappa + \gamma_a)E_x - i(\kappa\alpha + \gamma_p)E_x + \kappa(1 + i\alpha)(DE_x + idE_y), \quad (4.3.3)$$

$$\begin{aligned} \frac{dE_y}{dt} &= -(\kappa - \gamma_a)E_y - i(\kappa\alpha - \gamma_p)E_y + \kappa(1 + i\alpha)(DE_y - idE_x) \\ &\quad + \frac{t_2}{\tau_{in}}E_{inj}^0 \exp[i(\Delta\omega t + \Phi)], \end{aligned} \quad (4.3.4)$$

$$\frac{dD}{dt} = -\gamma_e \left[ D \left( 1 + |E_x|^2 + |E_y|^2 \right) - \mu + id(E_y E_x^* - E_x E_y^*) \right], \quad (4.3.5)$$

$$\frac{dd}{dt} = -\gamma_s d - \gamma_e \left[ d \left( |E_x|^2 + |E_y|^2 \right) + iD(E_y E_x^* - E_x E_y^*) \right]. \quad (4.3.6)$$

All the state variables and system parameters are the same as in section 3.2. The ratio  $t_2/\tau_{in}$  represents the coupling rate (or  $\kappa_{inj} = t_2/\tau_{in}$ ) while  $\Delta\omega$  is the frequency detuning between the master laser and free-running VCSEL:  $\Delta\omega = \omega_{inj} - \omega_{int}$ , where  $\omega_{inj}$  is the injected field frequency and  $\omega_{int}$  is an intermediate frequency between the frequencies of the  $x$ - and  $y$ - LP modes as defined in section 3.2:  $\omega_{x,y} = \mp\gamma_p \pm \alpha\gamma_a$ , thus  $\omega_{int} = (\omega_x + \omega_y)/2$ .  $\Phi$  is the injected field constant phase and is defined as:  $\Phi = \Delta\omega\tau_{in} + \Delta kL$  with  $\Delta k = k_{inj} - k$ .

The system represented by eqs. (4.3.3)-(4.3.6) is non autonomous because of the time-dependent term in the right-hand side of equation (4.3.4). However, by changing the frequency reference frame from the free-running lasing frequency  $\omega$  to the injected field frequency  $\omega_{inj}$ , one obtains an autonomous system. To this end, the following variable change is applied:

$$\tilde{E}(t) = E(t) \exp[i(\Delta\omega t + \Phi)]. \quad (4.3.7)$$

If, for simplicity, we keep the same variable notation as in eqs. (4.3.3)-(4.3.6), we obtain the following autonomous system for the SFM model with orthogonal optical injection:

$$\frac{dE_x}{dt} = \kappa(1 + i\alpha)(DE_x + idE_y - E_x) - i(\gamma_p + \Delta\omega)E_x - \gamma_a E_x, \quad (4.3.8)$$

$$\begin{aligned} \frac{dE_y}{dt} &= \kappa(1 + i\alpha)(DE_y - idE_x - E_y) + i(\gamma_p - \Delta\omega)E_y + \gamma_a E_y \\ &\quad + \kappa_{inj}E_{inj}^0, \end{aligned} \quad (4.3.9)$$

$$\frac{dD}{dt} = -\gamma_e \left[ D \left( 1 + |E_x|^2 + |E_y|^2 \right) \right] + \gamma_e \mu - i\gamma_e d(E_y E_x^* - E_x E_y^*), \quad (4.3.10)$$

$$\frac{dd}{dt} = -\gamma_s d - \gamma_e d \left( |E_x|^2 + |E_y|^2 \right) - i\gamma_e D(E_y E_x^* - E_x E_y^*). \quad (4.3.11)$$

In our orthogonal optical injection scheme, we assume that the coupling rate  $\kappa_{inj}$  is constant. Consequently, the amplitude of the injected field  $E_{inj}^0$  and the frequency detuning  $\Delta\omega$  are the external optical injection parameters.

#### 4.4 Intensity-induced polarization bistability in VCSEL under orthogonal optical injection: *theory*

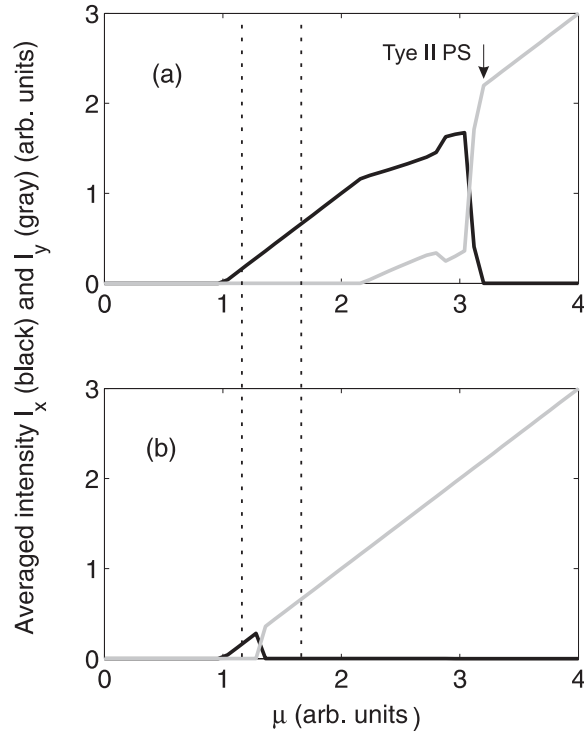


**Figure 4.4.1:** *Theoretical polarization-resolved Light-Current characteristics of the free-running VCSEL when the normalized injection current  $\mu$  is first increased (a) and then decreased (b). Black (gray) represents the low- (high-) frequency x-(y-) LP mode.*

Here, we numerically analyze optical injection intensity-induced polarization switching bistability. As in the experimental study we investigate how the averaged polarization-resolved intensity of the injected VCSEL evolves when varying the injection strength  $E_{inj}^0$  for selected detuning values. Furthermore, we analyze the effect of the bias current on the hysteresis associated to polarization switching (PS). We find intensity-induced switching scenarios which qualitatively agree with our experimental observations pre-

sented in section 4.2. Numerical simulations have been performed using the following parameters:  $\kappa = 300 \text{ ns}^{-1}$ ,  $\gamma_p = 6.28 \text{ rad/ns}$ ,  $\gamma_a = -0.2 \text{ ns}^{-1}$ ,  $\gamma_s = 50 \text{ ns}^{-1}$ ,  $\gamma_e = 0.55 \text{ ns}^{-1}$ ,  $\alpha = 3$ . With such a parameter choice, the free-running VCSEL starts emitting in the low-frequency mode ( $x$ -LP) close to the threshold. As the injection current  $\mu$  is increased [see Fig. 4.4.1(a)], polarization switching to the high-frequency mode ( $y$ -LP) is achieved (type II PS). If the injection current is then decreased a relatively large hysteresis zone associated to type II PS is resolved [see Fig. 4.4.1(b)]. As we have already mentioned in chapter 3, it is worth noting that the basic SFM model from which we develop our study is not sufficient to model a device whose light-current characteristic exhibits both type I and type II switching, as is experimentally observed in Fig. 4.2.2 unless one includes gain saturation mechanisms as it has been proposed by Prati *et al.* [65]. Nevertheless, the simple model proves useful for exploring main features which support the experimentally observed intensity-induced bistable switching.

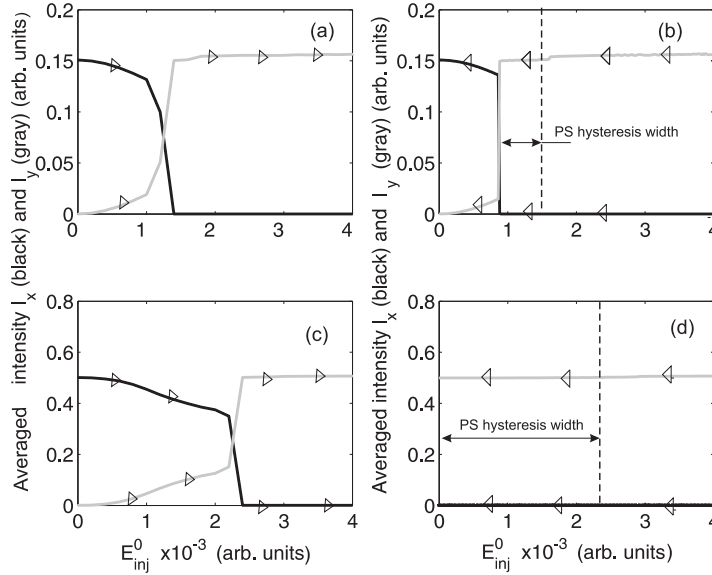


**Figure 4.4.2:** *Hysteresis in the polarization resolved averaged intensity of the VCSEL for two values of the bias currents: 1)  $\mu = 1.15$  when increasing (a) and then decreasing (b) the injection strength  $E_{inj}^0$ ; 2)  $\mu = 1.5$  when increasing (c) and then decreasing (d) the injection strength  $E_{inj}^0$ . The frequency detuning is fixed at  $\Delta\omega = 3 \text{ rad.ns}^{-1}$ . Black (gray) represents the low- (high-) frequency  $x$ -( $y$ -) LP mode*

Similarly to what has been achieved experimentally, we numerically analyze two biasing conditions. First, the normalized bias current  $\mu$  is set above threshold but still at a value less than the lower limit of the light-current

bistable region (e.g.  $\mu_1 = 1.15$ ). The steady state is such that the free-running VCSEL emits an  $x$ -LP mode. By progressively increasing the amplitude of the orthogonally polarized injected field [Fig. 4.4.2(a)], a switching from  $x$  to  $y$  polarization axis is achieved. Beyond that PS point, the VCSEL keeps emitting along the  $y$  polarization axis. If the injection strength is then decreased, a PS from  $y$  to  $x$  polarization occurs for an injected strength lower than what is required for achieving PS during the upwards scan of  $E_{\text{inj}}^0$ , thus displaying an intensity-induced polarization bistability [Fig. 4.4.2(b)]. Next, we fix the normalized bias current within the bistable region of the polarization resolved LI curve (e.g.,  $\mu_2 = 1.5$  in Fig. 4.4.1). The initial conditions are adequately chosen such that the free-running VCSEL lases in the  $x$ -LP mode. Similarly to the previous case, the injection strength  $E_{\text{inj}}^0$  is first increased [Fig. 4.4.2(c)] until a switch to the orthogonal polarization axis ( $y$ )-LP is achieved. If the injection strength is then decreased [Fig. 4.4.2(d)], the VCSEL keeps emitting in the  $y$ -LP mode even after the injection is suppressed, thus exhibiting a relatively large bistable region. The obtained numerical results are in qualitative agreement with our experimental observations as presented in Fig. 4.2.3. by showing how the biasing conditions can dramatically affect the VCSEL response to orthogonal optical injection. Both theory (Fig. 4.4.2) and experiments (Fig. 4.2.3) show that, as the VCSEL is driven close to PS by increasing the injection strength, the power of the injected  $y$ -LP mode increases progressively while that of the orthogonal noninjected  $x$ -LP mode decreases. Such a phenomenon denotes the existence of nonlinear dynamics accompanying the switching and which may involve a competition between the orthogonal LP modes. The evolution of polarization-resolved averaged intensities, as experimentally reported in section 4.2 and in ref. [120] does not provide sufficient information to identify possible fast nonlinear dynamics associated with PS. Therefore, for a better understanding of the switching mechanism in a VCSEL subject optical injection, it is important to map the underlying nonlinear dynamics as optical injection control parameters are tuned. An experimental mapping of nonlinear dynamics accompanying PS is discussed in Chap. 5 while the underlying bifurcations mechanisms are investigated in Chap. 6.

## 4.5 Frequency-induced polarization bistability in VCSEL with orthogonal optical injection

In the previous sections we have analyzed intensity-induced polarization bistability induced orthogonal optical injection. Here, we theoretically investigate a pure frequency-induced polarization bistability which complements the experimental work carried out by Hong *et al.* [132, 135, 136]. They experimentally demonstrated that bistable switching occurred when sweeping



the frequency detuning for a fixed injection strength. The result, taken from ref. [132], is shown in Fig. 4.5.1. As the frequency detuning is decreased from positive to negative detuning, Hong. *et al* observed two successive switching points. The first one is located in the high-frequency range and occurs from the slave laser polarization ( $X$ ) to the orthogonal master laser polarization ( $Y$ ). On the other hand, the second switching is achieved in the lower frequency range and corresponds to the switch-on of the slave polarization. A reverse switching scenario is observed when increasing the detuning from negative to positive detuning. Interestingly, a pure-frequency bistability is found for the switching located in the lower frequency regime while the switching in the high-frequency regime is achieved almost without hysteresis. Furthermore, it was observed that the width of the polarization bistability loop increases and reaches a maximum when changing the injection power from small to larger values. But for relatively much higher injection levels, the width of the switching hysteresis saturates [132].

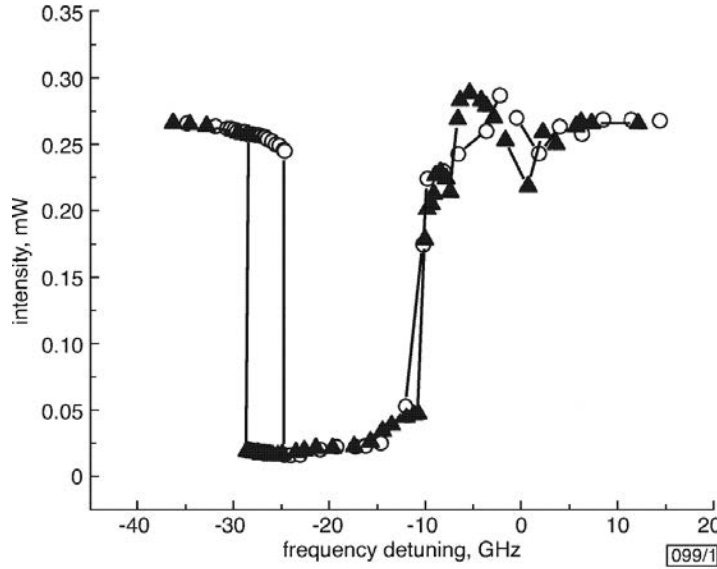


**Figure 4.5.1:** Intensity of  $X$ -component of slave laser light polarization as function of frequency detuning, after [132]

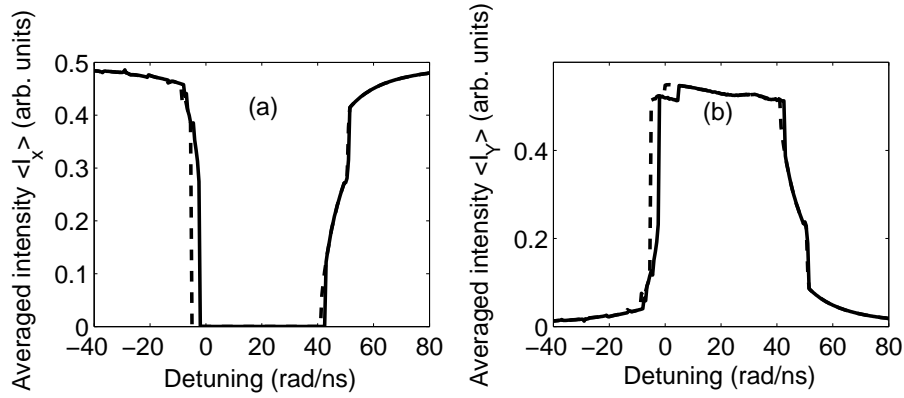
Our theoretical analysis of the pure frequency-induced polarization bistability mechanisms is based on the rate equations presented in eqs. (4.3.8)-(4.3.11). A first polarization bistability case is found to accompany the PS from the  $x$  linearly polarized [LP] low-frequency mode to the  $y$  LP high-

frequency mode. This switching to the orthogonal, injected light polarization is also called low-frequency [LF] PS since it occurs first as we increase the detuning from negative to positive values. The bistability accompanying the LF PS exhibits characteristics similar to those reported experimentally by Hong *et al.* [132]. Moreover, we find that a second bistability mechanism may accompany the second PS from the  $y$  LP high-frequency mode to the  $x$  LP low-frequency mode [later called the high-frequency (HF) PS point]. This bistability mechanism exhibits different characteristics from those of the bistability that accompanies the LF PS, in particular as regarding the dependency of the hysteresis width on the injected power. We furthermore report on the occurrence of polarization chaos for detuning values in between the polarization switching points. Interestingly, the width of the bistable regions can be tuned significantly by modifying the device parameters. We emphasize, for example, the important role of the linewidth enhancement factor ( $\alpha$  factor).

#### 4.5.1 Polarization bistability

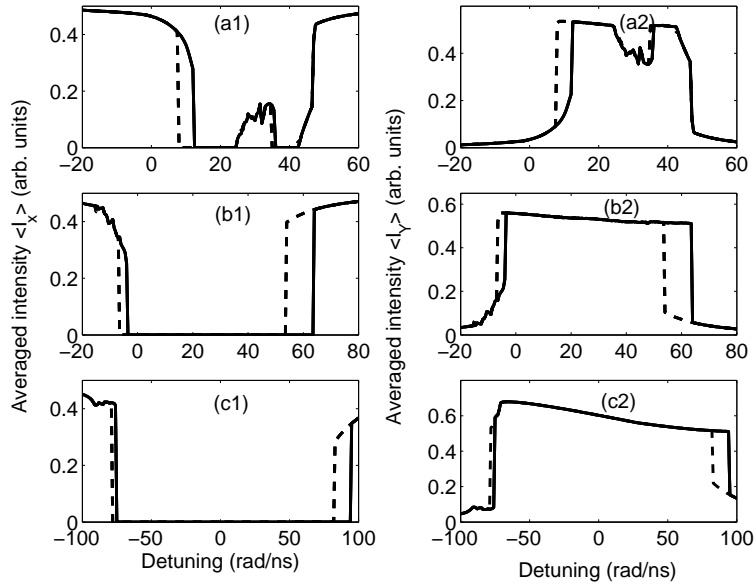
The main features associated to pure frequency-induced polarization bistability are analyzed. Bistability associated to LF PS and HF PS points is investigated as the detuning between the master and slave laser is scanned for different optical injection strength levels. Our numerical simulations have been performed using the following choice for the VCSEL parameters:  $\gamma_e = 1 \text{ ns}^{-1}$ ,  $\gamma_s = 50 \text{ ns}^{-1}$ ,  $\kappa = \kappa_{inj} = 300 \text{ ns}^{-1}$ ,  $\gamma_p = 30 \text{ rad/ns}$ ,  $\gamma_a = 0.5 \text{ ns}^{-1}$ ,  $\alpha = 3$ ,  $\mu = 1.5$ . With these parameters the free-running VCSEL exhibits a polarization switching from the  $y$  LP, high-frequency mode to the  $x$  LP low-frequency mode at  $\mu = 1.2$ , and the VCSEL light polarization at  $\mu = 1.5$  is therefore oriented along  $x$  before we apply the orthogonal optical injection. The injection parameters, i.e., the injection strength  $E_{inj}$  and the frequency detuning  $\Delta\omega$  are defined as in Section 4.3.

Figure 4.5.2 shows a typical polarization bistability observed when sweeping the frequency detuning from negative to positive values and then back, for a fixed value of the injected power. The injected power is normalized as  $P_{inj}/I_0$ , with  $P_{inj} = |E_{inj}^0|^2$ , and  $I_0 \equiv |E_x^0|^2 + |E_y^0|^2$ , where  $E_x^0$  and  $E_y^0$  are the LP components of the field in absence of optical injection. In our case  $I_0$  is equal to the intensity of the  $x$  LP mode in absence of optical injection, since the  $y$  LP mode in the solitary VCSEL is nonlasing. In the case of Fig. 4.5.2 we take  $P_{inj}/I_0 = 0.09\%$ . The averaged intensities  $\langle I_{x,y} \rangle = \langle |F_{x,y}|^2 \rangle$  are plotted for each set of injection parameters, in order to mimic the experimental observations made with a slow photodetector. The VCSEL exhibits two successive PSs. One PS, called the HF PS is located in the high-frequency detuning range and corresponds to the switch from  $y$  to  $x$  LP mode. The second PS, called the LF PS is located in the low-frequency detuning range



**Figure 4.5.2:** *Pure frequency polarization bistability induced by optical injection. Solid (dashed) line represents the evolution of the averaged optical intensity when the frequency detuning is increased from negative to positive values (decreased from positive to negative values) and for a fixed injection strength  $P_{inj}/I_0 = 0.09\%$ : (a)  $x$ -polarized mode, (b)  $y$ -polarization direction.*

and corresponds to the switch from  $x$  to  $y$  LP mode. The LF PS is found to be accompanied by bistability, while the HF PS occurs without hysteresis.



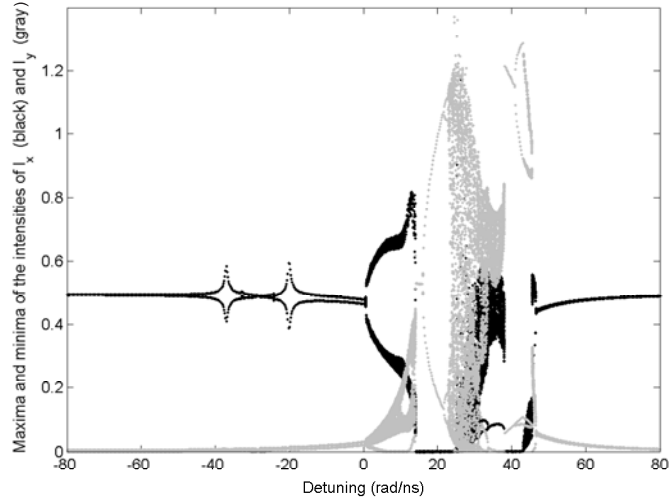
**Figure 4.5.3:** *Influence of the injection strength on pure-frequency polarization bistability. Same as Fig. 1 but for (a1), (a2):  $P_{inj}/I_0 = 0.05\%$ , (b1), (b2):  $P_{inj}/I_0 = 0.15\%$ , (c1), (c2):  $P_{inj}/I_0 = 1.5\%$ .*

Figure 4.5.2 resembles qualitatively the experimental observation by Hong *et al.* [132]. An increase or decrease of the fixed injection strength may however significantly modify this picture, as shown in Fig. 4.5.3. For a smaller injected power than in Fig. 4.5.2 [ $P_{inj}/I_0 = 0.05\%$ , see Figs. 4.5.3(a1) and 4.5.3(a2)], the normally depressed  $x$  LP may be excited in a small detuning range in between the two LF and HF PS points. It is worth noting that the switching off of the  $x$  LP mode in this small detuning region is also accompanied by hysteresis and therefore bistability. As shown in the following, this small detuning range in between the two PS points corresponds to a period-doubling route to chaos in the two modes and therefore to strong laser dynamical instabilities. When increasing the injected power, as is done in Figs. 4.5.3(b1), 4.5.3(b2), 4.5.3(c1), and 4.5.3(c2) ( $P_{inj}/I_0 = 0.05\%$  and  $1.5\%$ , respectively), the hysteresis width accompanying the LF PS event is found to decrease while, by contrast, hysteresis starts to appear on the HF PS event and its width increases with the increase of injected power.

## 4.5.2 Polarization dynamics accompanying polarization switching

The two-mode emission observed in between the LF and HF PS points as shown in Figs. 4.5.3(a1) and 4.5.3(a2) is studied in more detail in this section. Figure 4.5.4 shows a bifurcation diagram of the maxima and minima of the  $x$  LP (black) and  $y$  LP (gray) intensities as the detuning varies from negative to positive values, and the injection level is fixed at  $P_{inj}/I_0 = 0.04\%$ . Figure 5.5 shows typical intensity time traces for specific values of the frequency detuning. Our aim in this section is to complement the analysis of averaged mode intensities in Fig. 4.5.3 with the analysis of fast dynamics in the mode intensities in Figs. 4.5.4 and 4.5.5, and therefore to identify bifurcations of the mode dynamics underlying the two PSs (LF and HF PSs).

As shown in Fig. 4.5.4, at a detuning  $\Delta\omega = -80$  rad/ns the VCSEL emits in the  $x$  polarization direction. By increasing the frequency detuning to more positive values, the nonlinear interaction between the master laser and the VCSEL fields gives rise to wave mixing dynamics. However, when the detuning is close to the relaxation oscillation frequency of the VCSEL or its double, a dramatic change in the laser dynamics is observed. The computed value of the relaxation oscillation frequency, with our parameter choice, is  $\omega_{RO} = \sqrt{2\kappa\gamma_e(\mu - 1)} \approx 17.3$  rad/ns. These well-resolved amplified periodic regimes [Fig. 4.5.5(a)] correspond to subharmonic resonances and have been also reported theoretically and experimentally in edge-emitting lasers [137]. We also point out that this periodic dynamics involves mostly the  $x$  polarized mode, the orthogonal mode being almost depressed. As we move to positive detuning, the normally depressed  $y$  LP mode exhibits a strong time-periodic



**Figure 4.5.4:** Bifurcation diagram of the LP mode intensities when the frequency detuning is increased from  $-80$  rad/ns to  $80$  rad/ns and for a fixed injection level  $P_{inj}/I_0 = 0.04\%$ .

dynamics in competition with the  $x$  LP mode [Fig. 4.5.5(b)], until the VCSEL locks its polarization and frequency to the master laser [Fig. 4.5.5(c)]. This injection-locking steady state is achieved around a detuning value of  $15$  rad/ns and coincides with a switch-off of the  $x$  LP mode. As the detuning is increased further, the injection-locked state is exited through a Hopf bifurcation which gives rise to a time-periodic dynamics in the  $y$  LP mode only [Fig. 4.5.5(d)]. This limit cycle regime is then followed by a successive period-doubling route [Fig. 4.5.5(e)] to chaos [Fig. 4.5.5(f)]. It is worth noting that the  $x$  LP mode is suddenly excited when the  $y$  LP mode exhibits strong chaotic instabilities. For still larger positive detunings, the VCSEL evolves from a chaotic regime back to a time-periodic dynamics through an inverse period-doubling cascade of bifurcations, and switches back to the  $x$  LP mode. The analysis performed in this section therefore shows also that the two PS points (LF PS and HF PS) strongly differ in the associated polarization dynamics and corresponding bifurcation mechanisms. The first PS that appears when scanning the detuning from negative to positive values (LF PS) leads to an abrupt switch-off of the  $x$  LP mode and possibly to injection locking of the  $y$  LP mode to the master laser and polarization. A steady injection-locked state may be achieved (as in the case shown in Fig. 4.5.4) or not, depending on the value of the injection strength [133, 134]. By contrast, the second PS (HF PS) corresponds to a gradual decrease (increase) of the averaged  $y$  LP ( $x$  LP) mode intensity. Preceding this PS point the VCSEL

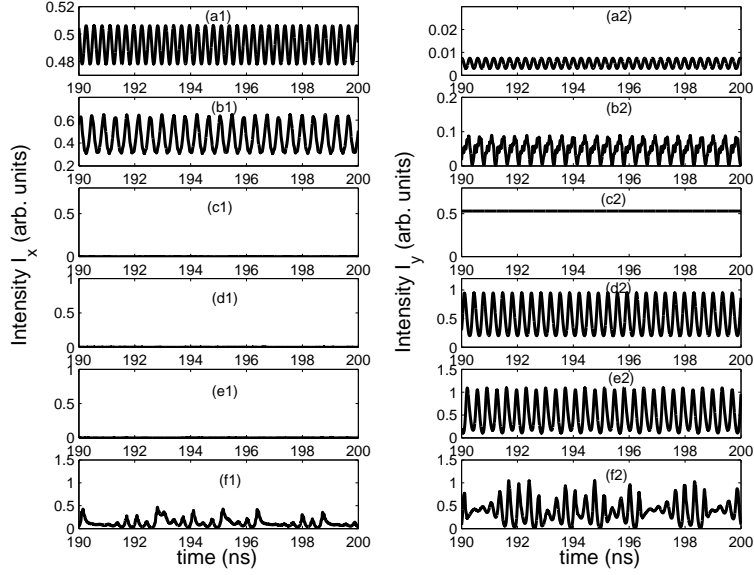


**Figure 4.5.5:** Polarization-resolved intensity time traces showing a period doubling route to chaos in between the two PS when the frequency detuning is increased from  $-80$  rad/ns to  $80$  rad/ns and for a fixed injection level  $P_{inj}/I_0 = 0.04\%$ . The left (right)-hand panels represent the evolution of the  $x$ -polarized ( $y$ -polarized) mode for selected detuning values : (a)  $\Delta\omega = -37.07$  rad/ns, (b)  $\Delta\omega = 5.00$  rad/ns, (c)  $\Delta\omega = 15.00$  rad/ns, (d)  $\Delta\omega = 19.31$  rad/ns, (e)  $\Delta\omega = 21.98$  rad/ns, (f)  $\Delta\omega = 28.96$  rad/ns.

may exhibit severe laser instabilities, depending on the value of the injection strength. The existence of a limit cycle dynamics resulting from a Hopf bifurcation on the injection locked steady-state has been experimentally observed by Hong *et al.* [132, 135, 136]. Our simulations predict moreover strong chaotic instabilities close to the HF PS point and wave-mixing dynamics between orthogonal LP modes close to the LF PS point.

### 4.5.3 Dependency of hysteresis width on injected power

In this section, we analyze the dependency of the bistability accompanying the two PS points (LF and HF PS) on the injected power. It is clear already from Fig. 4.5.3 that the hysteresis width accompanying bistability of the LF PS (HF PS) progressively decreases (increases) as the injection strength increases; however, it is interesting to perform here a more systematic and precise study of the hysteresis width as function of the injection strength.

We plot in Fig. 4.5.6 the evolution of the width of the hysteresis associated

with the HF PS when scanning the detuning for different injection strengths. For weak injection strengths  $P_{inj}/I_0$  that range between 0.01% and 0.09%, the HF PS is not accompanied by bistability, as already mentioned. However, for higher injection levels, a sudden increase in the width of the PS bistability loop is found over a narrow injection strength interval that ranges from 0.09% to 0.11%. Beyond this interval and for injected powers  $P_{inj}/I_0$  less than 0.4%, the width of the hysteresis loop decreases almost linearly. For further increase in the injected power, the width of the frequency-induced polarization bistability region increases again, showing a saturation behavior at strong injection levels.

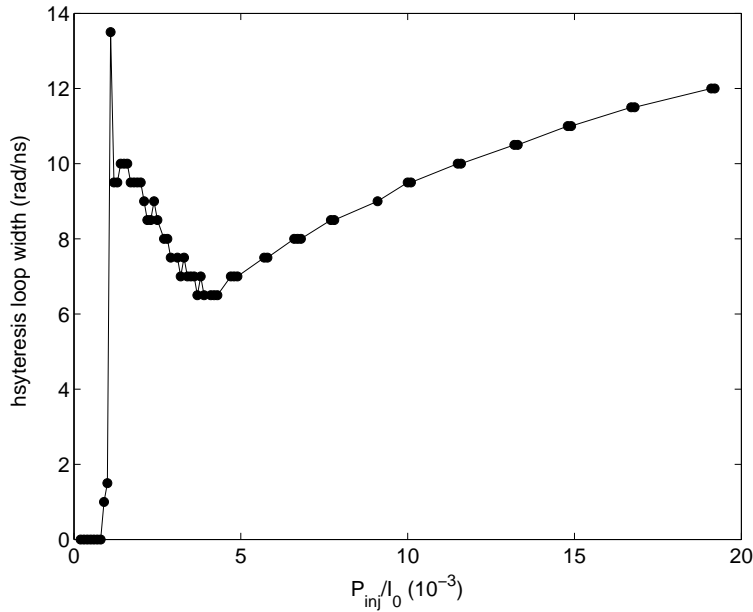


**Figure 4.5.6:** *Dependency of the hysteresis width associated with the HF PS on the injected power.*

The evolution of the hysteresis width associated to the LF PS as function of the injected power is plotted in Fig. 4.5.7. As the injection strength increases, the width of the polarization hysteresis exhibits a number of successive increases and then decreases. However, the overall tendency is to exhibit a global maximum for injected power close to  $P_{inj}/I_0 = 1.15\%$ . For larger injected power, the hysteresis width shrinks to relatively small values. The dependency of hysteresis width on injected power shown in Fig. 4.5.7 resembles qualitatively well the overall tendency shown experimentally by Hong *et al.* [132], i.e., existence of a maximum hysteresis width for a specific value of the injected power. The comparison between the two curves shown in Figs. 4.5.6 and 4.5.7 also shows that for relatively large values of

the injected power, the hysteresis width associated with the LF PS almost vanishes while the hysteresis width associated with the HF PS bistability remains relatively large.

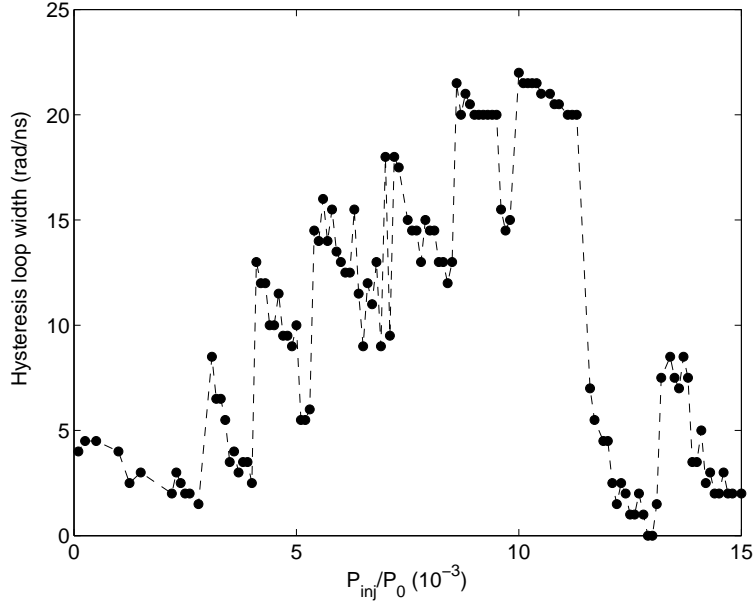


**Figure 4.5.7:** *Dependency of the hysteresis width associated with the LF-PS on the injected power.*

#### 4.5.4 Tunability of the hysteresis width

As mentioned earlier, the hysteresis width accompanying polarization bistability may be significantly tuned by modifying the injection strength. Interestingly, in this section we show that the hysteresis width may also be significantly tuned and possibly increased by modifying the slave laser parameters. First, we pay particular attention to the  $\alpha$  factor, or linewidth enhancement factor, since this parameter is of great current interest considering the development of new VCSEL structures based on quantum-dot-active regions and with expected small, close to zero,  $\alpha$  values [138, 139, 140].

Figure 4.5.8 plots the dependency of the hysteresis width associated with the LF PS point on the  $\alpha$  factor, for a weak (black) ( $P_{\text{inj}}/I_0 = 0.09\%$ ) or large ( $P_{\text{inj}}/I_0 = 1.50\%$ ) injection strength case. These two cases of either weak or large injection strength indeed correspond to the limits where the hysteresis width corresponding to the bistable region is relatively very small when the  $\alpha$  factor takes the typical value of  $\alpha = 3$ . As shown in Fig. 4.5.8, a



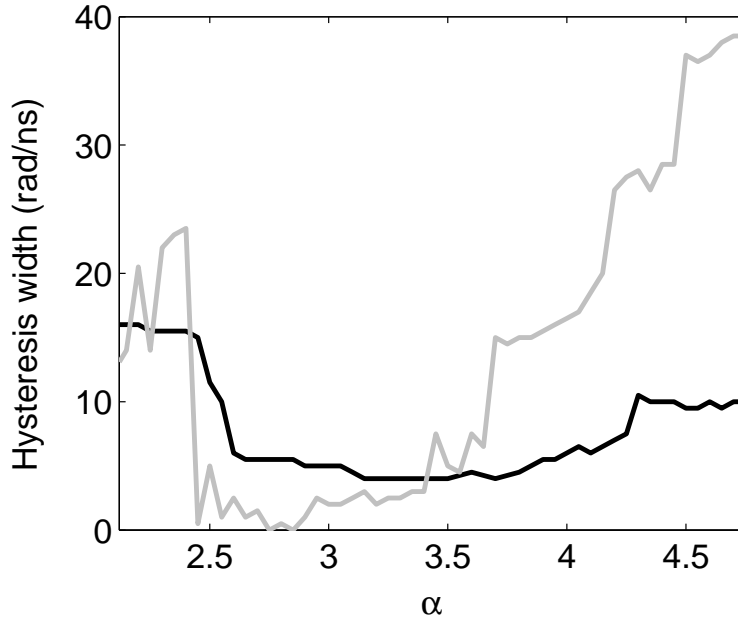


**Figure 4.5.8:** Influence of the linewidth enhancement factor  $\alpha$  on the width of the hysteresis associated with the LF-PS point, for either a weak (black) ( $P_{inj}/I_0 = 0.09\%$ ) or large (gray) ( $P_{inj}/I_0 = 1.50\%$ ) injection strength.

decrease or an increase of  $\alpha$  with respect to  $\alpha = 3$  will lead to an increase of the hysteresis width and therefore enhancement of polarization bistability. An enhancement with a factor of about 40 is even possible in the case of  $\alpha = 5$  and large injection strength. It is worth mentioning, however, that an increase of the  $\alpha$  factor not only leads to an enhancement of polarization bistability but may also give rise to stronger polarization mode competition and nonlinear dynamical instabilities in the positive detuning range. This situation is illustrated in Fig. 4.5.9 where the averaged intensity of the  $x$  LP mode is plotted as function of the detuning for a fixed injection strength ( $P_{inj}/I_0 = 0.09\%$ ) and for increasing values of  $\alpha$ . As  $\alpha$  increases while keeping the same injection parameters, we observe a sudden excitation of the  $x$  LP mode in the frequency detuning range in between the two PS points. This excitation of the  $x$  LP mode coincides with a decrease of the averaged intensity of the  $y$  LP mode, i.e., in this slightly positive detuning range the two modes strongly compete. Similarly to the case shown in Figs. 4.5.3(a1) and 4.5.3(a2) and analyzed in Figs. 4.5.4 and 4.5.5, the polarization mode competition occurs through a cascade of bifurcations to limit cycles, period doubling, and chaos.

Finally, we analyze whether the polarization bistability mechanisms re-

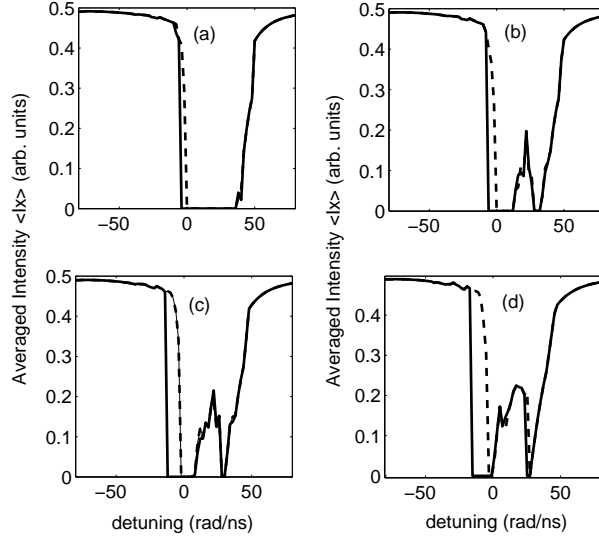


**Figure 4.5.9:** *Effect of the linewidth enhancement factor  $\alpha$  on the polarization bistability induced by frequency detuning. The averaged  $x$ -LP mode intensity is plotted as a function of the detuning, for a fixed injection strength ( $P_{inj}/I_0 = 0.09\%$ ) and for increasing values of  $\alpha$ : (a)  $\alpha = 3.4$ , (b)  $\alpha = 3.9$ , (c)  $\alpha = 4.3$ , (d)  $\alpha = 5.0$ .*

ported above are modified when considering smaller or larger values of the spin-flip relaxation rate  $\gamma_s$ . As already mentioned in Chapter 3, the spin-flip relaxation rate is an important parameter of the SFM, which aims at modelling several microscopic mechanisms responsible for the relaxation of the electron spin in quantum well semiconductor materials. In comparison between experiments and theory based on the SFM, the  $\gamma_s$  parameter is usually considered as a fitting parameter since its direct measurement is very difficult at room temperature and for the high levels of carrier density encountered in lasing operation. Reported values of  $\gamma_s$  from experimental fittings of different VCSEL devices range from  $\gamma_s \simeq 20 \text{ ns}^{-1}$  [64] up to very large values ( $\gamma_s > 1000 \text{ ns}^{-1}$  [63]). The expected value for  $\gamma_s$  may therefore be significantly different from one VCSEL device to another. In Fig. 4.5.10 we plot the averaged intensities of the  $x$  LP mode (left) and  $y$  LP mode (right) as we increase (solid line) the frequency detuning from negative to positive values, or decrease (dashed line) the frequency detuning from positive to negative values; for a fixed value of  $P_{inj}/I_0 = 0.09\%$  and for different  $\gamma_s$  values up to  $\gamma_s = 100 \text{ ns}^{-1}$ . We find that larger  $\gamma_s$  values together with our choice of parameters for linear cavity anisotropies and linewidth enhancement factor lead to a free-running VCSEL exhibiting not an  $x$  LP but a  $y$  LP mode. These larger  $\gamma_s$  values are therefore not compatible with our

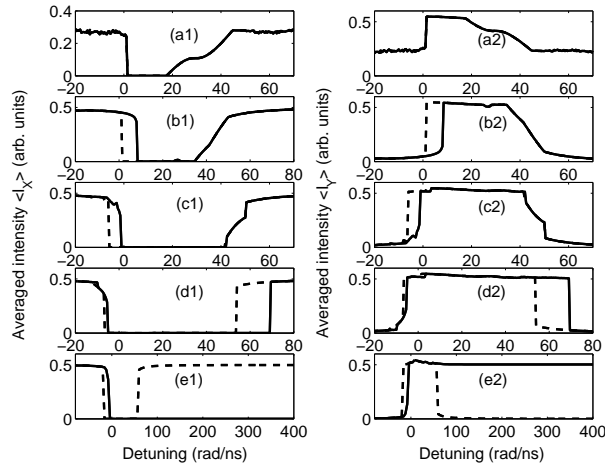


**Figure 4.5.10:** Effect of the spin-flip relaxation rate  $\gamma_s$  on the polarization bistability induced by frequency detuning. The averaged  $x$  LP mode (left) and  $y$  LP mode (right) intensities are plotted as a function of the detuning, for a fixed injection strength ( $P_{inj}/I_0 = 0.09\%$ ) and for increasing values of  $\gamma_s = (a1), (a2) 1; (b1), (b2) 20; (c1), (c2) 50; (d1), (d2) 75; \text{ and } (e1), (e2) 100 \text{ ns}^{-1}$ .

orthogonal optical injection and are not simulated. The situation analyzed in the previous sections corresponds to the case  $\gamma_s = 50 \text{ ns}^{-1}$ . A decrease of  $\gamma_s$  to for example  $\gamma_s = 20 \text{ ns}^{-1}$  leads first to an increase of the hysteresis width accompanying the LF PS [Fig. 4.5.10(b)] but a further decrease down to relatively low values of ( $\gamma_s = 1 \text{ ns}^{-1}$ ) then leads to a suppression of the LF PS hysteresis width [Fig. 4.5.10(a)]. Moreover, the decrease of  $\gamma_s$  in Fig. 4.5.10(b) and 4.5.10(a) leads to a more gradual HF PS behavior (the switching extends over a larger range of frequency detunings) but still without bistability. By contrast the increase of  $\gamma_s$  to  $\gamma_s = 75 \text{ ns}^{-1}$  [Fig. 4.5.10(d)] leads to a decrease of the hysteresis width accompanying the LF-PS and to a change from gradual to abrupt, bistable HF-PS behavior. An interesting case is shown in Fig. 4.5.10(e): for  $\gamma_s = 100 \text{ ns}^{-1}$  the slave VCSEL remains in the  $y$  LP mode once the LF PS occurs and does not switch back to the  $x$  LP mode as we increase the frequency detuning toward more positive values. If we force the slave VCSEL to exhibit an  $x$  LP mode at large positive detunings and then decrease the detuning toward negative values, we observe the dashed lines in Figs. 4.5.10(e1) and 4.5.10(e2), i.e., the  $x$  LP and  $y$  LP modes coexist in the slave laser dynamics for frequency detunings ranging from about 60 rad/ns up to relatively large positive values (we have limited our simulations up to the detuning of 1000 rad/ns). The hysteresis width accompanying the HF PS becomes therefore infinite for this large value of  $\gamma_s$ . The comparison between the different cases analyzed in Fig. 4.5.10 shows

that the  $\gamma_s$  value has little qualitative impact on the characteristics of the LF PS event (except that it does influence quantitatively the corresponding hysteresis width). By contrast, the  $\gamma_s$  value significantly modifies the qualitative features of the HF PS event, making the switching either gradual or abrupt and bistable and even possibly leading to a very large bistable region.

## 4.6 Conclusions

In summary, we have analyzed polarization switching (PS) mechanisms in a VCSEL subject to orthogonal optical injection. We have particularly focused on intensity-induced polarization switching characteristics and its related bistability. We have experimentally shown that whether the PS should be achieved with or without injection-locking to the master laser depends strongly on the frequency detuning. Concretely, the locking regime is determined by the VCSEL birefringence, i.e., the frequency offset between the orthogonally polarized VCSEL's fundamental modes. In agreement with what has been previously reported by Pan *et al.* [120], we have observed that the minimum switching power is obtained when the frequency of the master laser coincides with that of the injected mode, i.e., the mode with the same polarization as the injected field. In fact, when the frequency detuning is set on the negative side of the injected mode, the intensity-induced PS is always accompanied by injection-locking to the master laser frequency. However, when the detuning is set on the positive side of the injected mode, the switching to the orthogonal fundamental mode is achieved without locking. This contrasts with what has been reported in ref. [120] where injection-locking has been observed for the whole detuning range, regardless of the relative position between the master laser and the injected mode frequencies. Furthermore, we have presented a model of orthogonal optical injection built from an extension of the simple SFM model. Our numerical simulations of intensity induced PS are in qualitative agreement with our experimental observations, in particular concerning the role of the injection current on the hysteresis associated to PS. The obtained results show an intriguing evolution of the averaged-intensity in both the orthogonal polarization modes when increasing the injection strength close to the switching point. This behavior gives a hint of a possible existence of polarization mode competition mechanisms which shall be discussed in subsequent chapters, mostly in Chapters 5 and 6.

Concerning our theoretical analysis of the pure optical injection frequency-induced polarization bistability, we find that, as the frequency detuning is increased from negative to positive values, the VCSEL first switches its polarization to that of the injected light. For larger detuning values it switches its polarization back to the free-running slave laser polarization. The two

polarization switching points (LF PS and HF PS, respectively) may be accompanied by a relatively large bistability region. The hysteresis width accompanying the LF PS bistability is maximum for a specific value of the injected power and is relatively small for large injection strength, in agreement with recent experimental results [132, 135, 136]. By contrast, the hysteresis width accompanying the HF PS bistability increases with the increase of injected power. Both bistability mechanisms are found to significantly depend on device parameters and in particular the laser  $\alpha$  factor and the spin-flip relaxation rate  $\gamma_s$ . We furthermore report on the occurrence of polarization chaos with bistability between dynamical states for detuning values in between the polarization switching points. Our results are thought to bring additional light to physical mechanisms associated with recently experimentally reported bistability in VCSELs.

In the following chapter nonlinear dynamics accompanying PS and locking mechanisms in a VCSEL subject to orthogonal optical injection are experimentally analyzed.



## Chapter 5

# Experimental study of nonlinear dynamics accompanying polarization switching in VCSELs with orthogonal optical injection

We experimentally map the dynamical characteristics of a vertical-cavity surface-emitting laser (VCSEL) under orthogonal optical injection as a function of optical injection strength and detuning between the injection frequency and the frequency of the solitary laser. Such a mapping is obtained by scanning the injection strength for a relatively large detuning range. We unveil qualitatively different switching scenarios which strongly depend on the frequency detuning. Interestingly, we identify an injection parameter region where polarization switching is accompanied by rich nonlinear dynamics, including limit cycle, wave mixing, subharmonic resonance and period doubling route to chaos. We furthermore show that these dynamics are organized around a critical detuning value of 2 GHz which is close to the VCSEL birefringence. We also report on two qualitatively different switching scenarios which may involve two-polarization mode dynamics. The first one appears on the route to PS leading to injection locking and involves a limit cycle in the noninjected mode and a wave-mixing in the injected mode. The second one, does not lead to locking but manifests as switching between a two-polarization mode limit-cycle dynamics and a single-mode limit cycle in the injected mode. These dynamics are also mapped on the detuning vs. injection power plane.

This chapter is based on the following publications:

- I. Gatare, J. Buesa, H. Thienpont, M. Sciamanna, and K. Panajotov, “*Nonlinear dynamics accompanying polarization switching in vertical-cavity surface-emitting lasers with orthogonal optical injection*”, Appl. Phys. Lett., **88**, 101106 (2006).
- J. Buesa, I. Gatare, H. Thienpont, K. Panajotov, and M. Sciamanna, “*Mapping of the dynamics induced by orthogonal optical injection in vertical-cavity surface-emitting lasers*,” IEEE J. Quantum. Electron., **42**, 198 (2006).

## 5.1 Introduction

A semiconductor laser (SL) subject to external optical injection from a master laser can exhibit a wide range of rich nonlinear dynamics which are very attractive from both fundamental and application viewpoints [141, 142]. Depending on optical injection parameters, i.e., injection strength and detuning between the master laser frequency and that of the free-running laser, a stable optical injection-locking of the slave laser to the master laser frequency can be achieved [105, 108]. Besides the stable injection locking, by tuning the injection parameters, it has been experimentally and theoretically demonstrated that the slave laser may undergo a period doubling cascade leading to deterministic chaos. Specifically, this transition to chaos starts from a period one regime at the relaxation oscillation frequency and then develops as successive infinite series of period doubling bifurcations that appear while varying an injection parameter [11, 16]. Typically, a fully developed chaos manifests as a noise-like spectrum with a relatively broad pedestal. Another periodic dynamics, namely the subharmonic resonance regime, has been reported when scanning the frequency detuning between the master and slave lasers for a fixed injection power [137] or when varying the injection power for a fixed detuning [16]. In fact, the subharmonic resonance regime occurs when the injection-induced frequency shift of the slave laser with respect to the master laser frequency becomes close to the multiple (in our case to the double) of the relaxation oscillation frequency. As a result, an enhancement of the relaxation oscillations is observed as two strong sidebands on either side of the slave center spectrum line are excited.

In the weak injection regime, it has been demonstrated that the dynamics are mainly dominated by a wave-mixing between the injected signal and the injection-shifted central frequency of the slave laser [16, 137]. Using an experiment based on the injection-induced wave-mixing dynamics, Liu and Simpson showed that it is possible to accurately extract intrinsic laser characteristic parameters [143]. Subsequent research effort led to a successful comparison between experimental observations and theoretical model simu-



lations of nonlinear dynamics induced by optical injection [12, 16, 141, 144].

By mapping the injected laser output characteristics as a function of the injection strength and the frequency detuning between the master and free-running slave lasers, a global picture of nonlinear dynamics induced by optical injection has been successfully drawn [12, 16, 144, 145]. It is worth noting that most of these previous works concerned nonlinear dynamics in optically injected edge-emitting lasers. Systematic studies of nonlinear dynamics in VCSEL subject to optical injection remain scarce. Previous experimental studies have been carried out in the parallel optical injection scheme, i.e., a configuration in which the injected field is linearly polarized along the free-running VCSEL polarization direction [121, 122]. The results are similar to those in optically-injected single-mode EEL but the configuration does not bring the additional complexity of PS features since one mode, i.e., the noninjected mode, is suppressed by the polarized injection. In fact, by considering an *orthogonal* optical injection instead of parallel injection scheme, recent theoretical studies predict that the switching and locking mechanisms may involve complex nonlinear polarization dynamics [133, 134].

In this chapter, we experimentally investigate polarization switching dynamics in the *orthogonal* optical injection configuration. Our results are presented as follows: in Section 5.2, a detailed mapping of nonlinear dynamics accompanying polarization switching (PS) induced by orthogonal optical injection is performed in the injection parameter plane. In addition to PS and injection-locking, we unveil rich nonlinear dynamics including subharmonic resonance, wave mixing and period-doubling route to chaos. Samples of such dynamics are presented in Section 5.3 for selected frequency detunings. In section 5.4, we focus on a specific detuning range in which two-polarization mode dynamics can be excited before PS is achieved. Finally, in section 5.5 we provide a summary of our results and draw conclusions from our main findings.

## 5.2 Mapping of polarization dynamics

We experimentally investigate the richness of nonlinear dynamics accompanying polarization switching and locking in a VCSEL subject to orthogonal optical injection. We refer to Chapter 4 for a detailed description of the experimental setup as well as the light-current characteristics of the free-running VCSEL. The bias current of the free-running VCSEL is fixed at 2.105 mA and its temperature is stabilized at 20°C, which leads to an output power,  $P_{\text{out}}$ , of 1.28 mW (measured in front of the collimator COL, see Fig. 4.2.1). In such conditions, the free-running VCSEL emits a linearly polarized light along the horizontal axis. Orthogonal optical injection is

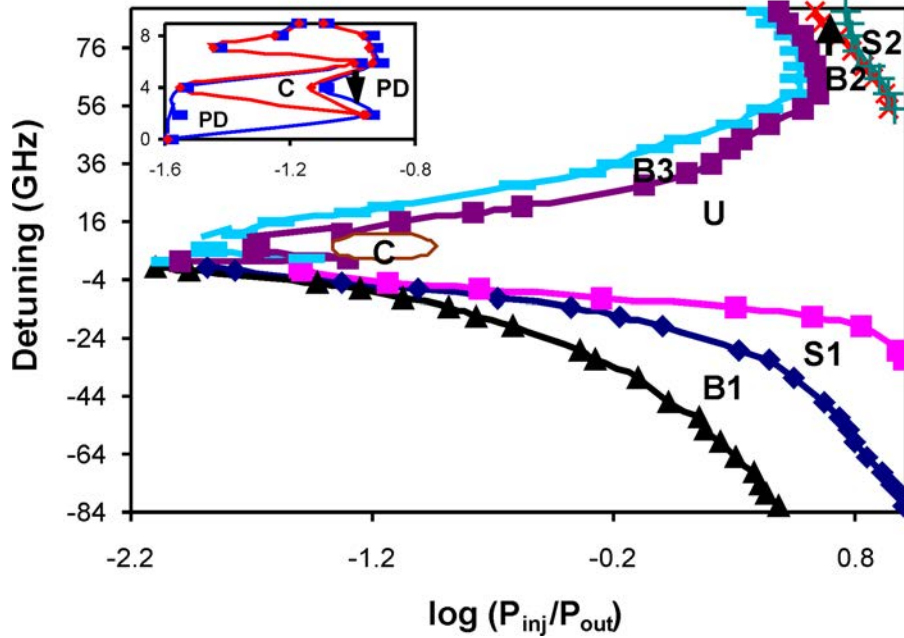


**Figure 5.2.1:** Mapping of the dynamics of the VCSEL<sub>2</sub> subject to optical injection. Different dynamical behaviors are shown when the injected power,  $P_{inj}$ , is swept for different frequency detunings ( $\Delta\nu = \nu_{ML} - \nu_{SL}$ ). B1, B2, B3: bistable regions; S1-S2: stable locking region; U: unlocking region; C: chaotic dynamics. The inset shows period doubling (PD) dynamics around the region of instabilities C. The injected power has been normalized to the power  $P_{out}$  emitted by the solitary VCSEL. The bias current of the VCSEL is fixed at 2.105 mA and its temperature maintained at 20°C.

achieved in the same way as explained in Chapter 4.

In Fig. 5.2.1 we provide a detailed mapping of the dynamical characteristics of the VCSEL subject to orthogonal optical injection. To this end, the boundaries of qualitatively different dynamics are represented in the plane of the injection parameters (frequency detuning and injected power). The injected power,  $P_{inj}$ , has been normalized to the output power of the solitary VCSEL and has been taken in a logarithmic scale [ $\log P_{inj}/P_{out}$ ]. We have defined the detuning as the frequency of the master laser (ML) minus the frequency of free-running slave laser (SL):  $\Delta\nu = \nu_{ML} - \nu_{SL}$ . Since the frequency of the free-running VCSEL is fixed in our experiments, we set the desired detuning value by changing the ML frequency via the bias current, the temperature or the piezoelectric control voltage from the ML driver. For each value of the frequency detuning, we perform a sweeping along the horizontal axis, that is, increasing and then decreasing the injected power. The horizontal axis is limited in the positive part by the maximum output power

of ML (12 mW measured in front of COL, see Fig. 4.2.1). The maximum negative detuning corresponds to the largest detuning for which we observe injection locking with the maximum injected power.

The polarization switch on (switch off) points for increasing (decreasing) the power of the injected light are represented by the dark blue and violet (black and light blue) lines in Fig. 5.2.1. We observe two stable injection locking regions, denoted respectively by S1 and S2, for which the VCSEL emission frequency is locked to that of ML. It is worth noting that S1 is related to injection-locking of the fundamental mode while S2 is associated to injection-locking of the first order transverse mode. Furthermore, we observe that the injection locking of the first order transverse mode is accompanied by the suppression of the fundamental transverse mode (this is the case when crossing the boundary delimited by the dark green line in Fig. 5.2.1 by increasing  $P_{\text{inj}}$ ). The unlocking of the first order transverse mode happens at smaller values of  $P_{\text{inj}}$ , leading to a region of bistability between the fundamental and the first order transverse modes both with the same polarizations (see the region B2 which is indicated by a vertical arrow and delimited by the dark green and red lines in Fig. 5.2.1). We refer to Chapter 7 for a detailed study of transverse mode switching and locking in a VCSEL subject to orthogonal optical injection.

In the fundamental mode emission, we observe two polarization bistable regions which correspond to two different switching scenarios. The first polarization bistable region is related to PS with injection-locking to ML and is confined between the dark blue and black lines (see B1 in Fig. 5.2.1). Analytical expressions for the steady states in this bistable region and for the time of PS were derived in [146] on the basis of a phenomenological two-mode rate equation model for VCSELS. The second polarization bistable region (see B3 in Fig. 5.2.1) is confined between light blue and the violet lines where PS is achieved without locking to the ML frequency. The two bistable regions are connected at a detuning of 2 GHz which, in fact, coincides with the birefringence frequency splitting between the two VCSEL fundamental LP modes. Therefore, when the ML is set above the frequency of the VCSEL vertical mode (i.e., the suppressed mode of the free-running VCSEL), a dramatic change in the switching dynamics is observed: from PS *with* injection locking to PS *without* locking. Interestingly, as also previously mentioned (see Chapter 4), the smallest power needed to achieved PS is obtained for this critical detuning value of 2 GHz. For positive or negative detunings relative to 2 GHz, the switching power is larger and, moreover, the switching power is larger for a negative than for a positive detuning value. This experimental feature agrees with previous theoretical results on a VCSEL rate equation model [133]. We have furthermore noticed that the widths of the injection locking regions S1 and the bistable region B1 increase when evolving towards larger negative detunings. Likewise, the width of the injection locking re-

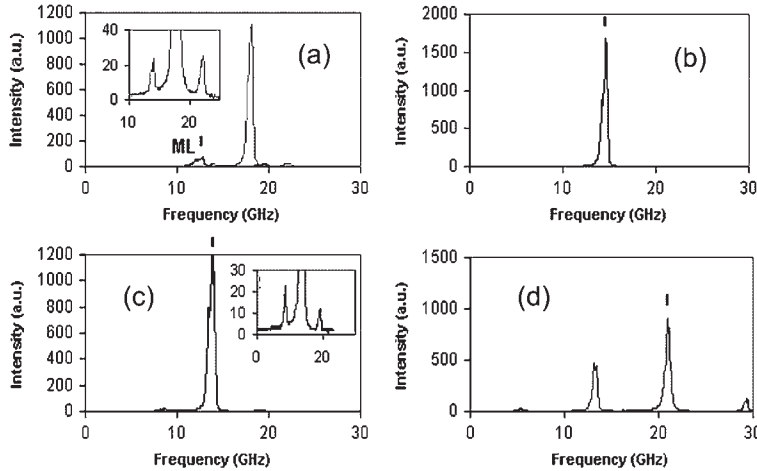


**Figure 5.2.2:** Polarization-resolved optical spectra of the VCSEL subject to optical injection at a frequency detuning of  $-4$  GHz and increasing the injected power  $P_{inj}$ : (a)  $P_{inj} = 40 \mu\text{W}$ ; (b)  $76 \mu\text{W}$ ; (c)  $103 \mu\text{W}$ ; (d)  $210 \mu\text{W}$ . In (a), the slave laser emits dominantly a horizontal LP light while the master light is LP in vertical direction. In (b)-(d), the slave laser emits a vertical LP light. The vertical line shows the ML frequency. The insets in (a) and (c) show the same spectra magnified.

gion S2 increases when evolving towards larger positive detuning values. By contrast, the width of the bistability region B3 remains approximately constant when changing the frequency detuning. We furthermore notice that the bistable region B3 is strongly influenced by the locking of the first-order LP transverse mode, its borderline turning backward at  $\Delta\nu \approx 50$  GHz. This phenomenon can be related to nonlinear dynamics arising from transverse mode competition and is widely discussed in Chapter 7.

In Fig. 5.2.2 we show a typical sequence of bifurcations to PS with injection locking. The described scenario corresponds to a negative detuning of  $\Delta\nu = -4$  GHz. Optical spectra are shown for four different injection powers. First, for very low injected power, the VCSEL is emitting in horizontal polarization and is progressively frequency-pulled toward ML as the injection power  $P_{inj}$  is increased. We observe that an increase in the injected power leads to undamped relaxation oscillations dynamics which are observed as side peaks appearing on each side of the SL central peak [Fig. 5.2.2(a) and the inset]. For still larger injection strength, PS with injection locking is achieved [see Fig. 5.2.2(b)]. By further increasing  $P_{inj}$ , the stable injection-locking regime is destabilized through excitation of a limit cycle or period one dynamics [see Fig. 5.2.2(c) and the inset]. Harmonics of the limit cycle are resolved for higher injection powers as shown in Fig. 5.2.2(d). As we further increase the injection strength, the period one dynamics is enhanced

and is accompanied by a slight increase in the frequency offset between the side peaks and the ML central peak. In agreement with what has previously been reported for the case of optically injected edge-emitting lasers, a strong asymmetry between the side peaks is also observed when evolving towards higher injection strengths. This phenomenon is attributed to the effect of a finite linewidth enhancement factor (or  $\alpha$ -factor) which is typical for semiconductor lasers [16]. A decrease in the injection power from the situation presented in Fig. 5.2.2(d) yields a reverse scenario. However, the boundaries of qualitatively different dynamics are located at different values of injection strength, hence showing bistability.

Scenarios similar to those depicted in Fig. 5.2.2 are observed for different negative detuning values. However, for negative detunings larger than 32 GHz, the stable injection-locking region is not exited by increasing the injection power. As shown in the mapping, Fig. 5.2.1, this is simply due to the limitation imposed by the maximum power of ML. For small positive detunings ranging from about 0 – 10 GHz, complicated dynamics like wave mixing, subharmonic resonance, sustained limit cycle oscillation, period doubling and possibly chaotic regimes (labelled C in Fig. 5.2.1 and inset) are observed. This detuning range of rich dynamics will be detailed in Section 5.3.

By contrast, for larger positive detunings the route to PS (the switching on and off of the fundamental LP modes form the boundaries of the bistable region B3) is not accompanied by severe laser instabilities. However, another injection locking region (S2) is resolved for very large positive detunings (50 GHz and more). In fact, by increasing the injected power, injection-locking of the first order transverse mode to the ML frequency is observed after the crossing of the dark green line in Fig. 5.2.1. As we have mentioned earlier, the onset of injection locking of the first order transverse mode is accompanied by a strong depression of the fundamental vertical mode (which has been excited after PS between the fundamental modes, i.e., after the crossing of violet line). By checking the cross section of the SL beam while the dark green borderline is crossed, one observe a change in its radial distribution from one single lobe (fundamental mode) to two lobes (first-order transverse mode) when increasing  $P_{\text{inj}}$ . When the injection power is decreased such that the borderline denoted by red crosses in Fig. 5.2.1 is crossed, the opposite behavior is observed, i.e., the VCSEL switches back to the unlocked fundamental transverse mode but still in the vertical polarization. By further decreasing  $P_{\text{inj}}$ , the VCSEL switches back to horizontal polarization after the light blue line is crossed.

A typical sequence of bifurcations leading to injection locking of the first-order transverse mode is shown in Fig. 5.2.3. As we increase the injected power, the slave laser is frequency pushed, i.e., the frequency offset between

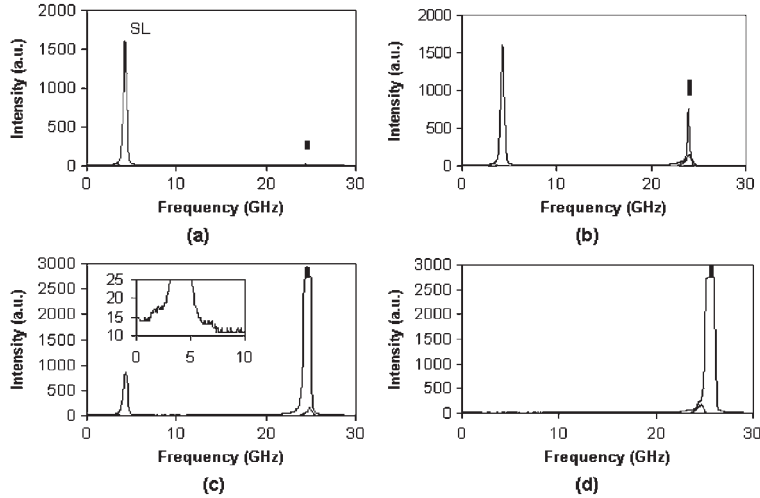


**Figure 5.2.3:** Polarization-resolved optical spectra of the VCSEL subject to optical injection at a frequency detuning of 50 GHz and increasing the injected power  $P_{inj}$ : (a)  $P_{inj} = 179 \mu W$ , before PS. (b)  $725 \mu W$ , PS without frequency locking of the VCSEL fundamental mode to ML. (c)  $972 \mu W$ , relaxation oscillation undamping before locking of the first-order transverse mode. (d)  $1017 \mu W$ , locking of the VCSEL first-order transverse mode to ML. In (a), the slave laser emits dominantly a horizontal LP light while the master light is LP in vertical direction. In (b)-(d), the slave laser emits dominantly a vertical LP light. The small peak close to the ML frequency in (b)-(d) corresponds to the residual and strongly depressed horizontal LP mode of the slave laser. The vertical line shows the ML frequency.

ML and SL spectra peaks increases with  $P_{inj}$ . A frequency pushing in the positive detuning range has also been observed by Li et al [122] but in the case of a VCSEL subject to a parallel optical injection. As the VCSEL is progressively frequency pushed, the switching is achieved without injection locking [from Fig. 5.2.3(a) to Fig. 5.2.3(b)] in contrast with what is found for negative detunings. If we further increase the injection power, injection locking of the first-order transverse mode ( $LP_{11}$ ) is observed. This is depicted in Fig. 5.2.3(d) where the fundamental mode is suppressed and the  $LP_{11}$  mode appears locked to the ML frequency [Fig. 5.2.3]. It is worth noting that, similarly to what is shown in Fig. 5.2.2(a), just before the locking is achieved small side peaks appear on each side of the SL central peak. Moreover, the frequency offset between these weak side lobes and the SL central peak is close to the relaxation oscillation frequency. However, one observes that the side peaks are much less visible in Fig. 5.2.3(c) than in Fig. 5.2.2(a) and are almost beyond the resolution of our Fabry-Perot interferometer. If the injection is decreased from the locking regime shown in Fig. 5.2.3(d), the side lobes are not observed.

## 5.3 Complex nonlinear dynamics

As indicated in the map in Fig. 5.2.1 and the inset, a richer nonlinear dynamics including period doubling route to chaos and even reverse period doubling from the chaotic zone are found for  $\Delta\nu = 2 - 10$  GHz. In this section, we investigate these dynamics as well as an evidence of strongly increased limit cycle behavior at specific frequency detuning between ML and VCSEL (subharmonic resonance).

### 5.3.1 Subharmonic resonances

We present in Fig. 5.3.1 the case of  $\Delta\nu = 10$  GHz which unveils the case of a resonance between limit cycle dynamics [undamping of relaxation oscillation (RO)] and wave mixing dynamics. In Fig. 5.3.1(a) the injection strength is such that PS has been achieved and the optical spectrum shows a main peak corresponding to the slave laser frequency, a peak corresponding to the master laser frequency, two small peaks on each side of the slave laser peak, and finally an additional peak on the low frequency side of the slave peak. The two almost symmetric peaks on each side of the slave laser peak correspond to undamping of the laser RO (limit cycle dynamics). Indeed they are separated from the slave laser peak by about 3.8 GHz which is close to the RO frequency of the free-running VCSEL ( $f_{RO} = 3.8$  GHz for a current of 2.105 mA). The additional peak on the low frequency side of the slave laser peak is the result of a wave mixing between ML and SL.

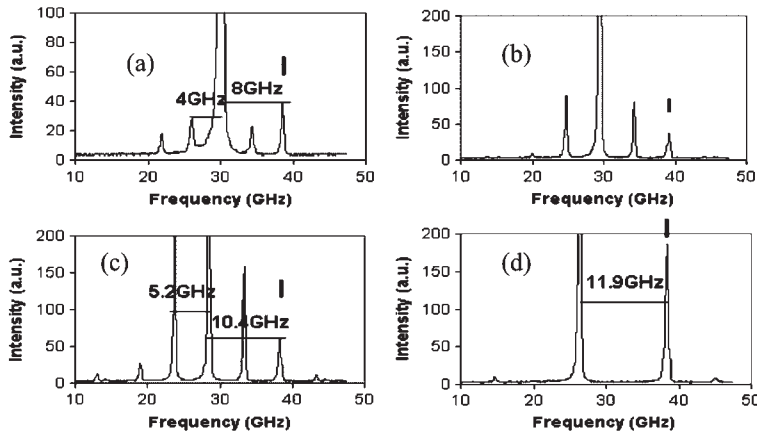


**Figure 5.3.1:** Polarization-resolved optical spectra of the VCSEL subject to optical injection at a frequency detuning of 10 GHz and increasing the injected power  $P_{inj}$ : (a)  $P_{inj} = 29\mu W$ . (b)  $70\mu W$ . (c)  $251\mu W$ . (d)  $800\mu W$ . (a)-(c) Subharmonic resonances with wave mixing. (d) Represents a limit cycle dynamics (period-one). Only vertical polarization is represented. The vertical line denotes the ML frequency.

The frequency splitting between the slave and master peaks is about 8 GHz, which is smaller than the initial frequency detuning (for zero injection) but which is also close to twice the RO frequency. This behavior is also called subharmonic resonance [16, 137]. As we increase the injected power, the slave laser is continuously pushed away from the master laser frequency, and as a result the distance between the peaks corresponding to WM also increases. The frequency splitting between the slave laser peak and the side peaks corresponding to RO undamping also increases and is still half of the master slave frequency difference [Figs. 5.3.1(b) and 5.3.1(c)]. The peak at the injection frequency is now dominated by the sidebands at half of the frequency offset between slave and master lasers. For still larger injected powers, the distance between SL and ML frequencies increases, the resonance disappears and the VCSEL stays in a limit cycle dynamic [Fig. 5.3.1(d)].

### 5.3.2 Period doubling route to chaos

A different sequence of bifurcations is shown in Fig. 5.3.2 when increasing the injection power at a fixed frequency detuning of 6 GHz. By contrast to the case shown in Fig. 5.3.1, wave mixing dynamics is now observed before PS is achieved. As shown in Fig. 5.3.2(a), an additional peak is indeed observed on the low frequency side of the horizontally polarized SL. The mapping presented in Fig. 5.2.1 shows that, for a detuning close to 6 GHz, PS occurs at a larger injected power than for a slightly smaller or larger



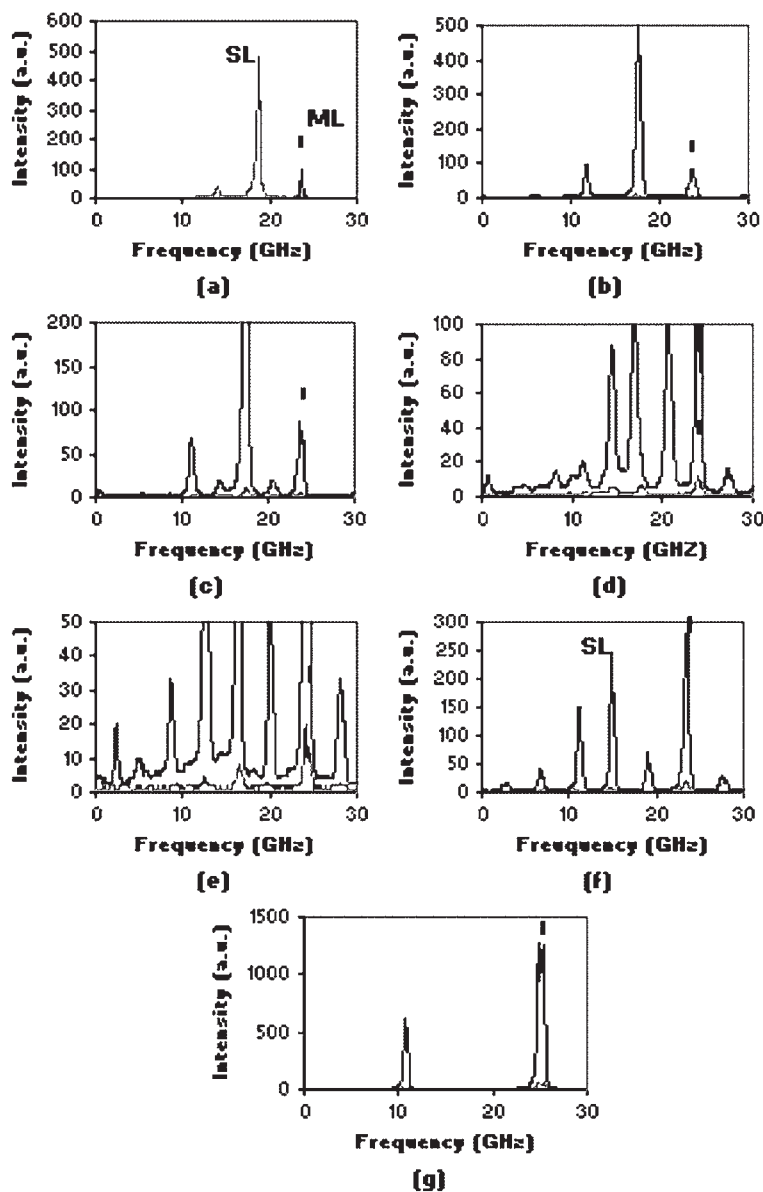


**Figure 5.3.2:** Polarization-resolved optical spectra showing dynamics of the VCSEL subject to optical injection at a frequency detuning of 6 GHz and increasing the injected power  $P_{inj}$ : (a)  $P_{inj} = 163 \mu W$ ; (b)  $115.6 \mu W$ ; (c)  $150 \mu W$ ; (d)  $226 \mu W$ ; (e)  $291 \mu W$ ; (f)  $387 \mu W$ ; (g)  $1000 \mu W$ . In (a), the slave laser emits dominantly a horizontal LP light while the master light is LP in vertical direction. The spectrum with lower intensity in (b)-(g) corresponds to the horizontal LP mode of the slave laser. The vertical line denotes the ML frequency.

positive detunings (in fact, the PS boundary in this region forms a kind of snake-like curve). In Fig. 5.3.2(b) PS is achieved, the SL now emits in the vertical polarization direction and still exhibits wave mixing dynamics. By further increasing the injection strength, similarly to what has been observed in Fig. 5.3.1, a subharmonic resonance regime is resolved when the frequency splitting between ML and SL under optical injection is close to the double of the relaxation oscillation frequency [Fig. 5.3.2(c)]

For still larger injected power, the slave VCSEL enters into a region of severe laser instabilities with strong periodic components. More and more frequency components appear, the optical spectrum is broadened and the intensity of the VCSEL main peak decreases [Fig. 5.3.2d)]. If the injection strength is further increased, small spectral features appear in between the strong peaks showing period doubling dynamics [Fig. 5.3.2(e)]. Such laser dynamics indicate the effect of a weak chaotic attractor bounded by period-doubling curves that may expand over a relatively large region of the mapping [147]. Interestingly, the two LP modes of the slave VCSEL are excited when the VCSEL is driven into this region of complex laser instabilities, i.e., the dominant vertical polarization as well as the horizontal polarization which has been depressed after the PS. For higher injection power, the complex features in the optical spectrum progressively disappear as we increase the injection strength. For much higher injection strength, a reverse period doubling [Fig. 5.3.2f)] cascade leads to a much simpler periodic dynamics [Fig. 5.3.2(g)].

A cascade of complex dynamics involving chaotic instabilities is presented also in Fig. 5.3.3 for a fixed detuning of  $\Delta\nu = 2$  GHz. This corresponds to the critical detuning value for which the ML frequency coincides with the frequency of the almost non lasing vertical mode of the free-running VCSEL. In Fig. 5.3.3(a) the injection power is such that injection locking is achieved and the SL has switched its polarization to that of the ML (vertical). However, for a slight increase in the injected power, the stable injection-locking regime is exited through the so-called Hopf bifurcation: the steady-state injection locked state destabilizes to a time-periodic dynamics at the RO frequency. This limit cycle dynamics is shown in Fig. 5.3.3(b) and is detected by the presence of side lobes on both sides of the ML frequency. Harmonics of the RO peaks can be observed for larger injection strength [Fig. 5.3.3(c)]. A further increase in the injected power leads to a period-doubling [Fig. 5.3.3(d)], with small peaks appearing in between the main peaks. The period-doubling cascade then leads to chaotic instabilities [Fig. 5.3.3(e)] indicated by the presence of a large pedestal in the VCSEL spectrum. It is important to note that these chaotic instabilities involve both vertical and horizontal LP modes. If the injection power is still increased, the zone of chaotic dynamics is exited through a reverse period-doubling [Fig. 5.3.3(e)] that leads to limit cycle [Fig. 5.3.3(g)]. For much larger injection power, this limit cycle may again

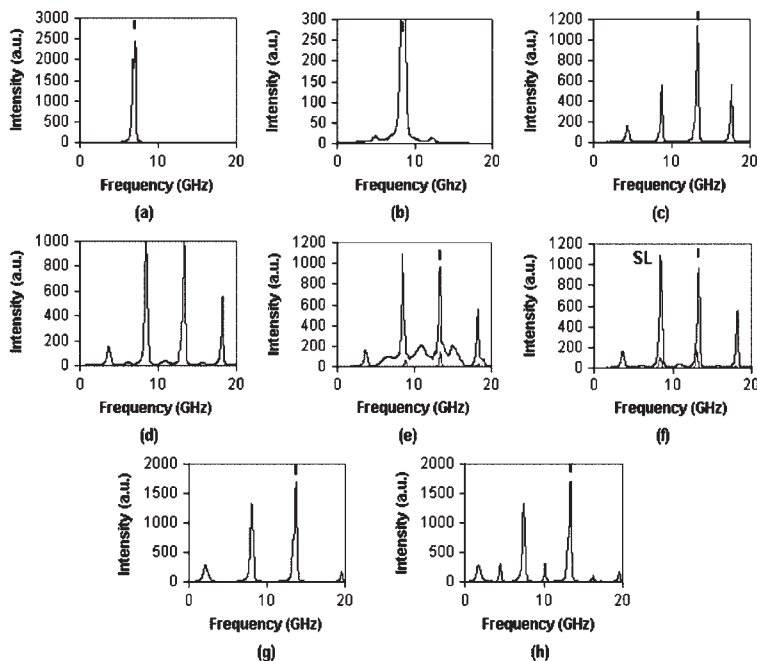


**Figure 5.3.3:** Polarization-resolved optical spectra showing dynamics of the VCSEL subject to optical injection at a frequency detuning of 2 GHz and increasing the injected power  $P_{inj}$ : (a)  $P = 13.2 \mu W$ ; (b)  $23.6 \mu W$ ; (c)  $36.6 \mu W$ ; (d)  $47.8 \mu W$ ; (e)  $80.3 \mu W$ ; (f)  $136.6 \mu W$ ; (g)  $204 \mu W$ ; (h)  $351 \mu W$ . The spectrum with lower intensity in (e)-(f) corresponds to the excited horizontal LP mode of the slave laser. The vertical line denotes the ML frequency.

evolve toward a second period doubling bifurcation [Fig. 5.3.3(h)].

## 5.4 Periodic dynamics on the route to polarization switching

We have shown in Fig. 5.2.2(a) of section 5.2 that, when increasing the injection strength in the negative detuning range, undamped relaxation oscillations in the horizontally-polarized mode are excited before achieving PS to vertically-polarized injection-locked regime. In the present section, such nonlinear dynamics are closely investigated by performing a polarization-resolved study of dynamics associated to the route to PS. In addition to the route to PS leading to injection-locking, we also report on another switching from a two-polarization mode regime to a single-mode periodic dynamics. This particular switching scenario is found for a relatively small detuning range over which a strong interplay between PS and complex nonlinear dynamics is observed.

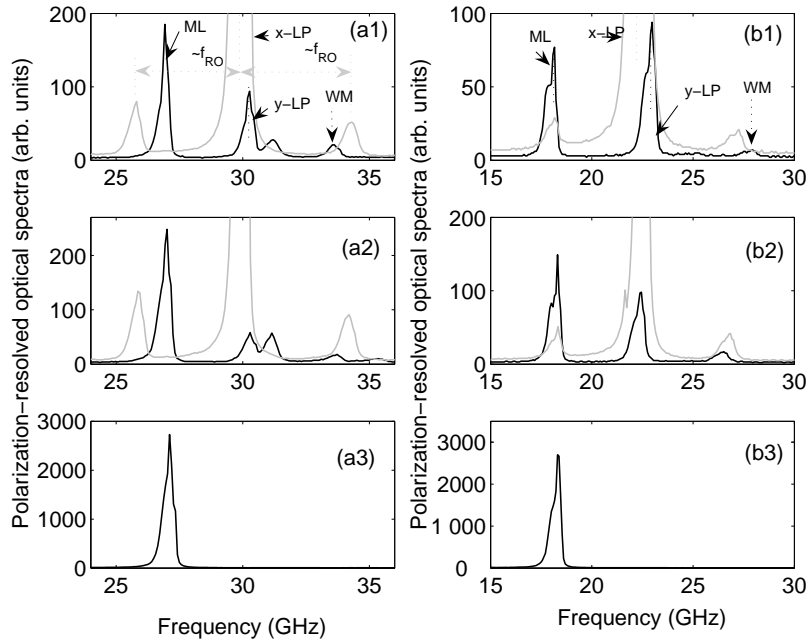


**Figure 5.4.1:** *Experimental polarization-resolved optical spectra of VCSEL<sub>2</sub> showing the dynamics leading to PS and locking when increasing the injection power for two detuning values: (a1)-(a3) for  $\Delta\nu = -3.45$  GHz and (b1)-(b3) for  $\Delta\nu = -5.37$  GHz. Black (grey) corresponds to vertical y- (horizontal x-) LP mode.*

In order to closely investigate the evolution of the VCSEL dynamics on the route to injection-locking regime as shown in Fig. 5.2.2(a), polarization-resolved optical spectra are presented in Fig. 5.4.1. To this end, we progressively increase the injection power and follow the dynamics for two different detuning values, i.e.,  $\Delta\nu = -3.45$  GHz [see (Fig. 5.4.1(a1)-a(3))] and  $\Delta\nu = -5.37$  GHz [see (Fig. 5.4.1(b1)-b(3))]. In fact, while increasing the injection power  $P_{inj}$  from zero, the VCSEL is frequency-pulled towards ML but without any qualitative change in its dynamics (not shown). When further increasing  $P_{inj}$ , similarly to what has been previously shown [see Fig. 5.2.2(a)], we observe an abrupt excitation of peaks on both sides of the VCSEL  $x$ -LP main frequency component [see Fig. 5.4.1(a1) for  $P_{inj} = 152$   $\mu$ W and Fig. 5.4.1(b1) for  $P_{inj} = 263.7$   $\mu$ W]. The side peaks appear with a frequency offset of 4.1 GHz which is close to the VCSEL RO frequency (The measured value is  $f_{RO} \approx 3.8$  GHz). However, in addition to what has been shown in Fig. 5.2.2(a), a wave mixing (WM) dynamics between  $y$ -LP mode and ML mode is also resolved in the  $y$  polarization direction. A further increase of  $P_{inj}$  leads to an enhancement of dynamics of both  $x$ - and  $y$ -polarization modes [see Fig. 5.4.1(a2) for  $P_{inj} = 210$   $\mu$ W and Fig. 5.4.1(b2) for  $P_{inj} = 303$   $\mu$ W]. It is worth noting that the frequency offset of the peaks on both sides of the  $x$ -LP main peak remains close to  $f_{RO}$  regardless of the change of the detuning [compare Figs. 5.4.1(a1) to 5.4.1(b1) and Figs. 5.4.1(a2) to 5.4.1(b2)]. For sufficiently larger  $P_{inj}$ , polarization switching followed by injection-locking of the VCSEL to the ML frequency is achieved [see Fig. 5.4.1(a3) for  $P_{inj} = 217$   $\mu$ W and Fig. 5.4.1(b3) for  $P_{inj} = 342.7$   $\mu$ W].

Similarly to what is depicted in Section 5.2, we perform another mapping of nonlinear dynamics accompanying PS which complements the previous one (Fig. 5.2.1). Here, we provide a closer investigation of the period-doubling mechanisms underlying the region of complex instabilities which we have denoted by C in Fig. 5.2.1. Furthermore, we focus on two-polarization mode dynamics which may precede PS and analyze their evolution in the injection parameter plane. The results are summarized in Fig. 5.4.2 which has been obtained using VCSEL<sub>1</sub><sup>1</sup>. The bias current is fixed at 1.175 mA and the temperature has been set at 20°C. With these operating conditions, the free-running VCSEL emits a horizontally-polarized ( $x$ ) single-mode<sup>2</sup>. The experimental procedure is the same as for Fig. 5.2.1: the injected power is progressively increased for fixed detuning values and any qualitative change in the injected VCSEL dynamics is recorded. In Fig. 5.4.2, the values of injected power and detuning corresponding to switching from horizontal to vertical polarization, when increasing the injection power, are represented by

<sup>1</sup>VCSEL<sub>2</sub>, used in the preceding sections, was damaged at the moment the present experimental study was carried out

<sup>2</sup>For more details, the LI curve of VCSEL<sub>1</sub> is shown in Chapter 3, Fig. 3.3.1

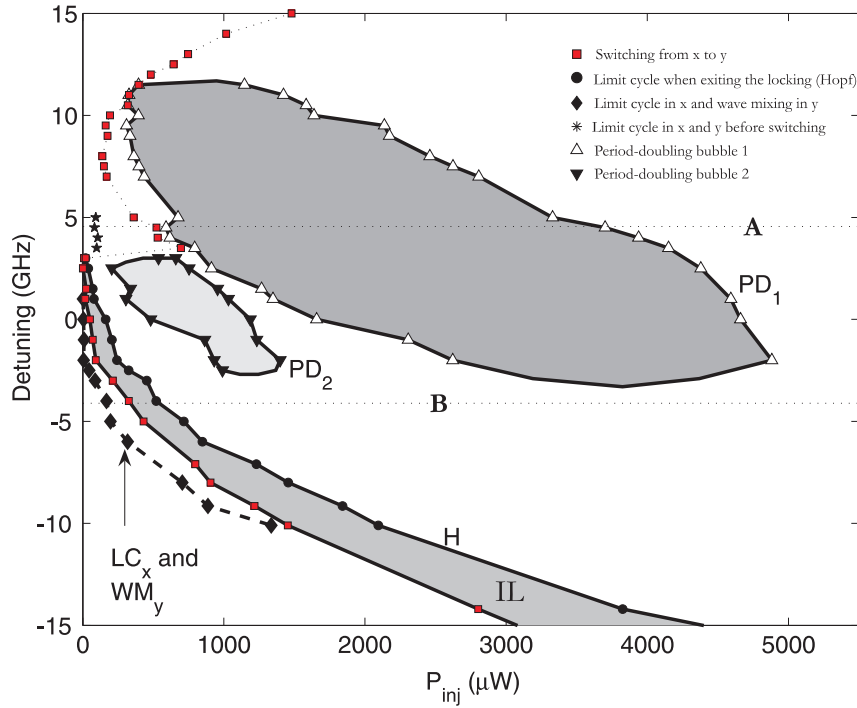


**Figure 5.4.2:** Mapping of nonlinear dynamics of the VCSEL<sub>1</sub> subject to orthogonal optical injection and when increasing the injected power  $P_{inj}$  for fixed detunings. Qualitatively different dynamics are shown: Injection locking of the VCSEL to ML (IL), two regions of period-doubling dynamics delimited by  $PD_1$  and  $PD_2$ , respectively. Periodic dynamics preceding the locking are also resolved (see the legend for details). The current is fixed at 1.175 mA and the temperature at 20°C. With these operating conditions, the free-running VCSEL emits a horizontal ( $x$ ) single LP mode.

red squares. Regions of qualitatively different dynamical states and their related boundaries are also shown. An injection-locking region (IL) is resolved when the detuning is set on the negative side of the VCSEL birefringence (for VCSEL<sub>1</sub>, the birefringence is 2.1 GHz). Interestingly, two different period-doubling bubbles (respectively  $PD_1$  and  $PD_2$ ) are now clearly displayed. The larger one ( $PD_1$ ) expands over a detuning range from around -3.5 to 11.5 GHz and the associated dynamics appears predominantly in the vertically-polarized mode after PS. The smaller period-doubling region ( $PD_2$ ) expands over a relatively short detuning range (from around -2.7 to 3 GHz). By contrast to  $PD_1$ ,  $PD_2$  delimits a region of chaotic instabilities that involve both vertical and horizontal LP modes. Dynamics related to the crossing of  $PD_2$  are similar to the period-doubling route to chaos shown in Figs. 5.3.3(d)-(f), i.e., the noninjected suppressed mode is reactivated when

the VCSEL undergoes well established chaotic instabilities. It is worth noting that the presence of two different period-doubling regions has also been experimentally [16] and theoretically [145] reported in the case of optically injected EEL. The key point here is that  $PD_1$  and  $PD_2$  are linked to PS in the global bifurcation map but occur after PS when increasing the  $P_{inj}$  for fixed detuning. Moreover, we show that the interplay between PS and  $PD_1$  may lead to complex nonlinear dynamics on the route to PS, i.e., before and after PS, while increasing  $P_{inj}$ .

For positive detuning larger than the upper limit of  $PD_1$  ( $\Delta\omega > 11.5\text{GHz}$ ), the VCSEL undergoes a frequency-pushing as the injection power is increased. By further increasing  $P_{inj}$ , PS to an unlocked period-one dynamics is observed. The switching between horizontal and vertical fundamental modes is achieved in the same way as shown in Fig. 5.2.2(a)-(b). For still larger  $P_{inj}$ , the period-one dynamics is progressively frequency-pushed until the maximum injection power is reached. A different switching scenario is observed when the detuning is set in between 5 and 10 GHz: after PS and by increasing  $P_{inj}$ , the obtained period-one dynamics undergoes a period doubling mechanism which corresponds to the crossing of  $PD_1$ . Then  $PD_1$  is exited through a reverse period-doubling dynamics, leading to the recovery of period-one dynamics accompanied by a frequency pushing as  $P_{inj}$  is increased. It is worth noting that when PS is followed by period-doubling dynamics, a dramatic change in the switching power curve, similar to what has also been observed for VCSEL<sub>2</sub> in Fig. 5.2.1, is found. In fact one can clearly see that in the vicinity of  $PD_1$ , the evolution of the PS curve displays a snakelike shape (see the dotted line connecting the PS squares). More specifically, for detunings ranging from around 3 to 8.5 GHz, the injection power needed to achieve PS decreases with the increase in the detuning.

We now focus on a small detuning range (from 3 to 5 GHz) in which we unveil nonlinear dynamics that involve both horizontal and vertical polarization modes of the injected VCSEL before PS is achieved. The onset of such two-polarization mode dynamics is marked with stars in Fig. 5.4.2. A representative switching scenario is provided in Fig. 5.4.3 for which  $P_{inj}$  is progressively increased when the detuning is set at  $\Delta\omega = 4.4$  GHz (see the dotted line “A” in Fig. 5.4.2). In the weak injection regime [see Fig. 5.4.3(a) for  $P_{inj} = 3 \mu\text{W}$ ], the VCSEL emits mainly a horizontally-polarized mode which is progressively frequency pushed as  $P_{inj}$  is increased. If the injection power is increased [see Fig. 5.4.3(b) for  $P_{inj} = 83 \mu\text{W}$ ], period-one limit cycle dynamics with a frequency close to the relaxation oscillation frequency are excited in both the vertical (black) and horizontal (gray) VCSEL modes. The limit cycle in the vertically polarized mode is similar to what has been experimentally reported by Simpson *et al.* [16] in the case of optically injected single-mode EEL and for positive detuning relative to the injection locking regime. The limit cycle manifests as two side lobes on each side

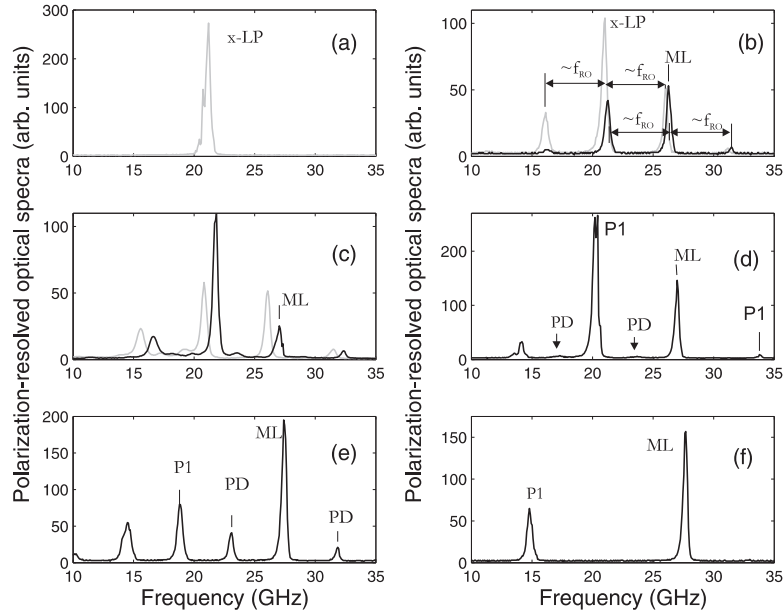


**Figure 5.4.3:** Polarization-resolved optical spectra showing dynamics of the VCSEL subject to optical injection at a frequency detuning of 4.4 GHz and increasing the injected power  $P_{inj}$ : (a)  $P_{inj} = 3 \mu W$ ; (b)  $83 \mu W$ ; (c)  $185 \mu W$ ; (d)  $265 \mu W$ ; (e)  $558 \mu W$ ; (f)  $3454 \mu W$ .  $P_1$  denotes a period-one limit cycle while  $PD$  denotes period doubling features. Black (gray) represents vertical (horizontal) mode.

of the ML central peak. The peak on the low-frequency side from ML is much stronger than the one located on the high frequency side of ML. The observed asymmetry in the limit cycle side peaks is a generic feature of semiconductor lasers and is due to a non-zero  $\alpha$ -factor [16]. By increasing  $P_{inj}$  the two-polarization mode limit cycle is destabilized: new frequency components appear in between the main peaks [see Fig. 5.4.3(c) for  $P_{inj} = 185 \mu W$ ]. A further increase of injection power leads to the switching off of the horizontal mode as shown in Fig. 5.4.3(d) for  $P_{inj} = 265 \mu W$ . The resulting dynamics is a period-one limit cycle in the vertical polarization characterized by two strongly asymmetric peaks on both sides of the ML peak [see the two peaks denoted by  $P_1$  in Fig. 5.4.3(d)]. The leftmost peak in Fig. 5.4.3(d) is associated to the excitation of harmonics of the limit cycle. There are relatively weak features which appear in between the ML and the main limit cycle peaks, and also between the main limit cycle peak and its harmonics. They are indicative of a period-doubling mechanism, namely  $PD_1$ , which accompanies PS. In fact, by further increasing  $P_{inj}$ , we observe a well-established



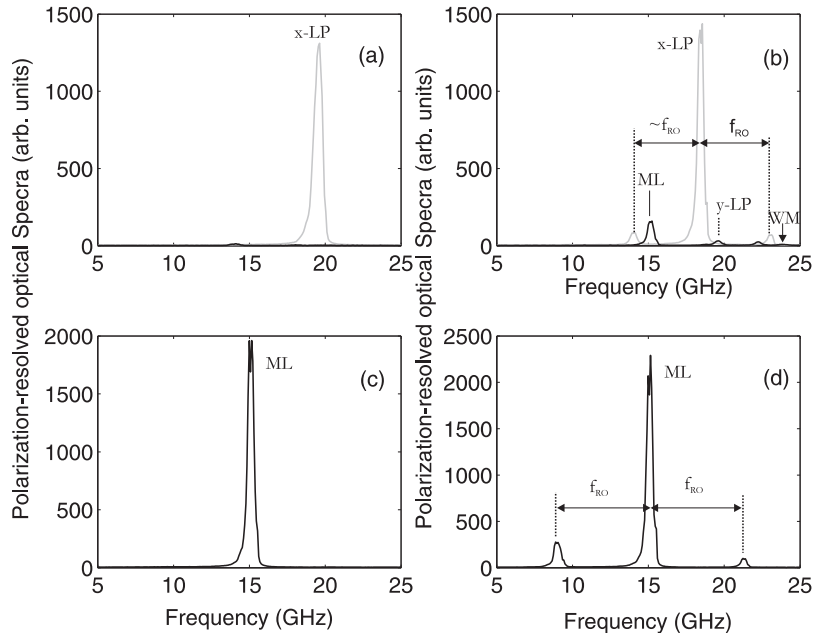


**Figure 5.4.4:** Polarization-resolved optical spectra showing dynamics of the VCSEL subject to optical injection at a frequency detuning of  $-4.1$  GHz and increasing the injected power  $P_{inj}$ : (a)  $P_{inj} = 19 \mu\text{W}$ ; (b)  $88 \mu\text{W}$ ; (c)  $114 \mu\text{W}$ ; (d)  $236 \mu\text{W}$ . Black (gray) represents vertical (horizontal) mode.

period-doubling dynamics accompanied by a frequency-pushing mechanism [see Fig. 5.4.3(e) for  $P_{inj} = 558 \mu\text{W}$ ]. Then, for sufficiently higher injection powers, the VCSEL exits the period doubling regime which results in a period-one limit cycle dynamics as shown in Fig. 5.4.3(f) for  $P_{inj} = 3454 \mu\text{W}$ .

We have systematically investigated the switching scenario similar to what is shown in Fig. 5.4.1 (obtained with VCSEL<sub>2</sub>) and which corresponds to a two-polarization mode dynamics, appearing on the route to simultaneous PS and injection-locking (see the dotted line “B” in Fig. 5.4.2). In Fig. 5.4.4 and using VCSEL<sub>1</sub>, we provide a sample of the evolution of such dynamics when increasing  $P_{inj}$  for  $\Delta\omega = -4.1$  GHz. The results are almost the same as those described in Fig. 5.4.1. In the weak injection regime the VCSEL predominantly emits in the horizontal polarization [Fig. 5.4.4(a)]. Similarly to what has been shown in Fig. 5.4.1, as  $P_{inj}$  is increased, the VCSEL is frequency-pulled towards the ML frequency peak. The system reaches a particular bifurcation point at which a limit cycle is observed in the horizontal, noninjected, mode while wave-mixing dynamics are found in the injected vertical mode [Fig. 5.4.4(b)]. A further increase in  $P_{inj}$  leads to PS accompanied by injection-locking of the VCSEL to the ML frequency

[Fig. 5.4.4(c)]. For sufficiently larger  $P_{inj}$ , the injection-locking steady state is destabilized through a Hopf bifurcation, denoted by  $H$  in Fig. 5.4.2, after which a limit cycle is excited [Fig. 5.4.4(c)]. The onset of this type of two-mode dynamics and its evolution in the injection-parameter plane is marked by full diamonds with a thick dotted line in Fig. 5.4.2. The observed dynamics are enhanced over a detuning range close to the relaxation oscillation frequency (the measured value is of  $f_{RO} = 5.2$  GHz). Moreover, we find that the injection power corresponding to the onset of two-polarization mode dynamics increases as one evolves towards larger negative detuning. As a result, the limit cycle and the wave mixing peaks become weaker until they disappear for a  $\Delta\omega \approx 10.5$  GHz. For larger negative detuning an abrupt PS, accompanied by injection-locking, is observed.

## 5.5 Conclusions

In conclusion, we have performed the first experimental investigation of the polarization dynamics accompanying PS in VCSELS with orthogonal optical injection. Our results are summarized in a detailed mapping of the bifurcation boundaries in the plane of the injection parameters, i.e., the injection power and frequency detuning. In this mapping we unveil different regions of qualitatively different dynamical behaviors: a region of frequency locking, a region of bistable PS, as well as wave mixing, subharmonic resonance, time-periodic, and chaotic dynamics which accompany the PS mechanism. We have particularly identified a detuning range over which, when increasing the injection power, PS leads to an injection-locking regime which may then be followed by a period-doubling route to chaos. Interestingly, we unveil that the onset of such chaotic dynamics involves not only the injected mode but also the noninjected mode which was suppressed after PS is achieved. We furthermore show that the presence of period-doubling dynamics can strongly affect the switching mechanism. This interplay between PS and nonlinear dynamics is clearly indicated in the mapping by an snakelike shape in the switching curve. In addition to the locking of the first-order transverse mode and for a relatively large positive detuning, we report on a switching scenario which involve the locking of the first order transverse mode, an issue that will be investigated in details in chapter 7.

By closely investigating the route to PS leading to injection locking, we have found a detuning range over which two-polarization mode dynamics are excited before achieving PS. We have shown that a limit cycle appears in the noninjected mode while wave-mixing dynamics is observed in the injected mode. For a relatively small positive detuning range which is located outside but close to the upper limit of the locking region, we identify an interesting scenario for which PS is achieved between a two-polarization mode dynamics

and single-mode limit cycle dynamics.

The experimentally observed polarization dynamics complements our investigation of PS and locking based on the evolution of the polarization-resolved averaged output power, as it has been performed in chapter 4 and in Ref. [120]. The experimentally observed interplay between PS induced by optical injection and the underlying nonlinear dynamics motivates further theoretical investigations. In the next chapter we perform a detailed theoretical study of bifurcation to PS and locking mechanisms in light of our experimental results.



## Chapter 6

# Bifurcation to polarization switching and locking in VCSELs with optical injection: *Theory*

In this chapter, we theoretically report on the interplay between polarization switching and bifurcations to nonlinear dynamics in a vertical-cavity surface-emitting laser (VCSEL) subject to orthogonal optical injection. Using the SFM model presented in Chap. 4, qualitatively different bifurcation scenarios leading to polarization switching are found and mapped out in the plane of the injection parameters, i.e., the frequency detuning vs. injection strength plane. A Hopf bifurcation mechanism, which significantly differs from that reported in optically injected edge-emitting lasers, is found to determine the injection locking region and influence polarization switching. We furthermore report on a torus bifurcation ( $TR$ ) emerging from a two-polarization mode time-periodic dynamics before polarization switching and injection locking appear. It corresponds to an interesting combination of relaxation oscillation dynamics in the noninjected linearly polarized (LP) mode together with wave mixing dynamics in the injected LP mode. We also unveil a period doubling route to chaos that involves both VCSEL orthogonal LP modes. The corresponding region of chaotic dynamics coincides with abrupt changes in the polarization switching boundaries in the plane of the injection parameters. In the positive detuning range outside but close to the limit of the locking zone, we unveil another interesting scenario which involves a switching from a two-mode time periodic solution to a single-mode time-periodic dynamics with the polarization of the injected field. By performing a bifurcation study based on the so-called two-mode model, we find

that such a transition involves two bifurcations, namely one torus bifurcation  $TR_2$  on both noninjected and injected LP modes and another torus bifurcation ( $TR_3$ ); the latter corresponding to the switching off of the noninjected mode. We show that the obtained bifurcations qualitatively support our experimental findings in Chap. 5 and that they are generic features of VCSEL two-polarization-mode models.

The results in the present chapter are based on the following publication:

- I. Gatare, M. Sciamanna, M. Nizette, and K. Panajotov, “*Bifurcation to Polarization Switching and Locking in Vertical-Cavity Surface-Emitting Lasers with Optical Injection*”, Phys. Rev. A **76**, 031803(R) (2007).

## 6.1 Introduction

As already mentioned in Chapter 5, semiconductor lasers subject to external optical injection can exhibit a wide range of nonlinear dynamics which have been extensively investigated, theoretically and experimentally, in the case of optically injected edge-emitting lasers (EEL) [137, 141, 142, 11, 148]. Depending on the injection parameters, i.e., the injection power and frequency detuning between the master and slave lasers, optical injection-induced instabilities such as period-one oscillations [149], period-three limit cycles [150], subharmonic resonance [137], wave mixing, period-doubling route to deterministic chaos [11, 141, 148], and excitable multipulses [151] have been reported. Typically, nonlinear dynamics in injected semiconductor lasers are characterized by identifying bifurcations, i.e., transitional operating points where a qualitative change in the dynamical response is observed, when varying one or both the injection parameters. An experimental mapping of bifurcations in the injection parameter plane, which provides a comprehensive description of nonlinear dynamics in optically-injected EEL, has been achieved [16]. This has been complemented by systematic theoretical model simulations using standard numerical integration methods [145] as well as advanced continuation techniques [152]. Continuation techniques provide a more insightful analysis because they allow detecting bifurcation on both stable and unstable solutions. Using such advanced techniques for the analysis of nonlinear dynamics phenomena in optically injected EEL, it has been theoretically demonstrated how seemingly different and isolated bifurcations can be related to each other, leading to a more global understanding of the injected laser dynamics [152].

The study and characterization of nonlinear dynamics in injected EEL has been thoroughly explored to reaching a good quantitative as well as an excellent qualitative agreement between theory and experiments [12]. How-

ever, the issue of nonlinear dynamics in optically injected VCSELs and the underlying bifurcations is still needed. In particular, in the case of orthogonal optical injection, the intrinsic VCSEL polarization degree of freedom is expected to play a key role. Indeed, as was shown in Chapter 5, we have experimentally observed a strong interplay between polarization switching (PS) mechanisms and nonlinear dynamics. We have particularly noticed that PS and locking mechanisms may be accompanied by polarization-resolved dynamics such as period-doubling route to chaos. The experimental mapping of PS, locking and nonlinear dynamics in the detuning vs. injection strength plane show that regions of chaotic dynamics affects the polarization switching points (see the snakelike shape in the PS curve in Fig. 5.4.2, Section. 5.4). We have furthermore experimentally observed that when the VCSEL is driven close to injection-locking by increasing the injection power for a fixed detuning, a limit cycle at the relaxation oscillation frequency is resolved for the noninjected mode, while the orthogonal mode, i.e., the VCSEL mode with the same polarization as ML, exhibits wave mixing dynamics. These experiments motivate additional theoretical investigations for a better understanding of nonlinear dynamics accompanying the switching and locking mechanisms in optically injected VCSEL.

In this chapter, we combine extensive standard numerical integration of rate equations with modern continuation techniques in order to theoretically investigate the interplay between polarization switching (PS) and nonlinear dynamics in VCSELs subject to orthogonal optical injection. Using the AUTO 97 [153] continuation software package for the computation of bifurcations on stable and unstable solutions, we can follow how the system dynamics and the switching mechanisms are organized and interconnected on a more global scale. This is done by mapping qualitatively different bifurcation curves in the injection parameter plane. As has been also reported for optically injected EEL, the injection locking region is bounded by a saddle-node ( $SN$ ) and a first Hopf ( $H_1$ ) bifurcation curves [152]. However, in our laser system, a new Hopf bifurcation curve (which we shall call  $H_2$ ) intersects with the  $SN$  and  $H_1$  curves on the injection-locked solution. We focus more attention on the key role played by  $H_2$  in both the locking and the switching mechanisms. We show that  $H_2$  delimits the stable injection locking region below the co-dimension-two saddle-node-Hopf point, in contrast to what has been reported for injected EEL [152]. Moreover, we find that  $H_2$  affects the switching mechanism. For instance, we reveal that the minimum power needed to achieve PS is located on  $H_2$  and corresponds to a dramatic change in the switching curve. In addition to  $H_2$ , we report more complex dynamics such as period doubling ( $PD$ ). In particular, we show that the combined effect of two different period-doubling route to chaos yields a snakelike shape in the switching curve, in qualitative agreement with our experimental observations undertaken in Chapter 5.

This chapter is organized as follows. In Section 6.2 we provide a detailed bifurcation analysis of nonlinear dynamics accompanying PS and locking mechanism in a VCSEL subject to orthogonal optical injection. Here, the SFM rate equation model with optical injection is used. In Section 6.3, we carry out another bifurcation study based on different VCSEL model, namely the so-called two-mode model [146, 154]. This complements our results presented in Section 6.2 by showing additional bifurcation mechanism such as a Hopf-Hopf associated with a Torus bifurcation to explain the switching from a two-mode to a single-mode unlocked periodic solution. Finally, a summary and conclusions of our results are drawn in Section 6.4.

## 6.2 Bifurcation study of nonlinear dynamics in a VCSEL with optical injection

We perform a detailed bifurcation analysis of nonlinear dynamics accompanying the switching and locking mechanisms in a VCSEL with orthogonal optical injection. The SFM model with optical injection is used, hence our investigations are limited to nonlinear dynamics involving only the orthogonal, linearly polarized fundamental transverse modes. We use standard integration methods to analyze the dynamics of the injected VCSEL for specific injection conditions. For a more insightful bifurcation analysis, we use continuation techniques to detect and follow bifurcation lines.

We have performed our numerical simulations using the rate equations (4.-8)-(4.11) presented in section 4.3. The following parameters for the VCSEL are used:  $\kappa = 300\text{ns}^{-1}$ ,  $\gamma_p = 30\text{rad.ns}^{-1}$ ,  $\gamma_a = 0.5\text{ns}^{-1}$ ,  $\gamma_e = 1\text{ns}^{-1}$ ,  $\gamma_s = 50\text{ns}^{-1}$ ,  $\mu = 1.5$ . The linewidth enhancement factor  $\alpha$  will be appropriately changed in order to analyze its effect on the dynamical characteristics of the injected VCSEL. For each parameter set, the orthogonal optical injection configuration will be preserved, i.e., the VCSEL operating conditions are such that it exhibits a stationary LP mode along  $x$  in the absence of optical injection.

### 6.2.1 Polarization switching scenarios

We provide different bifurcation scenarios which are obtained by scanning the injection strength  $E_{inj}$  for selected frequency detuning values  $\Delta\omega$  and for  $\alpha = 3$ . At this stage, the rate equations are integrated using classical methods which give access to the dynamics of *only stable* solutions. The results are presented in Fig. 6.2.1 as bifurcation diagrams and reveal qualitatively different switching scenarios depending on the detuning. At each injection strength of the bifurcation diagram, the minima and maxima of



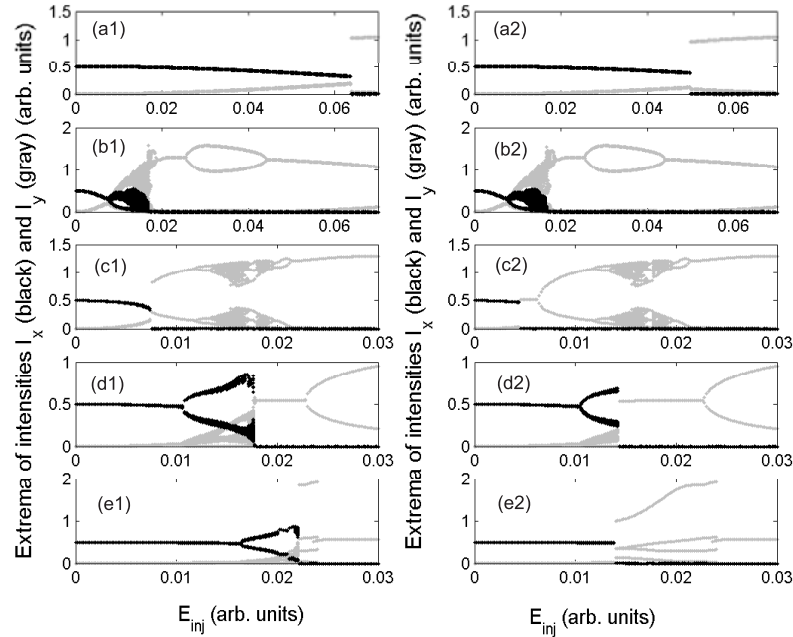


**Figure 6.2.1:** Bifurcation diagrams of the LP mode intensities showing the different scenarios of PS for (a)  $\Delta\omega = 72$ ; (b) 30; (c) 23; (d) 10; and (e)  $-2.2 \text{ rad.ns}^{-1}$ . Left panels: injection strength is increased; right panels: injection strength is decreased. Black (grey) corresponds to  $x$ - ( $y$ -) LP mode. The linewidth enhancement factor is  $\alpha = 3$ .

polarization-resolved intensities,  $I_{x,y} = |E_{x,y}|^2$ , are plotted for a time series of 50 ns after waiting for the transient to die out and when increasing (left panels) and decreasing (right panels) the injection strength  $E_{inj}$ .

Figures 6.2.1(a1) and 6.2.1(a2), which have been obtained for  $\Delta\omega = 72 \text{ rad.ns}^{-1}$ , correspond to a switching dynamics encountered in the range of relatively large detuning values. In this region, the upward switchings from  $x$  to  $y$  (when increasing  $E_{inj}$ ) as well as the downward switching from  $y$  to  $x$  (when decreasing  $E_{inj}$ ) appear abruptly and show polarization bistability. A more detailed analysis of this regime is presented in Fig. 6.2.2 which provides samples of intensity time traces and spectra obtained for two discrete injection strength values corresponding to the dynamics before PS [see Figs. 6.2.2(a1)-(a3)] and after PS [see Figs. 6.2.2(b1)-(b3)]. Before PS the two LP modes exhibit a very small time-periodic modulation of a steady-state dynamics (this modulation is very weak and therefore it is not resolved on the figure). By contrast, after PS the  $x$ -LP mode is switched off and the  $y$ -LP mode intensity exhibits a time-periodic dynamics at a frequency close to the detuning frequency between slave and master lasers [here

$(72/2\pi) \approx 11.5$  GHz].

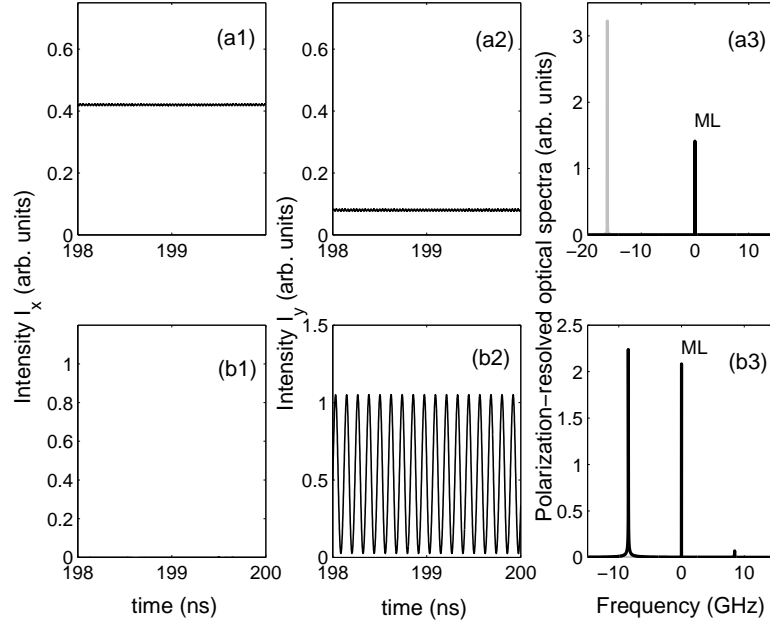


**Figure 6.2.2:** *Polarization-resolved intensities and optical spectra corresponding to the case of abrupt PS at  $\Delta\omega = 70$  rad.ns $^{-1}$  in Fig. 6.2.1(a). (a)  $E_{inj} = 0.04$ , before PS; (b)  $E_{inj} = 0.07$ , after PS. In the spectra black (grey) corresponds to  $y$ - ( $x$ -) LP mode.*

A more complex switching scenario is shown in Figs. 6.2.1(b1) and 6.2.1(b2) for which the detuning has been set to  $\Delta\omega = 30$  rad.ns $^{-1}$ . The corresponding intensity time-series and optical spectra are shown in Fig. 6.2.3. The bifurcation diagrams show that complicated time periodic dynamics in the two LP modes may occur before PS is achieved. As it will be shown later in Section 6.3, the onset of such dynamics is related to the presence of a torus bifurcation on which periodic dynamics in both  $x$  and  $y$ -LP mode are born. As the injection strength is increased, the two-mode periodic dynamics may then evolve to a more complex dynamics which develop through a torus bifurcation mechanism preceding the switching off of the  $x$ -LP mode. In contrast to what has been shown in Figs. 6.2.1(a1) and 6.2.1(a2), the upward PS is achieved in a rather progressive way. As we further increase the injection strength after PS, the VCSEL undergoes a period doubling bifurcation which is then followed by a reverse period doubling bifurcation leading to a period one, limit cycle, regime involving only the  $y$ -LP mode. Furthermore, if we compare Figs. 6.2.1(a1), (a2) with Figs. 6.2.1(b1), (b2), we find that the width of the hysteresis associated to PS has significantly decreased. In both

cases of Figs. 6.2.1(a1), (a2) and Fig. 6.2.1(b1), (b2) PS is not accompanied by injection-locking to the master laser. The numerically obtained switching scenario is in qualitative agreement with our experimental results shown in Fig. 5.4.3, i.e., when increasing the injection power, limit cycle dynamics in both  $x$  and  $y$  polarization modes are observed before achieving PS.

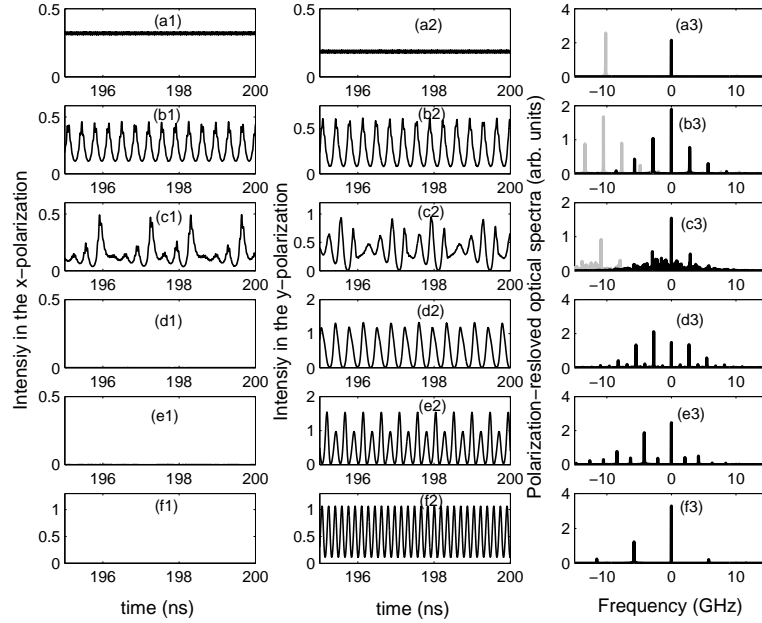


**Figure 6.2.3:** Polarization-resolved intensities and optical spectra for a detuning of  $\Delta\omega = 30 \text{ rad.ns}^{-1}$  corresponding to Fig. 6.2.1(b) and describing PS from a two-mode [ $x$  and  $y$ -LP, Fig. 6.2.3(b)] to a single mode [ $y$ -LP, Fig. 6.2.3(d)] periodic dynamics. Before PS, the two-mode periodic dynamics develop into a more complex, almost chaotic regime as shown in Fig. 6.2.3(c). (a)  $E_{inj} = 0.007$ , unlocked  $x$ -LP; (b)  $E_{inj} = 0.010$  quasiperiodic dynamics in  $x$  and  $y$ -LP mode; (c)  $E_{inj} = 0.0145$ , chaos in both  $x$  and  $y$ -LP mode; (d)  $E_{inj} = 0.0185$ , periodic  $y$ -LP mode; (e)  $E_{inj} = 0.035$ , period-doubling (f)  $E_{inj} = 0.07$  period-one dynamic after a reverse period-doubling bifurcation. In the spectra black (grey) corresponds to  $y$ - ( $x$ -) LP mode.

Another qualitatively different bifurcation scenario is illustrated in Figs.-6.2.1(c1) and 6.2.1(c2) for  $\Delta\omega = 23 \text{ rad.ns}^{-1}$ . The corresponding intensity time-series and optical spectra are shown in Fig. 6.2.4. In this case, by increasing  $E_{inj}$ , one induces an abrupt polarization switching which is then followed by a period doubling route to chaos. In fact, when the injection strength is increased [Fig. 6.2.1(c1)], PS is achieved from an unlocked  $x$ -LP to a  $y$ -LP time-periodic dynamics. As we further increase the injection strength,

the time-periodic dynamics undergoes a period doubling route to chaos. For larger injection strength, chaos is exited through a reverse period doubling cascade. By then decreasing the injection power [Fig. 6.2.1(c2)], a reverse scenario is obtained except that a region of injection locked steady-state dynamics is now found before the VCSEL switches back to  $x$ -LP. Moreover, we notice that the reverse switching point occurs for a relatively lower injection level, thus showing the existence of bistability between an unlocked solution (with  $x$ -LP mode dominant) and a locked solution ( $y$ -LP only) steady-state dynamics. As will be shown later, this bistable behavior results from the fact that, for such a detuning value and by increasing  $E_{inj}$ , PS is achieved after crossing the Hopf bifurcation that delimits the injection locking region. For a more insightful analysis of the dynamics described in Fig. 6.2.1(c), we present in Fig. 6.2.4 samples of polarization-resolved intensity time traces as well as optical spectra which have been obtained for selected injection strength values taken from Fig. 6.2.1(c1) [except Figs. 6.2.4(b1)-(b3) which correspond to an injected locked state from Figs. 6.2.1(c2), i.e., when decreasing  $E_{inj}$ ]. The situation before PS is shown in Figs. 6.2.4(a1)-(a3) for which the VCSEL exhibits an unlocked solution. For this small injection strength value the VCSEL emits only in the  $x$ -LP mode. As the injection strength is increased, the above mentioned period doubling route to chaos (which appears after PS is achieved) is now well-resolved: a period-one limit cycle [Figs. 6.2.4(c1)-(c3)] followed by a period-two [Figs. 6.2.4(d1)-(d3)] which then leads to chaotic dynamics [Figs. 6.2.4(e1)-(e3)] in the  $y$  LP mode. Furthermore, it appears from spectral analysis that the limit cycle is excited with a frequency close to the relaxation oscillation (RO). With our parameter choice,  $f_{RO} = (1/2\pi)\sqrt{2\kappa\gamma_e(\mu - 1)} \approx 2.8$  GHz which is close the frequency of the peaks on both sides of the master laser frequency (here  $f_{ML} = 0$  GHz since our equations are written in the reference frame of the master laser). As it will be shown in Section 6.2.3, the observed period-doubling dynamics which follow PS denote the existence of an injection-parameter region where the system is characterized by severe dynamical instabilities which depend strongly on the VCSEL linewidth enhancement factor (or  $\alpha$ -factor).

We next analyze the dynamics represented in Figs. 6.2.1(d1) and 6.2.1(d2) for which the detuning has been set at  $\Delta\omega = 10$  rad.ns<sup>-1</sup>. A detailed description of the corresponding switching scenario is shown in Fig. 6.2.5, in which polarization-resolved intensity time traces and optical spectra are presented. In the relatively weak injection regime [Figs. 6.2.5(a)], the VCSEL emits predominantly in the  $x$ -LP mode with a very weak time periodic modulation of the steady state. Interestingly, as the injection strength is increased and before PS occurs [Figs. 6.2.5(b1)- 6.2.5(b3)], the slave VCSEL exhibits a well-resolved time-periodic dynamics, which does not appear in the previously investigated switching scenarios. As shown in Figs. 6.2.5(b3), when the frequency offset between ML and the  $y$ -LP mode is close the relaxation

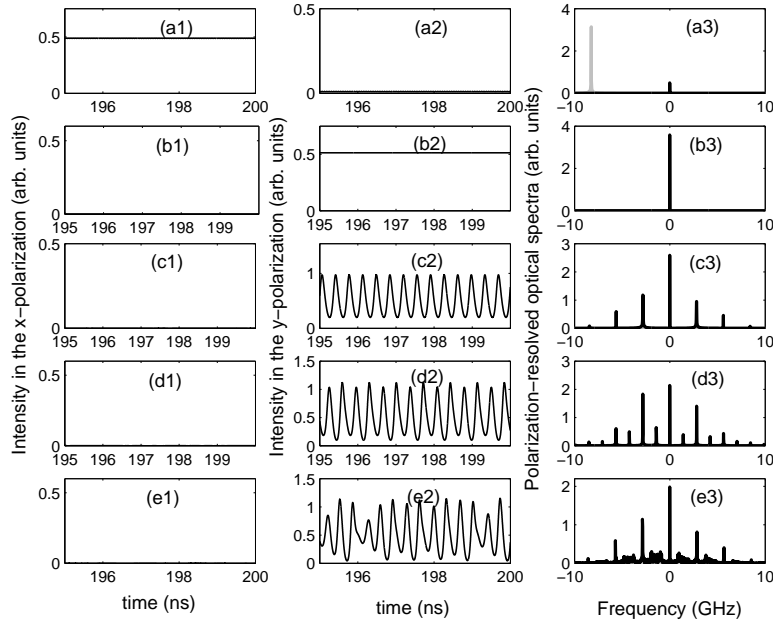


**Figure 6.2.4:** Polarization-resolved intensities and optical spectra showing PS accompanied by a period doubling route to chaos at  $\Delta\omega = 23 \text{ rad.ns}^{-1}$  corresponding to Fig. 6.2.1(c). (a)  $E_{inj} = 0.0025$ , unlocked  $x$ -LP; (b)  $E_{inj} = 0.0055$  (downward scan), injection locking to ML frequency; (c)  $E_{inj} = 0.0095$ , switching to a  $y$ -LP periodic regime; (d)  $E_{inj} = 0.013$ , period-doubling; (e)  $E_{inj} = 0.0155$ , chaos in both  $x$ -LP and  $y$ -LP modes. In the spectra black (grey) corresponds to  $y$ - ( $x$ -) LP mode.

oscillation frequency, two peaks are excited on both sides of the main  $x$ -LP peak with a frequency offset close to  $f_{RO}$ . The  $x$ -LP mode therefore exhibits a time-periodic dynamics at the RO frequency. However, the optical spectrum corresponding to the  $y$ -LP mode shows a wave-mixing between the  $y$ -LP slave laser main peak and the injected master laser field. Side peaks indeed appear at frequencies multiple of the frequency offset between the  $y$ -LP main peak and the master laser peak. If the injection strength is further increased, an abrupt polarization switching leads to injection-locking as shown in Figs. 6.2.5(c1)-(c3). For still higher injection strength levels, the injection locked state is exited through a Hopf bifurcation which corresponds to the onset of a limit cycle dynamics at the relaxation oscillation frequency, as plotted in Figs. 6.2.5(d1)-(d3). In contrast to what has been shown in Figs. 6.2.5(b1)-(b3), this limit cycle dynamics emerges from the injection locked  $y$ -LP steady state. The numerically obtained switching scenario is in qualitative agreement with our experimental results shown in Fig. 5.4.1 and

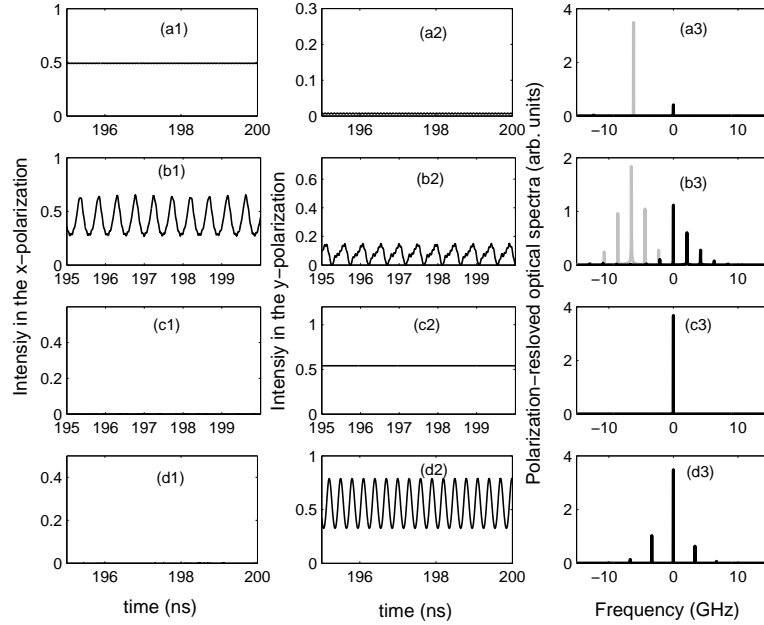


**Figure 6.2.5:** Polarization-resolved intensities and optical spectra at  $\Delta\omega = 10 \text{ rad.ns}^{-1}$  corresponding to Fig. 6.2.1(d) showing for: (a)  $E_{inj} = 0.005$ , weak injection regime, (b)  $E_{inj} = 0.013$ , excitation of limit cycle before PS for the  $x$ -LP mode and wave mixing between  $y$ -LP and ML; (b)  $E_{inj} = 0.020$ , injection locking; (c)  $E_{inj} = 0.025$ , limit cycle after crossing a Hopf bifurcation. In the spectra, black (grey) corresponds to  $y$ - ( $x$ -) LP mode.

Fig. 5.4.4, i.e., when increasing the injection power, limit cycle dynamics in the noninjected mode and wave mixing dynamics in the injected mode are observed before PS accompanied by injection locking.

Let us now investigate the dynamics depicted in Figs. 6.2.1(e1) and Fig. 6.2.1(e2) for a frequency detuning of  $\Delta\omega = -2.2 \text{ rad.ns}^{-1}$ . Here we focus on a new switching scenario in which, while increasing the injection strength, PS from two-polarization mode time-periodic dynamics to single-mode time-periodic dynamics is achieved before injection-locking of the VCSEL to ML. The details about this regime are shown in Fig. 6.2.6 for selected injection strengths taken from Fig. 6.2.1(e1), i.e., when increasing the injection strength. For a relatively low injection strength, the VCSEL emits a single  $x$ -LP mode characterized by a weak time-periodic modulation [Figs. 6.2.6(a1)- 6.2.6(a3)]. As the injection strength is increased and similarly to the above mentioned dynamics described in Fig. 6.2.1(d1) for  $\Delta\omega = 10 \text{ rad.ns}^{-1}$ , limit cycle and wave-mixing dynamics appear for the  $x$ - and the  $y$ -LP modes respectively [Figs. 6.2.6(b1)- 6.2.6(b3)]. By further

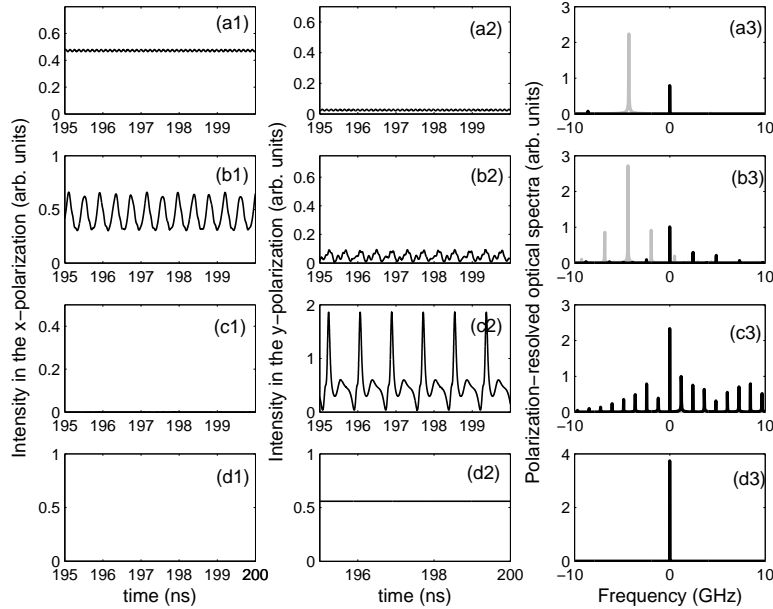


**Figure 6.2.6:** Polarization-resolved intensities and optical spectra showing PS accompanied by a period doubling route to chaos at  $\Delta\omega = -2.2 \text{ rad.ns}^{-1}$  corresponding to Fig. 6.2.1(e). (a)  $E_{inj} = 0.0150$ , unlocked  $x$ -LP; (b)  $E_{inj} = 0.0188$ , excitation of limit cycle before PS for the  $x$ -LP mode and wave mixing between  $y$ -LP and ML; (c)  $E_{inj} = 0.0230$ , switching to a  $y$ -LP periodic regime; (d)  $E_{inj} = 0.0271$ , Injection locking. In the spectra black (grey) corresponds to  $y$ - ( $x$ -) LP mode.

increasing the injection strength, PS is achieved from the two-polarization mode solution to a nearly pulsating time-periodic dynamics in the  $y$ -LP mode only [Figs. 6.2.6(c1)- 6.2.6(c3)]. A further increase in  $E_{inj}$  then leads to injection-locking to ML [Figs. 6.2.6(d1)- 6.2.6(d3)]. It is worth noting that the obtained switching is qualitatively different from the scenario described in Figs. 6.2.1(d1)- 6.2.1(d2) and detailed in Fig. 6.2.5 for which the switching is achieved from the two-polarization mode time-periodic solution to an injection-locked  $y$ -LP steady state. If  $E_{inj}$  is decreased from the injection-locked state [Fig. 6.2.1(e2)], a reverse scenario is found except that, unlike what is shown in Fig. 6.2.1(d2) for  $\Delta\omega = 10 \text{ rad.ns}^{-1}$ , the two-polarization time-periodic dynamics (in both  $x$  and  $y$ -LP modes) is no longer observed. The backward switching to  $x$ -LP is achieved abruptly and shows a relatively large hysteresis. As will be shown in the following section, the difference between the switching scenarios shown in Figs. 6.2.1(d1)- 6.2.1(d2) and Figs. 6.2.1(e1)- 6.2.1(e2) resides in the fact that, as one increases the

injection strength for selected detunings, the switching can be achieved after or before the crossing of the saddle-node bifurcation which partly delimits the injection-locking zone in the  $(E_{inj}, \Delta\omega)$  bifurcation mapping.

Before undertaking the mapping of bifurcation underlying the PS and nonlinear dynamics of the VCSEL with orthogonal optical injection, let us summarize our main findings on the polarization switching scenarios:

- For sufficiently large positive detunings, polarization switching (PS) is achieved abruptly as we scan the injection strength for a fixed frequency detuning [see Figs. 6.2.1(a) and 6.2.2]. The typical nonlinear dynamics is an unlocked state with injection-induced periodic modulation of the optical intensity with a frequency close to the frequency offset between master and slave lasers.
- For moderate positive detunings, we notice that PS may involve complex nonlinear dynamics [see Figs. 6.2.1(b) and 6.2.3]. Instead of an abrupt PS as it is the case in the preceding scenario, we report on a PS which is achieved rather progressively. In fact, before PS, time-periodic dynamics in both orthogonal linearly polarized fundamental transverse modes are first excited. As we increase the injection strength, the two-polarization-mode time-periodic dynamics evolve to more complex chaotic dynamics. Then the noninjected mode is switched off and, for larger injection strengths, the VCSEL exhibits time-periodic dynamics in the injected polarization-mode only.
- In Figs. 6.2.1(c) and 6.2.4, we report on a scenario for which, as the injection strength is scanned for a fixed detuning, the PS mechanism is accompanied by a period-doubling route to chaos. We show that the observed period doubling arises from undamped relaxation oscillations time-periodic dynamics, which are associated to the destabilization of an injection-locked steady state.
- We unveil another interesting polarization switching scenario in Figs. 6.2.1(d) and 6.2.5. The detuning is such that, by increasing the injection strength, PS leads to injection-locking. Here, the key point is that a two-polarization-mode time-periodic dynamics is excited before PS is achieved: periodic dynamics at the relaxation oscillation frequency in the noninjected mode together with wave-mixing dynamics in the injected mode.
- Finally, in Figs. 6.2.1(e) and 6.2.6, we identify a switching scenario which is almost similar to what is shown in Figs. 6.2.1(d) and 6.2.5. By increasing the injection strength, a two-polarization-mode time-periodic dynamics is excited but, this time, the switching off of the noninjected mode is not directly followed by injection locking. Instead,



and by contrast to what is shown in Figs. 6.2.1(d) and 6.2.5, the VCSEL switches to a nearly pulsating regime before injection-locking is achieved.

## 6.2.2 Bifurcation and polarization switching boundaries

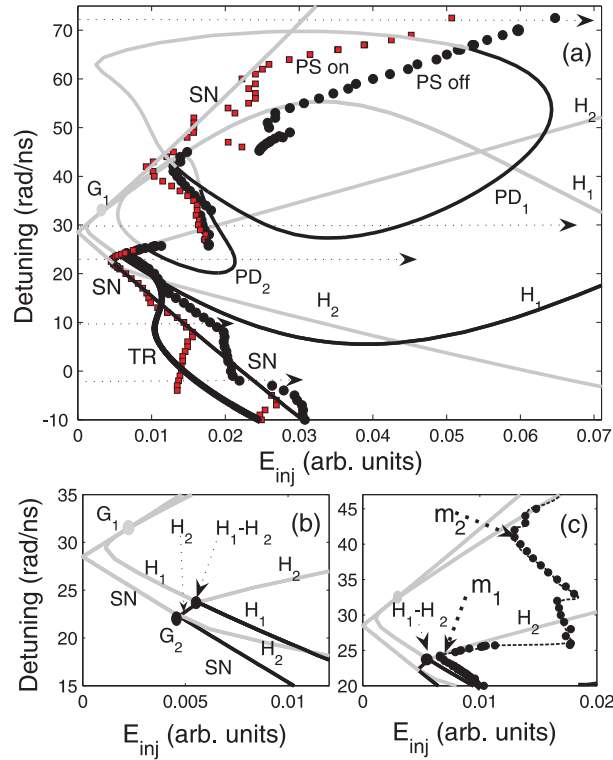


**Figure 6.2.7:** Bifurcation diagram in the plane  $(E_{inj}, \Delta\omega)$  (a). Horizontal dotted arrows indicate the switching scenarios detailed in Fig. 6.2.1. Close view of the codimension-two bifurcation mechanisms (b); and of the snake-like shape in the switching curve with local minima indicated by thick dotted arrows (c). Black (gray) denotes supercritical (subcritical) bifurcation. (TR; 'PS on'; 'PS off') and (TR; 'PS on') curves have been removed respectively in panels (b) and (c) for clarity.

We have so far presented different scenarios of PS dynamics by scanning the injection strength for fixed detuning values. In order to have a global understanding of how the PS interplays with the nonlinear laser dynamics resulting from eqs. (4.8)-(4.11), in Fig. 6.2.7 we perform a mapping of bifurcation curves in the plane of the injection parameters  $(E_{inj}, \Delta\omega)$  and for  $\alpha = 3$ . Qualitative changes in the VCSEL dynamics are detected and

followed using the continuation package AUTO 97 [153]. Different bifurcation curves are plotted: a saddle-node ( $SN$ ), two Hopf ( $H_1$  and  $H_2$ ) and a torus ( $TR$ ). We also report on two period-doubling bifurcation mechanisms denoted by  $PD_1$  and  $PD_2$ . The supercritical and subcritical parts of each bifurcation curve are represented in black and gray respectively. By supercritical bifurcation we mean a bifurcation of an attracting object, which typically corresponds to what is found in experiments or standard numerical simulations (like in the preceding Section). On the other hand, a subcritical bifurcation involves a repelling object, thus leading to a dynamical state that can neither be observed experimentally nor computed by standard numerical simulations. When increasing the injection strength, the VCSEL switches its polarization to that of the injected field. When decreasing the injection strength, the VCSEL switches back to its free-running polarization but for a smaller injection strength. These 'PS off' ( $x$ -LP mode off) and 'PS on' ( $x$ -LP mode on) points are shown with circles and squares respectively. The fact that PS on and PS off points do not occur for the same injected power and/or detuning makes clear the hysteresis associated to bistable PS.

The PS curves, which are obtained by standard numerical integration, interplay with the bifurcation curves.  $SN$  and  $H_1$  are bifurcations on a stationary injection-locked state and have also been reported in the case of optically injected EEL [152]. In the conventional case of EEL, the locking region is then delimited by the co-dimension two point  $G_1$  where  $SN$  and  $H_1$  become tangent. In our two-mode VCSEL system, the locking region is delimited by  $SN$ ,  $H_1$  but also by a new bifurcation  $H_2$ .  $H_2$  is tangent to  $SN$  and hence gives rise to a second codimension-two point labelled  $G_2$ . The maximum detuning leading to injection locking therefore stays well below the codimension-two saddle-node-Hopf point  $G_1$ . The case of two  $G$  points has also been reported in single-mode EEL subject to optical injection [152], however in the limit of small, close to zero,  $\alpha$  and for large negative detuning and large injection strength. Moreover, the two  $G$  points in that case appear from the same  $H_1$  bifurcation. Apart from its effect on the locking,  $H_2$  also affects the polarization switching mechanism. The supercritical part of  $H_2$  [see the bifurcation line which lays in between the  $G_2$  and  $H_1 - H_2$  codimension-two points in Fig. 6.2.7(b)] coincides with 'PS on' points, i.e., the switching on of the  $x$ -LP mode. Moreover, the smallest injection strength needed to achieve the switching off of the  $x$ -LP mode is located on  $H_2$  and corresponds to a dramatic change in the polarization switching curve [see the point labelled  $m_1$  in Fig. 6.2.7(c)]. This local minimum in the 'PS off' is distinct but close to the  $H_1 - H_2$  codimension-two point.

In addition to  $H_2$ , our results reveal that the presence of chaotic attractors such as those bounded by  $PD_1$  and  $PD_2$ , may affect the switching mechanism in a more intricate way. In fact the emergence of two regions of complex, possibly chaotic, dynamics delimited respectively by  $PD_1$  and

$PD_2$  coincides with the existence of the second local minimum denoted  $m_2$  in Fig. 6.2.7(c). As a result, the PS curve exhibits a snakelike shape with local minima of the injected power required for the switching off of the  $x$ -LP mode [For details see Fig. 6.2.7(c); the broken line is used there as a guide for the eyes]. The observed snakelike shape and the role played by complex period doubling mechanisms agrees qualitatively with our experimental results presented in Chapter 6, in Fig. 5.2.1 and 5.4.2.

We have indicated by dotted lines in Fig. 6.2.7(a) the detuning values which correspond to the qualitatively different polarization switching scenarios described in Fig. 6.2.1. We show that for  $\Delta\omega = 72 \text{ rad.ns}^{-1}$  [see also Figs. 6.2.1(a1) and 6.2.1(a2)] the switching is achieved without being followed by injection-locking or chaotic complex nonlinear dynamics. For  $\Delta\omega = 30 \text{ rad.ns}^{-1}$  [see also Fig. 6.2.1(b1) and 6.2.1(b2)] the regions of chaotic dynamics are crossed but not the injection locking region. The case of an abrupt PS accompanied by injection locking and a period doubling route to chaos is also shown for  $\Delta\omega = 23 \text{ rad.ns}^{-1}$  [corresponding to Fig. 6.2.1(c1) and 6.2.1(c2)]. In this case both the injection locking region and that of chaotic dynamics (bounded by  $PD_2$ ) are crossed. However, the PS point when increasing  $E_{inj}$  is located after the  $H_1$  bifurcation boundary [see Fig. 6.2.7(c) for details] and therefore injection locking is only observed when decreasing back the injection strength. Finally, the emergence of a relaxation oscillation dynamics in  $x$ -LP mode and wave mixing dynamics in  $y$ -LP mode before PS [see Fig. 6.2.1(d1)- 6.2.1(d2) and Fig. 6.2.1(e1)- 6.2.1(e2)] corresponds in fact to the torus bifurcation labelled  $TR$  in Fig. 6.2.7(a).

In order to investigate the role played by the torus bifurcation  $TR$  on the PS mechanism we revise the bifurcation scenarios presented in Fig. 6.2.1(e1)- 6.2.1(e2) and Fig. 6.2.1(d1)- 6.2.1(d2)] for, respectively,  $\Delta\omega = -2.2 \text{ rad.ns}^{-1}$  [Fig. 6.2.8(a1)-(a4)] and  $\Delta\omega = 10 \text{ rad.ns}^{-1}$  [Figs. 6.2.8(b1)-(b4)]. For a weak injection strength [see Figs. 6.2.8(a1) and 6.2.8(b1) for  $E_{inj} = 0.005$ ], the VCSEL emits predominantly an unlocked  $x$ -LP mode. The optical spectrum of the  $x$ -LP mode shows one peak located at about the free-running detuning between master and  $x$ -LP mode, i.e.  $f_x - f_{inj} = (-\gamma_p - \Delta\omega)/2\pi$ . The optical spectrum of the  $y$ -LP mode shows one very small contribution at the master laser frequency (0 GHz). If the injection is further increased, we show that the crossing of  $TR$  coincides with the onset of time-periodic dynamics which involves both  $x$ - and  $y$ -LP modes [see Fig. 6.2.8(a2) for  $E_{inj} = 0.0182$  and Fig. 6.2.8(b2) for  $E_{inj} = 0.0130$ ]. For the non-injected mode ( $x$ -LP), a limit-cycle dynamics at the RO frequency is excited. With our parameter set, the RO frequency is  $f_{RO} = (1/2\pi)\sqrt{2\kappa\gamma_e(\mu - 1)} \approx 2.8 \text{ GHz}$  which is close to the frequency offset of the two peaks located on both sides of the  $x$ -LP main peak. The spectrum of the injected-mode ( $y$ -LP) shows by contrast a wave-mixing dynamics between the  $y$ -LP mode and the ML. The  $y$ -LP mode frequency is initially detuned from the master frequency by  $f_y - f_{inj} = (\gamma_p -$

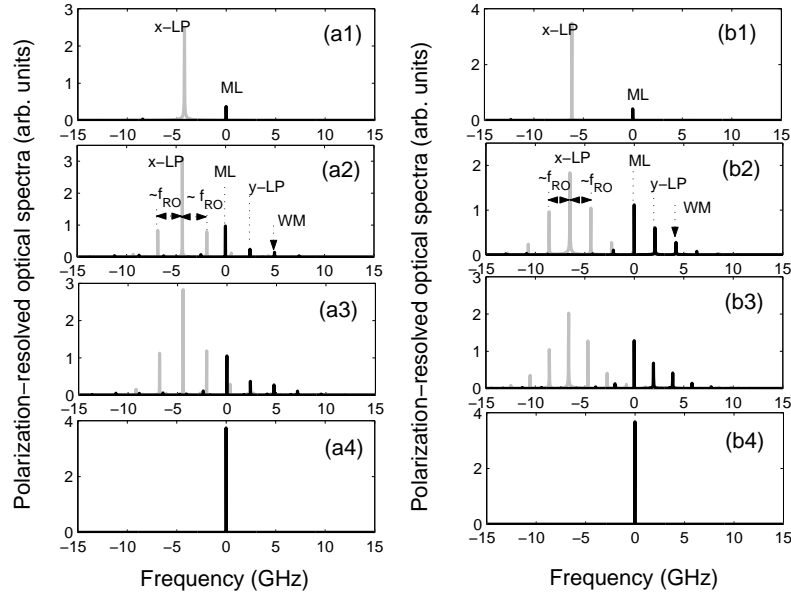


**Figure 6.2.8:** *Theoretical polarization-resolved optical spectra showing the dynamics leading to PS and locking when increasing the injection strength (from top to bottom) for: (a1)-(a4)  $\Delta\omega = -2.2 \text{ rad.ns}^{-1}$  and (b1)-(b4)  $\Delta\omega = 10 \text{ rad.ns}^{-1}$ . Black (grey) corresponds to  $y$ - ( $x$ -) LP mode.*

$\Delta\omega)/2\pi$ . However, this frequency is pulled towards that of the master laser as the injection strength increases. The resulting  $y$ -LP frequency (labelled ' $y$ -LP') and the master laser frequency (labelled 'ML') beat and give rise to new frequency components labelled 'WM'. For relatively larger injection levels [see Fig. 6.2.8(a3) for  $E_{inj} = 0.0195$  and Fig. 6.2.8(b3) for  $E_{inj} = 0.0145$ ], harmonics of the RO frequency are excited in the  $x$ -LP mode whereas we find, in the  $y$ -LP mode, spectral components with a frequency multiple of the frequency offset between ML and the  $y$ -LP mode. For sufficiently larger  $E_{inj}$ , polarization switching to an injection-locked single  $y$ -LP mode solution is achieved [see Fig. 6.2.8(a4) for  $E_{inj} = 0.0280$  and Fig. 6.2.8(b4) for  $E_{inj} = 0.0200$ ]. As it appears from the results obtained for two different detunings values [compare Fig. 6.2.8(a2) to Fig. 6.2.8(b2) and Fig. 6.2.8(a3) to Fig. 6.2.8(b3)], the TR bifurcation occurs when injection conditions ( $E_{inj}$  and  $\Delta\omega$ ) are such that the frequency offset between the pulled  $y$ -LP mode and master laser is close to the RO frequency.

### 6.2.3 Influence of the $\alpha$ factor on the injected VCSEL dynamics

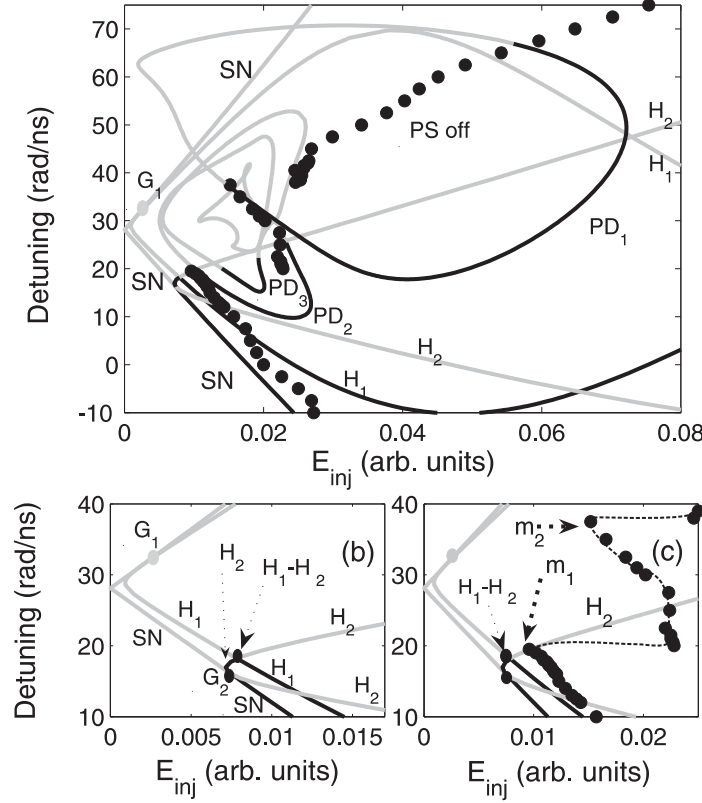


**Figure 6.2.9:** Bifurcation diagram in the plane  $(E_{inj}, \Delta\omega)$  for  $\alpha = 3.75$ . Black (grey) denotes supercritical (subcritical) part of each bifurcation curve. Bifurcation curves, codimension-two points, and switching points keep the same meaning as in Fig. 6.2.7.

As has been shown for edge-emitting lasers (EEL), the linewidth enhancement factor ( $\alpha$ ), which represents the phase-amplitude coupling, can dramatically influence the overall bifurcation mechanisms and is a key laser parameter in determining the nonlinear response of the optically injected semiconductor laser [145, 152]. For the case of VCSEL subject to orthogonal optical injection, one may expect a more intricate effect due to the polarization degree of freedom. In this section we analyze the effect of modifying the VCSEL  $\alpha$  factor on the bifurcation and PS boundaries. We plot in Fig. 6.2.9 and 6.2.10 the mappings corresponding to  $\alpha = 3.75$  and  $\alpha = 2.25$ , respectively. For the sake of clarity, we represent only the PS off points, i.e., the switching points from the  $x$ -LP mode to  $y$ -LP mode when increasing the

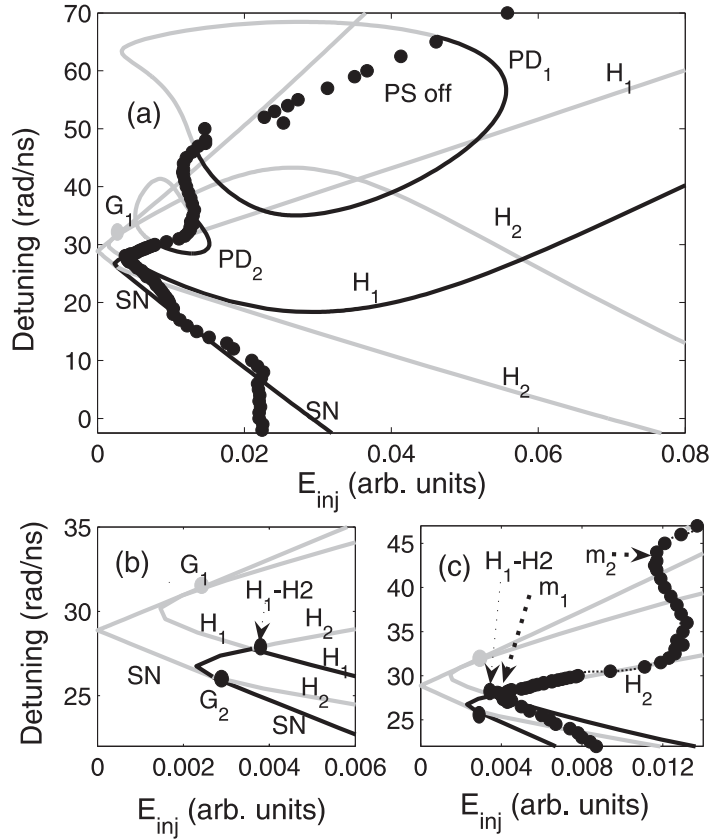


**Figure 6.2.10:** Bifurcation diagram in the plane  $(E_{inj}, \Delta\omega)$  for  $\alpha = 2.25$ . Black (grey) denotes the supercritical (subcritical) part of each bifurcation line. Bifurcation curves, codimension-two points, and switching points keep the same meaning as in Fig. 6.2.7.

injection strength for fixed detunings. If we compare Fig. 6.2.7, Fig. 6.2.9 and Fig. 6.2.10, we find that the change of  $\alpha$  affects the relative position between the different bifurcation curves and hence the location of the PS curve, the locking region and the regions of complex chaotic dynamics. In the preceding section, we have reported on the existence of codimension-two points  $G_1$  and  $G_2$  arising from the intersection between the saddle-node bifurcation curve  $SN$  with, respectively,  $H_1$  and  $H_2$  Hopf bifurcation curves. One observes that decreasing  $\alpha$  decreases the detuning range between  $G_1$  and  $G_2$ : as  $\alpha$  decreases,  $G_2$  is achieved for larger detunings and smaller injection strengths, while the location of  $G_1$  is less sensitive to  $\alpha$ . Conversely, the opposite effect is observed when increasing  $\alpha$ , i.e., the detuning range between  $G_1$  and  $G_2$  increases with  $\alpha$ . In addition, we show that the smallest injection strength needed to achieve PS, when increasing the injection

strength, is located on  $H_2$  for all the cases [see the location of the minimum denoted by  $m_1$  in Fig. 6.2.7(c), Fig. 6.2.9(c) and Fig. 6.2.10(c)].

We now closely investigate the consequence of the effect of  $\alpha$  on the period doubling bifurcations (and the associated bubbles of chaotic instabilities). In agreement with what has been theoretically demonstrated in injected edge-emitting lasers (EEL), decreasing  $\alpha$  may significantly shrink the injection parameter region over which complex nonlinear instabilities are observed [145]. In fact, if the linewidth enhancement factor is decreased from  $\alpha = 3$  (Fig. 6.2.7) to  $\alpha = 2.25$  (Fig. 6.2.10) with all other VCSEL's intrinsic parameters being kept the same, we find that the regions of complex nonlinear dynamics, bounded by the period-doubling curves  $PD_1$  and  $PD_2$ , shrink in size. Moreover, in the smaller  $\alpha$  case (see Fig. 6.2.10,  $\alpha = 2.25$ ) the initially overlapping period-doubling curves (see the relative position between  $PD_1$  and  $PD_2$  in Fig. 6.2.10) are now well separated in the  $(\Delta\omega, E_{inj})$  mapping. Increasing  $\alpha$  has, however, an opposite effect (compare Fig. 6.2.7 for  $\alpha = 3$  and Fig. 6.2.9 for  $\alpha = 3.75$ ). In this case the regions of complex nonlinear dynamics bounded by  $PD_1$  and  $PD_2$  expand in size and their overlapping is significantly enhanced. We furthermore notice that the associated chaotic instability regions are now extended over a larger injection parameter range and may involve additional period-doubling mechanism which may lead to more complex chaotic dynamics. This is the case in Fig. 6.2.9 where, in addition to  $PD_1$  and  $PD_2$ , a new period-doubling curve, denoted  $PD_3$  is now resolved. Moreover, we find that the expansion of the period-doubling (PD) bifurcation curves, due to the increase in  $\alpha$ , dramatically affects the switching mechanism by decreasing the detuning range between the two local minima,  $m_1$  and  $m_2$ , in the switching curve. Concretely, by increasing  $\alpha$ ,  $m_1$  and  $m_2$  are both achieved for smaller detunings and for larger injections strengths but this is accompanied by a decrease in the detuning range between them.

Here, we investigate the effect of the change of the  $\alpha$ -factor on nonlinear dynamics which accompanies the switching and locking mechanism. The results are presented in Fig. 6.2.11 where, for each value of  $\alpha$ , the detuning is adequately chosen in such a way that we operate in between the saddle-node-Hopf ( $G_2$ ) and the Hopf-Hopf ( $H_1$ - $H_2$ ) codimension-two points, i.e., such that the supercritical part of  $H_2$  is crossed when scanning  $E_{inj}$ . To this end, the selected detuning values are:  $\Delta\omega = 26.6$  for  $\alpha = 2.25$  [see Figs. 6.2.11(a1)-(a5)],  $\Delta\omega = 23$  for  $\alpha = 3$  [see Figs. 6.2.11(b1)-(b5)], and  $\Delta\omega = 17.3 \text{ rad.ns}^{-1}$  for and  $\alpha = 3.75$  [see Fig. 6.2.11(c1)-(c5)]. We represent the evolution of the dynamics of the injected VCSEL when increasing  $E_{inj}$  [except Fig. 6.2.11(a2), Fig. 6.2.11(b2) and Fig. 6.2.11(c2) which correspond to injected locked states, i.e. when decreasing  $E_{inj}$  from an initial state for which the VCSEL is operated in the higher-injection power regime and after the crossing of  $H_1$  and PS off curve]. When the VCSEL operates in the rel-

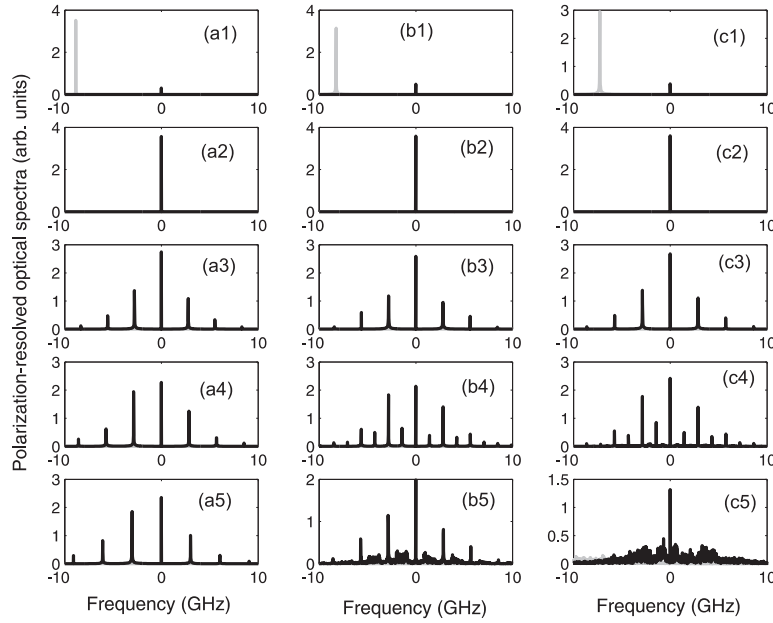


**Figure 6.2.11:** *Theoretical polarization-resolved optical spectra showing the dynamics leading to PS and locking when increasing the injection strength (from top to bottom) for: (a1)-(a5)  $\alpha = 2.25$  and  $\Delta\omega = 26.6 \text{ rad.ns}^{-1}$ ; (b1)-(b5)  $\alpha = 3$  and  $\Delta\omega = 23 \text{ rad.ns}^{-1}$ ; (c1)-(c5)  $\alpha = 3.75$  and  $\Delta\omega = 17.3 \text{ rad.ns}^{-1}$ . Black (grey) corresponds to  $y$ - ( $x$ -) LP mode.*

atively weak injection strength regime before achieving PS, [Fig. 6.2.11(a1) for  $\alpha = 2.25$ ; Fig. 6.2.11(b1) for  $\alpha = 3$ ; and Fig. 6.2.11(c1) for  $\alpha = 3.75$ ], qualitatively similar dynamics are observed for the three values of  $\alpha$ , i.e., the VCSEL predominantly emits an unlocked  $x$ -LP mode. Naturally the injection locking [Fig. 6.2.11(a2) for  $\alpha = 2.25$ ; Fig. 6.2.11(b2) for  $\alpha = 3$ ; and Fig. 6.2.11(c2) for  $\alpha = 3.75$ ] and the limit cycle, period-one, dynamics [Fig. 6.2.11(a3) for  $\alpha = 2.25$ ; Fig. 6.2.11(b3) for  $\alpha = 3$ ; and Fig. 6.2.11(c3) for  $\alpha = 3.75$ ] are also similar. In the smaller alpha case ( $\alpha = 2.25$ ), one observes that increasing  $E_{inj}$  does not lead to destabilization of the limit cycle, period-one, dynamics. Instead, only enhancement of the obtained limit cycle is observed [compare Fig. 6.2.11(a3) for  $E_{inj} = 0.008$ ; Fig. 6.2.11(a4) for  $E_{inj} = 0.0155$ ; and Fig. 6.2.11(a5) for  $E_{inj} = 0.020$ ]. However, for a larger alpha value ( $\alpha = 3$ ), as the injection strength is increased, the limit cycle, period-one, regime [Fig. 6.2.11(b3) for  $E_{inj} = 0.0095$ ] undergoes a period-doubling [Fig. 6.2.11(b4) for  $E_{inj} = 0.0155$ ] route to complex, possibly chaotic, instabilities [Fig. 6.2.11(b5) for  $E_{inj} = 0.020$ ]. Similarly, for larger  $\alpha$  value ( $\alpha = 3.75$ ), the period-doubling route to chaos is also ob-



served [Fig. 6.2.11(c3) for  $E_{inj} = 0.0119$ ; Fig. 6.2.11(c4) for  $E_{inj} = 0.0137$ ; and Fig. 6.2.11(c5) for  $E_{inj} = 0.0185$ ]. Nevertheless, we show that the complexity of the chaotic dynamics increases as  $\alpha$  is increased. Indeed, by comparing Figs. 6.2.11(b5) and Fig. 6.2.11(c5), one finds that the larger the  $\alpha$ -factor is the broader the spectrum of the chaotic regime becomes; which is indicative of a fully developed chaotic regime.

### 6.3 Bifurcation study using a two-mode model for VCSELS with orthogonal injection

The detailed bifurcation study performed in Section 6.2 provides interesting information about polarization switching (PS) induced by orthogonal optical injection and its interplay with nonlinear dynamics. In particular, the mapping of nonlinear dynamics in the detuning vs. injection strength plane (see Fig. 6.2.7) unveils two bifurcations, namely a Hopf bifurcation  $H_2$  and a torus bifurcation  $TR$ , which play a key role in the PS and injection-locking dynamics. Interestingly,  $TR$  bifurcation mechanism qualitatively supports our experimental results showing a two-polarization-mode time-periodic dynamics on the route to PS that leads to injection locking (see Chapter 5, Section 5.4). Furthermore, we theoretically report (see Fig. 6.2.3) on another intriguing bifurcation associated with PS and which also qualitatively supports what has been experimentally observed within a small detuning region outside but close to the injection-locking zone (see Fig. 5.4.2 and Fig. 5.4.3). In that region PS is achieved as follows: as the injection strength is increased for fixed detunings, the VCSEL is frequency pushed with respect to ML. By further increasing the injection, a limit cycle dynamics in both non-injected and injected modes is abruptly excited. For larger injection strengths, the VCSEL switches from the two-mode to a single-mode limit cycle dynamics which involves only the injected mode. Although the latter switching scenario is also qualitatively supported by our numerical simulations as shown in Fig. 6.2.3, it was not easy to fully characterize it in the mapping using continuation technique. In the framework of the SFM model, this is possibly due to the fact that the bifurcation mechanism associated with such a switching scenario may interplay with several attractors which were detected in the detuning range of interest (e.g., the period doubling bifurcations  $PD_1$  and  $PD_2$  in Fig. 6.2.7).

In the present Section, we undertake a new bifurcation study based on an alternative model, the so-called *two-mode model*, which has been successfully used in previous studies on polarization switching in VCSELS [146, 154]. Instead of conducting a detailed bifurcation analysis, as it has been the case in Section 6.2 using the SFM model, we restrict our new study to addressing the following issues: 1/ are  $H_2$  and  $TR$  generic features of VCSEL two-mode

systems?; 2/ is it possible to unfold the intriguing bifurcation mechanism underlying the interesting scenario which involves the switching between two-polarization mode and single-polarization mode limit-cycle dynamics?. Our results show that indeed both  $H_2$  and  $TR$  bifurcations are generic features of VCSEL subject to orthogonal optical injection. We furthermore show that the PS scenario which involves the switching between two-polarization mode limit cycle dynamics and single-polarization mode dynamics results from a combined effect of two torus bifurcation mechanisms, namely  $TR_2$  and  $TR_3$ .

### 6.3.1 The two-mode model

An alternative rate equation model for the optically injected VCSEL is based on two-mode rate equations with gain self- and cross-saturation [146, 154]:

$$\frac{d\hat{E}_x}{dt} = \frac{1}{2}(1+i\alpha) \left[ \Gamma_x G_x - \frac{1}{\tau_{px}} \right] \hat{E}_x + \kappa_{inj} E_{inj} - i\Delta\omega_x \hat{E}_x, \quad (6.3.1)$$

$$\frac{d\hat{E}_y}{dt} = \frac{1}{2}(1+i\alpha) \left[ \Gamma_y G_y - \frac{1}{\tau_{py}} \right] \hat{E}_y - i\Delta\omega_y \hat{E}_y, \quad (6.3.2)$$

$$\frac{d\hat{N}}{dt} = \frac{J}{eV} - \frac{\hat{N}}{\tau_e} - G_x |\hat{E}_x|^2 - G_y |\hat{E}_y|^2. \quad (6.3.3)$$

Here  $\hat{E}_x$  and  $\hat{E}_y$  are the slowly varying  $x$ - and  $y$ - LP components of the electric field with optical frequency at threshold  $\nu_{0x,y}$ ;  $\alpha$  is the linewidth enhancement factor,  $\Gamma_{x,y}$  are the confinement factors, and  $\tau_{px,y}$  are the photon lifetimes. Optical injection with strength  $\kappa_{inj}$ , amplitude  $E_{inj}$ , and optical frequency  $\omega_{inj}$  is considered for the  $x$ -LP injected mode. Within the injection frequency frame, the frequency detuning between the injecting mode and the injected mode is  $\Delta\omega = \Delta\omega_x = \omega_{inj} - \omega_x$  while the detuning between the injecting mode and the noninjected mode is  $\Delta\omega_y = \omega_{inj} - \omega_y$ . In the rate equation for the carrier density, Eqn. 6.3.3,  $\hat{N}$  is the carrier density,  $J$  is the injection current,  $V$  is the active region volume, and  $\tau_e$  is the carrier lifetime. The modal gains for the two polarization modes are given by:

$$G_x = v_g g_x (\hat{N} - N_{trx}) \left( 1 - \varepsilon_s |\hat{E}_x|^2 - \varepsilon_c |\hat{E}_y|^2 \right) \quad (6.3.4)$$

$$G_y = v_g g_y (\hat{N} - N_{try}) \left( 1 - \varepsilon_s |\hat{E}_y|^2 - \varepsilon_c |\hat{E}_x|^2 \right) \quad (6.3.5)$$

where  $v_g$  is the group velocity,  $N_{trx,y}$  are the carrier densities at transparency, and  $g_{x,y}$  are the differential gains for the  $x$ - and  $y$ - linearly polarized modes. The gain compression is taken into account through  $\varepsilon_s$  which represents the gain self saturation coefficient, and through  $\varepsilon_c$  which is the cross

saturation coefficient. In general, one also takes into account the red-shift of the cavity modes due to self-heating with the injection current. A solitary VCSEL, i.e., without optical injection or feedback, can undergo polarization switching with the injection current either through a region of polarization mode hopping or through a region of hysteresis [155]. In the two-mode model such a situation is modelled phenomenologically by allowing a change of the gain difference with injection current. By doing so, it is possible to study, e.g., the influence of optical injection on the steady-state polarization hysteresis curve and the critical slowing down of PS [146]. Here, we consider a VCSEL with a fixed injection current and study the bifurcation route with increasing the injection strength. Therefore, we do not need to explicitly define the parametric dependence of the LP mode frequencies, gains, and losses on the injection current.

We can simplify Eqs. (6.3.1)-(6.3.3) by reducing the number of free parameters. This is done by introducing proper nondimensional variables. To this end, we define the average threshold carrier density  $N_0 = (N_{trx} + N_{try})/2$  as well as its corresponding difference  $d = (N_{trx} - N_{try})/2$ . The photon average lifetime is also defined as  $\tau_0 = (\tau_{px} + \tau_{py})/2$ . The quantities  $N_0$ ,  $d$  and  $\tau_0$  are used to obtain, respectively, nondimensional time and carrier density variables  $T = t/\tau_0$  and  $N = \hat{N}/N_0$ . Furthermore, the slowly varying amplitudes of the electric field can also be nondimensionalized by considering  $E_{x,y} = \hat{E}_{x,y}\sqrt{\epsilon_s}$ . Using the newly defined nondimensional variables, the rate equations Eqs. (6.3.1)-(6.3.3), complemented by Eqs. (6.3.4)-(6.3.5), can be rewritten as follows:

$$\begin{aligned} \frac{dE_x}{dT} &= \frac{1}{2} (1 + i\alpha) \left[ \zeta_x (N - 1 - d) \left( 1 - |E_x|^2 - \varepsilon |E_y|^2 \right) - \gamma_x \right] E_x \\ &\quad + \kappa E_{inj} - i\delta_x E_x, \end{aligned} \quad (6.3.6)$$

$$\begin{aligned} \frac{dE_y}{dT} &= \frac{1}{2} (1 + i\alpha) \left[ \zeta_y (N - 1 + d) \left( 1 - \varepsilon |E_x|^2 - |E_y|^2 \right) - \gamma_y \right] E_y \\ &\quad - i\delta_y E_y, \end{aligned} \quad (6.3.7)$$

$$\begin{aligned} \frac{dN}{dT} &= R_i - sN - \eta_x (N - 1 - d) \left( 1 - |E_x|^2 - \varepsilon |E_y|^2 \right) |E_x|^2 \\ &\quad - \eta_y (N - 1 + d) \left( 1 - \varepsilon |E_x|^2 - |E_y|^2 \right) |E_y|^2, \end{aligned} \quad (6.3.8)$$

where  $\zeta_{x,y} = \Gamma_{x,y} v_g g_{x,y} N_0 \tau_0$ ;  $\varepsilon = \varepsilon_c / \varepsilon_s$ ;  $\gamma_{x,y} = \tau_0 / \tau_{px,y}$ ;  $R_i = J\tau_0 / (VN_0)$ ;  $s = \tau_0 / \tau_e$ ; and  $\eta_{x,y} = v_g g_{x,y} \tau_0 / \varepsilon_s$ . The nondimensionalized frequency detuning between the master laser and , respectively, the  $x$ - and the  $y$ -LP modes are  $\delta_x = \Delta\omega_x \tau_0$  and  $\delta_y = \Delta\omega_y \tau_0$ .

The external optical injection parameters are:  $\Delta\nu = \Delta\omega_x / 2\pi$ , the detuning between the injection frequency and that of the injected mode, and the injection strength  $\kappa_{inj}$ . It is worth noting that the detuning  $\Delta\omega_y$  does

**Table 6.3.1:** *Parameters used for the simulation of the injected VCSEL using the two-mode model*

SYMBOL	VALUE	MEANING OF THE SYMBOL
$\alpha$	3	<i>Linewidth enhancement factor</i>
$\Gamma_x$	0.05	<i>confinement factor of x-LP mode</i>
$\Gamma_y$	0.05	<i>confinement factor of y-LP mode</i>
$\tau_{px}$	0.0019 ns	<i>photon lifetime for the x-LP mode</i>
$\tau_{py}$	0.0019 ns	<i>photon lifetime for the y-LP mode</i>
$\tau_e$	1 ns	<i>carrier lifetime</i>
J	9.6 mA	<i>injection current</i>
$v_g$	$8.85 \times 10^9 \text{ cm.s}^{-1}$	<i>group velocity</i>
$g_x$	$4.22 \times 10^{-16} \text{ cm}^2$	<i>differential gain for x-LP mode</i>
$g_y$	$4.40 \times 10^{-16} \text{ cm}^2$	<i>differential gain for y-LP mode</i>
$\varepsilon_s$	$2 \times 10^{-18} \text{ cm}^3$	<i>self-gain saturation coefficient</i>
$\varepsilon_c$	$4 \times 10^{-18} \text{ cm}^3$	<i>cross-gain saturation coefficient</i>
$N_{trx,y}$	$2 \times 10^{18} \text{ cm}^{-3}$	<i>carrier density at transparency</i>
$E_{inj}$	1	<i>Optical injection amplitude</i>

not play a role in the injected laser dynamics since the phase equation for the non-injected ( $y$ -LP) mode field is decoupled from the other equations. The birefringence of the free-running VCSEL is:  $\nu_x - \nu_y = -10$  GHz. We use the normalized injection strength parameter which is defined as:

$$\kappa = \frac{\kappa_{inj}\tau_p}{\sqrt{\varepsilon_s}}. \quad (6.3.9)$$

We use both standard numerical integration methods as well as continuation techniques to analyze the dynamics of the injected VCSEL. Simulations are performed using the set of parameters presented in Table 6.3.1 which lead to:  $\zeta_x = 0.71$ ,  $\zeta_y = 0.74$ ,  $\eta_x = 3.53$ ,  $\eta_y = 3.68$ ,  $\varepsilon = 2$ ,  $d = 0$ ,  $s = 0.0019$ ,  $\gamma_x = \gamma_y = 1$  and  $R_i = 0.0076$ . With these parameters the free-running VCSEL emits a stationary  $y$ -LP mode only, thus eqs. (6.3.6)-(6.3.8) describe an orthogonal optical injection configuration.

### 6.3.2 Bifurcation study

A bifurcation analysis of eqs. (6.3.6)-(6.3.8) has been performed using continuation techniques. A mapping of relevant bifurcation curves is plotted in Fig. 6.3.1, in the detuning  $\Delta\nu$  vs. injection strength  $\kappa$  plane. Similarly to what has been obtained in the framework of the SFM model (see Fig. 6.2.7 in Section 6.2), Fig. 6.3.1 shows that the injection-locking zone is delimited

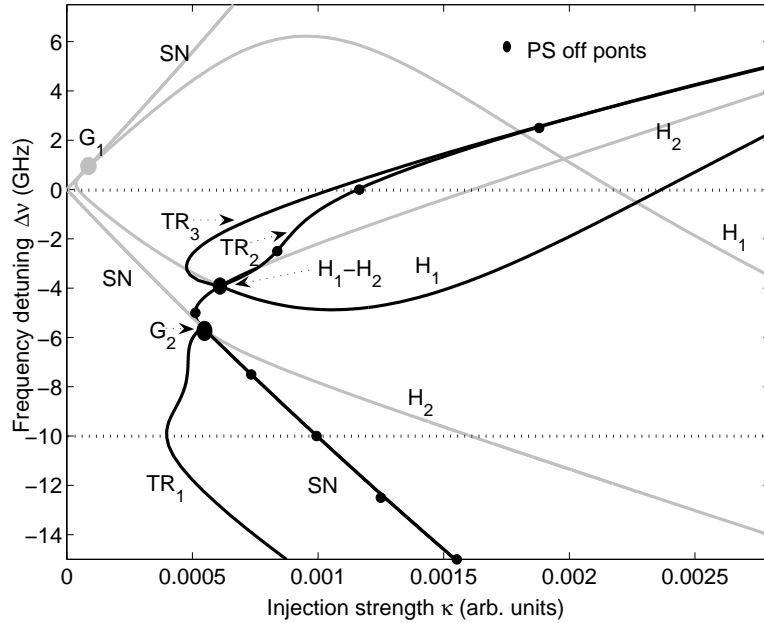


**Figure 6.3.1:** Bifurcation diagram of the two-mode model in the  $(\kappa, \Delta\nu)$  plane. Black (grey) denotes supercritical (subcritical) bifurcation. The dotted lines indicates the bifurcation scenarios analyzed in Fig. 6.3.2 and detailed in Fig. 6.3.3 and Fig. 6.3.4.

by the supercritical parts of a saddle-node (SN) and two Hopf ( $H_1$  and  $H_2$ ) bifurcation curves.  $H_2$  affects also the PS mechanism in such a way that the supercritical part of  $H_2$  coincides with PS points. Furthermore, on the route to PS that leads to injection-locking, we identify a torus bifurcation  $TR_1$ , similar to the one obtained within the framework of the SFM model (see the bifurcation curve  $TR$  in Section 6.2, Fig. 6.2.7). Indeed, by closely investigating nonlinear dynamics underlying  $TR_1$  as shown in Fig. 6.3.2(a) and 6.3.3, one notices that  $TR$  coincides with the onset a two-polarization mode time-periodic dynamics when the VCSELS is driven towards the injection-locking zone by increasing the injection strength for a fixed detuning value.

Besides  $SN$ ,  $H_1$ ,  $H_2$  and  $TR_1$  bifurcations, we highlight two new torus bifurcation curves, namely  $TR_2$  and  $TR_3$ , which complement our results in Section 6.2. In fact, using the two-mode model, as displayed in Fig. 6.3.1, we are now able to follow bifurcation curves which support a particular switching scenario that has been already suggested in the framework of the SFM model. It concerns a small detuning range located outside but close to the limit of the locking zone. We show in the following that within that relatively small detuning range, PS occurs as a result of the combined effects of both

$TR_2$  and  $TR_3$ . The underlying bifurcation mechanisms are analyzed in detail in Fig. 6.3.2(b) and 6.3.4. It is worthy noting that both  $TR_2$  and  $TR_3$  originate from the Hopf-Hopf codimension-two point, i.e., the intersection between  $H_1$  and  $H_2$  Hopf bifurcation curves (see the codimension-two point denoted by  $H_1-H_2$  in Fig. 6.3.1). As one evolves towards positive detunings from the  $H_1-H_2$ ,  $TR_2$  and  $TR_3$  are clearly two distinguishable bifurcation curves but, for sufficiently larger positive detunings, they merge in a single bifurcation curve. These results support our conclusions drawn in Section. 6.2 by showing that  $H_1-H_2$  is a key codimension-two point that drives nonlinear dynamics accompanying PS and locking mechanisms in VCSELS with orthogonal optical injection.

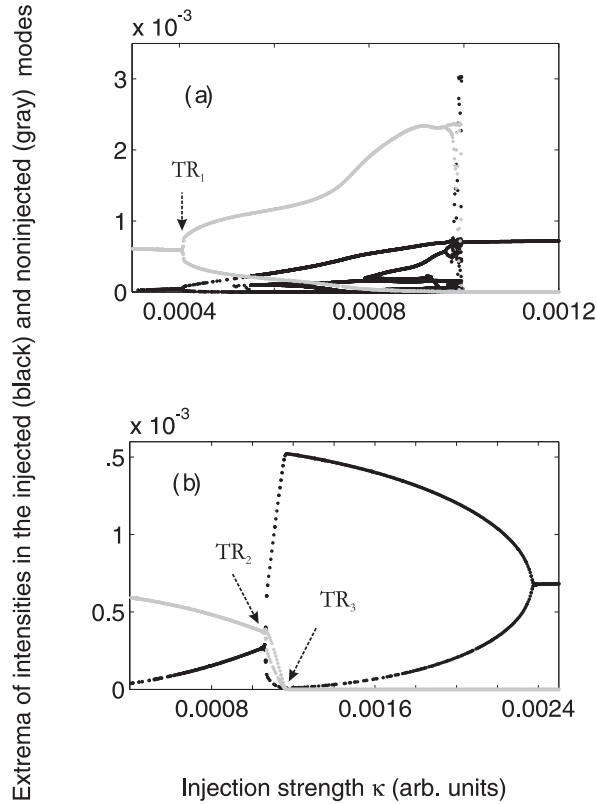


**Figure 6.3.2:** Bifurcation diagram showing the maxima and minima of the intensities of the injected mode (black) and the noninjected mode (gray) as a function of the injection strength,  $\kappa$ , when the detuning is fixed at: (a)  $\Delta\nu = -10$  GHz and, (b)  $\Delta\nu = 0$  GHz.

The scenario of polarization switching leading to injection locking and the underlying  $TR_1$  torus bifurcation mechanism are described in Fig. 6.3.2(a). We show the evolution of minima and maxima of intensities in both the in-

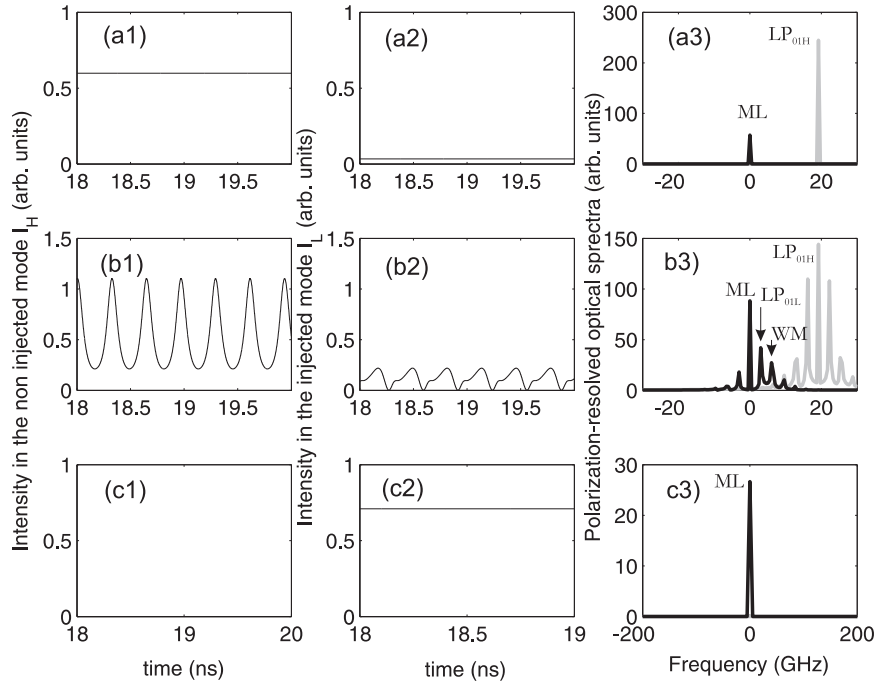


**Figure 6.3.3:** Polarization-resolved intensities time traces and optical spectra showing PS scenario involving limit cycle dynamics in the noninjected mode and wave mixing in the injected mode for a detuning of  $\Delta\nu = -10$  GHz, when increasing the injection strength  $\kappa$ : (a)  $\kappa = 0.00035$ , unlocked noninjected mode ( $I_H$ ); (b)  $\kappa = 0.00055$ , limit cycle in the noninjected mode injected ( $I_H$ ) and wave-mixing in the injected mode ( $I_L$ ); (c)  $\kappa = 0.0011$ , injection-locking after PS is achieved. In the spectra black (grey) corresponds to injected low-frequency mode (noninjected high-frequency mode).

jected (black) and noninjected (gray) VCSEL's modes, when increasing the injection strength,  $\kappa$ , for a detuning  $\Delta\nu = -10$  GHz. Polarization-resolved time-traces and optical spectra of qualitatively different dynamics are provided in Fig. 6.3.3 for selected injection strengths. In the weak injection regime, the VCSEL exhibits an unlocked steady-state regime predominantly in the noninjected polarization mode [see Figs. 6.3.3(a1)-(a3)]. As the injection strength is increased, the VCSEL undergoes a torus bifurcation (see the bifurcation curve denoted by  $TR_1$  in Fig. 6.3.1). In fact, the crossing of  $TR_1$  corresponds to excitation of time-periodic dynamics in both orthogonal polarization modes [see Figs. 6.3.3(b1)-(b3)]. The noninjected mode exhibits a limit cycle dynamics denoted by the presence of peaks which are symmetrically located on both sides of the noninjected main frequency peak [the latter is denoted by  $LP_{01H}$  in Fig. 6.3.3(b3)]. In the injected polarization

mode, a wave mixing dynamics between the ML and the noninjected mode ( $LP_{01L}$ ) is resolved. The main frequency resulting from the beating between ML and  $LP_{01L}$  is denoted by  $WM$  in Fig. 6.3.3(b3). By increasing the injection further, the VCSEL undergoes complex nonlinear dynamics. Then, for sufficiently larger injection strength, the noninjected mode is switched off and injection-locking is achieved [see Figs. 6.3.3(c1)-(c3)].

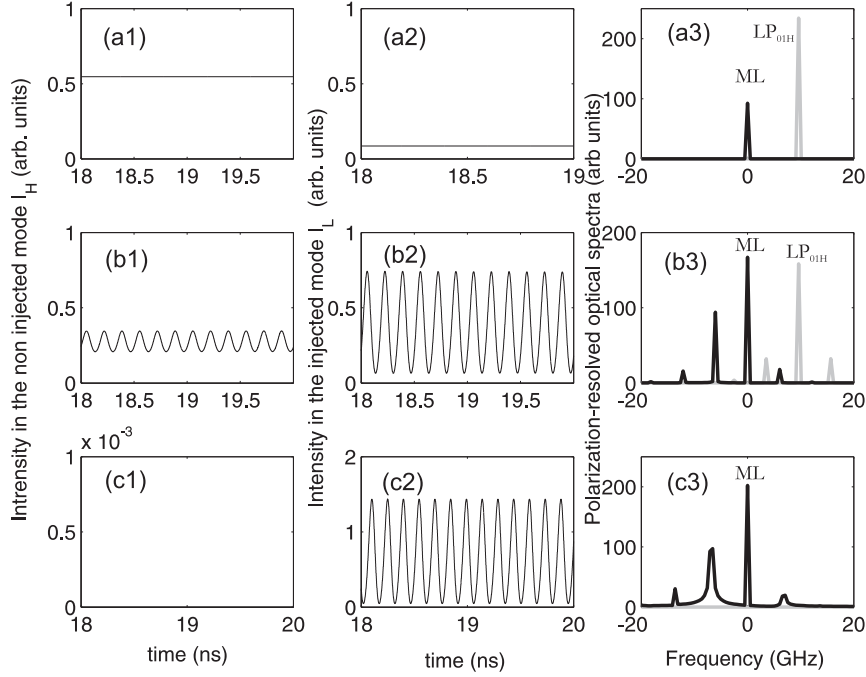


**Figure 6.3.4:** Polarization-resolved intensities time traces and optical spectra showing PS scenario involving a two-mode limit cycle dynamics for a detuning of  $\Delta\nu = 0$  GHz, when increasing the injection strength  $\kappa$ : (a)  $\kappa = 0.0006$ , unlocked noninjected mode ( $I_H$ ); (b)  $\kappa = 0.00108$ , limit cycle in both injected ( $I_L$ ) and noninjected ( $I_H$ ) modes; (c)  $\kappa = 0.0015$ , limit cycle in the injected mode ( $I_L$ ) after PS is achieved. In the spectra black (grey) corresponds to injected low-frequency mode (noninjected high-frequency mode).

We now focus on the polarization switching scenario involving both  $TR_2$  and  $TR_3$  bifurcation mechanisms. We plot, in Fig. 6.3.2(b), the evolution of minima and maxima of the intensities in both injected (black) and noninjected (gray) VCSEL's modes, when increasing the injection strength for a representative detuning of  $\Delta\nu = 0$  GHz. The underlying nonlinear dynamics are described in detail in Fig. 6.3.4 where samples of relevant polarization-resolved dynamics are depicted for selected injection strengths. For a relatively small injection strength [see Fig. 6.3.4(a1)-(a3) for  $\kappa = 0.0006$ ], the



emission is dominated by an unlocked noninjected mode with a weak emission at the master laser frequency. As the injection is increased, the intensity in the noninjected polarization mode decreases at the expense of the emission at the ML frequency. Interestingly, by further increasing  $\kappa$ , we show that the crossing of  $TR_2$  coincides with the onset of time-periodic limit-cycle dynamics in both injected and noninjected orthogonal polarization modes, as depicted in Figs. 6.3.4(b1)-(b3) for  $\kappa = 0.00108$ . The noninjected mode is still unlocked but now exhibits a time-periodic regime. The corresponding optical spectra in Fig. 6.3.4(b3) show two small peaks which are symmetrically located on both sides of the noninjected frequency, with an offset close to the relaxation oscillation frequency. On the other hand, the injected mode also exhibits a limit cycle dynamics denoted by the onset of peaks which appear on both sides of the ML frequency with an offset, from ML, equal to the relaxation oscillation frequency and its harmonics. As aforementioned, the asymmetry in the intensity of the side peaks is due to non-zero linewidth enhancement factor or  $\alpha$ -factor. If we further increase the intensity, the two-polarization mode limit-cycle dynamics is destabilized when the injected VCSEL undergoes a torus bifurcation, i.e., when crossing  $TR_3$ . Specifically, after the crossing of  $TR_3$ , the noninjected mode switches off, i.e., PS is achieved. This leads to a limit-cycle dynamics in only the injected polarization mode, as shown in Figs. 6.3.4(c1)-(c3). It is worth noting that for much larger injection strengths, the injection-locking regime is reached (see Fig. 6.3.1 and Fig. 6.3.2(b)).

## 6.4 Discussions and conclusions

Bifurcation studies undertaken for a VCSEL with orthogonal optical injection, using either the SFM model or the two-mode model, unveil interesting bifurcation mechanisms which are found to be generic of two-polarization mode VCSEL systems and qualitatively support the experiments in Chap. 5.

- In the detuning vs. injection strength bifurcation map, we have identified the role played by a second, new Hopf bifurcation (named  $H_2$  in Fig. 6.2.7 and Fig. 6.3.1 in order to distinguish it from the well-known Hopf bifurcation typical for injected EEL that bounds the locking region) on the injection-locked solution. We have shown that  $H_2$  delimits the stable locking zone below the codimension-two saddle-node-Hopf point  $G_1$ . This result clearly contrasts with what has been reported for injected EELs in which the injection-locking is limited by  $G_1$  where the saddle-node (SN) and the first Hopf ( $H_1$ ) bifurcation curves become tangent [152]. Furthermore, we show that the supercritical part of  $H_2$  coincides with PS and that  $H_2$  determines the smallest injection strength needed to achieve PS, i.e., the minimum in the PS boundary.

- Using both the SFM and the two-mode model, we have identified a torus bifurcation [named  $TR$  in Fig. 6.2.7(a) and  $TR_1$  in Fig. 6.3.1] which explains nonlinear dynamics arising on the route to polarization switching leading to injection-locking, and which supports qualitatively the experimental results presented in Section 5.4. The typical bifurcation scenarios related to  $TR$  (see Fig. 6.2.5 for the SFM model) and  $TR_1$  (see Fig. 6.3.1 for the two-mode model) show that, by increasing the injection strength for a fixed detuning, the crossing of the torus bifurcation leads to the onset of combined relaxation oscillation limit cycle dynamics in the noninjected mode and wave mixing dynamics in the injected mode, before PS leading to injection locking is achieved.
- There is an interesting bifurcation mechanism which occurs outside but close to the limit of the locking region. It concerns a small detuning range over which, as one increases the injection strength for a fixed detuning, PS is achieved from a two-mode limit cycle dynamics, i.e., in both noninjected and injected polarization modes, to a single limit cycle dynamics in the injected polarization mode. The experimental evidence of such a switching scenario is described in Section 5.4, Fig. 5.4.3. We interestingly show that the observed nonlinear dynamics are supported by both the SFM model (see Fig. 6.2.3) and the two-mode model (see Fig. 6.3.4). The results based on the SFM model provide interesting information about possible interplay between the PS mechanism with other complex nonlinear dynamics, such as period-doubling bifurcations as it is suggested by the experiments in Section 5.4. On the other hand, the two-mode model has the merit of allowing the continuation of two additional torus bifurcations, namely  $TR_2$  and  $TR_3$ , whose combined effects explain the bifurcation mechanism underlying PS between two limit cycle regimes. Moreover,  $TR_2$  and  $TR_3$  highlight the key role played by  $H_2$  as well as the  $H_1$ - $H_2$  codimension-two point in the switching and injection-locking dynamics.
- Besides the fact that the results from both the SFM and the two-mode model qualitatively support the experimental mapping of PS, injection-locking, and the underlying nonlinear dynamics mechanisms, one observes some differences. For instance, by comparing the bifurcation mapping in Fig. 6.2.7(a) and Fig. 6.3.1, we show that in the framework of the two-mode model, the torus bifurcation  $TR_1$  terminates on the codimension-two point  $G_2$  where  $H_2$  is tangent to  $SN$ . In the SFM model, however, the torus bifurcation  $TR$  (which plays a similar role as  $TR_1$  in the framework of the two-mode model) terminates on  $H_2$  after crossing the injection locking region.

Though, a complete comparison of bifurcation mechanisms from the two models is beyond the scope our thesis, we conjecture that the

observed discrepancies and its possible impact on the PS mechanism may result from the presence of additional complex bifurcations which are supported by the SFM model. The study of such bifurcations would necessitate further bifurcation analysis, including global bifurcations like homoclinic bifurcations. In the case of optically injected EELs, for example, a detailed bifurcation study has demonstrated that global bifurcations are very useful to explain multipulse excitability [140, 151].

In the framework of the SFM model, by scanning the injection strength for particular detuning values, we obtain polarization switching scenarios and corresponding bifurcations involving a period-doubling route to chaos, in qualitative agreement with our experimental measurements described in Chapter 5. For example, we report on a period doubling route to chaos that accompanies an abrupt PS with injection locking. Both theory and experiments show that the presence of a period doubling may lead to a dramatic change in the switching curve. Typically, this effect manifests as a snakelike shape in the switching curve, displaying two local minima of the power needed to achieve PS. We furthermore theoretically show that the  $\alpha$ -factor may strongly modify the overall bifurcation and polarization switching picture, while still preserving our general conclusions on the role played by  $H_2$  bifurcation boundary and the snakelike shape PS boundary.

Our study therefore reports on new bifurcation mechanisms resulting from the two mode polarization dynamics of VCSELs and reveals how the polarization switching properties of VCSELs are influenced by these emerging nonlinear dynamics. Such a complex interplay between bistable polarization switching properties and possibly complex two mode polarization chaotic dynamics is thought to be of great interest for recently suggested applications making use of polarization chaos for chaos secure communications [156]. Our results are also thought to contribute to the more general problem of bifurcation study of multimode lasers with optical injection, which remained largely unexplored.



## Chapter 7

# Transverse mode switching and locking in VCSEL subject to orthogonal optical injection

We theoretically and experimentally explore the transverse mode switching and locking mechanisms in a VCSEL subject to orthogonal optical injection. The operating conditions, i.e., the bias current and temperature, are such that the free-running VCSEL emits in the fundamental mode regime. The present study extends our experiments in Chapter 5 where we report in Figs. 5.2.1 and 5.2.3 on a switching mechanism which involves the injection-locking of the first-order transverse mode to the master laser frequency. Using a model which accounts for polarized multi-transverse mode operation, we theoretically analyze the issue of optical injection-induced competition between the fundamental and the first-order transverse modes. The experimental results in Chapter 5 are revisited by extending the detuning range to larger positive detunings (180 GHz) in order to fully investigate the transverse mode behavior. Our theoretical and experimental results reveal that the injection power necessary to induced polarization switching (PS) is minimum at two different frequency detuning values. The first minimum corresponds to the frequency splitting between the two fundamental, linearly polarized, transverse modes. The second one is observed at larger positive detuning, close to the frequency splitting between the fundamental and the first-order transverse modes of the free-running VCSEL. We particularly show that the position of the second minimum is determined by the relative losses between the fundamental and first-order transverse modes. We also identify an injection-parameter region where the first-order transverse mode is locked to the ML, a result that corroborates our experimental observations.

This chapter is based on the following publication:

- A. Valle, I. Gatare, K. Panajotov, and M. Sciamanna “*Transverse mode switching and locking in vertical-cavity surface-emitting lasers subject to orthogonal optical injection,*” *IEEE J. Quantum Electron.* **43**, 322 (2007).

## 7.1 Introduction

As already mentioned (see Chapter 3), injection-locking techniques have been extensively used to improve semiconductor laser characteristics such as spectral narrowing, chirp reduction [111], or single mode operation [110]. Furthermore, several studies based on different types of laser have demonstrated that optical injection can dramatically affect the lasing mode structure and dynamics [157, 158, 159]. For example, by using optical injection in a Fabry-Perot edge-emitting laser (EEL), one can generate an optical pulse train with high frequency repetition rate through mode locking of longitudinal modes [157]. Under intermodal injection, for which the injection frequency is set close to the frequency of the longitudinal nonlasing side mode of a single-mode EEL, an injection-induced switching from the free-running lasing mode to the nonlasing side mode has been reported [158, 159, 160]. In multimode broad-area lasers, a coherent high-power emission with a narrow linewidth can be achieved using a CW optical injection to achieve injection locking to a single-longitudinal and transverse mode [161].

Although VCSELs are intrinsically single longitudinal mode devices, they may exhibit a multi-transverse mode emission in their free-running operation, depending on their structure and operating conditions such as the bias current and temperature. For instance, it has been experimentally [29, 36] and theoretically [32] demonstrated that at high injection currents, higher-order transverse modes may be excited due to spatial hole burning. Similarly to what has been observed for optically injected EEL, previous reports show that optical injection can affect the VCSEL transverse mode dynamics [120, 122, 124]. Experimental observations by Hong *et al.* showed that optical injection can be used to achieve single-mode operation in a VCSEL which originally operates in a multi-transverse mode regime [124]. In fact, Hong *et al.* [124] observed that this is the case when the master laser frequency is set close and parallelly injected to one of the two orthogonally-polarized transverse modes. On the other hand, the same authors reported also that, when still using a parallel injection scheme but with a VCSEL that exhibits two parallel linearly-polarized transverse modes, no injection-induced single-mode operation could be achieved [124]. By contrast to EEL, such observations highlight the key role played by the polarization on the dynamics of a multimode VCSEL subject to optical injection. Transverse mode competition was also reported when a VCSEL, biased such that high-order transverse

modes are excited, is subject to parallel optical injection. It was observed that when the master laser frequency coincides with that of one particular transverse mode, this mode is enhanced at the expense of other transverse modes, which then are partially or even totally suppressed [122]. In the present study, we analyze transverse mode locking and switching dynamics in a VCSEL subject to orthogonal optical injection. It is worth noting that we consider a VCSEL which is biased well below the first-order transverse mode threshold such that, in the free-running operation, only fundamental transverse modes are excited.

In chapter 5, we have experimentally demonstrated that due to orthogonal optical injection, injection-locking of the first-order transverse mode accompanied by a strong suppression of the fundamental mode is possible, even if the free-running VCSEL is biased far below the first-order transverse mode threshold. Here we extend this experimental investigation over larger detunings. The newly obtained results are analyzed and complemented by a theoretical investigation, using a model which accounts for different modal profiles for both the fundamental and first-order transverse modes [163]. This chapter is organized as follows. In Section 7.2, we first present a model which take into account the transverse mode behavior. We then present our numerical results while experimental results are discussed in Section 7.3. A comparison between numerical and theoretical results is provided in Section 7.4. Finally conclusions are presented in Section 7.5.

## 7.2 Theoretical study of optical injection-induced transverse mode competition

In this section, we theoretically investigate the polarization and transverse mode behavior of a VCSEL under orthogonal optical injection as a function of the injection strength and the detuning between the injection frequency and the free-running frequency of the solitary laser. To this end we use a model that accounts for both the fundamental and first-order transverse modes in the orthogonal VCSEL's polarization directions. We use standard integration methods to analyze optical injection-induced competition between the fundamental and first-order transverse modes.

### 7.2.1 The Model

We consider a model that takes into account two of the mechanisms which determine the polarization of VCSEL [162, 163]. The first one is associated with the combined effect of the VCSEL's linear phase and amplitude anisotropies, the linewidth enhancement factor and the spin-flip relaxation

processes which are encountered within the framework of the SFM model [48]. The second mechanism is related to the effect of having different electrical field profiles for each linear polarization due to the birefringence of the device [47]. We consider cylindrically symmetric weakly index-guided devices with the structure illustrated in the inset of Fig. 7.2.1(a). The radius of the core region and the length of the cavity are denoted as  $a$  and  $L$ , respectively. Subscripts  $x$  and  $y$  are used to denote the polarization direction. Birefringence is taken into account by assuming that the core refractive index in the  $x$  direction,  $n_{core,x}$ , is larger than in the  $y$  direction,  $n_{core,y}$ , hence, the  $x$  polarized mode emission frequency is lower than that of the  $y$  polarized mode, while the cladding refractive index,  $n_{cladd}$ , is the same in both directions. We will consider a small value of the index step (0.011) in such a way that the appropriate transverse modes of the structure are the  $LP_{mn}$  modes. That index step is greater than the contribution due to the carrier-induced refractive index [164] and then the evolution obtained with our model, based on a modal expansion, coincides with the one obtained with a full spatiotemporal model [164]. Here we treat the case of VCSELs that can operate in the fundamental ( $LP_{01}$ ) and in the first-order ( $LP_{11}$ ) transverse modes. Subscripts 0, 1 are used to denote the  $LP_{01}$  and  $LP_{11}$  modes, respectively. In the basis of the linearly polarized modes and considering radial symmetry of the cavity the optical field can be written as [162, 163]:

$$\begin{aligned} \vec{E}(r, t) = & [(E_{0x}(t) \psi_{0x}(r) + E_{1x}(t) \psi_{1x}(r)) \vec{x}] e^{ik\alpha t} \\ & + [(E_{0y}(t) \psi_{0y}(r) + E_{1y}(t) \psi_{1y}(r)) \vec{y}] e^{ik\alpha t} + c.c. \end{aligned} \quad (7.2.1)$$

Where  $\psi_{0j}$  and  $\psi_{1j}$  are, respectively, the modal profiles of the  $LP_{01}$  and  $LP_{11}$  modes and are obtained by solving the Helmholtz equation [162].  $E_{0j}$  and  $E_{1j}$  are the modal amplitudes of these modes; the subindex  $j$  stands for the linear polarization state of the given mode;  $k$  is the electric field decay rate that includes the internal and facet losses [165]; and  $\alpha$  is the alpha factor or linewidth enhancement factor which represents phase-amplitude coupling mechanisms in semiconductor lasers [165]. The rate equations describing the polarization and transverse mode behavior of the VCSEL with an injected optical field, written appropriately in the cylindrical basis, read [163]:

$$\begin{aligned} \frac{dE_{0x}}{dt} = & k(1 + i\alpha)(E_{0x}(g_{0x} - 1) + iE_{0y}g_{0xy}) \\ & - (\gamma_a + i\gamma_{p0})E_{0x} + \frac{k_{0x}}{\tau_{in}}e^{i\Delta\omega t} \\ & + \sqrt{\frac{\beta}{2}} \left( \sqrt{N + \bar{n}}\xi_{0+}(t) + \sqrt{N - \bar{n}}\xi_{0-}(t) \right), \end{aligned} \quad (7.2.2)$$

$$\begin{aligned} \frac{dE_{0y}}{dt} = & k(1 + i\alpha)(E_{0y}(g_{0y} - 1) - iE_{0x}g_{0yx}) \\ & + (\gamma_a + i\gamma_{p0})E_{0y} + \frac{k_{0y}}{\tau_{in}}e^{i\Delta\omega t} \\ & - i\sqrt{\frac{\beta}{2}} \left( \sqrt{N + \bar{n}}\xi_{0+}(t) - \sqrt{N - \bar{n}}\xi_{0-}(t) \right), \end{aligned} \quad (7.2.3)$$



$$\begin{aligned} \frac{dE_{1x}}{dt} = & k(1+i\alpha)(E_{1x}(g_{1x}-\kappa_r)+iE_{1y}g_{1xy}) \\ & + i\gamma_p^{tr}E_{1x} - (\gamma_a+i\gamma_{p1})E_{1x} + \frac{k_{1x}}{\tau_{in}}e^{i\Delta\omega t} \\ & + \sqrt{\frac{\beta}{2}}\left(\sqrt{N+\bar{n}}\xi_{1+}(t)+\sqrt{N-\bar{n}}\xi_{1-}(t)\right), \end{aligned} \quad (7.2.4)$$

$$\begin{aligned} \frac{dE_{1y}}{dt} = & k(1+i\alpha)(E_{1y}(g_{1y}-\kappa_r)-iE_{1x}g_{1yx}) \\ & + i\gamma_p^{tr}E_{1y} + (\gamma_a+i\gamma_{p1})E_{1y} + \frac{k_{1y}}{\tau_{in}}e^{i\Delta\omega t} \\ & - i\sqrt{\frac{\beta}{2}}\left(\sqrt{N+\bar{n}}\xi_{1+}(t)-\sqrt{N-\bar{n}}\xi_{1-}(t)\right), \end{aligned} \quad (7.2.5)$$

for the polarization-resolved optical fields,

$$\begin{aligned} \frac{\partial N(r,t)}{\partial t} = & I(r) + D\nabla_{\perp}^2 N \\ & - \gamma_e \times \left[ N \left( 1 + \sum_{i=0,1} \sum_{j=x,y} |E_{ij}|^2 \psi_{ij}^2(r) \right) \right] \\ & + \gamma_e \times \left[ in \sum_{i=0,1} \left( E_{ix}E_{iy}^* - E_{iy}E_{ix}^* \right) \psi_{ix}(r) \psi_{iy}(r) \right], \end{aligned} \quad (7.2.6)$$

$$\begin{aligned} \frac{\partial n(r,t)}{\partial t} = & -\gamma_s n + D\nabla_{\perp}^2 n \\ & - \gamma_e \times \left[ n \sum_{i=0,1} \sum_{j=x,y} |E_{ij}|^2 \psi_{ij}^2(r) \right] \\ & + \gamma_e \times \left[ iN \sum_{i=0,1} \left( E_{ix}E_{iy}^* - E_{iy}E_{ix}^* \right) \psi_{ix}(r) \psi_{iy}(r) \right] \end{aligned} \quad (7.2.7)$$

for the carrier densities,

where  $N(r,t)$  is the total carrier number and  $n(r,t)$  is the difference in the carrier numbers of the two magnetic sublevels.  $\kappa_r$  is the relative loss of the mode  $LP_{11}$  with respect to the  $LP_{01}$  mode. That parameter determines the value of the injection current at which the  $LP_{11}$  mode begins lasing.  $I(r)$  represents a uniform current injection over a circular disk of  $3\text{-}\mu\text{m}$  radius,  $I(r) = I$ , i.e.,  $I(r) = I$  if  $r < 3\mu\text{m}$ , and  $I(r) = 0$ , elsewhere. The normal gain normalized to the threshold gain,  $g_{ij}$  ( $i = 0, 1, j = x, y$ ), is defined as

$$g_{ij} = \frac{\int_0^{\infty} N(r,t) \psi_{ij}^2(r) r dr}{\int_0^{\infty} \psi_{ij}^2(r) r dr} \quad (7.2.8)$$

and  $g_{i,jk}$  ( $i = 0, 1; jk = xy, yx$ ) is given by

$$g_{i,jk} = \frac{\int_0^{\infty} n(r,t) \psi_{ij}(r) \psi_{ik}(r) r dr}{\int_0^{\infty} \psi_{ij}^2(r) r dr} \quad (7.2.9)$$

Note that the modal gains for the  $x$  and  $y$  polarizations are different due to the different optical mode profiles. However, we neglect the material gain

**Table 7.2.1:** Parameters used for the simulation of the VCSEL

SYMBOL	VALUE	MEANING OF THE SYMBOL
a	3 $\mu\text{m}$	Radius of the core region
L	1 $\mu\text{m}$	Length of the cavity
$n_{core,x}$	3.50002084	Refractive index of the core in the x-direction
$n_{core,y}$	3.5	Refractive index of the core in the y-direction
$n_{cladd}$	3.489	Refractive index of the cladding region
$k$	300 $\text{ns}^{-1}$	Field decay rate
$\alpha$	3	Linewidth enhancement factor
$\gamma_e$	0.55 $\text{ns}^{-1}$	Decay rate of the total carrier population
$\gamma_s$	91	Spin-flip relaxation rate
$D$	10 $\text{cm}^2\text{s}^{-1}$	Diffusion coefficient
$\beta$	$10^{-1}\text{s}^{-1}$	Spontaneous emission coefficient
$\gamma_a$	-0.81 $\text{ns}^{-1}$	Dichroism
$\eta_{inj}$	1	Coupling efficiency
$R$	0.995	Output-mirror reflectivity

difference since the frequency splitting is very small compared to the width of the gain curve.  $\gamma_a$  represents the linear amplitude anisotropy (anisotropic gain/losses also named dichroism) between the LP orthogonal modes. The injection terms are characterized by the injection strengths,  $k_{ij}$ , the VCSEL round-trip time,  $\tau_{in} = 2L/v_g$ , where  $v_g$  is the group velocity, and the detuning  $\Delta\omega = \omega_{inj} - \omega_{int}$ , where  $\omega_{inj}$  is the frequency of the ML and  $\omega_{int} = (\omega_{0x} + \omega_{0y})/2$ , is the central frequency between the two polarizations of the fundamental mode. The injection strength  $\kappa_{ij}$  is given by

$$k_{ij} = \left( \frac{1}{\sqrt{R}} - \sqrt{R} \right) \sqrt{\eta_{inj}} \sqrt{P_{inj,ij}} \quad (7.2.10)$$

where  $R$  is the output-mirror reflectivity,  $\eta_{inj}$  is the coupling efficiency of the injected light to the optical field in the laser cavity, and  $P_{inj,ij}$  is the power injected in the  $j$ -polarization of the  $i$ -transverse mode [165]. The rest of the parameters that appear in the equations are specified in the Table 7.2.1. The frequency splitting between the orthogonal polarizations of the  $LP_{01}$  mode,  $2\gamma_{p0}/(2\pi)$ , between the orthogonal polarizations of the  $LP_{11}$  mode,  $2\gamma_{p1}/(2\pi)$ , and between the two transverse modes with the same polarization,  $2\gamma_{p1}^{tr}/(2\pi)$ , are obtained from the calculation of the waveguide modes via the Helmholtz equation. We have chosen the values of  $n_{core,x}$ ,  $n_{core,y}$ , and  $n_{cladd}$  in such way that  $2\gamma_{p0}/(2\pi) = 2$  GHz and  $2\gamma_{p1}/(2\pi) = 193$  GHz, that correspond to the experimental values found for the solitary VCSEL of Section 7.3. Spontaneous emission noise processes are modelled by the terms  $\xi_{\pm}$  taken as complex Gaussian white noise sources of zero mean and delta-correlated in time. In the noise terms, the carrier distribution is integrated

over the active region

$$\bar{N} = \frac{\int_0^a N(r, t) r dr}{a^2} \quad (7.2.11)$$

$$\bar{n} = \frac{\int_0^a n(r, t) r dr}{a^2} \quad (7.2.12)$$

Theoretical results presented in the following have been obtained by numerically integrating eqs. (7.2.2)-(7.2.7). We have used, respectively, time and space integration steps of 0.01 ps and 0.12  $\mu\text{m}$ . The following boundary conditions for the carrier distribution have been considered:  $N(\infty, t) = 0$ ,  $n(\infty, t) = 0$ . In our simulations, the initial conditions correspond to the below threshold stationary solution, i.e, to  $I = 0.1I_{th}$ , where  $I_{th}$  is the threshold current.

### 7.2.2 Theoretical results

We first present some results corresponding to the solitary VCSEL operation. The transverse and polarization mode-resolved light-current characteristics of the solitary VCSEL are shown in Fig. 7.2.1(a). The VCSEL begins to emit in the fundamental mode with the smallest frequency,  $LP_{01,x}$ . A type II PS, i.e., from the lower to the higher frequency, within the fundamental mode, is obtained at around 2.5 times the threshold current. The VCSEL then emits in the  $LP_{01,y}$  mode until the higher order mode with orthogonal polarization appears at around  $4.7I_{th}$ . The value of the relative losses of the  $LP_{11}$  with respect to the  $LP_{01}$  mode has been chosen ( $\kappa_r = 1.2$ ) in such a way that the mode  $LP_{11}$  appears near the experimental value found for the solitary VCSEL (see Section 7.3). In Fig. 7.2.1(b), we also show the light-current characteristics obtained when decreasing the current in the same way. The VCSEL switches back to the  $x$  direction at  $1.83I_{th}$ , hence demonstrating a hysteresis zone.

We now consider the effect of the orthogonal optical injection on the transverse mode and polarization behavior of the VCSEL. We first set the current at a value,  $I = 1.7I_{th}$ , slightly smaller than the lowest current of the hysteresis region of the solitary VCSEL. Orthogonal optical injection is then modelled by choosing  $k_{ix} = 0$  and  $k_{iy} > 0$  since at that value of the current the VCSEL emits in the  $x$  polarization of the  $LP_{01}$  mode. We show in Fig. 7.2.2 the boundaries of PS in the plane of injection parameters (the detuning and the injected power). The injected power has been normalized to the output power of the solitary VCSEL and has been taken in logarithmic scale. For each value of the frequency detuning we have performed a sweeping along the horizontal axis, that is, increasing and then decreasing the injected

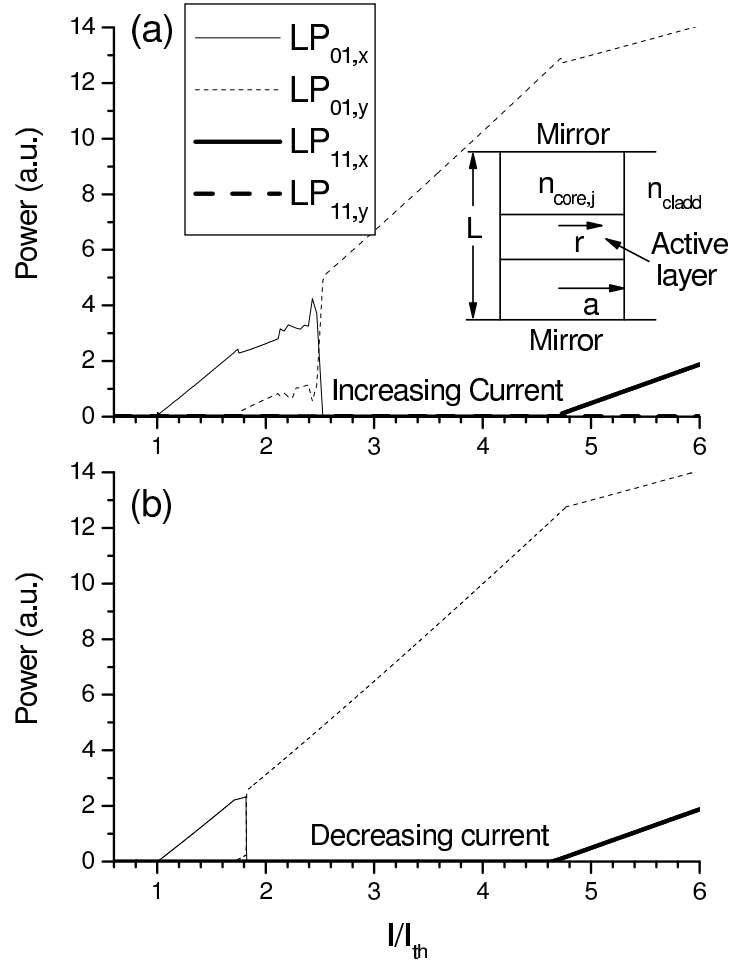


**Figure 7.2.1:** (a) Light-current characteristics of a multimode VCSEL without optical injection. This figure is obtained by fixing  $k_{ij} = 0$ ,  $\kappa_r = 1.2$ , and by increasing linearly the value of the current  $I$  from  $0.1I_{th}$  to  $6I_{th}$  during  $10\mu s$ . (b)  $L$ - $I$  characteristics when decreasing the current from  $6I_{th}$  to  $0.1I_{th}$  during  $10\mu s$ . The inset of Fig. 7.2.1(a) shows an schematic diagram of the VCSEL.

power. That sweeping is performed in the following way: we first let the solitary VCSEL to reach the steady state and then we change the injected power step by step. We consider 100 steps between the minimum and the maximum value of the injected power. We calculate the average of each polarized transverse mode over the last nanosecond of each step (of 2-ns duration). We consider that a polarization switch-off (switch-on) is obtained when the averaged total  $y$ -polarized power becomes larger (smaller) than the averaged total  $x$ -polarized power. The polarization switch-off (switch-on) points for increasing (decreasing) the power of the injected light are represented by solid (dotted) lines in Fig. 7.2.2, respectively.

In Fig. 7.2.2(a), the results for the case of  $I = 1.7I_{th}$  and  $\kappa_r = 1.2$  show that there are two minima in the injected power required for switching. Those minima appear at around 0 and 155 GHz for both the cases of increasing and decreasing the injection power. The detuning at which the second minimum appears is near the frequency difference between the  $LP_{01}$  and  $LP_{11}$  transverse modes of the solitary VCSEL. The injection power for the PS-on is smaller than the one required for the PS-off and then a region of bistable operation of the device is obtained. Bistable operation is obtained over wider ranges of injection powers when the detuning is near the 0 GHz minimum.

The effect of the transverse mode dichroism on the mapping of PS is analyzed in Fig. 7.2.2(b). In that figure, we compare the results obtained with the previously described VCSEL ( $\kappa_r = 1.2$ ) with another VCSEL in which the higher order modes are much more suppressed  $\kappa_r = 1.4$ ; in fact, the first higher order mode appears at  $I = 17.5I_{th}$  when  $\kappa_r = 1.4$ . The injected power required for PS keeps on having two minima. The PS boundaries do not change in a significant way if the detuning is smaller than 35 GHz. For higher values of the detuning, there are several changes: the minimum injected power required for switching increases and the detuning at which this minimum appears decreases to 127 GHz. The effect of the injection current is also analyzed in Fig. 7.2.2(c). In that figure, we have decreased the injection current applied to the VCSEL of Fig. 7.2.2(a) to a value that is clearly below the hysteresis region,  $I = 1.4I_{th}$ . No appreciable effects are observed for the switch-off curve when changing the injection current. However, the switch-on curve changes in such a way that the width of the hysteresis region decreases when decreasing the injection current.

The interpretation of some of the previous results can be obtained with the help of Figs. 7.2.3-7.2.5. In Fig. 7.2.3, the averaged power of the different transverse modes is plotted as a function of the injected power for three representative values of the frequency detuning: 13, 62, and 113 GHz. The upper (lower) part of the figure corresponds to  $x$ -( $y$ -) polarized power. Those averaged powers are normalized to the power of the solitary VCSEL. The

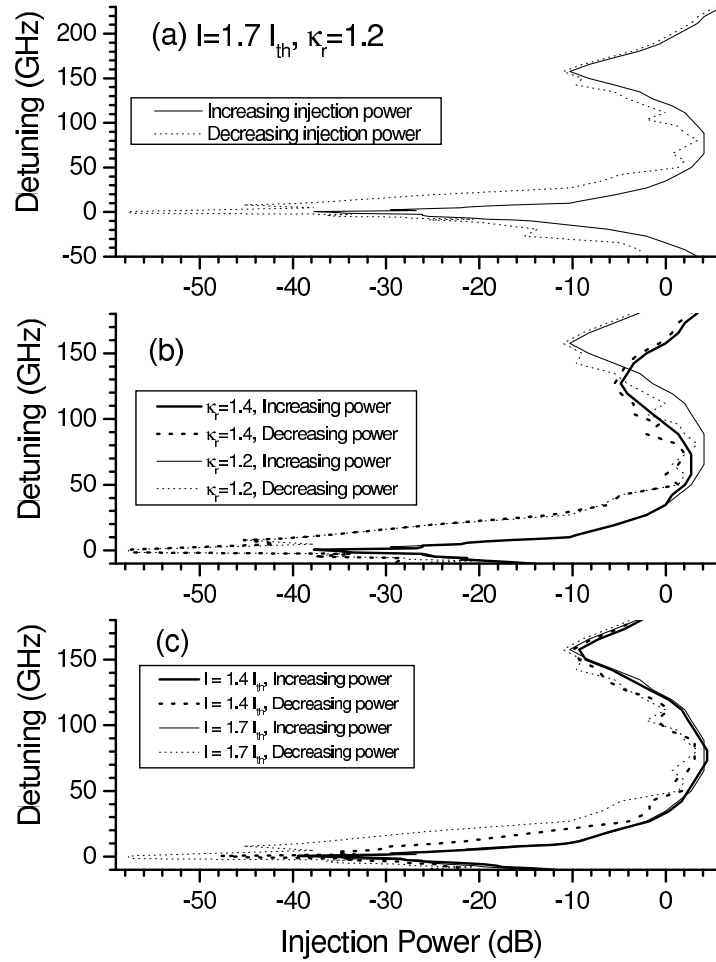


**Figure 7.2.2:** Injection power required for PS in a VCSEL subject to orthogonal optical injection. Switching from  $x$  to  $y$  ( $y$  to  $x$ ) polarization when increasing (decreasing) the injection power is shown with solid (dotted) lines. (a) Corresponds to  $I = 1.7I_{th}$  and  $\kappa_r = 1.2$ . (b) Results for  $I = 1.7I_{th}$  and  $\kappa_r = 1.4$ . (c) Results for  $I = 1.4I_{th}$  and  $\kappa_r = 1.2$ .

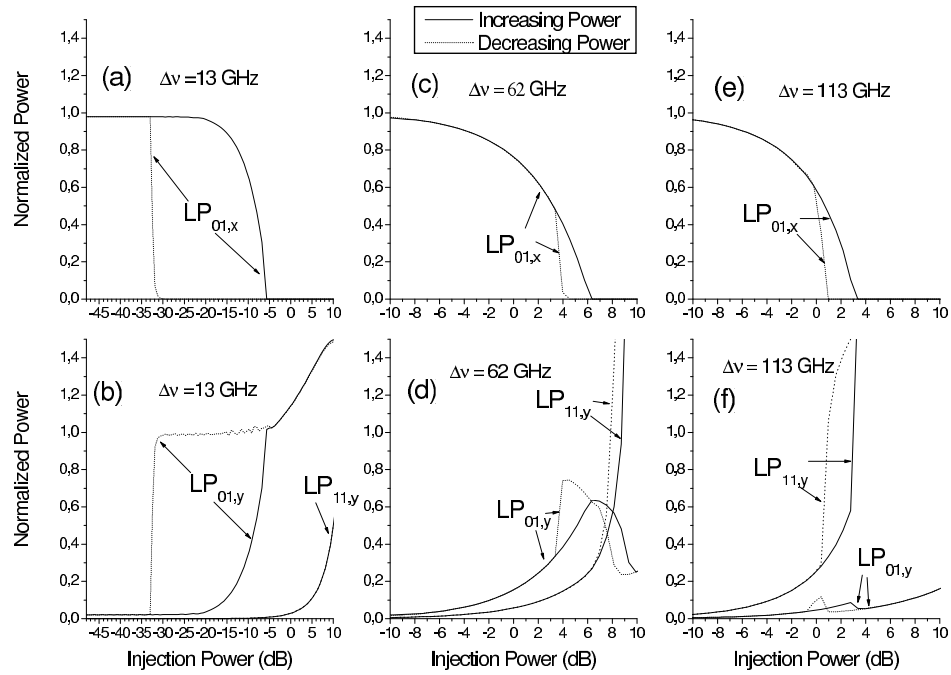


**Figure 7.2.3:** Averaged powers of the polarized transverse modes as a function of the injection power. The upper (lower) part of the figure corresponds to  $x$ - ( $y$ -) polarized light. First, second, and third columns correspond to 13, 62, and 113 GHz frequency detunings, respectively. Results obtained when increasing (decreasing) the injection power are plotted with solid (dotted) lines.

results corresponding to a frequency detuning of 13 GHz, slightly larger than the one of the first minimum, are shown in Fig. 7.2.3(a) and 7.2.3(b). The solitary VCSEL is mainly emitting in the  $LP_{01,x}$  mode. We first analyze the behavior obtained when increasing the injection power. When the injection power is less than  $-23$  dB, no appreciable changes are observed in the averaged modal powers. However, some changes are apparent from the optical spectra. Different optical spectra corresponding to representative values of the injection power when the detuning is 13 GHz are shown in Fig. 7.2.4. Figure. 7.2.4(a) shows that a contribution to the  $y$ -polarized spectrum at the injection frequency appears for small values of the injection power. That contribution increases when the injection power increases. However the  $x$ -polarized spectrum is very similar to the corresponding solitary spectrum. When the injection power increases beyond  $-23$  dB, the  $LP_{01,x}$  averaged power begins to decrease while the one of the  $LP_{01,y}$  begins to increase, as seen in Fig. 7.2.3(a) and 7.2.3(b). Fig. 7.2.4(b) shows that the increase of the  $LP_{01,y}$  power appears mainly at the injection frequency. Wave mixing is also observed by the peaks in the  $x$ - and  $y$ - polarization appearing at multiples of the frequency difference  $\nu_M - \nu_{01,x}$  between the ML frequency and the VCSEL mode. PS within the fundamental mode appears at  $-8$  dB and is illustrated in Fig. 7.2.3(a) and 7.2.3(b) and Fig. 7.2.4(c). After the PS, the VCSEL emits at a several frequencies at multiples of  $\nu_M - \nu_{01,x}$ . Figure. 7.2.3(b) also shows that further increase of the injected power leads to the excitation of the  $LP_{11,y}$  mode as well.

A typical optical spectrum in the injection-locking regime is the one shown in Fig. 7.2.4(e) that corresponds to an injection power of 0 dB. The optical spectrum is such that only one peak of the  $y$ -polarized light at the injection frequency appears, i.e., injection locking has been achieved. The previously described situation changes when decreasing the injection power, as it can be seen in Fig. 7.2.3(a) and 7.2.3(b): a wide bistability region appears for the  $LP_{01,x}$  and  $LP_{01,y}$  modes. However, no bistability is observed for the  $LP_{11,y}$  mode. A value of the injection power of  $-20$  dB, in the middle of the hysteresis region has been chosen in Fig. 7.2.4(b) and 7.2.4(d) to illustrate the bistability by using optical spectra.

Let us now describe the results for a detuning of 62 GHz that corresponds to the local maximum of the injection power required for the PS in the mapping in Fig. 7.2.2(a). We first analyze the behavior obtained when increasing the injection power. A monotonic decrease of the  $LP_{01,x}$  averaged power together with monotonic increases of the  $LP_{01,y}$  and  $LP_{11,y}$  averaged powers are obtained, as it can be seen in Fig. 7.2.3(c) and 7.2.3(d). PS-off occurs at around 3.5-dB injection power. There is an appreciable contribution of the  $LP_{11,y}$  mode to that PS, in contrast to the 13-GHz detuning case. We also observe that there is a value of the injection power, around 8 dB, beyond which the main contribution to the optical power is given



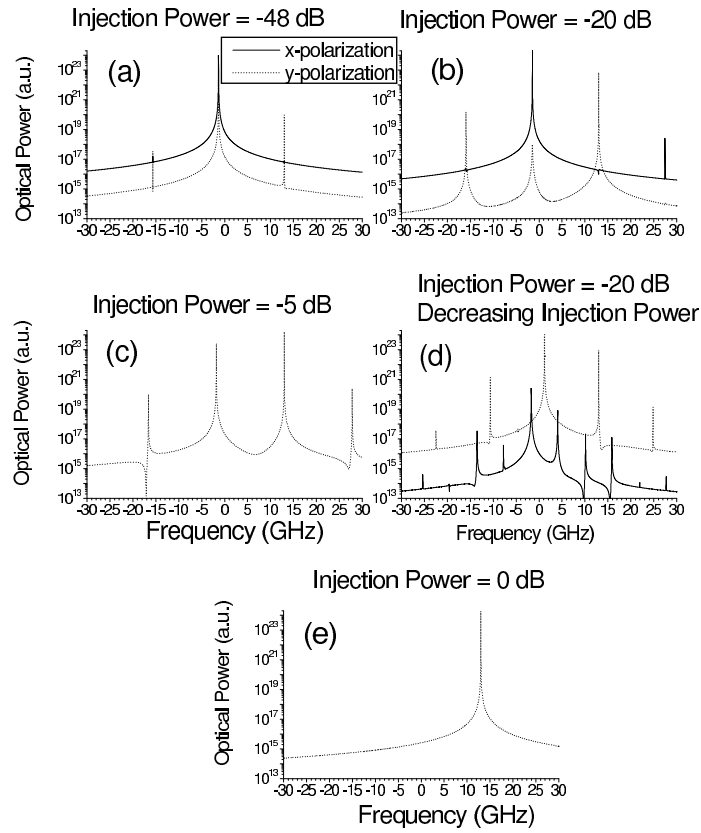


**Figure 7.2.4:** Polarization resolved optical spectra for several values of the injected power when the frequency detuning is 13 GHz.  $x$ - and  $y$ -polarized spectra are plotted with solid and dotted lines, respectively. (a), (b), (c), and (e) correspond to increasing injection power while (d) corresponds to decreasing power. Zero frequency corresponds to injection at the central frequency between the two polarizations of the fundamental mode.

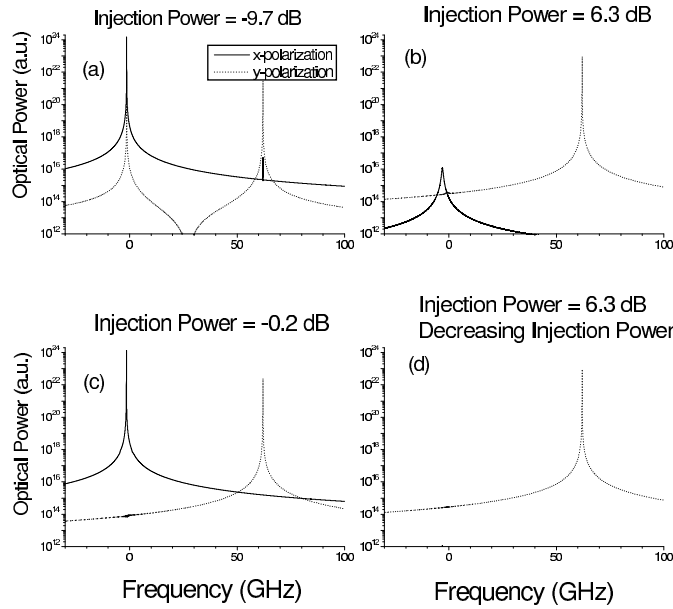


**Figure 7.2.5:** Polarization resolved optical spectra for several values of the injected power when the frequency detuning is 62 GHz.  $x$  and  $y$ -polarized spectra are plotted with solid and dotted lines, respectively. (a)-(c) correspond to increasing injection power while (d) corresponds to decreasing power.

by the  $LP_{11,y}$  mode. The situation again changes when decreasing the injection power because bistability regions appears now for all the transverse modes with orthogonal polarization. The width of the bistable region of the  $LP_{01}$  modes is smaller than the one for the 13-GHz detuning case. However, bistability also appears for the  $LP_{11,y}$  mode. Typical optical spectra for the 62-GHz detuning case are illustrated in Fig. 7.2.5. Again, the component near the zero frequency (at the injection frequency) of the  $y$ -polarized spectrum decreases (increases) when increasing (decreasing) the injection power as it can be seen in Fig. 7.2.5(a) and 7.2.5(c). Optical spectra at 6.3 dB, beyond the PS point, are also illustrated in Fig. 7.2.5(b) and 7.2.5(d), for increasing and decreasing optical injection, respectively. Only one peak of the  $y$ -polarized light at the injection frequency appears in both figures. Comparison between those figures also illustrate the bistability regime because the  $x$ -polarized power has disappeared when decreasing the injection power.

The results obtained for a frequency detuning approaching the second minimum of Fig. 7.2.2(a) are shown in Fig. 7.2.3(e) and 7.2.3(f). Again,

a PS appears at around 1 dB injection power but now the contribution of the  $LP_{01,y}$  power to that switching is small. In fact the switching is mainly performed between the  $LP_{01,x}$  and the  $LP_{11,y}$  modes. We also show that when the averaged power of  $LP_{01,x}$  vanishes the growth of the  $LP_{11,y}$  modes becomes much larger while there is a small range of injection power, around 3 dB, where the  $LP_{01,y}$  averaged power decreases. Figs. 7.2.3(e) and 7.2.3(f) also show that the qualitative behavior obtained when decreasing the injection power is similar to the one obtained for the 62-GHz detuning case.

### 7.3 Experimental study of optical injection-induced transverse mode competition

The experimental results presented here have been obtained using the same orthogonal injection setup as in previous Chapters (Chaps. 4 and 5). We use VCSEL<sub>2</sub> for our investigation. The bias current is fixed at 2.105 mA and the temperature is set at 20°C, such that the free-running VCSEL emits a horizontally polarized single fundamental transverse-mode. At the moment of our experimental investigations, we noticed a quantitative change in the L-I curve of the light-current characteristic with respect to the one shown in Chap. 4. The newly measured L-I curve has been already described in Chap. 3 (see Fig. 3.3.2). However, apart from the change of the switching points of the L-I curve, the other VCSEL intrinsic characteristics such as the birefringence, the fundamental and first-order transverse mode threshold current remain unchanged. As a result, there is no qualitative change in the dynamical response of the VCSEL under orthogonal optical injection. Since the switching and locking mechanism in the fundamental transverse-mode regime have been extensively investigated in Chapter 5, we limit our investigation to a relatively large positive detuning range (from 2 to 180 GHz) where transverse-mode competition phenomena are observed.

#### 7.3.1 Experimental mapping

In this section, transverse mode switching and locking of the VCSEL with orthogonal optical injection are experimentally investigated in the plane of the injection parameters, i.e., the frequency detuning versus injection power plane. The free-running VCSEL is biased at 2.105 mA, which is less than the lower limit of the hysteresis region associated to type II PS (see the L-I curve in Fig. 3.3.2). Its temperature is stabilized at 20°C. With these operating conditions, the free-running VCSEL emits a horizontal linearly polarized ( $x$ -LP) fundamental mode. In Fig. 7.3.1, the mapping of the VCSEL subject to optical injection is presented for a very large positive detuning range, i.e.,

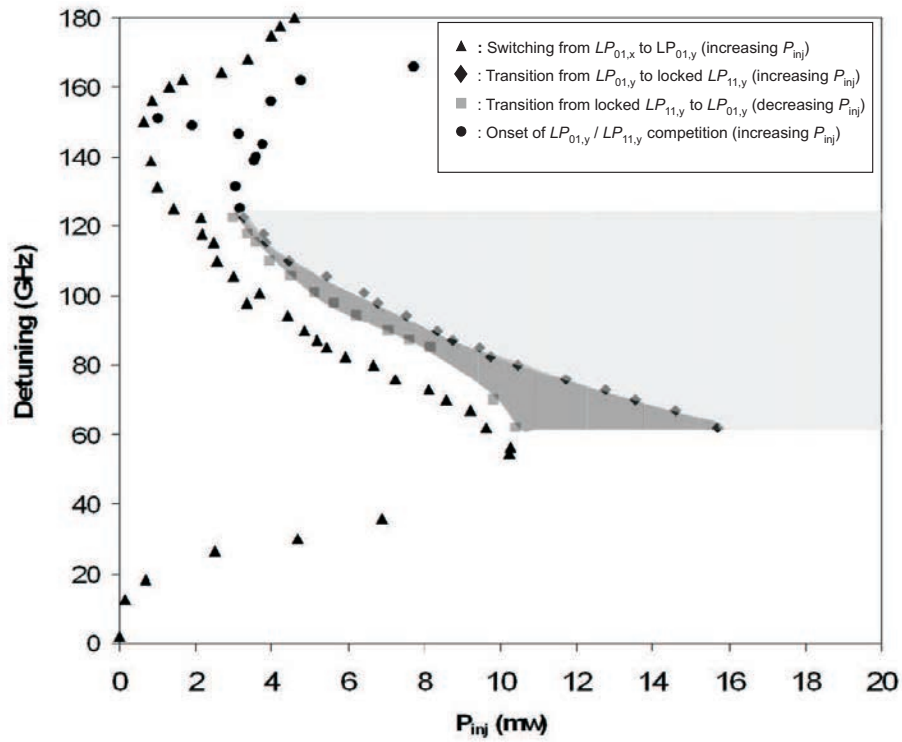


**Figure 7.3.1:** *Experimental mapping of PS and transverse modes competition in the plane detuning versus injection power ( $P_{inj}$ ). The bias current and the operating temperature are fixed at 2.105 mA and 20°C, respectively.*

from 2 to 180 GHz. For a fixed detuning value, polarization-resolved dynamics as well as transverse mode competition are analyzed when the injection strength is scanned. If the injection strength is increased, and depending on the frequency detuning, different switching scenarios are resolved. A switching mechanism that involves the VCSEL fundamental orthogonal transverse modes, i.e., from the horizontal ( $x$ -LP) to the vertical ( $y$ -LP) mode, is observed for the whole frequency detuning range. The corresponding boundary is labeled by black triangles in Fig. 7.3.1. This boundary exhibits two minima of switching power. A first minimum is located at a detuning of 2 GHz for which PS is achieved at  $7.1 \mu\text{W}$ . A second minimum of the switching power is found for a detuning of 150 GHz and an injection power of  $623.9 \mu\text{W}$ . It is worth mentioning that the second minimum is at much larger power than the one for a detuning of 2 GHz.

### 7.3.2 Polarization-resolved switching scenarios

We analyze in more detail the transverse mode competition behavior for detunings ranging from 61 to 120 GHz (see Fig. 7.3.1). With increasing the injection power we first observe PS between the  $LP_{01,x}$  and the  $LP_{01,y}$  modes (denoted by black triangles). When increasing further the injection power we observe injection locking of the  $LP_{11,y}$  mode, i.e., its frequency locks to the one of the ML, together with suppression of the fundamental transverse mode  $LP_{01,y}$ . The corresponding injection locking boundary is denoted by black diamonds. Fig. 7.3.2 represents a sample of such a scenario for a detuning of 100 GHz by using the experimental optical spectra.

The experimental spectra shown in this chapter have been recorded in the vertical polarization direction only. For a detuning of 100 GHz, as the injection strength is increased, the VCSEL is initially frequency pushed but still emits a horizontal  $x$ -LP mode [Fig. 7.3.2(a)]. For a further increase in the injection strength, switching from horizontal  $x$ -LP to vertical  $y$ -LP fundamental mode is achieved, as shown by the sudden increase of the SL peak in vertical polarization direction in Fig. 7.3.2(b). By further increasing the injection strength, an abrupt injection locking of the first-order transverse mode to ML with suppression of the fundamental mode is resolved [see Fig. 7.3.2(c)]. It is worth noting that for a much higher injection power, a relatively weak emission of the fundamental  $y$ -LP mode can be observed with still the injection locked  $LP_{11,y}$  mode dominating [Fig. 7.3.2(d)]. Bistability is observed if the injection power is decreased after injection locking of the  $LP_{11,y}$  mode is achieved, i.e., the VCSEL unlocks at an injection strength less than the one necessary to induce the locking regime (see the boundary labelled with light gray squares in Fig. 7.3.1. As indicated by the zone with a dark gray shading in Fig. 7.3.1, the width of the bistable region associated to the locking of the  $LP_{11,y}$  mode decreases as we increase the detuning.

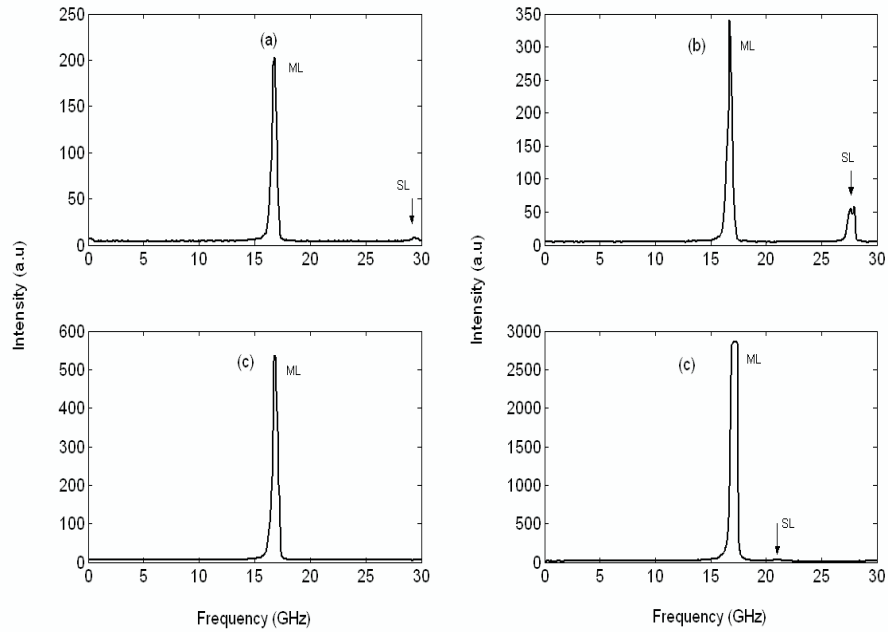


**Figure 7.3.2:** Polarization mode competition when the detuning is fixed at 100 GHz. (a) VCSEL emits in horizontal before PS,  $P_{inj} = 3.26\text{mW}$ . (b) After PS to vertical polarization,  $P_{inj} = 5.24\text{ mW}$ . (c) Injection locking of the  $LP_{11,y}$  mode,  $P_{inj} = 7.99\text{ mW}$ . (d) Injection locking of the  $LP_{11,y}$  mode with relatively weak recovery of the VCSEL fundamental mode  $P_{inj} = 18\text{ mW}$ . All the spectra have been measured in the vertical polarization direction, the small feature in (a) is a remains of the lasing  $x$ -LP horizontal mode.

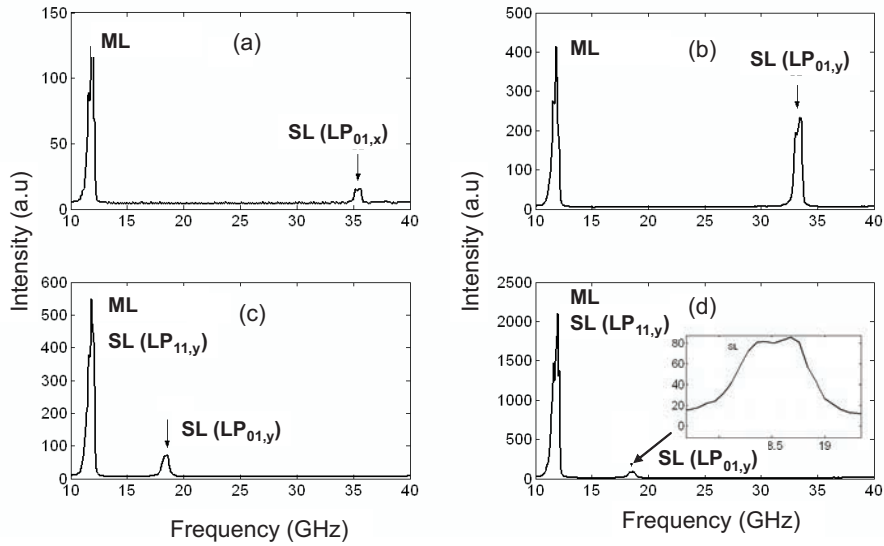


**Figure 7.3.3:** Polarization mode competition when the detuning is fixed at 125 GHz. (a) VCSEL emits in horizontal before PS,  $P_{inj} = 0.72\text{mW}$ . (b) After PS to vertical polarization,  $P_{inj} = 2.23\text{mW}$ . (c) Injection locking of the LP mode to the ML after a progressive decrease of power at the SL frequency  $P_{inj} = 6.97\text{mW}$ . (d) Injection locking of the LP mode with a relatively weak recovery of the VCSEL fundamental LP mode,  $P_{inj} = 22.13\text{mW}$ . All the spectra have been measured in the vertical polarization direction, the small feature in (a) is a remains of the lasing  $x$ -LP horizontal mode.

For frequency detunings larger than 120 GHz, injection locking of the  $LP_{11,y}$  mode, accompanied by suppression of the fundamental transverse mode  $LP_{01,y}$ , is not observed anymore [see Fig. 7.3.3(d)]. Figure. 7.3.3(a) represents the situation for which the VCSEL is under optical injection but the injection strength is not sufficient to induce PS. By increasing the injection level, PS from  $x$ -LP to  $y$ -LP fundamental modes is achieved [Fig. 7.3.3-(b)]. A further increase in the injection strength leads to a strong competition between the  $LP_{01,y}$  and  $LP_{11,y}$  modes. The onset of such a mode competition is shown on the mapping in Fig. 7.3.1 by black circles which correspond to the observation of a progressive decrease of the intensity at the SL frequency and a relatively strong increase of power at the ML frequency [see Fig. 7.3.3(c)]. Again, at a much stronger injection, a weak increase of the intensity at the SL frequency, i.e., a recovery of the  $y$ -LP fundamental mode, has been observed [Fig. 7.3.3(d) and the inset]. As shown in Fig. 7.3.1, the transverse mode competition appears at much lower injection power for a detuning of 150 GHz, which corresponds to the second minimum of the switching power. For larger positive detunings up to around 165 GHz, the mode competition is still resolved but at progressively increasing injection levels. Above this detuning range and as we increase the injection power, PS between the fundamental modes is still observed but afterwards the VCSEL keeps emitting an unlocked  $y$ -LP fundamental mode.

## 7.4 Comparison between theory and experiments

We discuss here the similarities and the differences between the theoretical results on transverse mode switching and locking in a VCSEL subject to orthogonal optical injection with our experimental results. The experimental light-current curve shows a switching from the higher to the lower frequency orthogonally polarized modes at a current of around 2 mA (see Fig. 3.3.2) that does not appear in our theoretical results (see Fig. 7.2.1). That switching would also appear in our theoretical results if we would consider an additional physical mechanism with a significant influence on the polarization of the device, for instance, successive types I and II switchings have been observed when adding thermal mechanisms to SFM model [166] or polarization dependent gain/loss mechanisms to the two-mode model [45]. However, the absence of such switching in the theoretical results is not so important because the PS which we have been investigating is the second one, from the lower to the higher frequency polarization mode. In both, experiment and theory, this switching occurs within the fundamental mode of the device. Also in both cases small bumps in the  $y$ -polarization appear for currents smaller than the PS current due to the appearance of elliptically polarized states. Excitation of the first-order mode occurs at similar cur-



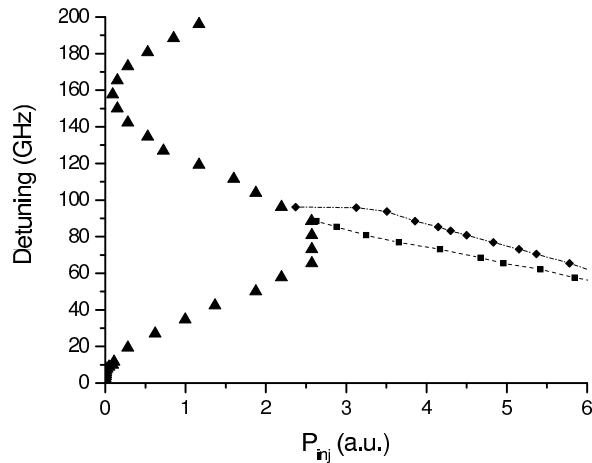


**Figure 7.4.1:** Injection power required for PS in a VCSEL subject to orthogonal optical injection. Switching from  $x$ - to  $y$ -polarization when increasing the injection power is shown with triangles. The injection power required for the  $LP_{11,y}$  modal power to reach an appreciable value, 0.5, has been plotted if  $P_{inj}$  is increased (diamonds) and if  $P_{inj}$  is decreased (squares). Parameters correspond to those in Fig.7.2.2(a).

rents (at around five times the threshold current). A wide bistability region also appears in both cases in such a way that the switching from the  $y$ - to the  $x$ -polarization when decreasing the current is also similar (at around two times the threshold current). We then conclude that the essential qualitative features of the experimental light-current characteristics are well described by our model.

A comparison between the theoretical (Fig. 7.2.2) and the experimental (Fig. 7.3.1) mapping of the injection power required for PS shows that both theory and experiment feature a new minimum at a frequency detuning of around 150 GHz. A more detailed comparison is done in Fig. 7.4.1 where we have plotted the results from Fig. 7.2.2(a) in a linear horizontal axis. The injection power required for PS when increasing the injection power is plotted with black triangles. The experimental detuning frequencies at which the injection power is minimum or maximum are similar to the theoretical ones. As shown in Section 7.2, the detuning frequency at which the new minimum occurs depends on the relative losses between the two transverse modes. The theoretical relative losses in Fig. 7.4.1 correspond to a VCSEL that becomes multimode at 4.7 times threshold. This result is consistent with the experimental result in which the first-order mode appears at five times threshold. The experimental  $P_{inj}$  required for PS at the second min-

imum at 150 GHz detuning, is 19.5 dB higher than the first one at 2 GHz detuning, while the corresponding theoretical quantity is 23.8 dB. Also, the experimental (theoretical)  $P_{inj}$  required for PS at 150 GHz, is 16 (27) times smaller than the maximum one.

We find experimentally that, in the whole frequency detuning range we investigate, the PS involves the VCSEL fundamental orthogonally polarized transverse modes, i.e., from the  $LP_{01,x}$  to the  $LP_{01,y}$  modes. However our theoretical results also unveil an additional possible scenario, in which a switching from the  $LP_{01,x}$  to the  $LP_{11,y}$  mode is observed when increasing the injection strength [see Fig. 7.2.3(e) and 7.2.3(f)]. Theoretically, we find that this second switching scenario appears for frequency detunings larger than 85 GHz and for a value of the injection strength larger than that leading to a switching between the orthogonal fundamental transverse modes [compare Fig. 7.2.3(a) and 7.2.3(b) with Fig. 7.2.3(e) and 7.2.3(f)]. We find that this second switching scenario appears at smaller frequency detunings when increasing the  $\kappa_r$  parameter (65 GHz when  $\kappa_r = 1.4$ ). In this way, a wider range of frequency detunings over which the  $LP_{01,x}$  switches to the  $LP_{11,y}$  modes would be obtained if the  $\kappa_r$  parameter is decreased. We also find experimentally that the  $LP_{11,y}$  mode appears locked to the injection. This is also the case for our theoretical results since our optical spectra indicate that locking of the  $LP_{11,y}$  mode can be achieved for all the considered frequency detuning range. Bistability in PS has been found in the experiment and theory and is demonstrated in Fig. 7.4.1 where the injection power required for the  $LP_{11,y}$  modal power to reach an appreciable value has been plotted when increasing (diamonds) and when decreasing (squares) the injection power. Theoretically, this bistability can be for the fundamental mode only or for both transverse modes. In such a way, our numerical results complement the experiment, which can not distinguish the contribution to the PS and the hysteresis of the two transverse modes separately.

## 7.5 Conclusions

In summary, we have performed theoretical and experimental investigations of transverse mode switching and locking in a VCSEL subject to orthogonal optical injection. Our theoretical results qualitatively agree with our experiments by showing the existence of two minima of the injection power needed to obtain PS. The first minimum appears for a detuning close to the VCSEL birefringence while the second one appears at a frequency detuning that is near the frequency difference between the fundamental and the first-order transverse modes of the solitary VCSEL. We have found that both the depth and the frequency position of the second minimum increase when considering lasers that become multitransverse mode at lower injec-

tion currents. In agreement with our experiments, the theoretical results have also shown that bistability in PS is obtained for all the frequency detuning range. Such a bistability is obtained for the fundamental mode only or for both transverse modes, depending on the value of the detuning. The theoretical and experimental optical spectra have shown that the first-order transverse mode appears locked to the external injection. Our theoretical model have captured most of the fundamental features of the experiment.



## Chapter 8

# Polarization-resolved dynamics and chaos synchronization of unidirectionally coupled VCSELs

We theoretically analyze the polarization-resolved synchronization characteristics of two unidirectionally coupled VCSELs. Instead of injecting the VCSEL with a single-frequency light from the master laser as was so far the case, we investigate here a quite different injection scheme in which the master laser (ML) can exhibit chaotic dynamics. In our study, such a chaotic regime is obtained through delayed optical feedback, i.e., the master laser light is partially reflected back into the VCSEL using a mirror which is adequately aligned with the master laser to form an external cavity. We consider the case in which only the master laser is subject to isotropic feedback, which implies that both orthogonal linearly-polarized (LP) modes are fed back into the VCSEL's internal cavity with the same coupling rate. Two optical injection coupling configurations are investigated. We first study the isotropic injection scheme for which both ML orthogonal LP modes are coupled into the slave VCSEL with the same coupling rate. In this case, we show that the degree of chaos synchronization between master and slave VCSELs depends strongly on optical-feedback-induced polarization dynamics in the ML. We reveal that chaos synchronization can be significantly enhanced when the operating conditions of the ML are such that a two-polarization mode chaos is achieved. On the other hand, a degradation of the synchronization quality is observed when the ML operates in the single-polarization-mode chaotic regime. By tuning the birefringence such that the VCSELs operate in either their single or bistable polarization regimes, we interestingly show that our

results are robust even in the presence of spontaneous emission noise.

We furthermore report on synchronization characteristics of two unidirectionally coupled VCSELS in the orthogonal injection configuration case similar to what has been experimentally investigated by Hong *et al.* [167]. The master laser is subject to isotropic optical feedback. The slave VCSEL is subject to an orthogonal optical injection from the master VCSEL, i.e., only one of the linearly-polarized ML chaotic modes is selected and then injected orthogonally to the dominant linearly polarized mode of the free-running slave VCSEL. In this configuration, by appropriately changing the injection VCSEL parameters, i.e., the injected strength and the detuning, one may induce polarization switching between slave VCSEL orthogonal LP modes. In the plane of the injection parameters, we identify two regions of qualitatively different synchronization between the injected LP mode and the corresponding slave LP mode. In the so-called region II the slave VCSEL exhibits anticorrelated dynamics in its two LP modes while in the so-called region I the slave VCSEL exhibits dynamics in only one LP mode, which corresponds to the polarization of the injected field. We furthermore analyze the dependency of the synchronization quality on the parameter mismatch between master and slave VCSELS and on the polarization switching properties of each VCSEL. In particular we show that synchronization between the injected field and the slave VCSEL mode with the same polarization is more robust against parameter mismatch for region II than region I. This chapter is based on the following publications:

- I. Gatare, M. Sciamanna, A. Locquet, and K. Panajotov, “*Influence of polarization mode competition on the synchronization of two unidirectionally coupled vertical-cavity surface-emitting lasers,*” *Opt. Lett.*, **32**, 1629 (2007).
- M. Sciamanna, I. Gatare, A. Locquet, and K. Panajotov, “*Polarization synchronization in unidirectionally coupled vertical-cavity surface-emitting lasers with orthogonal optical injection,*” *Phys. Rev E* **75**, 056203 (2007).

## 8.1 Introduction

### Historical overview and basic concepts

The concept of synchronization is a universal phenomenon encountered in quite diverse nonlinear systems in physics, chemistry, biology and in engineering science. Generally, synchronization can be defined as adjustment of rhythms of two or several nonlinear self-sustained oscillating systems due to their weak interaction [168]. By rhythm, we mean the variation in time of a

specific system state variable. The first scientific report about synchronization is probably the famous experimental observation in 1665, by Huygens, of two pendulum clocks hanging on a common beam [100]. He clearly noticed the fact that the two clocks reached a common oscillating rhythm was due to their seemingly imperceptible mutual coupling through the beam, without which they may oscillate with different rhythms. A resurgence of interest in the study of synchronization can be traced back to 1920 with the discovery of synchronization properties of basic electrical devices, such as triode generators based on a vacuum tube [169]. This found interesting applications in radio communication systems in which one could stabilize the frequency of a powerful triode generator by synchronizing it with a weak but precise one.

Furthermore, intriguing synchronization phenomena have been demonstrated in several complex natural ensembles such as the synchrony of flashing fireflies [170], chirping crickets [171] and cardiac pacemaker cells [172]. In neuroscience, there is a growing interest in the study of synchronization which is thought to be a key mechanism for neuronal information processing within a brain. This may contribute to a better understanding of brain functions such as visual pattern recognition [173] and motor processes [174]. In engineering science, synchronization has found applications in control electronic circuits such as phase-locked loops (PLL), commonly present in communication and computer systems or in stabilization of electrical power generation plants. In optoelectronics, a single highly coherent master laser can be used to precisely achieve the frequency stabilization of an array of slave lasers through optical injection phase locking [117].

Most of the studies concerned the synchronization between two or several periodic oscillating systems (see the above mentioned examples). Figure 8.1.1 illustrates a simple synchronization mechanism between forcing and driven single-frequency oscillating systems which are unidirectionally coupled. By tuning the frequency range of the forcing oscillator ( $\omega$ ) around  $\omega_0$  (the frequency of the driven oscillator in the absence of coupling), one observes a frequency range over which synchronization is achieved, i.e., the frequency of the driven system  $\Omega$  equals that of the forcing oscillator:  $\Omega - \omega = 0$ . Moreover, the bandwidth of the synchronization range increases with the amplitude of the forcing signal  $\varepsilon$  following a triangle-like shape, the so-called *Arnold tongue* [175] (see the inset in Fig. 8.1.1). As a result of frequency-locking, the difference between the phases of the forcing ( $\phi$ ) and driven ( $\Phi$ ) oscillators is bounded, i.e.,  $|\phi - \Phi| \leq \text{constant}$ . In the general framework of synchronization, one may consider high-order synchronization for which the frequency-locking condition is:  $n\omega - m\omega = 0$ ,  $n$  and  $m$  being two integers. Thus, the phase bounding condition writes:  $|n\phi - m\Phi| \leq \text{constant}$  [168].

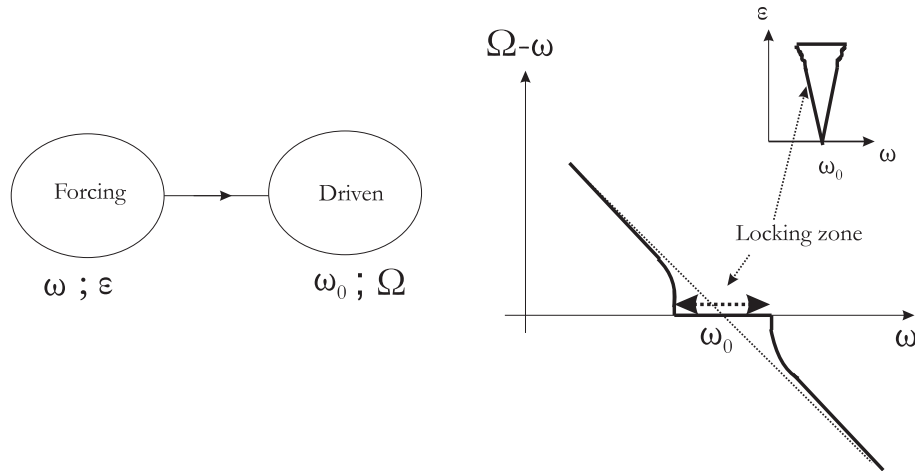


**Figure 8.1.1:** Sketch of synchronization between two unidirectionally-coupled periodic oscillators.  $\omega$  and  $\varepsilon$  are respectively the frequency and amplitude of the forcing oscillator.  $\Omega$  ( $\omega_0$ ) represents the frequency of the driven oscillator in the presence (absence) of the coupling. The diagram shows the evolution of the frequency offset  $\Omega - \omega$  as a function of the frequency of the forcing oscillator. Synchronization (or Frequency locking, i.e.,  $\Omega = \omega$ ) is only achieved for a particular range of the detuning  $\Delta\omega = \omega - \omega_0$  distributed around  $\omega_0$ . The width of this range depends on  $\varepsilon$ .

### Chaos synchronization

Two identical nonlinear chaotic systems operating independently exhibit quite different oscillations even if their initial conditions are very close [176]. Such a behavior is due to the fact that chaotic systems are inherently very sensible to initial conditions, i.e., any slight difference in the initial conditions would quickly lead to uncorrelated deterministic chaotic outputs. However, when a weak coupling is established, Pecora and Carrol [177] have theoretically and experimentally demonstrated that two chaotic systems may synchronize with each other, i.e., they show the same outputs under certain conditions and system parameters. This chaos synchronization report was a case of complete synchronization, which complements the phase synchronization case since not only the phases of the coupled oscillators are locked but also the amplitudes of the oscillators become identical or are to each other with a constant scaling. Following this pioneering observation, chaos synchronization has attracted much attention due to its potential in many applications, particularly in secure chaos-based communications. Chaos synchronization and its possible application for secure communication was demonstrated in an electronic circuit that features the so-called Lorenz system [178]. In principle, the concept of chaos-based communication systems is simple: the message is embedded in the transmitter chaotic output



signal and then sent to the receiver. The recovery of the message at the reception stage is achieved by comparing the input and the output signals of the receiver. In fact, the receiver synchronizes only with the chaotic carrier and not with the message. Therefore, by achieving the difference between the input (chaotic carrier and message) and output (chaos) of the receiver one can recover the message. It is worthy noting that chaos obtained from electronic circuits has a relatively narrow bandwidth (tens of kHz), which represents a drawback for implementing a realistic secure communication link.

An extensive research has been undertaken to investigate chaos synchronization in several laser systems. The advantage of laser systems over electronic ones is that it is possible to generate a high-dimensional chaotic signal with a bandwidth of several GHz. Moreover, the obtained signals are immune against noise and electromagnetic disturbances usually encountered in electronic circuits. Optical chaos synchronization has been successively demonstrated in CO<sub>2</sub> [179] and NH<sub>3</sub> [180] gas lasers, and in Nd:YAG solid-state lasers [181]. Chaos synchronization with implementation of a secure communication link between the transmitter and receiver erbium-doped fiber-ring lasers has been also demonstrated [182, 183]. Then, the concept of chaos synchronization using semiconductor lasers attracted much attention owing to their competitive advantages as cheap, compact and efficient light sources for optical communication systems [184, 185, 186, 187]. A field experiment of secure chaos communication, based on semiconductor lasers and using a commercial optical fiber link, was recently demonstrated. Transmission rate in the Gbits/s range has been successfully achieved with a low bit error rate (BER) [15].

In Fig. 8.1.2, we provide a schematic representation of different setups which are commonly adopted for achieving chaos synchronization, using two unidirectionally-coupled semiconductor lasers. Figure. 8.1.2(a) represents the so-called closed-loop configuration for which both the master (ML) and the slave laser (SL) are subject to optical feedback from, respectively, external cavity mirrors  $M_M$  and  $M_S$ . Thus, they can independently exhibit chaotic dynamics. If one suppresses the external cavity mirror  $M_S$ , one obtains the so-called open-loop synchronization setup. This is the case in Fig. 8.1.2(b) but the corresponding injection coupling scheme is different from that in Fig. 8.1.2(a). In Fig. 8.1.2(b), which represents an orthogonal injection scheme, the ML output polarization plane is first subject to a 90° rotation using a half-wave plate (HWP). A polarizing beam-splitter (PBS) is then used to solely select the linearly polarized component of the ML, orthogonal to the linearly polarization field of the free-running SL. As will be shown later (see Section 8.3), such orthogonal injection scheme is mostly relevant in the study of synchronization of vertical-cavity surface-emitting lasers for which the master VCSEL can exhibit a feedback-induced chaotic

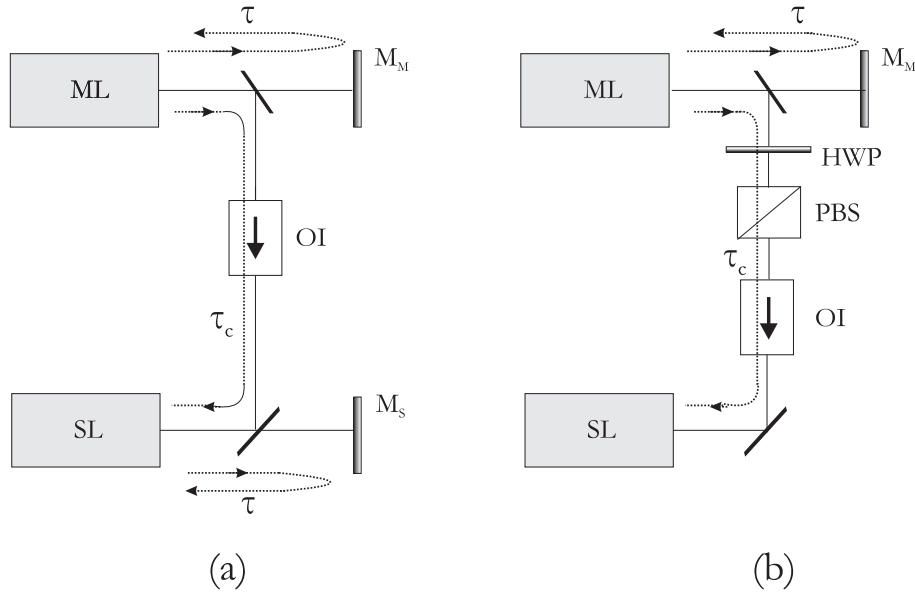


**Figure 8.1.2:** Synchronization setups: (a) closed-loop with unidirectional isotropic optical injection and isotropic optical feedback; (b) open-loop with unidirectional orthogonal optical injection and isotropic optical feedback. ML: master laser; SL: slave laser;  $M_M$ : external cavity mirror for ML;  $M_S$ : external cavity mirror for SL; OI: optical isolator; BS: nonpolarizing beam-splitter; PBS: polarizing beam-splitter; HWP: half-wave plate;  $\tau$ : round-trip time in the external cavity;  $\tau_c$ : flight time between ML and SL.

regime in both orthogonal LP modes [167]. It is worth mentioning that, besides its applications in VCSEL experiments, a configuration based on polarization-rotated optical injection has also recently received interest in coupled edge-emitting lasers to demonstrate identity synchronization [188].

In the case of coupled edge-emitting lasers (EEL), chaos synchronization properties have been explored in detail [189, 190, 191, 192, 193]. A summary of major experimental and theoretical results can be found in Ref. [194]. By contrast, studies on VCSEL synchronization remain scarce. The first theoretical studies by Spencer *et al.* [195, 196] have unveiled the possibility to synchronize chaos in coupled VCSELS in master-slave configuration. However, they did not take into account the complex polarization dynamics of VCSELS. Additional more recent theoretical investigations have modelled synchronized coupled VCSELS, however focusing mostly on the total intensity synchronization properties [197]. First experiments have demonstrated chaos synchronization in VCSELS in either master-slave unidirectional configuration [167] or in mutually coupled configuration [198]. The practical use of chaos synchronized VCSELS for secure message transmission has also been tested recently in laboratory [156], with successful encoding/decoding of a

200 MHz sinusoidal message. In this chapter, we theoretically contribute to the study of synchronization in unidirectionally coupled VCSELS, taking into account complex nonlinear polarization dynamics and polarization switching properties in VCSELS.

The present chapter is organized as follows. In Section 8.2, we investigate chaos synchronization in the open-loop, isotropic injection scheme. We particularly analyze the influence of polarization mode competition on the synchronization between ML and SL. In section 8.3, we investigate polarization-resolved synchronization mechanisms by adopting the so-called orthogonal optical injection scheme similarly to what has been experimentally proposed by Hong *et al.* [167]. Here, the synchronization properties are analyzed as a function of injection parameters. We furthermore report on the effect of parameter mismatch between ML and SL on chaos synchronization. Finally, we conclude our results in Section 8.4.

## 8.2 Influence of polarization mode competition on the synchronization of two unidirectionally coupled VCSELS

In this section, we theoretically analyze the effect of polarization mode competition on the synchronization of two unidirectionally coupled VCSELS. Chaos in the master laser is induced by delayed optical feedback and the slave laser is subject to isotropic optical injection from the master VCSEL. We show that the synchronization quality can be enhanced when the chaotic regime in the master VCSEL involves both fundamental orthogonal linearly polarized modes. The robustness of the obtained results is verified by varying the VCSEL birefringence such that it is possible to operate either in the polarization bistable region or in the single-mode region. Indeed, a dramatic degradation of the chaos synchronization quality is resolved when shifting from the two-polarization mode to the single-mode chaotic regime.

### 8.2.1 The Model

Our rate equation model extends the Spin Flip Model (SFM) for single transverse mode VCSELS described in Chapter 3. The master laser rate equations take into account the effect of isotropic feedback. Similarly, the slave laser

equations take into account isotropic optical injection from ML.

$$\begin{aligned} \frac{E_{x_M}}{dt} &= \kappa(1 + i\alpha) [(D_M - 1)E_{x_M} + id_M E_{y_M}] \\ &\quad - (\gamma_a + i\gamma_p)E_{x_M} + fE_{x_M}(t - \tau) \exp(i\omega_M\tau) + F_{x_M}, \end{aligned} \quad (8.2.1)$$

$$\begin{aligned} \frac{E_{y_M}}{dt} &= \kappa(1 + i\alpha) [(D_M - 1)E_{y_M} - id_M E_{x_M}] \\ &\quad + (\gamma_a + i\gamma_p)E_{y_M} + fE_{y_M}(t - \tau) \exp(i\omega_M\tau) + F_{y_M}, \end{aligned} \quad (8.2.2)$$

$$\begin{aligned} \frac{dD_M}{dt} &= -\gamma_e \left[ D_M \left( 1 + |E_{x_M}|^2 + |E_{y_M}|^2 \right) \right] \\ &\quad + \gamma_e \mu - i\gamma_e d_M (E_{y_M} E_{x_M}^* - E_{x_M} E_{y_M}^*), \end{aligned} \quad (8.2.3)$$

$$\begin{aligned} \frac{dd_M}{dt} &= -\gamma_s d_M - \gamma_e d_M \left( |E_{x_M}|^2 + |E_{y_M}|^2 \right) \\ &\quad - i\gamma_e D_M (E_{y_M} E_{x_M}^* - E_{x_M} E_{y_M}^*) \end{aligned} \quad (8.2.4)$$

For the master laser, and for the slave laser

$$\begin{aligned} \frac{E_{x_S}}{dt} &= \kappa(1 + i\alpha) [(D_S - 1)E_{x_S} + id_S E_{y_S}] \\ &\quad - (\gamma_a + i\gamma_p)E_{x_S} - i\Delta\omega E_{x_S} + \eta E_{x_M} + F_{x_S}, \end{aligned} \quad (8.2.5)$$

$$\begin{aligned} \frac{E_{y_S}}{dt} &= \kappa(1 + i\alpha) [(D_S - 1)E_{y_S} - id_S E_{x_S}] \\ &\quad + (\gamma_a + i\gamma_p)E_{y_S} - i\Delta\omega E_{y_S} + \eta E_{y_M} + F_{y_S}, \end{aligned} \quad (8.2.6)$$

$$\begin{aligned} \frac{dD_S}{dt} &= -\gamma_e \left[ D_S \left( 1 + |E_{x_S}|^2 + |E_{y_S}|^2 \right) \right] \\ &\quad + \gamma_e \mu - i\gamma_e d_S (E_{y_S} E_{x_S}^* - E_{x_S} E_{y_S}^*), \end{aligned} \quad (8.2.7)$$

$$\begin{aligned} \frac{dd_S}{dt} &= -\gamma_s d_S - \gamma_e d_S \left( |E_{x_S}|^2 + |E_{y_S}|^2 \right) \\ &\quad - i\gamma_e D_S (E_{y_S} E_{x_S}^* - E_{x_S} E_{y_S}^*). \end{aligned} \quad (8.2.8)$$

The subscripts  $M$  and  $S$  are used for the master and slave VCSELS respectively.  $E_{x_{M,S}}$  and  $E_{y_{M,S}}$  are the slowly varying amplitudes of the  $x$ - and  $y$ -LP field components.  $D_{M,S}$  is the total carrier inversion between conduction and valence bands while  $d_{M,S}$  accounts for the difference between carrier inversions with opposite spins.  $\kappa$  is the photon decay rate,  $\gamma$  is the carrier decay rate, and  $\gamma_s$  accounts for microscopic processes leading to the homogenization of carrier spin.  $\alpha$  is the linewidth enhancement factor and  $\mu$  is the normalized injection current ( $\mu = 1$  at threshold).  $\gamma_a$  and  $\gamma_p$ , respectively, model the linear cavity dichroism and phase anisotropy. The frequency detuning is:  $\Delta\omega = \omega_M - \omega_S$ , where  $\omega_M$  and  $\omega_S$  are, respectively, the frequency of the master and slave VCSELS in the absence of linear anisotropies.  $f$  is the feedback rate. The isotropic optical feedback in the master laser eqs. (8.2.1)-(8.2.4) has been included in the same way as in Ref. [199].  $\eta$  is the injection rate.  $\tau$  is the delay time in the external cavity. Without loss

of generality, we consider a zero flight time ( $\tau_C$ ) between master and slave lasers. Spontaneous emission noise is modelled by Langevin sources:

$$F_{x_{M,S}} = \sqrt{\beta_{sp}/2} \left( \sqrt{D_{M,S} + d_{M,S}} \xi_{1_{M,S}} + \sqrt{D_{M,S} - d_{M,S}} \xi_{2_{M,S}} \right) \quad (8.2.9)$$

$$F_{y_{M,S}} = -i\sqrt{\beta_{sp}/2} \left( \sqrt{D_{M,S} + d_{M,S}} \xi_{1_{M,S}} - \sqrt{D_{M,S} - d_{M,S}} \xi_{2_{M,S}} \right) \quad (8.2.10)$$

With  $\xi_{1_M}$ ,  $\xi_{1_S}$ ,  $\xi_{2_M}$ , and  $\xi_{2_S}$ , independent Gaussian white noises with zero mean and unitary variance [60] and  $\beta_{sp}$  is the spontaneous emission factor. We keep the following parameters fixed:  $\alpha=3$ ,  $\gamma_e = 1 \text{ ns}^{-1}$ ,  $\gamma_s = 50 \text{ ns}^{-1}$ ,  $\gamma_a = 0.1 \text{ ns}^{-1}$ ,  $\kappa = 300 \text{ ns}^{-1}$ ,  $\Delta\omega = 0$ ,  $\tau = 3 \text{ ns}$ ,  $\omega_M\tau=6 \text{ rad}$ ,  $\mu = 1.2$ .

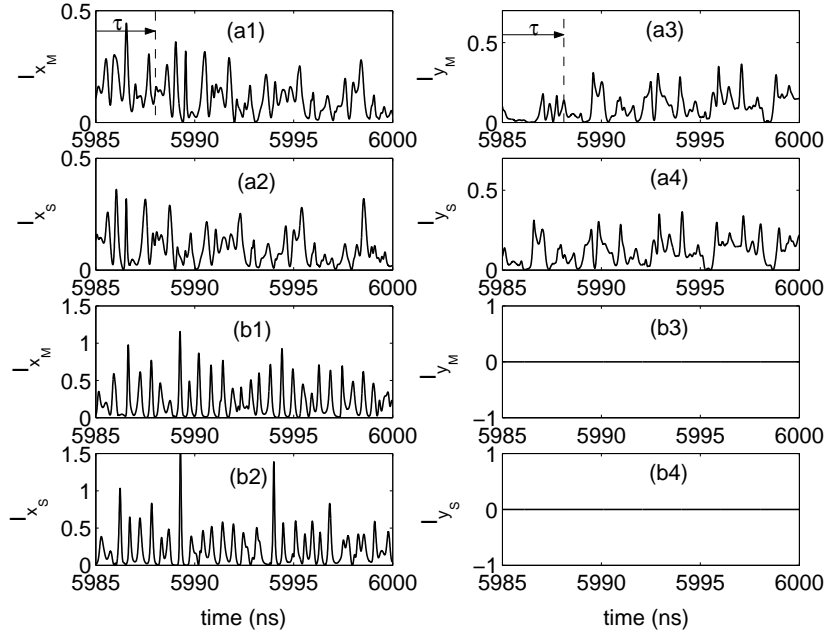
In our isotropic optical feedback/injection configuration, the two VCSELS can exhibit either an *anticipating* or *isochronous* (injection-locking) type of synchronization [191, 200]. Anticipating (perfect) synchronization is achieved when  $I_{x_M, y_M}(t) = I_{x_S, y_S}(t - \tau)$ ,  $D_M(t) = D_S(t - \tau)$  and  $d_M(t) = d_S(t - \tau)$ , with  $I_{x_M, y_M} = |E_{x_M, y_M}|^2$  and  $I_{x_S, y_S} = |E_{x_S, y_S}|^2$ . Necessary conditions for the existence of such a solution are that both lasers exhibit the same device parameters, bias currents, zero detuning and also  $f = \eta$ . The field of the slave laser anticipates the injected field by an anticipation time equal to  $\tau_C - \tau$ . On the other hand, the isochronous synchronization solution is of the type:  $I_{x_M, y_M}(t) = aI_{x_S, y_S}(t)$  with  $a$  being a constant. In this case, due to the finite speed of light propagation, the slave laser synchronizes with the injected field but lags in time (the delay is  $\tau_C$ ) behind the master laser. In order to discriminate between isochronous and anticipative synchronizations, and to evaluate the synchronization quality, we use the following correlation coefficients [191], respectively:

$$C_{1x,y} = \frac{\langle [I_{x_M, y_M}(t) - \langle I_{x_M, y_M} \rangle] [I_{x_S, y_S}(t) - \langle I_{x_S, y_S} \rangle] \rangle}{\left\{ \langle [I_{x_M, y_M}(t) - \langle I_{x_M, y_M} \rangle]^2 \rangle \langle [I_{x_S, y_S}(t) - \langle I_{x_S, y_S} \rangle]^2 \rangle \right\}^{\frac{1}{2}}}, \quad (8.2.11)$$

$$C_{2x,y} = \frac{\langle [I_{x_M, y_M}(t + \tau) - \langle I_{x_M, y_M} \rangle] [I_{x_S, y_S}(t) - \langle I_{x_S, y_S} \rangle] \rangle}{\left\{ \langle [I_{x_M, y_M}(t) - \langle I_{x_M, y_M} \rangle]^2 \rangle \langle [I_{x_S, y_S}(t) - \langle I_{x_S, y_S} \rangle]^2 \rangle \right\}^{\frac{1}{2}}}. \quad (8.2.12)$$

## 8.2.2 Polarization mode competition and its effect on chaos synchronization

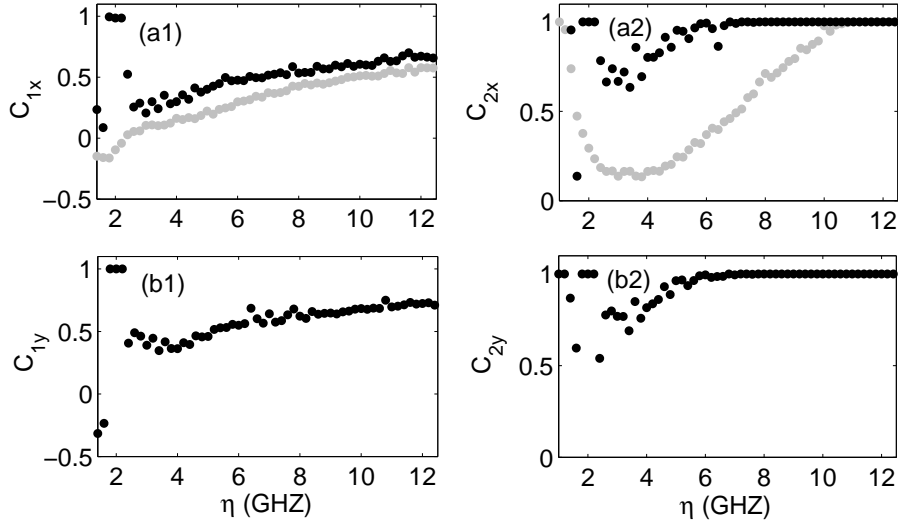
To examine the effect of the polarization mode competition on the synchronization quality we consider first  $\gamma_p = 6 \text{ ns}^{-1}$  such that the free-running VCSELS operate in a parameter region where both  $x$ - and  $y$ -LP modes are stable [60]. We first analyze mode competition without spontaneous emission noise (i.e.  $\beta_{sp} = 0$ ). With these parameters, we find that the dynamics



**Figure 8.2.1:** Time-traces of master and slave laser LP mode intensities for  $\eta = f = 6 \text{ ns}^{-1}$ : (a1-a4) chaos in both  $x$ - and  $y$ -LP modes and (b1-b4) single-mode chaos.

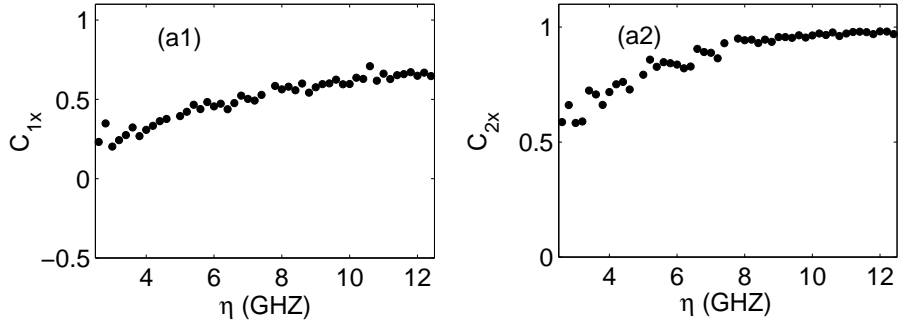
induced by the delayed optical feedback in the master laser will also exhibit bistability. Depending on the system initial conditions, the master laser can exhibit either a chaotic dynamics involving both LP modes or a single mode chaotic dynamics, as shown in, respectively, Figs. 8.2.1(a1),(a3) and Figs. 8.2.1(b1),(b3). We then analyze in each case the slave laser synchronization, as we progressively increase the injection rate. We consider the injection and feedback conditions such that the necessary conditions for anticipative synchronization are met. Taking for example  $\eta = f = 6 \text{ ns}^{-1}$  we observe first in Fig. 8.2.1(a2),(a4) that the slave laser exhibits an almost perfect anticipative synchronization ( $C_{2x} = 0.94$ ) for each pair of corresponding LP modes. However, we find interestingly that for the same parameters but considering a single mode chaotic dynamics in the master laser leads to a significant decrease of the synchronization quality ( $C_{2x} = 0.36$ ); see Figs. 8.2.1 (b1), (b2). The master laser total intensity exhibits more frequent power dropouts in the one-mode case than in the two-mode case, where, as a result of antiphase mode competition, the decrease of, e.g.,  $x$ -LP mode intensity is accompanied by a build-up of  $y$ -LP mode intensity. However, we find that the desynchronization events are not necessarily related to these power dropouts in the injected total intensity. Therefore the change of synchro-

nization quality between the cases of Figs. 8.2.1 (a1)-(a4) and (b1)-(b4) are not attributed to a change of injection level but rather to the intrinsic polarization competition mechanism.



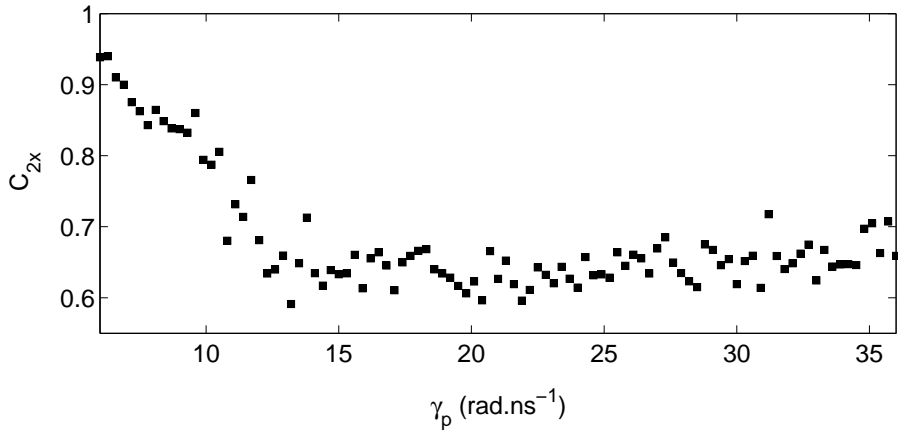
**Figure 8.2.2:** Evolution of the correlation coefficients related to isochronous (a1 and b1) and anticipative (a2 and b2) synchronization as a function of  $\eta$ . The gray (black) color corresponds to the case of single-mode (two-mode) chaos.

Figure 8.2.2 shows the evolution of the isochronous and the anticipative correlation coefficients when the injection rate  $\eta$  is varied but still equal to the feedback rate  $f$ . In Figs. 8.2.2 (a1),(a2), we add in gray curves the evolution of  $C_{1x}$  and  $C_{2x}$  in the case of single  $x$ -LP mode chaotic dynamics. In the whole range of  $\eta$ ,  $C_2 > C_1$ , whatever the LP modes that are analyzed ( $x$  or  $y$ ) and independently of the single  $x$ -LP mode or two LP mode cases in the laser dynamics (black or gray curves). The lasers therefore exhibit anticipative synchronization. The still large isochronous correlation coefficient  $C_1$  can be related to the presence of a periodicity at  $\tau$  in the intensity time-traces. For  $\eta < 3 \text{ ns}^{-1}$  the lasers exhibit either weakly synchronized irregular dynamics or locked steady-states (see the small range of  $\eta$  with perfect synchronization in the two-LP mode case). For larger  $\eta$  the synchronization quality improves with  $\eta$ . Indeed, the lasers exhibit desynchronization bursts, but the averaged time between them increases as  $\eta$  increases, hence leading to better synchronization over a given time window. The comparison between the black and gray curves in Figs. 8.2.2 (a1) and (a2) unveils moreover that the correlation coefficients (and therefore the synchronization quality) improve in the two-LP mode case, hence confirming the observation of Fig. 8.2.1 in the whole range of  $\eta$ .



**Figure 8.2.3:** Same as Fig. 8.2.2 but with  $\beta_{sp} = 10^{-6} \text{ ns}^{-1}$ .

If we now include spontaneous emission noise, we find that the master laser exhibits only a two mode chaotic dynamics, independently of the system initial condition. Figure 8.2.3 plots  $C_{1x}$  and  $C_{2x}$ , as a function of  $\eta$  and for the same parameters as in Fig. 8.2.2 but  $\beta_{sp} = 10^{-6} \text{ ns}^{-1}$ . By comparing Fig. 8.2.3 to Fig. 8.2.2, we find that the synchronization quality is slightly degraded by the inclusion of the spontaneous emission noise, as also seen in other systems [190]. However, both correlation coefficients are still larger than those obtained in the case of a deterministic single-mode chaotic dynamics [compare Figs. 8.2.3(a1) and 8.2.3(a2) to the gray curves in Figs. 8.2.2(a1) and 8.2.2(a2) respectively]. The enhancement of synchronization quality, in the case of a two-mode dynamics, can therefore not be attributed to noise, which has typically the opposite effect, but rather to the two-mode dynamics itself.



**Figure 8.2.4:** Evolution of anticipating synchronization quality  $C_{2x}$  when varying the VCSEL birefringence  $\gamma_p$ .

As a final test, we investigate how the anticipative synchronization qual-



ity evolves when the system is driven from its bistability region to a region where only a single mode solution exists even in the presence of spontaneous emission. In fact, we show that, by varying  $\gamma_p$ , a robust feedback-induced single-mode chaotic dynamics can be obtained. Fig. 8.2.4 shows the evolution of  $C_{2x}$  when  $\gamma_p$  is changed but for a fixed injection parameter ( $\eta = f = 8 \text{ ns}^{-1}$ ). We start with  $\gamma_p = 6 \text{ rad.ns}^{-1}$  for which the system operates in a bistability region. As discussed in Fig. 8.2.3, the system exhibits a chaotic dynamics in both LP modes and a very good anticipative synchronization is achieved. If  $\gamma_p$  is then increased, we observe an abrupt degradation of the synchronization around  $\gamma_p = 10 \text{ rad.ns}^{-1}$ . In fact for  $\gamma_p > 10 \text{ rad.ns}^{-1}$  only the  $x$ -LP mode is stable in the free-running VCSEL [60]. The system exhibits then a robust single mode dynamics even with noise and the decrease of synchronization quality corresponds to this transition from two mode to one mode dynamics. As  $\gamma_p$  is increased further, the synchronization quality does not vary anymore.

Our conclusions remain valid also when accounting for frequency detuning and additional optical feedback on the slave laser (closed loop). However, as already observed for edge-emitting lasers [192], an increase of the detuning and/or an increase of the slave laser feedback rate leads to a decrease of the synchronization quality, both for one-mode and two-mode dynamics cases.

### 8.3 Polarization synchronization in unidirectionally coupled VCSELS with orthogonal optical injection

In this section, we analyze theoretically the synchronization properties and polarization dynamics of two VCSELS that are unidirectionally coupled in a master-slave configuration that has been investigated experimentally by Hong *et al.* [167] and M. W. Lee *et al.* [156]. The configuration, represented in Fig. 8.1.2(b), is such that 1/ the master VCSEL is rendered chaotic via optical feedback, 2/ the master laser exhibits chaos in its two orthogonal  $x$  and  $y$ -LP modes, 3/ the  $x$ -LP mode of the chaotic emitter is rotated to  $y$ -LP direction and injected into the slave laser, 4/ the free-running slave VCSEL emits almost only the  $x$ -LP mode, the  $y$ -LP mode being strongly suppressed, and finally 5/ the slave laser is only subject to optical injection and not to optical feedback (open-loop configuration). The coupled VCSEL configuration is therefore based on an isotropic optical feedback on the master laser, and an orthogonal optical injection on the slave laser.

Our theoretical analysis successfully reproduces qualitatively the VCSEL experimental results, that is, coupling light from the master to the slave VCSEL makes it possible to excite the normally depressed  $y$ -LP mode in the

slave laser and to induce a good synchronization between the  $y$ -LP mode dynamics of the slave laser and the chaotic dynamics in the injected LP mode of the master laser. The chaos synchronization between  $y$ -LP slave laser mode and  $x$ -LP injected master laser mode is furthermore accompanied by an anti-synchronization between the  $x$ -LP slave laser mode and the  $x$ -LP injected master laser mode. The anti-synchronization is the result of the anti-correlated dynamics between LP modes in the slave laser.

### 8.3.1 Rate equation model

Similarly to what has been performed in the preceding section, the polarization dynamics in each of the two coupled VCSELS is modelled by an extension of the spin-flip model (SFM) that accounts for the isotropic optical feedback in the master laser equations, and for an orthogonal optical injection in the slave laser equations. The parameters of the slave laser are adjusted in such a way that it emits  $x$ -LP light when not coupled. The  $x$ -LP mode of the master laser is then rotated to the  $y$  direction before being injected into the slave laser, i.e., the polarization of the coupled light is parallel to the suppressed LP mode of the slave laser. Our rate equations are:

$$\begin{aligned} \frac{dE_{x_M}}{dt} &= \kappa(1+i\alpha)[(D_M-1)E_{x_M} + id_M E_{y_M}] \\ &\quad - (\gamma_{a_M} + i\gamma_{p_M})E_{x_M} \\ &\quad + fE_{x_M}(t-\tau)\exp(-i\omega_M\tau), \end{aligned} \quad (8.3.1)$$

$$\begin{aligned} \frac{dE_{y_M}}{dt} &= \kappa(1+i\alpha)[(D_M-1)E_{y_M} - id_M E_{x_M}] \\ &\quad + (\gamma_{a_M} + i\gamma_{p_M})E_{y_M} \\ &\quad + fE_{y_M}(t-\tau)\exp(-i\omega_M\tau), \end{aligned} \quad (8.3.2)$$

$$\begin{aligned} \frac{dD_M}{dt} &= -\gamma_e \left[ D_M \left( 1 + |E_{x_M}|^2 + |E_{y_M}|^2 \right) \right] \\ &\quad + \gamma_e \mu_M - i\gamma_e d_M (E_{y_M} E_{x_M}^* - E_{x_M} E_{y_M}^*), \end{aligned} \quad (8.3.3)$$

$$\begin{aligned} \frac{dd_M}{dt} &= -\gamma_s d_M - \gamma_e d_M \left( |E_{x_M}|^2 + |E_{y_M}|^2 \right) \\ &\quad - i\gamma_e D_M (E_{y_M} E_{x_M}^* - E_{x_M} E_{y_M}^*) \end{aligned} \quad (8.3.4)$$

for the master laser, and for the slave laser:

$$\begin{aligned} \frac{dE_{xS}}{dt} &= \kappa(1+i\alpha)[(D_S-1)E_{xS}+id_S E_{yS}] \\ &\quad -(\gamma_{a_S}+i\gamma_{p_S})E_{xS}, \end{aligned} \quad (8.3.5)$$

$$\begin{aligned} \frac{dE_{yS}}{dt} &= \kappa(1+i\alpha)[(D_S-1)E_{yS}-id_S E_{xS}] \\ &\quad +(\gamma_{a_S}+i\gamma_{p_S})E_{yS} \\ &\quad +\eta E_{xM}(t-\tau_c)\exp[i(\omega_M-\omega_S)t]\exp(-i\omega_M\tau_c) \end{aligned} \quad (8.3.6)$$

$$\begin{aligned} \frac{dD_S}{dt} &= -\gamma_e\left[D_S\left(1+|E_{xS}|^2+|E_{yS}|^2\right)\right] \\ &\quad +\gamma_e\mu_S-i\gamma_e d_S(E_{yS}E_{xS}^*-E_{xS}E_{yS}^*), \end{aligned} \quad (8.3.7)$$

$$\begin{aligned} \frac{dd_S}{dt} &= -\gamma_s d_S -\gamma_e d_S\left(|E_{xS}|^2+|E_{yS}|^2\right) \\ &\quad -i\gamma_e D_S(E_{yS}E_{xS}^*-E_{xS}E_{yS}^*). \end{aligned} \quad (8.3.8)$$

$E_{xM,yM}$  and  $E_{xS,yS}$ ,  $D_M$  and  $D_S$ ,  $d_M$  and  $d_S$  are defined as in eqs. (8.2.1)-(8.2.8). Likewise, the internal VCSEL parameters ( $\kappa$ ,  $\gamma_e$ ,  $\gamma_{aM}$ ,  $\gamma_{aS}$ ,  $\gamma_{pM}$ ,  $\gamma_{pS}$ ,  $\gamma_s$ ,  $\alpha$ ),  $f$ ,  $\eta$ , and  $\mu$  have the same meaning as in Section 8.2.  $\omega_M$  being the optical frequency of the  $x$ - and  $y$ -polarized modes at the solitary laser threshold in the absence of linear anisotropies.  $\tau_c$  is the propagation delay time between the coupled VCSELS. The detuning is defined as  $\Delta\omega = \omega_M - \omega_S$ , where  $\omega_S$  is the slave optical frequency and is defined in the same way as  $\omega_M$ . We first consider the case for which all parameters of the master and slave lasers are identical, except for the laser frequencies. We take the following values for the laser parameters:  $\gamma_e = 1 \text{ ns}^{-1}$ ,  $\kappa = 300 \text{ ns}^{-1}$ ,  $\alpha = 3$ ,  $f = 5 \text{ GHz}$ ,  $\tau_c = 0$ ,  $\gamma_s = 50 \text{ ns}^{-1}$ ,  $\omega_M\tau = 6 \text{ rad}$ ,  $\tau = 3 \text{ ns}$ ,  $\gamma_{a_S} = \gamma_{a_M} = -0.1$ ,  $\gamma_{p_S} = \gamma_{p_M} = 8.5 \text{ rad/ns}$ , and  $\mu_M = \mu_S = 1.2$ . With these values of the VCSEL parameters the free-running lasers exhibit a single  $x$ -LP mode stationary dynamics.

### 8.3.2 Polarization switching and polarization synchronization

As a result of the optical feedback, the master laser dynamics exhibits optical chaos in its two LP modes. The master laser  $x$ -LP mode is then rotated to orthogonal direction and injected into the slave VCSEL. We show in Fig. 8.3.1(a) the evolution of the averaged intensities in the two LP modes of the slave laser (with dots) and of the slave laser total intensity (with circles) as we vary the frequency detuning between master and slave lasers and for a fixed value of the injected power  $\eta = 100 \text{ GHz}$ . As we scan the frequency detuning from negative to positive detuning values we can observe a polarization switching from the normally dominant  $x$ -LP slave laser mode to the

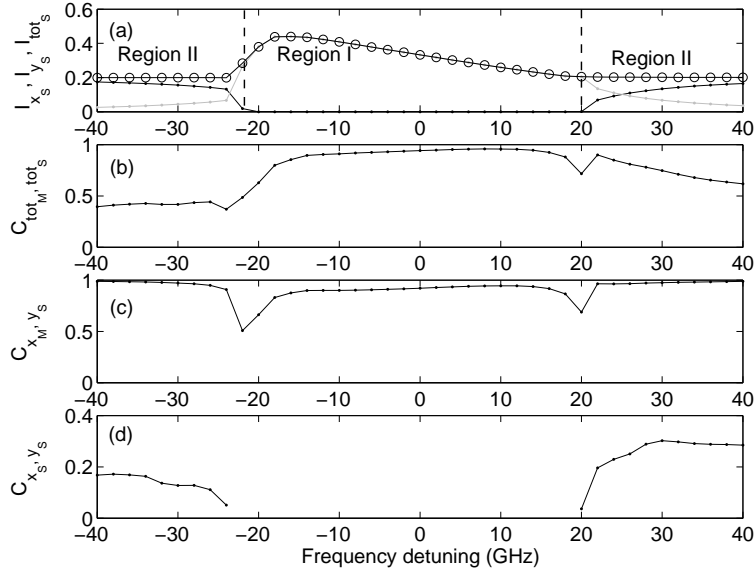


**Figure 8.3.1:** Evolution of the time-averaged LP mode and total intensities in the slave laser (a), of the correlation coefficient  $C_{tot_M,tot_S}$  (b),  $C_{x_M,y_S}$  (c),  $C_{x_S,y_S}$  (c) as function of the frequency detuning, for a fixed injection rate  $\eta = 100$  GHz. Parameters are specified in the text.

normally suppressed  $y$ -LP slave laser mode and then back to the  $x$ -LP mode. We find therefore a detuning interval inside which the slave laser switches its polarization to that of the injected light, and moreover inside which the normally dominant slave laser  $x$ -LP mode is fully suppressed. We shall call this region 'region I' to emphasize that the slave VCSEL only exhibits a single-mode dynamics (in the  $y$ -LP mode). As shown in Fig. 8.3.1(a) the region I expands from frequency detuning of -22 GHz up to about 20 GHz. Outside region I the slave VCSEL exhibits dynamics in its two LP modes, and therefore we shall call this region 'region II'. In region I the total intensity emitted by the slave VCSEL is larger than in region II and depends on the frequency detuning. In region II the total intensity of the slave laser light is kept constant whatever the frequency detuning, which relates to the fact that the intensity in the  $x$ -LP mode decreases at the benefit of the increase in the  $y$ -LP mode intensity. In region I the total intensity of the slave laser light increases because the slave laser mode emits only in the  $y$ -LP mode and the injected light therefore interacts coherently with the slave  $y$ -LP mode and supports the  $y$ -LP mode intensity. In region II the slave laser dynamics consists of a dominant  $x$ -LP mode dynamics interacting incoherently with the injected light and, hence, the slave total intensity is purely the incoherent addition of its two LP mode intensities.

An interesting question, motivated by previous studies on chaos synchronization in coupled edge-emitting lasers, is whether the chaotic dynamics of the slave laser, induced by the optical injection, is able to synchronize to the master laser optical chaos. We find that indeed not only the LP mode dynamics but possibly also the total intensity dynamics can be synchronized between master and slave lasers, depending on the injection strength and frequency detuning. In the following we analyze quantitatively the synchronization quality between the intensity time-traces by using the following cross-correlation coefficients  $C_{x_M, y_S}$ ,  $C_{x_S, y_S}$  and  $C_{tot_M, tot_S}$ :

$$C_{x_M, y_S} = \frac{\langle [I_{x_M}(t-\tau_c) - \langle I_{x_M} \rangle][I_{y_S}(t) - \langle I_{y_S} \rangle] \rangle}{\sqrt{\langle [I_{x_M}(t) - \langle I_{x_M} \rangle]^2 \rangle \langle [I_{y_S}(t) - \langle I_{y_S} \rangle]^2 \rangle}} \quad (8.3.9)$$

$$C_{x_S, y_S} = \frac{\langle [I_{x_S}(t-\tau_c) - \langle I_{x_S} \rangle][I_{y_S}(t) - \langle I_{y_S} \rangle] \rangle}{\sqrt{\langle [I_{x_S}(t) - \langle I_{x_S} \rangle]^2 \rangle \langle [I_{y_S}(t) - \langle I_{y_S} \rangle]^2 \rangle}} \quad (8.3.10)$$

$$C_{tot_M, tot_S} = \frac{\langle [I_{tot_M}(t-\tau_c) - \langle I_{tot_M} \rangle][I_{tot_S}(t) - \langle I_{tot_S} \rangle] \rangle}{\sqrt{\langle [I_{tot_M}(t) - \langle I_{tot_M} \rangle]^2 \rangle \langle [I_{tot_S}(t) - \langle I_{tot_S} \rangle]^2 \rangle}} \quad (8.3.11)$$

For the coupling configuration considered here, we only observe synchronization of the isochronous type [191, 200, 201], which leads to a maximum of the correlation for a time lag equal to  $\tau_c$  between the intensity time-traces. In our case we have chosen  $\tau_c = 0$ . Anticipating synchronization [189, 191, 202] is not observed, as could be expected for such a dissymmetric coupling in which we have orthogonal injection of only one of the two LP components.

Figure 8.3.1 shows the correlation degree between the time-traces of the total intensity in master and slave lasers [Fig. 8.3.1(b)], the  $x$ -LP master laser intensity and the  $y$ -LP slave laser intensity [Fig 8.3.1(c)], and between the intensities of the slave laser modes [Fig 8.3.1(c)], as we scan the frequency detuning and for a fixed injection strength. Interestingly, Fig. 8.3.1(b) shows that the total intensities in master and slave lasers are badly synchronized in region II (correlation coefficient very small) even though the correlation coefficient  $C_{x_M, y_S}$  [in Fig. 8.3.1(c)] is close to 1, which implies an almost perfect synchronization between the  $x$ -LP injected light intensity dynamics and the dynamics in the slave laser  $y$ -LP mode. By contrast, in region I the total intensities of the master and slave reveal a degree of synchronization similar to that existing between the master  $x$ -LP and slave  $y$ -LP modal intensities, with a maximum correlation coefficient around 0.9. Even though, for the parameter set considered here, the synchronization of the total intensities is better in region I than in region II, the synchronization quality between the master  $x$ -LP and the slave  $y$ -LP components is better in region II than in region I. This outlines the importance of considering polarization-resolved synchronization. The analysis of the correlation between slave LP mode intensities in Fig. 8.3.1(d) does not provide clear indication of correlated or

anticorrelated dynamics, since the computed correlation coefficient is very close to zero. The cross-correlation  $C_{x_S, y_S}$  is not computed in region I since there the  $x$ -LP slave laser mode is fully suppressed.

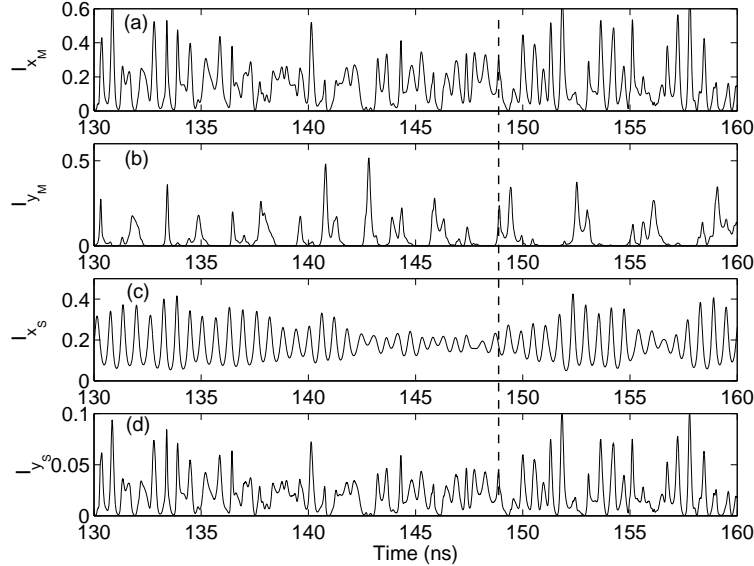


**Figure 8.3.2:** *Time-series of master laser and slave laser LP mode intensities, for  $\eta = 100$  GHz and  $\Delta\omega = -40$  GHz (corresponding to region II).*

Figure 8.3.2 analyzes in more detail the time-traces of master and slave laser LP intensities, in the synchronization conditions corresponding to region II ( $\eta = 100$  GHz and  $\Delta\omega/2\pi = -40$  GHz). The comparison between the time-traces in Fig. 8.3.2(a) and Fig. 8.3.2(d) shows that the intensity corresponding to the depressed  $y$ -LP mode of the slave laser is almost perfectly synchronized with the injected  $x$ -LP intensity of the master laser, with a time-lag equal to  $\tau_c = 0$  between the intensity time-traces (as better seen with the reference dashed line). The comparison between the time-traces in Fig. 8.3.2(a) and Fig. 8.3.2(b), i.e., the time-traces of intensities in the LP master laser modes, shows that the LP mode intensities exhibit fast in-phase pulsing but also anticorrelated dynamics on a slower time-scale: when one mode is dominant, the other mode is depressed and vice-versa. Such a mode competition with inphase fast pulsing when the two modes are excited together has been already observed theoretically and experimentally in VCSELS subject to optical feedback [203, 204]. The comparison between the time-traces in Fig. 8.3.2(c) and Fig. 8.3.2(d), i.e., the time-traces of intensities in the LP slave laser modes, shows no clear indication of correlated or anticorrelated dynamics on the pulsing time-scale, which corresponds to the close to zero correlation coefficient plotted in Fig. 8.3.1(d).

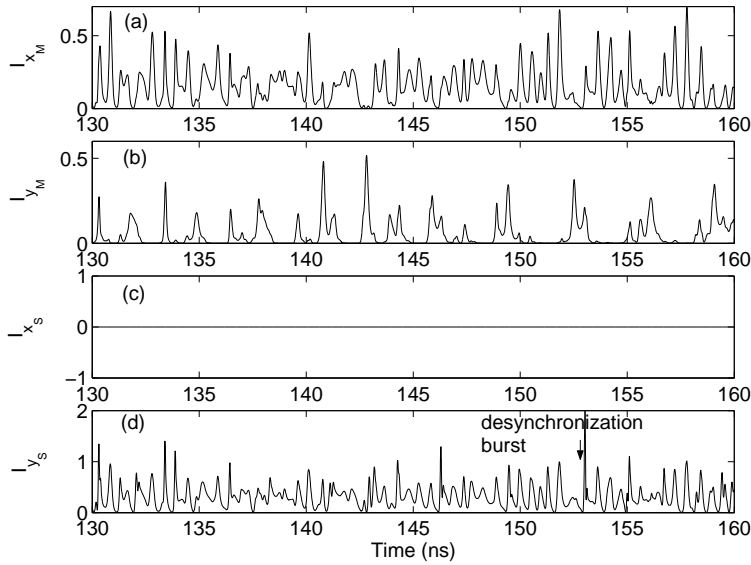


**Figure 8.3.3:** Time-series of master laser and slave laser LP mode intensities, for  $\eta = 100$  GHz and  $\Delta\omega = 0$  GHz (corresponding to region I).

Figure 8.3.3 is the same as Fig. 8.3.2 but for different coupling conditions ( $\eta = 100$  GHz and  $\Delta\omega/2\pi = 0$  GHz), corresponding to region I. As shown in Fig. 8.3.3(c), in this region the slave laser  $x$ -LP mode is fully depressed and the slave VCSEL switches its polarization from a normally dominant  $x$ -LP light polarization to a now dominant  $y$ -LP light polarization. The comparison between the time-traces in Fig. 8.3.3(a) and Fig. 8.3.3(d) shows that the slave laser  $y$ -LP intensity dynamics is relatively well synchronized with the injected master laser  $x$ -LP intensity dynamics. We observe, however, desynchronization bursts in particular during short time-periods following the switch-off of the injected light. The arrow in Fig. 8.3.3(d) indicates such a desynchronization burst following the switch off of the  $x$ -LP master laser intensity: the  $y$ -LP slave laser mode intensity [in Fig. 8.3.3(d)] exhibits a large pulse before recovering a similar pulsing dynamics than the injected one [in Fig. 8.3.3(a)]. It should also be noticed that the slave  $y$ -LP intensity is significantly larger than that of the master laser  $x$ -LP intensity, as already illustrated in Fig. 8.3.1 (a). As a result of the partial loss of synchronization, the correlation coefficient taken on average on a long time-trace is smaller than the computed one for the case of region II in Fig. 8.3.2. As for Region II, the synchronization occurs with a time-lag equal to  $\tau_c = 0$ .

In order to further complement the time-series analysis and to emphasize the qualitatively different synchronization properties of regions I and II, we show in Fig. 8.3.4 (a1), (a2) the synchronization diagrams corresponding to

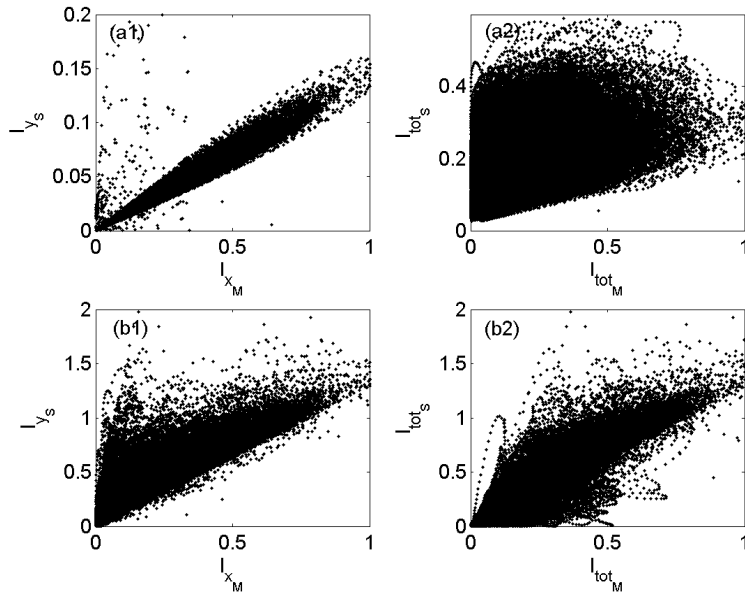


**Figure 8.3.4:** Synchronization diagrams corresponding to regions II [(a1), (a2)] and I [(b1), (b2)] of qualitatively different synchronization properties: (a1), (b1)  $I_{y_s}$  as function of  $I_{x_M}$ , (a2), (b2)  $I_{tot_s}$  as function of  $I_{tot_M}$ .

Fig. 8.3.2 and in 8.3.4(b1),(b2) the synchronization diagrams corresponding to Fig. 8.3.3. In Figures. 8.3.4(a1),(b1) is plotted the intensity of the slave laser  $y$ -LP mode as function of the intensity of the injected master  $x$ -LP mode; in Fig. 8.3.4(a2),(b2) is plotted the slave laser total intensity as function of the master laser total intensity. In the case of injection parameters corresponding to region II, the slave  $y$ -LP mode intensity is almost perfectly synchronized with the injected  $x$ -LP mode intensity of the master laser, but with the slave laser synchronized  $y$ -LP mode intensity much smaller than the injected master  $x$ -LP mode intensity. However the total intensities of the two lasers are almost uncorrelated, as shown in Fig. 8.3.4(a2) and also pointed out by the computation of the correlation coefficient in Fig. 8.3.1(b). The fact that the slave laser total intensity is badly synchronized to the master laser total intensity can be attributed to the fact that only the weak LP mode of the slave laser synchronizes very well with the dominant master LP mode. Therefore the contribution of the synchronized slave LP mode dynamics to the slave total intensity dynamics is very small. The synchronization diagram of Fig. 8.3.4(b1) better shows the desynchronization bursts between the  $y$ -LP slave laser intensity dynamics and the  $x$ -LP master laser intensity dynamics. In spite of these desynchronization events, the two LP mode intensity dynamics are relatively well synchronized in region I but the synchronization quality is clearly smaller than that observed in region II



[see the comparison between Fig. 8.3.4(b1) and Fig. 8.3.4(a1)]. Moreover, the comparison between the synchronization diagram of Fig. 8.3.4(b2) and that of Fig. 8.3.4(a2) shows that in region I the total intensity dynamics are much better synchronized than in region II, as it was already clear from the computation of the correlation coefficient in Fig. 8.3.1(b).

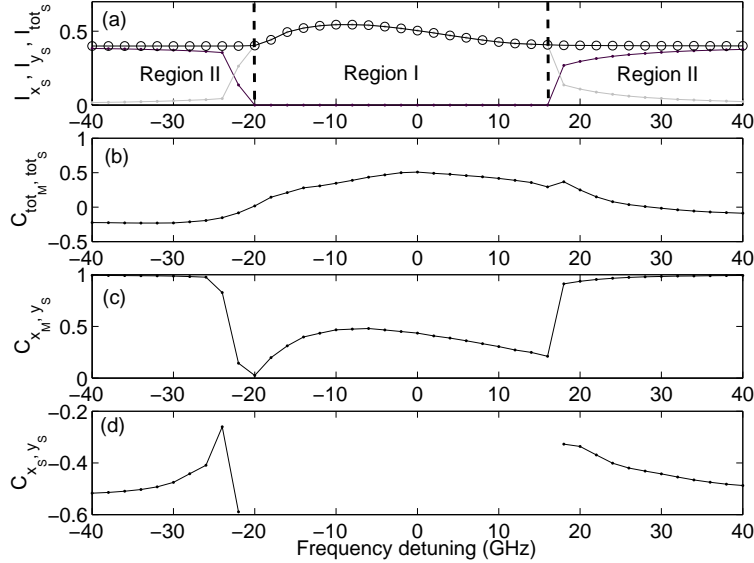


**Figure 8.3.5:** Same as Fig. 8.3.1 but considering mismatch in VCSEL linear cavity anisotropies and injection currents:  $\gamma_{a_M} = 0.1$ ,  $\gamma_{p_M} = 6$  rad/ns,  $\mu_M = 1.2$  and  $\gamma_{a_S} = -0.1$ ,  $\gamma_{p_S} = 8.5$  rad/ns,  $\mu_S = 1.4$

The previous figures have considered a case of unidirectionally coupled VCSELS but where the two coupled lasers have the same internal parameters, in particular the same linear cavity anisotropies and injection currents. However, it is commonly observed in VCSEL experiments that the polarization switching and polarization dynamical properties are strongly dependent on the device linear anisotropies and operating condition such as injection current or temperature [205]. We therefore consider now different values of the linear anisotropies  $\gamma_a$  and  $\gamma_p$  for the master and slave VCSELS, as well as different values of the injection current  $\mu$ . The VCSEL parameters and operating conditions are chosen such that the polarization properties are qualitatively similar to those used in the experimental results of Ref. [167]. The master laser is simulated with  $\gamma_{a_M} = 0.1$ ,  $\gamma_{p_M} = 6$  rad/ns and  $\mu_M = 1.2$ . The master laser exhibits a polarization switching from  $x$ -LP to  $y$ -LP mode at about  $\mu \sim 1.3$  with bistability. The slave laser is simulated with  $\gamma_{a_S} = -0.1$ ,  $\gamma_{p_S} = 8.5$  rad/ns and  $\mu_S = 1.4$ . The slave laser exhibits a single  $x$ -LP mode up to about  $\mu = 1.6$ . In order to analyze the effect of the

parameter mismatch on the polarization and total intensity synchronization properties, we plot in Fig. 8.3.5 the evolution of the LP mode and total output intensities and the correlation coefficients  $C_{x_M, y_S}$ ,  $C_{x_S, y_S}$  and  $C_{tot_M, tot_S}$  as we scan the frequency detuning for a fixed injection strength, all other parameters remaining the same as those used for Fig. 8.3.1. We still observe in Fig. 8.3.5 the existence of two regions of qualitatively different polarization and synchronization properties. In region I, the slave has switched its polarization to that of the injected field and emits only the corresponding  $y$ -LP mode. In region II the slave laser exhibits a two-LP mode dynamics. Region II is characterized by an almost perfect synchronization between the  $y$ -LP slave intensity and the injected  $x$ -LP master intensity [see Fig. 8.3.5(c)], with a correlation coefficient very close to 1. However in region II the total intensities of both master and slave VCSELS are almost uncorrelated [see Fig. 8.3.5(b)]. In region I the synchronization between  $y$ -LP slave laser intensity and  $x$ -LP master laser intensity is much weaker than that observed in region II, with a maximum correlation coefficient close to 0.5. In region I the total intensities of the two VCSELS synchronize as badly as do the corresponding polarization modes (maximum correlation coefficient close to 0.5), however the synchronization between total intensities is much better than the one observed in region II. The inclusion of mismatch between the device parameters has strongly influenced the synchronization quality inside region I since, by comparing Fig. 8.3.1(b) and Fig. 8.3.5(b) [or Fig. 8.3.1(c) and Fig. 8.3.5(c)], we see that the correlation coefficients  $C_{tot_M, tot_S}$  [or  $C_{x_M, y_S}$ ] have decreased from about maximum 0.9 to about maximum 0.5. However, and interestingly, the synchronization quality in region II between  $y$ -LP slave laser mode and injected  $x$ -LP mode has not decreased when accounting for parameter mismatch: the comparison between Fig. 8.3.1(c) and Fig. 8.3.5(c) in region II shows a correlation coefficient  $C_{x_M, y_S}$  still close to 1. We also notice from Figs. 8.3.5(b) and (c) that the maximum correlation does not occur for zero detuning but is slightly shifted towards negative detuning values. As already mentioned in other laser configurations and laser systems [192], and as will be explained further in sec. 8.3.3, this result is the consequence of the linewidth enhancement factor  $\alpha$  which influences the injection-locking mechanism. Additionally, comparing Figs. 8.3.5(d) and 8.3.1(d), we observe that the cross-correlation coefficient  $C_{x_S, y_S}$  between the slave laser mode intensities is now negative and larger in absolute value. The correlation coefficient close to -0.5 indicates a tendency for anticorrelation between the slave laser mode intensities. Our observation of synchronization of the injected light with the slave mode parallel to it and of therefore (weaker) antisynchronization with the orthogonal slave mode, qualitatively agrees with the experimental observations of Ref. [167]. On the basis of our study, we conjecture that the experimental conditions were such that the slave laser was operating in region II. The set of parameters leading to Fig. 8.3.5 being the most representative of the realistic experimental conditions of Ref. [167],

we keep these parameters fixed for the numerical simulations performed in the remainder of this Chapter, unless otherwise specified.

### 8.3.3 Mapping of correlation coefficient

In the previous section we have discussed two synchronization mechanisms in our coupled VCSEL problem. One corresponding to region I in which the normally depressed  $y$ -LP slave laser mode synchronizes with the injected  $x$ -LP master laser mode, while the slave  $x$ -LP mode is completely suppressed by the orthogonal injection. The second corresponding to region II in which the slave laser exhibits a two-mode dynamics, with a depressed  $y$ -LP mode almost perfectly synchronized with the injected  $x$ -LP master laser mode and with anticorrelation between the slave laser LP mode dynamics.

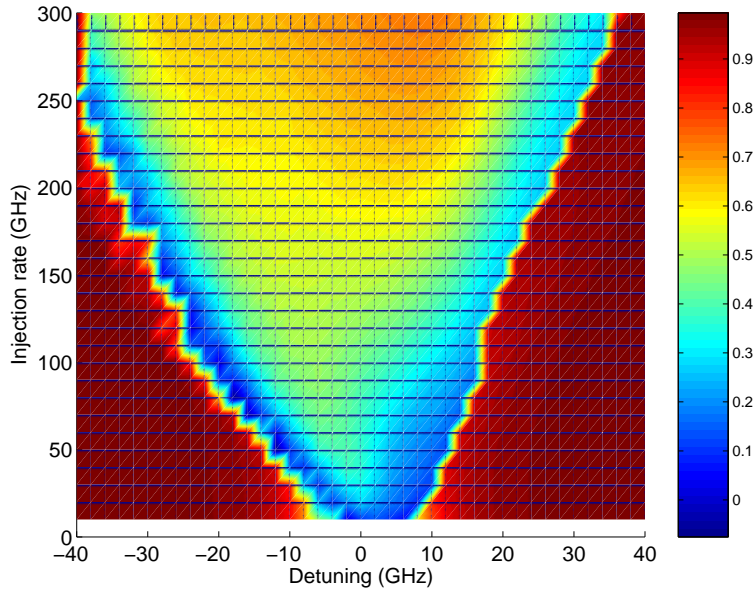


**Figure 8.3.6:** Mapping of correlation coefficient  $C_{x_M, y_S}$  at zero time-lag between the time-traces corresponding to master  $x$ -LP mode and to slave  $y$ -LP mode, in the plane of the injection parameters.

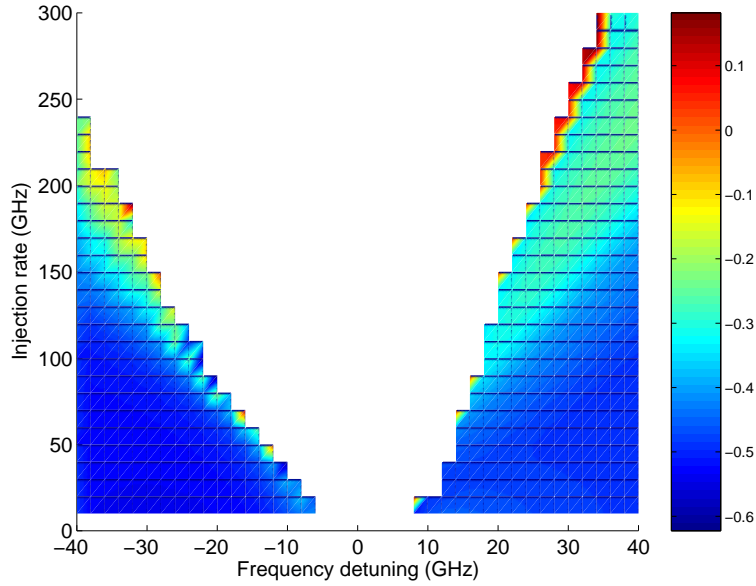
We analyze in Fig 8.3.6 and Fig. 8.3.7 the dependency of the  $C_{x_M, y_S}$  and  $C_{x_S, y_S}$  correlation coefficients, respectively, on the coupling parameters: injection rate  $\eta$  and frequency detuning  $\Delta\omega/2\pi$ . A color map is used in each case and plotted on the right of the figure. The maximum injection rate is chosen such that it corresponds to a realistic value for VCSEL devices. Indeed we can write  $\eta = r(1 - r^2)t_{ext}/(r\tau_{in})$ , where  $r$  is the amplitude

reflectivity of the VCSEL output mirror,  $t_{ext}$  is the amplitude transmissivity in the path between the coupled VCSELS, and  $\tau_{in}$  is the intra-cavity round-trip time. In the optimal case for which there is no attenuation in the path between coupled VCSELS, i.e.,  $t_{ext} = 1$ , taking  $r = 0.995$  and  $\tau_{in} = 3 \times 10^{-5}$  ns as typical values for VCSELS [206] gives  $\eta \sim 330$  GHz.

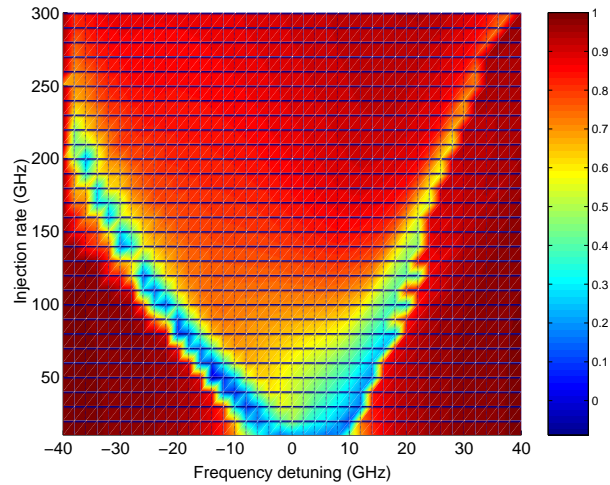
As shown in Fig. 8.3.6, Region I is approximately centered around zero frequency detuning and its boundaries span larger frequency detunings as we increase the injection strength. This region I corresponds to a relatively good synchronization quality, as the correlation coefficient can be as large as 0.8 for sufficiently large injection strengths. In this region, an injection locking-type of synchronization occurs, which is induced by the increase of the injected field strength [207]. The synchronization therefore increases in quality with the increase of the injection rate, and is progressively lost when the detuning is increased. Region I displays a triangle-like shape typical to the so-called Arnold's tongue. By contrast, region II is found for either large positive or negative detunings, with a boundary that depends on the injection strength. Region II corresponds to an almost perfect synchronization (correlation coefficient close to 1), and this independently of the value of the injection rate. As already discussed in Figs. 8.3.1 and 8.3.5, the boundary between region I of good synchronization and region II of perfect synchronization also corresponds to the polarization switching boundaries. Importantly, we observe that Fig. 8.3.6 is consistent with the conclusions on polarization switching induced by optical injection of stationary light as reported in Chapter 5, i.e., the injected power required to induce the polarization switching of the slave laser decreases as the frequency detuning moves towards zero.

Figure 8.3.7 analyzes the mapping of the cross-correlation between slave laser LP mode intensities in the plane of the coupling parameters. As mentioned earlier, the two slave laser LP mode intensities show some degree of anticorrelation in a large range of injection parameters inside region II, which also means that the slave laser  $x$ -LP mode shows some degree of anti-synchronization with the injected master  $x$ -LP mode. Interestingly, the degree of anticorrelation (and therefore anti-synchronization) increases as the injection rate decreases.

The synchronization quality inside region I (injection-locking-type synchronization) can be significantly improved if we remove the parameter mismatch between master and slave laser linear cavity anisotropies, as shown in Fig. 8.3.8 for  $\gamma_{aM} = \gamma_{aS} = -0.1$ ,  $\gamma_{pM} = \gamma_{pS} = 8.5$  rad/ns, all the other parameters remaining the same than in Fig. 8.3.5. Interestingly, for large injection strength the synchronization quality in region I can be as good as that in region II, which means that the two VCSELS synchronize well their LP mode dynamics regardless of their frequency detuning range. This result significantly differs from what is observed in comparable studies in edge-emitting



**Figure 8.3.7:** Mapping of cross-correlation coefficient  $C_{x_S, y_S}$  between slave laser LP mode intensities in the plane of the injection parameters.



**Figure 8.3.8:** Mapping of correlation coefficient  $C_{x_M, y_S}$  at zero time-lag between the time-traces corresponding to master  $x$ -LP mode and to slave  $y$ -LP mode, in the plane of the injection parameters with no mismatch between the values of linear cavity anisotropies in slave and master VCSELS.

lasers [191], where a good modal or total intensity synchronization occurs in relatively small parameter regions corresponding to injection-locking conditions, or to anticipative synchronization mechanisms. This result is here the consequence of the LP mode dynamics in VCSELS which makes it possible to observe two regions I and II in which good synchronization occurs.

### 8.3.4 Influence of $\gamma_s$ on the two regions of synchronization

We pay particular attention in this section to the influence of the spin-flip relaxation rate  $\gamma_s$  on the results observed earlier. This parameter of the laser model accounts for microscopic processes that lead to the homogenization of the carrier spins. Several experiments have shown a good agreement with the SFM model when including a large or even infinite value for the  $\gamma_s$  parameter [63], which also means that in such experiments the time-scale for carrier spin relaxation processes is very short and hence does not play a role in the physics underlying polarization dynamics in VCSELS. By contrast, other experiments have resulted in a good fitting with the SFM model for a small value of  $\gamma_s$  down to  $\gamma_s = 10 \text{ ns}^{-1}$  [64]. The spin-flip relaxation time-scale becomes then comparable to other internal time-scales of the VCSEL such as carrier relaxation time or inverse of birefringence frequency. In comparisons between numerical simulations performed with SFM model and experiments it is therefore crucial to investigate the specific role of the  $\gamma_s$  as a fitting parameter whose value may significantly vary from one VCSEL device to another one.

Figure 8.3.9 analyzes the mapping of correlation properties between  $y$ -LP mode intensity of the slave VCSEL and injected  $x$ -LP mode intensity of the master laser, for increasing values of  $\gamma_s$  and all other parameters remaining the same as those used in Fig. 8.3.6. The color code for the mappings is the same as that used previously, hence making easier the comparison with previous mappings for different parameters. As shown in Fig. 8.3.9(d), increasing  $\gamma_s$  up to  $300 \text{ ns}^{-1}$  does not significantly modify the picture of the mapping of the correlation coefficient. This also interestingly means that our results are valid even for VCSELS in which spin-flip relaxation mechanisms do not play a significant role in the physics of polarization switching. A decrease of  $\gamma_s$ , however, leads to interesting new conclusions. The boundaries corresponding to region I, with single  $y$ -LP mode dynamics in the slave laser, are almost unaffected by a change in  $\gamma_s$ . However, the synchronization quality inside region I increases when the spin-flip relaxation rate  $\gamma_s$  decreases. By contrast, the comparison between Figs. 8.3.9(a)-(c) and Fig. 8.3.6 shows that the decrease of  $\gamma_s$  significantly influences the synchronization properties inside region II, where the normally depressed  $y$ -LP mode of the slave laser synchronizes with the injected  $x$ -LP mode of the master laser. For small values of  $\gamma_s$  such as in Figs 8.3.9(a) and Fig. 8.3.9(b) the synchronization

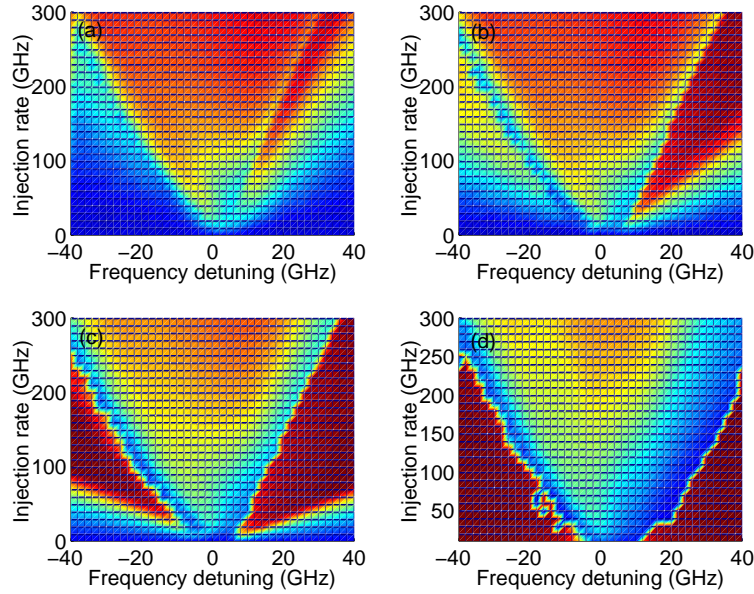


**Figure 8.3.9:** Mapping of correlation coefficient  $C_{x_M, y_S}$  at zero time-lag between the time-traces corresponding to master  $x$ -LP mode and to slave  $y$ -LP mode, in the plane of the injection parameters with different values of the spin-flip relaxation rate parameter: (a)  $\gamma_s = 10 \text{ ns}^{-1}$ , (b)  $\gamma_s = 30 \text{ ns}^{-1}$ , (c)  $\gamma_s = 40 \text{ ns}^{-1}$ , (d)  $\gamma_s = 300 \text{ ns}^{-1}$ .

quality between the master  $x$ -LP and slave  $y$ -LP modes in region II is now comparable or only slightly better than in region I. Additionally, region II of synchronization expands over small ranges of injection rates and frequency detuning and is located mostly in the positive frequency detuning side. For larger values of  $\gamma_s$  such as in Fig. 8.3.9(c) and Fig. 8.3.9(d) the synchronization quality of region I is significantly smaller than that of region II and moreover, the region II of synchronization expands towards smaller injection rates and larger positive or negative frequency detunings. A region II of almost perfect synchronization quality between  $y$ -LP slave laser mode and  $x$ -LP master laser mode is therefore more easily observed in VCSELS with a relatively large  $\gamma_s$  value.

The improvement of the synchronization quality in region II as  $\gamma_s$  increases from the situation corresponding to Fig. 8.3.9(a) ( $\gamma_s = 10 \text{ ns}^{-1}$ ) to the situation corresponding to Fig. 8.3.9(c) ( $\gamma_s = 40 \text{ ns}^{-1}$ ), is made clear in Fig. 8.3.10. The time-traces of the  $x$ -LP master laser intensity and of the  $y$ -LP slave laser intensity are plotted for these two values of  $\gamma_s$ . In the case of small  $\gamma_s$  [Fig. 8.3.10(a) and Fig. 8.3.10(b)], the time-traces exhibit a

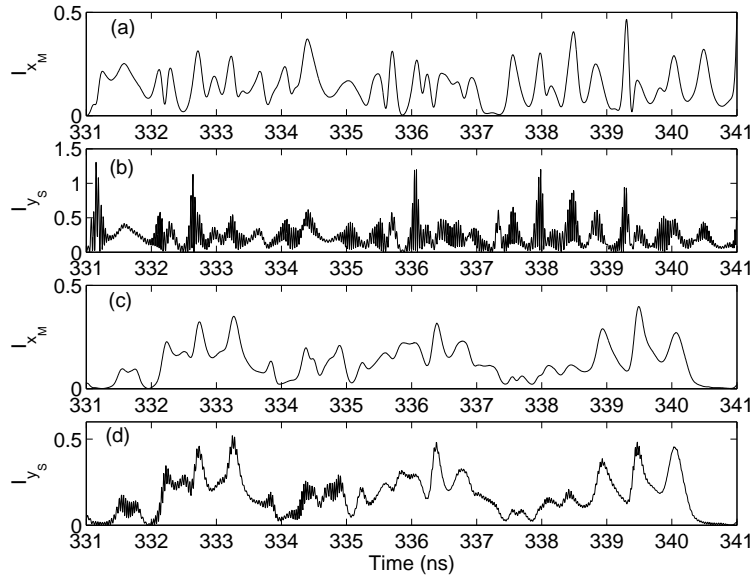


**Figure 8.3.10:** Time traces of the  $x$ -LP master laser intensity and  $y$ -LP slave laser intensity for  $\eta = 200$  GHz,  $\Delta\omega/2\pi = 30$  GHz and for two different values of the spin-flip relaxation rate parameter: (a), (b)  $\gamma_s = 10$  ns $^{-1}$  and (c), (d)  $\gamma_s = 40$  ns $^{-1}$ .

relatively good synchronization when looking at the envelopes of the pulses. The slave laser dynamics, however, exhibits more complex pulsing behavior with faster pulsating dynamics not present in the master laser dynamics. In the case of larger  $\gamma_s$  [Fig. 8.3.10(c) and Fig. 8.3.10(d)] the synchronization between the  $x$ -LP master laser intensity and the  $y$ -LP slave laser intensity is significantly improved and almost perfect.

The modifications of LP mode synchronization properties as the spin-flip relaxation rate varies also coincide with qualitative changes in the free-running slave laser LP mode dynamics, as better seen in Fig. 8.3.11. Figure 8.3.11 plots the slave laser LP mode intensity time-traces when not subject to injection from the master laser, i.e., in the free-running operation, and for the values of  $\gamma_s$  corresponding to the cases of Fig. 8.3.9(a)-(d). In each case, the slave laser LP mode dynamics is such that the  $x$ -LP mode is the dominant LP mode, in agreement with our orthogonal optical injection scheme. In the case of Fig. 8.3.11(d), as for  $\gamma_s > 50$  ns $^{-1}$ , the  $y$ -LP mode is completely suppressed. However, for smaller values of  $\gamma_s$  the free-running slave VCSEL exhibits a two-mode dynamics with either the LP mode intensities steady in time [Fig. 8.3.11(c)] or exhibiting a chaotic [Fig. 8.3.11(b)] or even a time-periodic dynamics [Fig. 8.3.11(a)]. It is indeed well known from previous studies of SFM model for a free-running VCSEL that the decrease of the



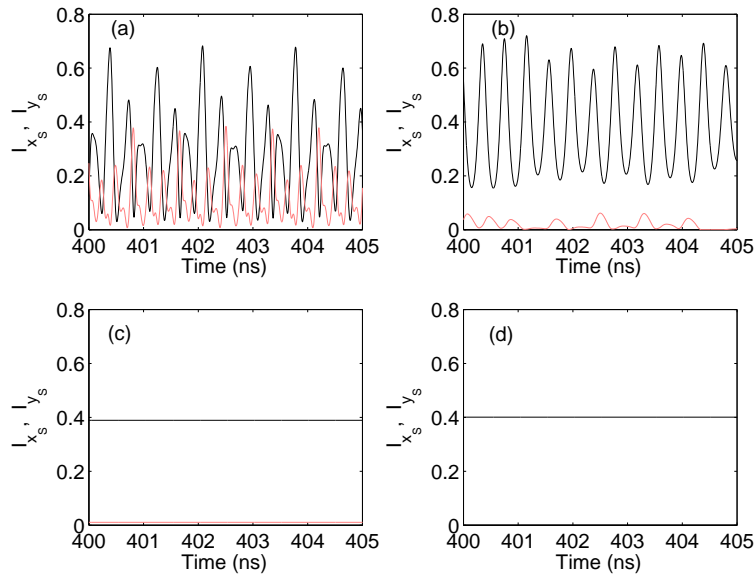


**Figure 8.3.11:** Time-traces of the  $x$ -LP (black) and  $y$ -LP (red) slave laser mode intensities for different values of the spin-flip relaxation rate parameter: (a)  $\gamma_s = 10 \text{ ns}^{-1}$ , (b)  $\gamma_s = 30 \text{ ns}^{-1}$ , (c)  $\gamma_s = 40 \text{ ns}^{-1}$ , (d)  $\gamma_s = 300 \text{ ns}^{-1}$ .

value for the  $\gamma_s$  parameter allows for stable elliptically polarized steady-state solution or time-dependent two mode dynamics [60]. Stable stationary elliptically polarized states and complex time-dependent two LP mode-dynamics have been demonstrated experimentally in free-running VCSELs [208]. The results of Fig. 8.3.11 together with the corresponding synchronization results in Fig. 8.3.9 suggest that the difference of LP mode dynamics in the slave VCSEL, as a result of modifications of nonlinearities related to spin-flip relaxation mechanisms, strongly influences the synchronization properties in our orthogonally polarized master-slave injection scheme. More specifically, the existence of a strong, complex, two-mode dynamics in the free-running VCSEL [such as in Fig. 8.3.11(a)] seems to favor the existence of a large region I of good synchronization and a small region II of similar or slightly better synchronization quality. By contrast, the only  $x$ -mode dynamics in the slave laser as obtained in Fig. 8.3.11(d) favors the existence of a large region II of perfect synchronization.

## 8.4 Conclusions

In conclusion, we have shown that polarization-resolved chaotic dynamics can dramatically affect the quality of synchronization between two unidirect-

ionally-coupled VCSELS. In the isotropic injection scheme, we unveil that the synchronization quality between unidirectionally coupled VCSELS can be significantly enhanced when the feedback-induced chaos in the master laser involves both orthogonal LP fundamental transverse modes. This effect is particularly clear when tuning the VCSEL birefringence and even in the realistic presence of spontaneous emission noise. Concretely, by varying the VCSEL birefringence, we have observed that a relatively strong degradation of the synchronization quality appears around the transition region between the VCSEL's bistable polarization zone (a parameter zone where two-mode chaotic dynamics are resolved) and the single-mode stability zone. Our results are interesting for dedicated experiments where the linear cavity anisotropies, and therefore the VCSEL polarization mode behavior, can be modified by strain and/or temperature effects [205]. They are also thought to be important in the context of emerging VCSEL chaos based communication systems.

We have also investigated in detail the synchronization properties and polarization dynamics of two VCSELS unidirectionally coupled in a master-slave configuration with isotropic optical feedback on the master laser and orthogonal optical injection on the slave laser. The free-running slave laser is such that it emits only in  $x$ -LP mode and the injected light is polarized in the orthogonal,  $y$ -LP direction. Such a coupled VCSEL configuration has been analyzed experimentally by Hong *et al.* [167]. Our results show interestingly two regions of different synchronization mechanisms. In the so-called region I the slave VCSEL switches its polarization to that of the injected light and emits only in a locked  $y$ -LP mode. The intensity of the  $y$ -LP slave laser mode is relatively well synchronized with the injected master  $x$ -LP mode, with a synchronization quality that strongly depends on the parameter mismatch between coupled VCSELS. In this region I the total intensity of the slave laser synchronizes to the total intensity of the master laser as well as the  $y$ -LP mode slave intensity synchronizes to the injected  $x$ -LP mode. In the so-called region II, by contrast, the slave VCSEL emits a two mode-dynamics. The slave laser  $y$ -LP mode is almost perfectly synchronized with the injected  $x$ -LP mode, although with a significant attenuation. The slave laser  $x$ -LP mode is moreover anticorrelated with the slave laser  $y$ -LP mode, hence is anti-synchronized with the injected master laser  $x$ -LP mode. Although the polarization modes exhibit an excellent synchronization, the total intensities of master and slave lasers are almost uncorrelated. The range of frequency detuning in which region II is found increases as the injection strength decreases, and moreover the boundaries of the region II are found to significantly depend on the  $\gamma_s$  parameter which models the non-linearity associated with spin-flip relaxation mechanisms in VCSELS. Both synchronization mechanisms, associated with regions I and II, are found to be robust against modifications of the device parameters, hence making their

observations general to different VCSEL devices. Our results agree qualitatively with the synchronization properties found experimentally [167], but they also report on new findings that stimulate further investigation. In particular the experiment reports only on the region II type of synchronization, and does not analyze its interesting dependency on the injection strength and internal device parameters, nor the synchronization properties of the total intensities. The theory predicts the existence of another synchronization region (region I), which also behaves very differently with respect to the total intensity synchronization, robustness on parameter mismatch, and influence of spin-flip relaxation rate.



# Chapter 9

## Conclusions

### 9.1 Summary of our main results

Vertical-cavity surface-emitting lasers (VCSELs) have competitive advantages with respect to conventional edge-emitting lasers such as the fabrication of dense two-dimensional VCSEL arrays for optical interconnects. On the other hand, VCSELs exhibit intriguing polarization properties which are critical in polarization-sensitive applications. Polarization switching (PS) between two VCSEL's preferential orthogonal LP modes may be induced by changing the bias current, temperature or externally through current modulation, optical feedback or optical injection. In the particular case of optical injection, depending on optical injection parameters, i.e., the injected power and the frequency detuning, injection-locking of the VCSEL can be achieved. Applications of injection-locking range from laser spectral narrowing, frequency chirp reduction to all-optical add-drop functionality in optical networks.

Considerable research efforts have been undertaken not only to understand VCSEL's unique polarization properties but also to address the key issues of polarization stabilization and control. Previous experimental and theoretical studies have demonstrated that optical injection can efficiently be used to achieve the control of polarization bistability and switching. To this end, the commonly adopted injection scheme is the *orthogonal optical injection* in which the injected light polarization direction is orthogonal to that of the free-running VCSEL.

Optically injected VCSELs can also exhibit nonlinear dynamics similar to those observed in edge-emitting lasers. Typical dynamics include wave-mixing, undamped relaxation oscillation time-periodic dynamics and period-doubling route to chaos. Optical injection-induced nonlinear dynamics were mostly investigated in the so-called *parallel optical injection* configuration in

which the injected light polarization and that of the free running VCSEL are parallel. In such optical injection scheme, polarization mode competition is relatively weak since the injected VCSEL keeps its free-running polarization state.

In this thesis we mainly report on bistable polarization switching (PS), injection-locking, nonlinear dynamics and transverse mode competition in a VCSEL subject to orthogonal continuous-wave optical injection. Polarization chaos synchronization of unidirectionally coupled chaotic VCSELs is also investigated. Here is the summary of our achievements.

In chapter 3, we experimentally and theoretically analyze bistable polarization switching properties in a solitary VCSEL when varying the bias current. We focus on two qualitatively different types of polarization switching (PS), namely the type I and type II PS. In particular, we report on an elliptically polarized state which is associated to type II PS, a property that is supported by the so-called spin-flip model (SFM). On the route to PS when scanning the injection current, we show that the solitary VCSEL can exhibit complex nonlinear dynamics including period-doubling route to chaos.

The characterization of the free-running VCSEL undertaken in Chapter 3 allows us to adequately choosing the bias current for achieving orthogonal optical injection. In chapter 4, bistable polarization switching (PS) and injection-locking in a VCSEL subject to orthogonal continuous-wave optical injection are investigated. Optical intensity-induced polarization bistability is first studied in the fundamental transverse mode regime. We analyze how PS leading to injection-locking is achieved when scanning the injection strength for fixed detuning. Our experiments unveil that injection-locking is determined by the VCSEL birefringence, i.e, the frequency offset between the fundamental linearly polarized (LP) transverse modes. In particular, we show that the minimum power needed to achieve PS is obtained when the master laser frequency coincides with that of the injected mode. Whether bistable PS is achieved with or without injection locking depends strongly on the sign of the relative frequency between the master laser and the injected mode. We then theoretically analyze pure frequency-induced bistability by changing the frequency detuning for fixed injection power. Here, we complement previous experimental results and show that the width of the bistable region can be significantly tuned by modifying intrinsic VCSEL's parameters such as the linewidth enhancement factor or the spin-flip relaxation rate. Our results are interesting for controlling polarization bistable VCSELs which are relevant in all-optical signal processing.

In Chapter 5, we experimentally demonstrate that bistable PS and locking may involve rich nonlinear dynamics including wave mixing, subharmonic resonances or a period-doubling route to chaos. In the frequency detuning

vs. injection power plane, we comprehensively analyze the interplay between PS, injection-locking and nonlinear dynamics, and unveil the underlying bifurcation mechanisms. Let us summarize our main results:

- We observe periodic dynamics at the relaxation oscillation frequency in the noninjected mode together with wave-mixing dynamics in the injected mode. These dynamics precede the polarization switching leading to injection locking.
- In a small positive detuning range outside but close to the limit of the injection-locking region, we unveil a scenario for which the switching is achieved between a two-polarization-mode and a single mode limit cycles. The observed limit cycles occur at the relaxation oscillation frequency.
- The interplay between period-doubling dynamics and PS is also analyzed. We demonstrate that when operating close to the injection parameter region where period doubling dynamics are found, the PS curve exhibits a snakelike shape, i.e., the sign of the PS curve slope changes dramatically and we observe two local minima of the injected power required for the switching.
- We identify a scenario for which PS leading to injection locking is followed by a period-doubling route to chaos. Interestingly, we show that chaos involves not only the injected mode but also the otherwise switched off non-injected mode.
- Even though the free-running VCSEL was biased far below the first-order transverse mode threshold, we report on injection-locking of the first order transverse mode, which is accompanied by the suppression of the fundamental transverse mode. This strongly affects the switching conditions between the fundamental transverse modes.

In order to gain more insight into the mechanism underlying the interplay between PS, injection-locking and nonlinear dynamics in the fundamental mode regime, we complement our experiments in Chapter 5 by a detailed bifurcation study. The results, which we obtained by combining both standard numerical simulations as well as continuation techniques, are presented in chapter 6. Most of our theoretical findings qualitatively support our experiments and are found to be generic features of two-mode VCSEL's models:

- We show that periodic dynamics at the relaxation oscillation frequency in the noninjected mode together with wave-mixing dynamics in the injected mode that precede the PS leading to injection locking are

attributed to a torus bifurcation which arises on a two-polarization mode solution.

- Two additional torus bifurcations which qualitatively support the switching scenario that involves a two-polarization-mode and a single mode limit cycles are uncovered. In qualitative agreement with our experiments, the observed dynamics occur over a small positive detuning range outside but still close to the limit of the injection-locking region.
- A Hopf bifurcation, not reported for conventional EELs, delimits the injection locking region and influences the polarization switching conditions. We notice that the newly obtained Hopf bifurcation bounds the injection-locking below the so-called codimension-two point  $G_1$ , in contrast to what has been previously reported in the case of optically injected EELs (in the case of EELs,  $G_1$  delimits the injection locking region).
- The interplay between period-doubling dynamics and PS is also theoretically investigated. In qualitative agreement with our experiment, this interplay is manifested by a snakelike shape with two local minima in the theoretical switching curve. Moreover, we show that this behavior strongly depends on the VCSEL's linewidth enhancement factor ( $\alpha$  factor).

The results in Chapter 5 and 6 uncover nonlinear dynamics and its underlying bifurcation mechanisms. We show that by adequately choosing the injection parameters, these dynamics can be controlled. Our investigations of nonlinear dynamics in a two-polarization mode system may be interesting to address the more general case of bifurcations in externally driven multi-mode oscillators.

The transverse mode competition reported in Chapter 5 has motivated further investigations. By extending the study of polarization switching and injection locking to a much larger positive detuning than what was considered in Chapter 5, we experimentally observe and theoretically show the existence of two minima of injection power need to achieve PS:

- The first minimum, which was already reported in Chapter 5, is resolved when the detuning is set such that the frequency of the injected light is close to that of the injected fundamental LP mode. Interestingly, we also show the existence of a new minimum which appears for a detuning close to the frequency offset between the first order LP transverse mode and the fundamental LP transverse mode. Our theoretical results unveil that the injection power as well as the detuning at which the second minimum is located depends on the relative losses between the fundamental and first order LP transverse modes.



- We report on a relatively large detuning range where PS between the orthogonal fundamental LP modes is followed by injection locking of the first-order transverse mode with a strong suppression of fundamental mode. We observe that the onset of such mode competition dramatically affects the switching between fundamental LP modes. Specifically, this coincides with a change of PS curve slope in the detuning vs. injection strength power.

The obtained results therefore unveil the existence of interplay between optical injection-induced polarization switching and transverse mode competition in a free-running VCSEL which is biased far below the first-order transverse mode threshold.

Finally, polarization chaos synchronization of coupled VCSELs is theoretically investigated in Chapter 8. We consider an open-loop configuration in which only the master laser is subject to optical feedback. The chaotic light from the master VCSEL is unidirectionally injected into the slave VCSEL. Two injection schemes, namely the so-called isotropic and orthogonal optical injection schemes have been investigated:

- In the case of isotropic injection scheme, we show that the synchronization quality can be enhanced when the feedback-induced chaos in the master VCSEL involves both fundamental orthogonal linearly polarized modes. Conversely, when the master VCSEL operates in a single transverse mode chaotic regime, the synchronization quality is strongly deteriorated. By changing the VCSEL birefringence, we are able to tune the master VCSEL between a two-polarization-mode to single-mode chaotic regime. We furthermore observe that the synchronization behavior is robust even in the presence of spontaneous emission noise.
- By considering an orthogonal injection scheme, we unveil two qualitatively different synchronization region. The first one involves only the injected mode and is associated to injection-locking mechanisms. In this region, the synchronization quality depends strongly on optical injection parameters and displays (in the frequency detuning vs. injection strength map) a triangle-like shape typical to the so-called Arnold's tongue. Outside this region, we identify another region of synchronization which involve both orthogonal fundamental LP modes of the slave laser. In this region we resolve a very good synchronization quality which we attribute to polarization mode competition. In this regime, we interestingly notice that a very good synchronization quality can be achieve even for relatively small injection strengths. Moreover, in agreement with previous experimental results, we find

that the observed mode competition phenomenon is accompanied by antiphase polarization dynamics.

## 9.2 Perspectives

- Our results unveil that the injection locking region of VCSELs with orthogonal optical injection is different from that reported for optically injected EELs. In particular, we have shown that the key mechanism underlying this behavior is a new Hopf bifurcation ( $H_2$ ). This is true using two different polarization-mode models. We can therefore believe that this behavior is generic to VCSEL devices. In order to observe it experimentally, our simulations suggest that a VCSEL with large linewidth enhancement factor ( $\alpha$  factor) is needed. This is due to the fact that increasing  $\alpha$  allows a large detuning range that would facilitate experimental observation.
- Using orthogonal optical injection, it would be interesting to investigate if excitability mechanisms involving two polarization modes can be observed in VCSELs. This may extend previous work on optically injected EELs for which an excitable multipulse regime has been reported when operating close to the locking region. However, as theoretically predicted in the case of injected EELs, this would necessitate extending our study to global bifurcations, such as homoclinic bifurcations, which seemed to play a key role in excitability mechanisms.
- Our theoretical results on pure frequency-induced bistability show good qualitative agreement with previous experimental observations. Furthermore, our results predict other phenomena which motivate further experimental investigation. This concerns, for example, the existence of hysteresis region for the two different polarization switching points.
- An elliptically injection-locking state, for which both VCSELs linearly-polarized fundamental transverse modes are frequency locked to the master (two mode injection locking), has been theoretically predicted in the case of orthogonal optical injection. It would be interesting to experimentally investigate this intriguing regime. However, as it has been suggested theoretically, this would necessitate a VCSEL with larger birefringence (the birefringence of the VCSELs we use in our experiment is about 2 GHz).
- Finally, our study on polarization synchronization can be extended to the study of chaos synchronization when taking into account a message. This is attractive for secure chaos communication schemes using polarization carriers.

## Appendix A

# Modelling optical injection by a travelling wave approach

The simplest system that can be used to model a semiconductor laser subject to optical injection is a Fabry-Perot cavity coupled to external optical injected field as shown in Fig. A.0.1. Here, we analyze the dynamical operation of such a system and derive the rate equation for the slowly varying amplitude of the electric field using the travelling wave approach.

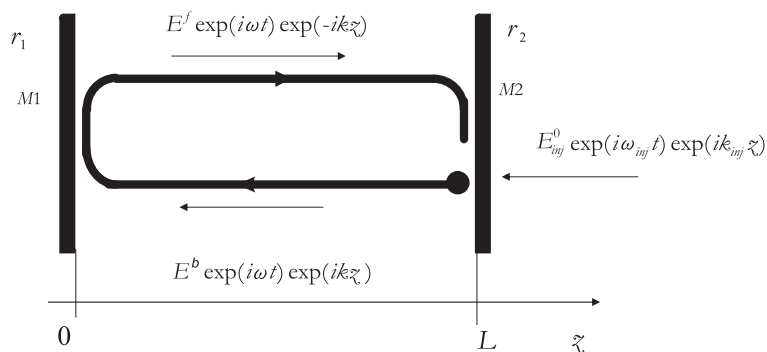


**Figure A.0.1:** Schematic of a Fabry-Perot cavity for the modelling of a semiconductor laser under optical injection. The superscripts  $f$  and  $b$  denote the forward and backward internal travelling field wave.

We assume that the amplitude of the travelling wave inside the cavity changes with time and that only the propagation effects along the lasing direction  $z$  are considered. The injected beam is coupled to the cavity through one of the partially reflecting cavity mirror ( $M2$ ) with a transmission coefficient  $t_2$ .

The field inside the cavity can be modelled as a plane wave with a complex propagation constant  $k$  and an angular frequency  $\omega$ . The forward and the

backward propagating fields can be written as follows:

$$\tilde{E}^f(t, z) = E^f(t) \exp[i(\omega t - kz)], \quad (\text{A.0.1})$$

$$\tilde{E}^b(t, z) = E^b(t) \exp[i(\omega t - kz)], \quad (\text{A.0.2})$$

where  $E^f$  and  $E^b$  are, respectively, the slowly varying amplitudes of the forward and backward electric fields.

The externally injected field is written as:

$$E_{\text{inj}}(t, z) = E_{\text{inj}}^0 \exp[i(\omega_{\text{inj}}t + k_{\text{inj}}z)]. \quad (\text{A.0.3})$$

Where  $E_{\text{inj}}^0$  is the constant amplitude of the injected field, and  $\omega_{\text{inj}}$  and  $k_{\text{inj}}$  are, respectively, the frequency and the the propagation constant of the injected field.

If we consider that the starting point is the backward propagating field at  $z = L$  (see Fig. A.0.1), the boundary conditions at the internal facet of mirror  $M2$  imposes the matching between the electric field at time  $t$  and that after the internal cavity round-trip time ( $\tau_{\text{in}}$ ):

$$\begin{aligned} r_1 r_2 E^b(t, L) \exp(-ikL) \exp(-ikL) \\ + t_2 E_{\text{inj}}(t + \tau_{\text{in}}, L) = E^b(t + \tau_{\text{in}}, L), \end{aligned} \quad (\text{A.0.4})$$

where  $r_1$  and  $r_2$  are the reflectivities of mirrors  $M1$  and  $M2$ , respectively;  $t_2$  is the amplitude transmission coefficient of the injected field through the mirror  $M2$ .

By using the definition of  $E^b(t, z)$  in eq. (A.0.1) and that of  $E_{\text{inj}}$  in eq. (A.0.3), the condition described by eq. (A.0.4) can be written as:

$$\begin{aligned} r_1 r_2 E^b(t) \exp(i\omega t) \exp(ikL) \exp(-2kL) \\ + t_2 E_{\text{inj}}^0 \exp(i\omega_{\text{inj}}t) \exp(i\omega_{\text{inj}}\tau_{\text{in}}) \exp(ik_{\text{inj}}L) \\ = E^b(t + \tau_{\text{in}}) \exp[i\omega(t + \tau_{\text{in}})] \exp(ikL). \end{aligned} \quad (\text{A.0.5})$$

If we assume the approximation that the slowly varying amplitude of the electric field  $E$  varies little during one internal cavity round-trip time  $\tau_{\text{in}}$ , we can write:

$$\frac{dE}{dt} \simeq \frac{E(t + \tau_{\text{in}}) - E(t)}{\tau_{\text{in}}}. \quad (\text{A.0.6})$$

Using eq. (A.0.5), eq. (A.0.6) can be rewritten as:

---


$$\frac{dE}{dt} \simeq \frac{\exp\left[-\frac{1}{2}\ln\left(\frac{1}{R_1R_2}\right) - 2ikL\right] - 1}{\tau_{\text{in}}} E(t) + \frac{t_2}{\tau_{\text{in}}} E_{\text{inj}}^0 \exp[i(\Delta\omega t + \Phi)], \quad (\text{A.0.7})$$

where  $R_1$  and  $R_2$  are the power reflection coefficients defined as  $\sqrt{R_{1,2}} = r_{1,2}$ ;  $\Phi \equiv \Delta\omega\tau_{\text{in}} + \Delta kL$  is a constant phase (with  $\Delta\omega = \omega_{\text{inj}} - \omega$  and  $\Delta k = k_{\text{in}} - k$ ).

The first term of eq. (A.0.7) refers to the rate equation for the slowly varying amplitude of the electric field of a solitary laser. In this case, taking into account the boundary conditions, the condition for the stationary operation writes:

$$\sqrt{R_1R_2} \exp(-i2kL) = 1, \quad (\text{A.0.8})$$

The complex propagation constant is defined as  $k = n_t\omega/c - i\alpha_{\text{abs}}/2$ ; where  $n_t$  is the total refractive index,  $c$  is the light velocity and  $\alpha_{\text{abs}}$  is the absorption coefficient.  $\alpha_{\text{abs}}$  is related to optical gain,  $G$ , and internal losses,  $\alpha_{\text{int}}$ , as follows:

$$\alpha_{\text{abs}} = -G + \alpha_{\text{int}}. \quad (\text{A.0.9})$$

One can obtain the gain condition at threshold from the modulus of eq. (A.0.8):

$$G_{\text{th}} = \alpha_{\text{int}} + \frac{1}{2L} \ln \frac{1}{R_1R_2}, \quad (\text{A.0.10})$$

or, equivalently,  $G = \alpha_{\text{int}} + \alpha_m$ , where  $\alpha_m = (1/2L) \ln(1/R_1R_2)$  is the mirror losses.

From the phase of eq. (A.0.8) one obtains the frequency condition at threshold:

$$\omega_{\text{th}} = m \frac{\pi c}{n_t L} \alpha_{\text{int}}, \quad (\text{A.0.11})$$

where  $m$  is an integer.

The numerator of the first term in right-hand side of eq. (A.0.7) can be approximately written as:

$$F \equiv -\frac{1}{2} \ln\left(\frac{1}{R_1R_2}\right) - 2ikL, \quad (\text{A.0.12})$$

since the argument of the exponential is small.

By using the definition of  $\alpha_m$  and  $k$ , eq. (A.0.12) can be written as:

$$F = -\alpha_m L - 2i \frac{n_t \omega}{c} L - \alpha_{abs} L. \quad (\text{A.0.13})$$

In eq. (A.0.13), the term  $n_t \omega / c$  represents the actual laser frequency. Moreover, the refractive index  $n_t$  depends on both the frequency and the carrier population inversion  $N$ . By expanding the actual frequency term around the threshold one obtains:

$$\frac{n_t \omega}{c} \simeq \frac{n_{t,th} \omega_{th}}{c} + \frac{\omega_{th}}{c} \frac{\partial n_t}{\partial N} (N - N_{th}) + \frac{1}{c} \left( n_{t,th} + \omega \frac{\partial n_t}{\partial \omega} \right) (\omega - \omega_{th}) \quad (\text{A.0.14})$$

We can therefore rewrite eq. (A.0.13), taking into account eqs. (A.0.14) and (A.0.10):

$$F = -\alpha_m L - 2i \frac{n_{t,th} \omega_{th}}{c} L - 2i L \frac{\omega_{th}}{c} \frac{\partial n_t}{\partial N} (N - N_{th}) - [-G(N) + \alpha_{int}] L - 2i \frac{n_g L}{c} (\omega - \omega_{th}), \quad (\text{A.0.15})$$

where  $n_g = n_{t,th} + \omega \partial n_t / \partial \omega$  is the group refractive index.

By taking into account the definition of  $\omega_{th}$  (see eq. (A.0.11)), we can write:

$$\exp \left( \frac{-2i n_{t,th} \omega_{th} L}{c} \right) = \exp(im2\pi) = 1, \quad (\text{A.0.16})$$

and, consequently, the second term of the right-hand side of eq. (A.0.15) is equal to zero. If we consider the lasing frequency  $\omega$  being that at the threshold  $\omega_{th}$ , the last term in eq. (A.0.15) is also equal to zero.

By assuming that the gain  $G(N)$  varies linearly with the carrier population inversion  $N$ , we can therefore consider the following first order Taylor expansion around the threshold:

$$G(N) = G(N_{th}) + \frac{\partial G}{\partial N} (N - N_{th}). \quad (\text{A.0.17})$$

Let us now come back to the rate equation for the slowly varying amplitude as defined by eq. (A.0.7).

The internal round-trip time is:

$$\tau_{in} \equiv 2L n_g / c \equiv 2L / v_g, \quad (\text{A.0.18})$$

where  $v_g$  is the group velocity.

---

Furthermore, at threshold:

$$-G(N_{th}) + \alpha_{int} + \alpha_m = 0. \quad (\text{A.0.19})$$

Using eqs. (A.0.18) and (A.0.19), we simplify eq. (A.0.16) and insert it into the rate equation (A.0.7) to obtain the following expression:

$$\begin{aligned} \frac{dE}{dt} = & \frac{1}{2} v_g \frac{\partial G}{\partial N} (N - N_{th}) E(t) - \left( \frac{\omega_{th}}{c} \frac{\partial n_t}{\partial N} \right) i \frac{1}{2} v_g (N - N_{th}) E(t) \\ & + \frac{t_2}{\tau_{in}} E_{inj}^0 \exp [i (\Delta\omega t + \Phi)], \end{aligned} \quad (\text{A.0.20})$$

If we introduce the  $\alpha$  factor through which the change in the refractive index with the carrier is related to the change in the gain with the carrier as follows:

$$\alpha \equiv -2 \frac{\omega_{th}}{c} \frac{\partial n_t / \partial N}{\partial G / \partial N}, \quad (\text{A.0.21})$$

Equation (A.0.20) writes:

$$\frac{dE}{dt} = \frac{1}{2} (1 + i\alpha) \xi (N - N_{th}) E(t) + \frac{t_2}{\tau_{in}} E_{inj}^0 \exp [i (\Delta\omega t + \Phi)], \quad (\text{A.0.22})$$

where  $\xi \equiv v_g \partial G / \partial N$  is the differential gain coefficient.

The same approach is used in Chapter 4 for the modelling of a VCSEL subject to orthogonal optical injection in the framework of the SFM model.







Vrije Universiteit Brussel



## **THESE: résumé en français**

# **Basculement de polarisation, contrôle et synchronisation de lasers à cavité verticale émettant par la surface (VCSELs) soumis à injection optique**

Présentée dans le cadre d'une cotutelle entre la Vrije Universiteit Brussel, Supélec et l'Université Paul Verlaine - Metz pour l'obtention du grade de Docteur de l'Université Paul Verlaine-Metz en Physique

**Gatare Gahangara Ignace**

Thèse présentée et soutenue publiquement le 08 février 2008



Metz, February 2008





## B.1 Introduction et contexte de notre thèse

Les lasers à semi-conducteurs ont connu un développement qui a été essentiellement accéléré par leur application dans le domaine des télécommunications par fibre optique. Les lasers à semi-conducteurs y sont utilisés comme sources émettrices de lumière qui, comparées aux lasers à gaz, sont compacts, ont une bonne efficacité ainsi qu'une plus longue durée de vie. Ils permettent une vitesse de modulation dans la gamme des GHz, très intéressante pour les réseaux modernes de communication à haut débit. Par ailleurs, les lasers à semi-conducteurs sont appelés à jouer un rôle important dans les nouvelles applications telles le routage tout optique ainsi que le traitement optique de l'information. Hormis leurs applications dans les télécommunications, les lasers à semi-conducteurs sont présents dans une gamme variée de dispositifs optoélectroniques utilisés dans notre vie quotidienne: CD-ROM, lecteurs DVD, imprimantes, lecteurs de code barres, etc. On les rencontre également dans de nombreuses applications spécialisées telles la spectroscopie, les capteurs optiques, la métrologie.

Le marché des lasers à semi-conducteurs a été longtemps dominé par les lasers conventionnels émettant par le côté - *edge-emitting lasers* (EELs)- pour lesquels le faisceau laser est émis parallèlement au plan de la couche active du laser (Figure B.1.1). Cependant, le concept d'émission par la surface a récemment attiré un intérêt particulier qui a conduit à l'émergence d'un nouveau type de composant: le laser à cavité verticale émettant par la surface - *vertical-cavity surface-emitting laser* (VCSEL). Compte tenu de leur structure (voir la Figure B.1.2), les VCSELs présentent des avantages compétitifs par rapport aux lasers émettant par le côté. Notamment, l'émission par la surface permet la fabrication de matrices bidimensionnelles de VCSELs qui sont intéressantes pour les réseaux d'interconnexion et le routage tout optique [10].

La structure typique d'un laser à semi-conducteurs de type VCSEL est schématiquement décrite à Figure B.1.2. La région active se compose généralement d'une structure mince à puits quantiques (typiquement 5-10 nm d'épaisseur). Cette zone active est placée entre deux réflecteurs distribués de Bragg caractérisés par une très grande réflectivité (supérieure à 99%). Les propriétés d'émission du VCSEL sont dictées par la géométrie de la cavité laser, la largeur de bande des réflecteurs de Bragg ainsi que le profil du gain du milieu amplificateur dans la zone active. En général, les VCSELs sont caractérisés par un seul mode longitudinal du fait de la très courte cavité laser. Cependant, selon les conditions de fonctionnement (courant d'injection ou température), les VCSELs peuvent émettre un ou plusieurs modes transverses [28, 29, 30, 31, 32].

Les VCSELs sont typiquement caractérisés par une géométrie symétrique

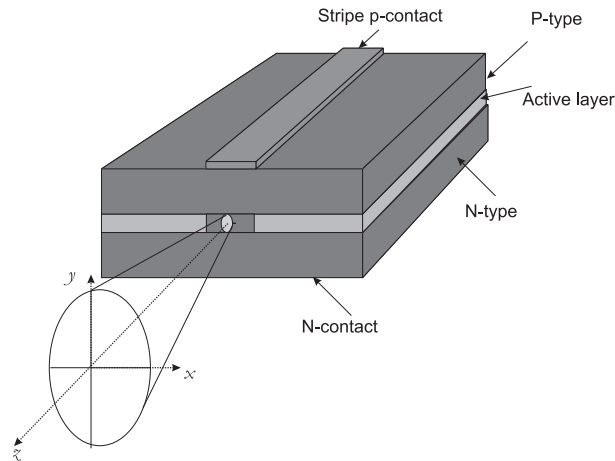


**Figure B.1.1:** Schéma d'un laser conventionnel émettant par le côté. La direction d'émission ( $z$ ) est parallèle au plan de la zone active (active layer) placée entre deux enveloppes respectivement dopés N et P.

dans le plan transversal qui permet l'émission d'un faisceau circulaire symétriquement divergent. Contrairement aux lasers émettant par le côté, la direction de polarisation du faisceau émis par les VCSELS n'est pas *a priori* fixe. En effet, suite à une anisotropie structurale, inévitablement introduite lors du processus de fabrication, le VCSEL présente souvent deux modes de polarisation linéaire orthogonaux avec des fréquences et des gains optiques presque identiques. Dès lors, de faibles perturbations telles que des modifications du courant d'injection ou de la température peuvent facilement induire des basculements de polarisation. Toutefois, en utilisant un schéma d'injection optique du VCSEL par un faisceau laser externe, il est possible de contrôler ces instabilités de polarisation

Notre thèse est essentiellement consacrée à l'étude du VCSEL soumis à injection optique d'un faisceau laser externe. L'étude de l'influence de l'injection optique sur la dynamique des lasers conventionnels émettant par le côté a été largement décrit dans la littérature. Ces études précédentes ont montré que, selon les paramètres d'injection (puissance injectée et désaccord en fréquence entre le lasers maître et esclave), le laser esclave peut exhiber des dynamiques non-linéaires complexes. Cependant les travaux concernant l'influence de l'injection optique sur la dynamique des VCSELS sont peu nombreux. On peut s'attendre à ce que le degré de liberté de polarisation intrinsèque aux VCSELS joue un rôle très important dans leur réponse dynamique à l'injection optique. Une étude approfondie de la dynamique de polarisation du VCSEL soumis à injection optique est donc nécessaire. D'une part, une telle étude *contribue à l'étude du contrôle de polarisation* qui est crucial pour les applications sensible à la polarisation de la lumière. D'autre

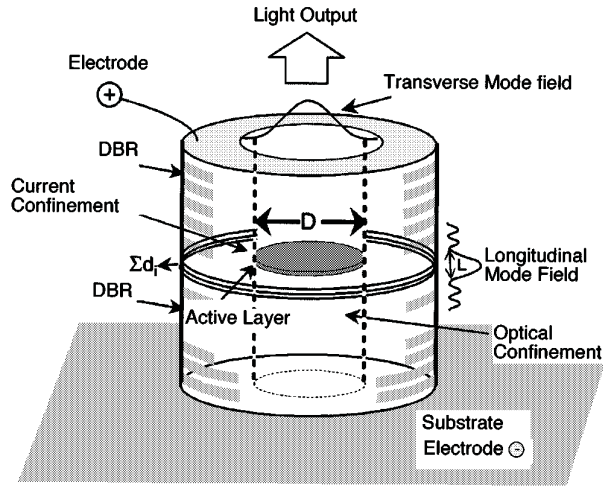


**Figure B.1.2:** *Vue schématique d'un laser à cavité verticale émettant par la surface (vertical-cavity surface-emitting laser-VCSEL). Une mince couche active est placée entre deux réflecteurs distribués de Bragg (DBR). L'émission se fait selon une direction perpendiculaire à au plan de la couche active). Tirée de [27].*

part, nous pensons qu'une meilleure compréhension des dynamiques de polarisation est indispensable si l'on tient compte de l'intérêt grandissant des VCSELs dans les schémas de commutation tout optique rapides ou dans le traitement optique de l'information.

Le résumé de notre travail de thèse est organisé de la manière suivante. Les propriétés de polarisation d'un VCSEL opérant en régime solitaire, c'est-à-dire sans perturbation externe, sont tout d'abord présentées à la Section B.2. Nous insistons particulièrement sur les propriétés de basculement de polarisation du VCSEL lorsqu'on modifie le courant d'injection. Nous montrons l'existence de deux types de basculement de polarisation qualitativement différent (basculement de polarisation de type I et II). Nos résultats expérimentaux sont commentés en utilisant un modèle théorique qui tient compte des phénomènes de relaxation d'états de spin des porteurs (spin flip model ou SFM).

Le VCSEL soumis à injection optique est introduit à la Section B.3. Le schéma d'injection optique orthogonale est brièvement décrit: le faisceau injecté est linéairement polarisé selon une direction orthogonale à celle de la polarisation du VCSEL sans d'injection optique. Dans cette configuration, nous montrons qu'il est possible de contrôler le basculement de polarisation ainsi que la bistabilité y associée. Ceci est réalisé en variant les paramètres d'injection, c'est-à-dire la puissance du faisceau injecté ou le désaccord en fréquence entre les lasers maître et le VCSEL.

A la Section B.4 nous résumons nos résultats expérimentaux qui montrent que le basculement de polarisation d'un VCSEL soumis à injection optique peut s'accompagner des dynamiques non-linéaires complexes. Dans le plan des paramètres d'injection optique, nous mettons en évidence une large zone de verrouillage par injection (*injection-locking*) dans laquelle le VCSEL se verrouille sur la fréquence et la polarisation du laser maître. Le régime de verrouillage du VCSEL ainsi que les dynamiques non-linéaires qui accompagnent le basculement de polarisation du VCSEL soumis à injection optique sont caractérisés dans le plan des paramètres d'injection optique.

Une étude théorique des dynamiques non-linéaires qui accompagnent le basculement de polarisation du VCSEL soumis à injection optique, ainsi que les bifurcations sous-jacentes, est présentée à la Section B.5. Ces résultats théoriques sont analysés à la lumière de nos travaux expérimentaux exposés à la Section B.4. Nous discutons des deux types de bifurcations, notamment une bifurcation de Hopf ainsi qu'une bifurcation de tore, qui jouent un rôle particulièrement important dans les mécanismes de basculement de polarisation et de verrouillage du VCSEL sur le laser maître. Par ailleurs, en utilisant deux modèles différents pour décrire la dynamique du VCSEL soumis à injection optique, nous montrons que ces bifurcations sont génériques des systèmes VCSEL à deux modes fondamentaux de polarisations orthogonales.

Les Sections B.3, B.4 et B.5 s'intéressent essentiellement à la dynamique de basculement de polarisation qui implique seulement les modes fondamentaux du VCSEL. Dans la Section B.6 le problème de compétition des modes transverses induite par injection optique est expérimentalement et théoriquement discuté. En analysant la dynamique de basculement de polarisation dans le plan des paramètres d'injection, et sur une gamme relativement très large de désaccord en fréquence entre les lasers maître et le VCSEL (ou plus simplement *detuning*<sup>1</sup>), nous montrons que le basculement de polarisation entre les modes transverses fondamentaux peut être accompagné de l'excitation du mode transverse de premier ordre. Plus intéressant, nous mettons en évidence l'existence de deux minima de puissance d'injection nécessaire pour induire le basculement de polarisation pour deux valeurs de *detuning*.

Dans la Section B.7, nous présentons nos résultats théoriques sur l'influence des dynamiques de polarisation du VCSEL sur la synchronisation de deux VCSELS en mode de couplage unidirectionnel. Contrairement aux études présentées dans les Sections B.3, B.4, B.5 et B.6 (pour lesquelles on considère l'injection optique d'un faisceau en régime stationnaire), nous analysons un schéma dans lequel le VCSEL esclave est injecté par un VC-

---

<sup>1</sup>par souci de commodité nous emprunterons cette terminologie anglaise dans la suite de ce résumé en Français pour désigner le désaccord en fréquence entre les laser maître et le VCSEL.

SEL maître en régime chaotique. Le chaos optique dans le VCSEL maître est généré par une rétro-action optique isotrope, c'est-dire sans discrimination entre les deux modes de polarisations orthogonales. Nos investigations concernent deux schémas d'injection: 1/ Le premier schéma adopté correspond au cas d'un VCSEL esclave soumis à une injection isotrope; 2/ Dans le second schéma, le VCSEL est soumis à une injection d'un faisceau dont la polarisation est orthogonale à celle du VCSEL esclave sans injection. Dans les deux cas, nous montrons que la qualité de synchronisation entre les VCSELs maître et esclave est meilleure lorsque le VCSEL esclave opère dans un régime de chaos optique dans les deux modes fondamentaux de polarisations orthogonales. Par contre, dans le cas d'un régime chaotique dans un seul mode, on observe une détérioration très significative de la qualité de synchronisation.

Finalement, à la Section B.8 nous résumons les résultats de notre travail de thèse.

Nous mentionnons que notre travail de thèse de doctorat a été préparée dans le cadre d'une convention de cotutelle entre la *Vrije Universiteit Brussel* (VUB), l'École Supérieure d'Électricité (Supélec) et l'Université Paul Verlaine-Metz. La présente partie résume, en français, les résultats principaux de notre travail de thèse qui a été essentiellement conduite en Anglais. Nous invitons donc le lecteur intéressé à consulter le manuscrit complet en version anglaise pour plus de détails.

## B.2 Propriétés de polarization du VCSEL

Dans cette Section, nous analysons les propriétés d'un VCSEL opérant en mode solitaire, c'est-à-dire sans perturbation externe. Tout d'abord, nous présentons très succinctement les mécanismes physiques à la base du basculement de polarisation avant d'analyser les propriétés de basculement de polarisation du VCSEL lorsqu'on varie progressivement le courant d'injection. Nous montrons deux types de basculement de polarisation, notamment les basculements de type I et de type II et analysons leurs caractéristiques. En particulier, nous montrons que le basculement de polarisation de type II est précédé par l'excitation d'un régime de polarisation elliptique. La bistabilité associée au basculement de polarisation est également analysée.

### B.2.1 Basculement de polarization dans un VCSEL: *mécanismes physiques*

En décrivant la structure d'un VCSEL, nous avons mentionné qu'une anisotropie structurelle, inévitablement introduite lors du processus de fabrication du composant, explique l'existence de deux modes de polarisation linéaire orientés selon deux axes orthogonaux préférentiels [43, 44]. Les deux états de polarisation sont caractérisés par une légère différence d'indice de refraction qui est responsable de la birefringence, c'est-à-dire que les deux modes accusent un désaccord en fréquence [43, 44]. Les travaux expérimentaux antérieurs ont montré que le VCSEL émet généralement dans le mode fondamental pour des courants d'injection relativement modérés. En variant le courant d'injection, il est possible d'induire un basculement de polarisation entre les modes fondamentaux de polarisations orthogonales [36]. Pour des courants d'injection suffisamment élevés, l'excitation des modes transverses d'ordre supérieur est souvent observée [36].

Plusieurs mécanismes physiques ont été proposés dans le but d'expliquer les phénomènes de basculement de polarisation dans un VCSEL. A cet effet, deux types d'approches ont été suggérés:

- D'une part, une première approche associe le phénomène de basculement de polarisation au fait que le changement des paramètres de fonctionnement (courant d'injection ou température) peut entraîner une compétition pour le gain entre les deux modes de polarisations orthogonales [36, 45, 46, 47]. En effet, la largeur du spectre de gain de la cavité laser est généralement très large par rapport à la birefringence entre les modes transverses de polarisations orthogonales, qui, par conséquent, se caractérisent par une faible différence de gains (ou pertes) optiques.



- Une autre approche basée sur le phénomène de relaxation des états de spin des porteurs (*spin flip model* ou SFM) a été suggéré pour expliquer le basculement de polarisation [48]. Le modèle SFM comporte quatre niveaux correspondant à une paire des bandes de valence et de conduction. Les deux paires correspondent à deux transitions radiatives de spins opposés. Le mécanisme de relaxation des états de spin des porteurs (*spin-flip relaxations mechanism*), qui tend à homogénéiser les spins, est phénoménologiquement introduit. Dans le modèle SFM, le basculement de polarisation se manifeste comme une instabilité non-linéaire entre deux modes de polarisation linéaire orthogonaux.

### B.2.2 Basculement de polarisation de type I et de type II: *observation expérimentale*

Deux types de basculement de polarisation sont mis en évidence expérimentalement. Nous suivons l'évolution de la puissance émise par le VCSEL (en régime de fonctionnement solitaire) dans les deux modes fondamentaux de polarisations linéaires orthogonales. Lorsque, en augmentant le courant d'injection du VCSEL, le basculement de polarisation s'effectue du mode avec haute fréquence (HF) optique vers mode avec basse fréquence (BF) optique, on parle de basculement de type I. Par contre, lorsque le basculement de polarisation s'effectue du mode BF au mode HF, il s'agit du basculement de type II. Nos résultats expérimentaux, qui ont été réalisés avec deux VCSELS différents, montrent que le scénario de basculement (type I ou II) dépend fortement du composant.

La Figure B.2.1 représente la courbe expérimentale qui montre l'évolution de la puissance de sortie du VCSEL<sub>1</sub> dans les deux modes de polarisations orthogonales. En augmentant progressivement le courant d'injection [Figure B.2.1(a)], le VCSEL commence à émettre dans le mode BF au delà du courant seuil. Au fur et à mesure que le courant d'injection est augmenté, le VCSEL bascule du mode BF au mode HF (basculement de type II). Nous observons que le basculement de polarisation de type II est précédé par une émission dans les deux modes de polarisations orthogonales. En fait, cela correspond à l'excitation d'un état de polarisation elliptique dans lequel les deux modes sont émis à la même fréquence mais avec des polarisations orthogonales. Après basculement de polarisation de type II, en diminuant progressivement le courant d'injection [Figure B.2.1(b)], un basculement vers le mode BF est observé pour une valeur de courant d'injection inférieure à celle correspondant au basculement de polarisation de type II. Ainsi, une zone d'hystérèse associée au basculement de polarisation de type II est observée.

Un scénario de basculement de polarisation différent de celui observé à la

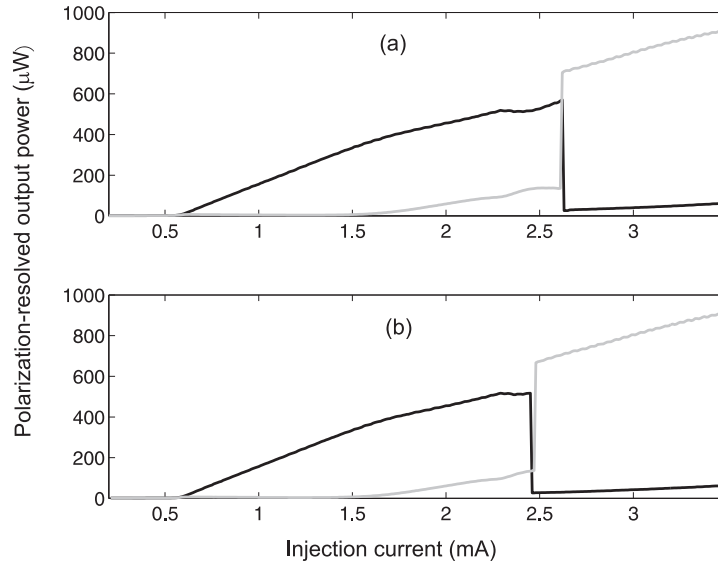


**Figure B.2.1:** *Evolution des courbes de puissance de sortie dans les modes basse fréquence BF (x en noir) et haute fréquence HF (y en gris) du VCSEL<sub>1</sub>, pour un courant d'injection croissant (a1) et décroissant (b1). La température du VCSEL est stabilisée à 20°C.*

Figure B.2.1 est présentée à la Figure B.2.2. Cette dernière décrit l'évolution de la puissance de sortie du VCSEL<sub>2</sub> dans les deux modes de polarisations orthogonales. En augmentant progressivement le courant d'injection, et contrairement à ce qui a été observé pour le VCSEL<sub>1</sub>, le VCSEL<sub>2</sub> commence à émettre dans le mode HF au delà du courant de seuil [Figure B.2.2(a)]. Au fur et mesure qu'on augmente le courant d'injection, on observe un premier basculement de polarisation du mode HF vers le mode BF (basculement de type I). Puis un deuxième basculement du mode BF vers le mode HF (basculement de type II) est observé. Notons que le basculement de type II se produit quasiment comme dans le cas précédent [voir la Figure B.2.1(a)], c'est-à-dire qu'il est précédé par l'excitation d'un état de polarisation elliptique). Si le courant d'injection est progressivement diminué après que le basculement de type II soit réalisé, le VCSEL rebasculé vers le mode BF pour une valeur de courant d'injection beaucoup plus faible, ce qui met en évidence une zone relativement large d'hystérèse de polarisation. Toutefois, il est important de noter que le basculement de type I est réalisé sans hystérèse.

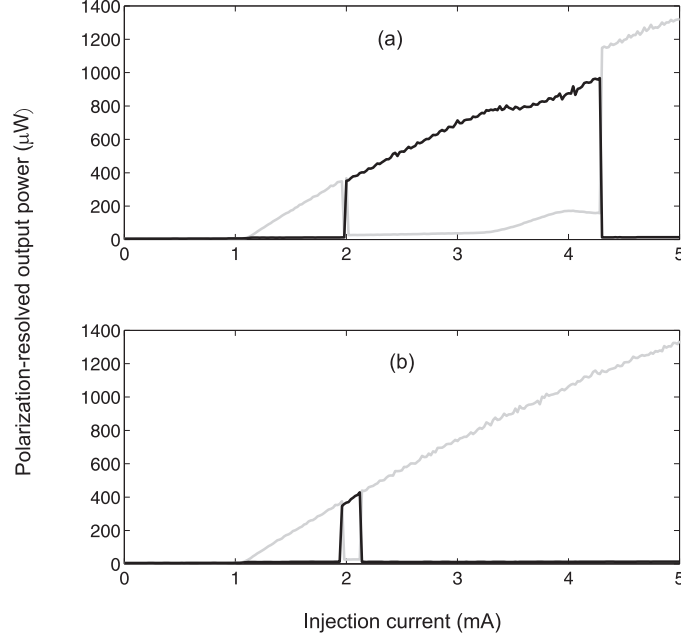


**Figure B.2.2:** Evolution des courbes de puissance de sortie dans les modes basse fréquence BF ( $x$  en noir) et haute fréquence HF ( $y$  en gris) du VCSEL<sub>2</sub>, pour un courant d'injection croissant (a1) et décroissant (b1). La température du VCSEL est stabilisée à 20°C.

### B.2.3 Basculement de polarisation de type II: mise en évidence théorique

Nous analysons théoriquement analysé le basculement de polarisation dans un VCSEL en mode de fonctionnement solitaire en nous basant sur le modèle SFM [48, 60]. Le modèle utilisé tient compte des anisotropies d'amplitude (dichroïsme) et de phase (birefringence). Les équations de taux décrivant l'évolution temporelle de l'amplitude du champ électrique et des porteurs se présentent comme suit:

$$\frac{dE_x}{dt} = -(\kappa + \gamma_a)E_x - i(\kappa\alpha + \gamma_p)E_x + \kappa(1 + i\alpha)(DE_x + idE_y), \quad (\text{B.2.1})$$

$$\frac{dE_y}{dt} = -(\kappa - \gamma_a)E_y - i(\kappa\alpha - \gamma_p)E_y + \kappa(1 + i\alpha)(DE_y - idE_x), \quad (\text{B.2.2})$$

$$\frac{dD}{dt} = -\gamma_e \left[ D \left( 1 + |E_x|^2 + |E_y|^2 \right) - \mu + id(E_y E_x^* - E_x E_y^*) \right], \quad (\text{B.2.3})$$

$$\frac{dd}{dt} = -\gamma_s d - \gamma_e \left[ d \left( |E_x|^2 + |E_y|^2 \right) + iD(E_y E_x^* - E_x E_y^*) \right]. \quad (\text{B.2.4})$$

$E_x$  et  $E_y$  représentent, respectivement, les amplitudes lentement variables des champs électriques des modes linéairement polarisés selon les directions  $x$  et  $y$  (polarisations orthogonales).  $D$  est l'inversion totale des populations de porteurs dans les deux sous-canaux représentant les transitions à spin opposés.  $d$  est la différence d'inversions des populations associées aux transitions de spins opposés.  $\kappa$  est le taux de décroissance de l'amplitude du champ électrique.  $\gamma_p$  et  $\gamma_a$  représentent, respectivement, la birefringence et le dichroïsme.  $\gamma_e$  est le taux de décroissance de  $D$  tandis que  $\gamma_s$  est le taux de décroissance de  $d$ : il est également appelé le taux de relaxation d'états de spin des porteurs.  $\gamma_s$  est un paramètre qui modélise phénoménologiquement un ensemble de mécanismes microscopiques qui tendent à homogénéiser les spins des porteurs.  $\alpha$  est le facteur de Henry qui est générique aux lasers à semi-conducteurs.  $\mu$  est le courant d'injection normalisé ( $\mu = 1$  au seuil).

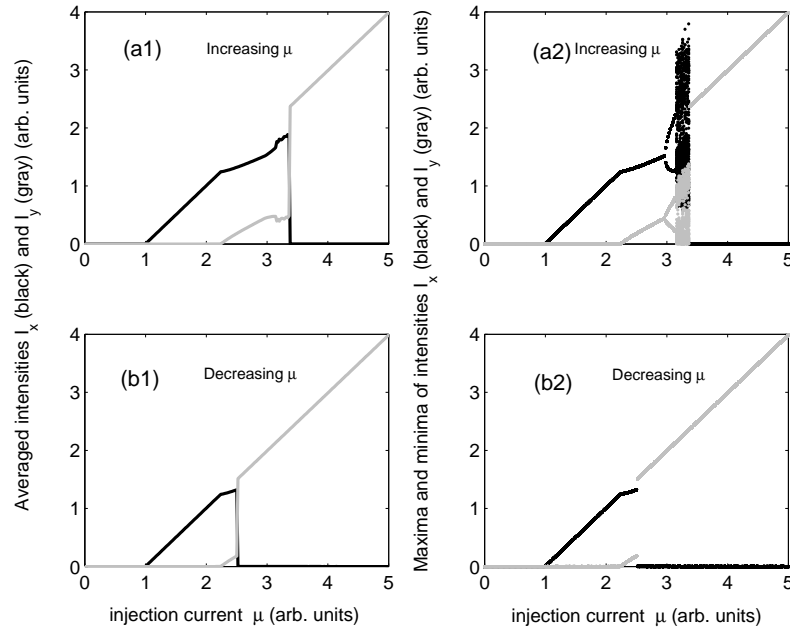


**Figure B.2.3:** *Evolution des intensités moyennes du champ pour les modes basse fréquence BF ( $x$  en noir) et haute fréquence HF ( $y$  en gris) lorsque le courant d'injection est croissant (a1) et décroissant (b1). Diagramme de bifurcation montrant l'évolution des maxima et minima des intensités instantanées du champ pour les modes basse fréquence BF ( $x$  en noir) et haute fréquence HF ( $y$  en gris) lorsque le courant d'injection est croissant (a2) et décroissant (b2). Les paramètres du modèle SFM sont fixés comme suit:  $\kappa = 300 \text{ ns}^{-1}$ ,  $\gamma_p = 6.3 \text{ rad/ns}$ ,  $\gamma_a = -0.81 \text{ ns}^{-1}$ ,  $\gamma_s = 91 \text{ ns}^{-1}$ ,  $\gamma_e = 0.55 \text{ ns}^{-1}$ ,  $\alpha = 3$ .*

En utilisant le modèle SFM nous avons simulé le basculement de polarisation de type II dans un VCSEL en régime de fonctionnement solitaire. En effet, les paramètres indiqués à la Figure B.2.3 nous ont permis de reproduire qualitativement le basculement de polarisation du mode BF au mode HF, lorsque le courant d'injection  $\mu$  est progressivement varié [voir l'évolution des intensités moyennes ( $\langle I_{x,y} \rangle = |E_{x,y}|^2$ ) dans les deux modes de polarisation orthogonales [Figures B.2.3(a1) et (b1)]. En effet, l'état elliptique qui précède le basculement de type II ainsi que la zone de bistabilité de polarisation y associé sont bien reproduits. Par ailleurs, les diagrammes de bifurcation qui montrent l'évolution des maxima et minima des intensités instantanées dans les modes BF et HF lorsqu'on varie le courant d'injection  $\mu$  [Figures B.2.3(a2) et (b2)], apportent une information riche. En effet, les simulations numériques suggèrent que l'état elliptique est déstabilisé via une dynamique de doublement de période vers un régime complexe, probablement chaotique.

### B.3 Contrôle du basculement et bistabilité de polarisation d'un VCSEL soumis à injection optique orthogonale

L'injection optique dans les lasers à semi-conducteurs a fait l'objet d'une intense activité de recherche, surtout pour les lasers conventionnels émettant par le côté [105, 106]. Il a été démontré que l'injection optique peut être efficacement utilisé pour améliorer les caractéristiques d'émission d'un laser à semi-conducteurs tels la stabilisation de la fréquence d'émission [105] des lasers modulés, réduction du chirp [111], élargissement de la bande de modulation [113] du laser.

L'injection optique est également un moyen de contrôler la dynamique des états bistables dans les lasers à semi-conducteurs. Le contrôle de la bistabilité des lasers à semi-conducteurs est intéressant pour les applications dans les domaines du routage optique, des mémoires optiques ainsi que du traitement optique de l'information [125, 126]. En ce qui concerne les VCSELs, le contrôle de la bistabilité de polarisation a attiré une attention particulière [125, 126, 131] d'autant plus que leur structure se prête bien à la fabrication des matrices bidimensionnelles de lasers très intéressantes pour les applications tels le routage tout-optique, le traitement de l'information ainsi que les mémoires optiques. La bistabilité de polarisation du VCSEL peut être contrôlée soit électriquement en variant le courant d'injection (voir Section B.2) soit via une méthode tout optique utilisant la rétro-action optique [99] ou l'injection optique [120, 132, 133, 135].

Nous contribuons à l'étude du contrôle du basculement et de la bistabilité

de polarisation dans un VCSEL soumis à injection optique. Nous adoptons le schéma d'injection optique orthogonale dans lequel le faisceau injecté est linéairement polarisé selon une direction orthogonale à celle de la polarisation du VCSEL libre d'injection optique. D'une part, nous étudions expérimentalement et théoriquement le contrôle du basculement et de la bistabilité de polarisation lorsqu'on varie la puissance du faisceau injecté pour un detuning fixe. Ensuite, nous présentons nos résultats théoriques sur le contrôle de la bistabilité de polarisation en variant le detuning pour une puissance injectée fixe. Cette dernière étude complète les résultats expérimentaux rapportés précédemment par Hong *et al* [132].

### B.3.1 Bistabilité de polarisation induite par variation de la puissance injectée: *résultats expérimentaux*

#### B.3.1.1 Description du banc expérimental

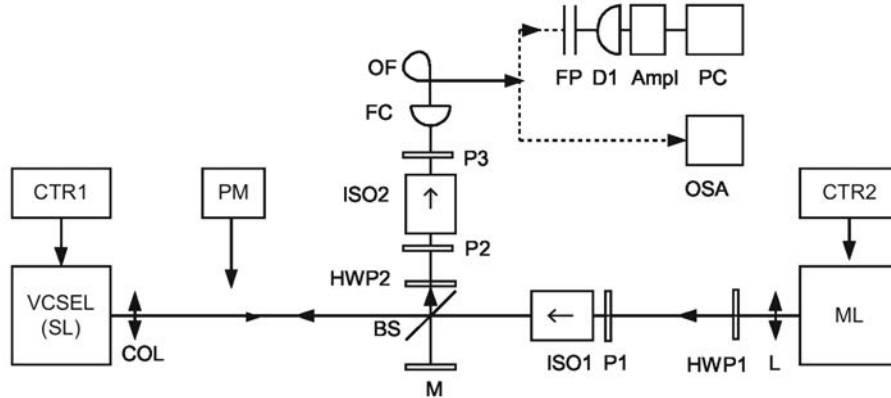


**Figure B.3.1:** Banc expérimental d'un VCSEL soumis à injection optique orthogonale. *SL*: VCSEL ou laser esclave, *ML*: laser maître, *COL*: collimateur, *BS*: séparateur de faisceau, *HWP1-HWP2*: lame demi-onde, *ISO1*, *ISO2*: isolateur optique, *L*: lentille, *P1-P3*: polariseur, *M*: miroir, *FC*: unité de couplage fibrée, *OF*: fibre optique, *FP*: interféromètre Fabry-Pérot, *D1*: photodiode, *Ampl*: amplificateur, *PC*: ordinateur, *OSA*: analyseur de spectre optique, *PM*: wattmètre optique, *CTR1* (*CTR2*): contrôleur de courant d'injection et de température de *SL* (*ML*). La température du VCSEL est a été fixée à 20° C.

Nous présentons à la Fig. B.3.1 le banc expérimental ayant servi à l'étude de la dynamique de basculement de polarisation d'un VCSEL sous injection optique. Le VCSEL est injecté par un laser maître (master laser, ML) accordable. La configuration d'injection est telle que la direction de polarisation

du faisceau lumineux injecté est orthogonale par rapport à celle de la lumière émise par le VCSEL lorsque ce dernier est libre d'injection. Le choix de ce schéma d'injection permet d'étudier le basculement de polarisation ainsi que les dynamiques non linéaires qui l'accompagnent. Un ensemble de dispositifs et équipements de mesure ont été utilisés. Une lentille (L) pour focaliser le faisceau de lumière injecté, un isolateur ISO1 pour éviter les effets de rétroaction optiques susceptibles de perturber l'émission du laser Maître, une lame demi-onde (HWP1) pour ajuster la polarisation de ML dans la direction souhaitée. Un séparateur de faisceau (BS) et un miroir M permettent d'aligner les faisceaux du VCSEL et du laser maître sur la branche de détection. Un collimateur est monté en face du VCSEL afin d'optimiser l'injection optique. Le VCSEL et le laser maître ML sont contrôlés en courant électrique et en température par les contrôleurs CTR1 et CTR2 respectivement. La puissance optique injectée dans le VCSEL est variée grâce au polariseur P1. Le décalage en fréquence entre le VCSEL et le laser maître est obtenu en ajustant le contrôle de ML via CTR2 (contrôle du courant électrique, contrôles thermique et piézoélectrique). La branche de détection comprend une lame demi-onde (HWP2) qui permet de sélectionner la direction de polarisation à détecter, un isolateur pour limiter les effets de rétroaction optique ainsi qu'une unité de couplage fibrée. Un interféromètre Fabry-Pérot (FP) équipé d'un dispositif amplificateur est utilisé pour l'analyse spectrale des dynamiques non linéaires induites par l'injection optique dans le VCSEL. Un analyseur de spectre optique (OSA) est également utilisé.

### B.3.1.2 Résultats expérimentaux

La Figure B.3.2 montre l'évolution de la puissance de sortie dans les deux modes orthogonaux du VCSEL soumis à injection optique orthogonale, lorsque la puissance injectée est variée pour un detuning fixe. Nous avons choisi deux valeurs de courant d'injection. Dans chacun des cas, le VCSEL libre d'injection émet dans le mode fondamental avec une polarisation linéaire horizontale et l'injection optique est réalisée selon la direction de polarisation verticale. Dans le premier cas, le courant d'injection est fixée à 1.9 mA et par conséquent plus faible que la borne inférieure de la zone de bistabilité de polarisation de la courbe puissance-courant du VCSEL (consulter la version anglaise, Figure 4.2.2, Page 50). Le désaccord en fréquence entre les lasers maître et esclave (*detuning*) est fixé à  $\Delta\nu = \nu_{\text{ML}} - \nu_{\text{SL}} = -36$  GHz (avec  $\nu_{\text{ML}}$  la fréquence du laser maître et  $\nu_{\text{SL}}$  la fréquence du VCSEL en régime solitaire). Dans ces conditions, en augmentant progressivement la puissance injectée, on observe un basculement de polarisation induit par injection optique [Figure B.3.2(a)]. Si ensuite on diminue progressivement la puissance injectée, un basculement de polarisation dans le sens inverse est observé (du mode vertical vers le mode horizontal) [Figure B.3.2(b)]. Ce dernier

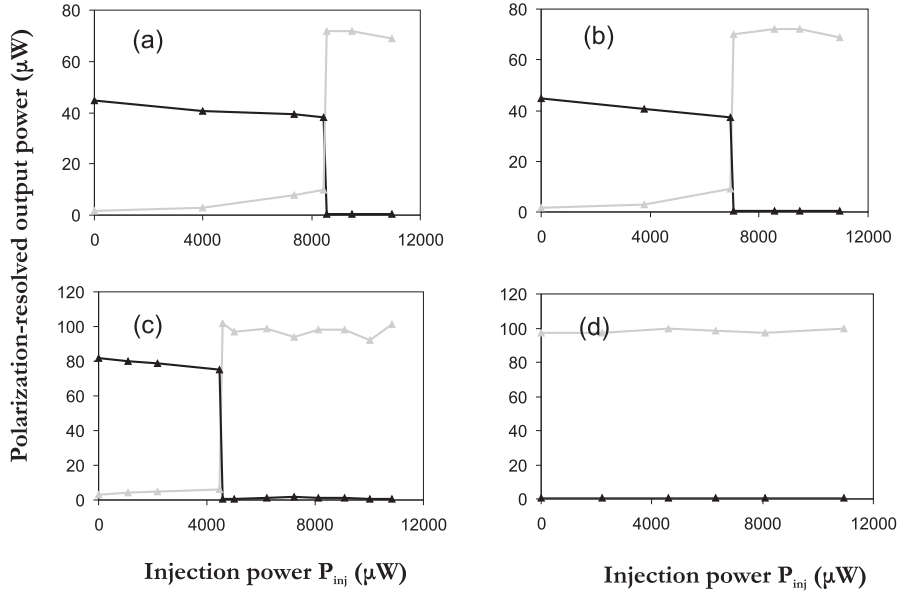


**Figure B.3.2:** *Evolution de la puissance de sortie des modes basse fréquence BF (x-polarisation horizontale en noir) et haute fréquence HF (y-polarisation verticale en gris) du VCSEL<sub>2</sub> lorsqu'on varie la puissance injectée  $P_{inj}$  pour deux valeurs distinctes de courant d'injection  $I_{SL}$ :  $I_{SL} = 1.9$  mA et detuning  $\Delta\nu = -36$  GHz: (a)  $P_{inj}$  croissant, (b)  $P_{inj}$  décroissant ;  $I_{SL} = 2.603$  mA et detuning  $\Delta\nu = -20$  GHz: (c)  $P_{inj}$  croissant, (d)  $P_{inj}$  décroissant.*

basculé est réalisé pour une puissance d'injection plus faible que celle correspondant au premier, mettant ainsi en évidence une zone de bistabilité de polarisation.

Nous fixons maintenant le courant d'injection à 2.603 mA, tel que le VCSEL libre d'injection fonctionne à l'intérieur de la zone de bistabilité de polarisation de la courbe puissance-courant (consulter la version anglaise, Figure 4.2.2, Page 50). En augmentant progressivement la puissance injectée, on observe également un basculement du mode horizontal vers le mode vertical [Figure B.3.2(c)]. Cependant, si ensuite on diminue la puissance injectée [Figure B.3.2(d)], et contrairement à la situation montrée à la Figure B.3.2(b), le VCSEL maintient une émission dans le mode vertical même lorsque l'injection optique est supprimée.



### B.3.2 Bistabilité de polarisation induite par variation la de puissance injectée: *résultats théoriques*

Dans cette partie, nous présentons nos résultats théoriques sur la bistabilité de polarisation dans un VCSEL soumis à injection optique. Les simulations numériques ont été menées en utilisant le modèle SFM étendu à l'injection optique. Les paramètres du modèle sont choisis de telle sorte que le VCSEL en régime solitaire émet dans le mode basse fréquence (mode BF). L'injection optique est alors réalisée selon la direction de polarisation orthogonale à celle du mode BF. Les équations de taux du modèle SFM modifié ont la forme suivante:

$$\frac{dE_x}{dt} = \kappa(1 + i\alpha)(DE_x + idE_y - E_x) - i(\gamma_p + \Delta\omega)E_x - \gamma_a E_x, \quad (\text{B.3.1})$$

$$\begin{aligned} \frac{dE_y}{dt} &= \kappa(1 + i\alpha)(DE_y - idE_x - E_y) + i(\gamma_p - \Delta\omega)E_y + \gamma_a E_y \\ &+ \kappa_{inj}E_{inj}^0, \end{aligned} \quad (\text{B.3.2})$$

$$\frac{dD}{dt} = -\gamma_e \left[ D \left( 1 + |E_x|^2 + |E_y|^2 \right) \right] + \gamma_e \mu - i\gamma_e d (E_y E_x^* - E_x E_y^*), \quad (\text{B.3.3})$$

$$\frac{dd}{dt} = -\gamma_s d - \gamma_e d \left( |E_x|^2 + |E_y|^2 \right) - i\gamma_e D (E_y E_x^* - E_x E_y^*). \quad (\text{B.3.4})$$

Les variables d'état  $E_x$ ,  $E_y$ ,  $D$ ,  $d$  ainsi que les paramètres du modèle  $\kappa$ ,  $\gamma_p$ ,  $\gamma_a$ ,  $\gamma_e$ ,  $\gamma_s$ ,  $\alpha$  et  $\mu$  ont la même signification que dans les Eqs. (B.2.1)-(B.2.4). L'injection optique est prise en compte via le taux d'injection,  $\kappa_{inj}$ , l'amplitude du champ injecté,  $E_{inj}^0$ , ainsi que le detuning  $\Delta\omega$  (qui représente le désaccord en fréquence entre les lasers maître et esclave).  $\Delta\omega = \omega_{inj} - \omega_{int}$ , où  $\omega_{inj}$  la fréquence du champ électrique injecté et  $\omega_{int}$  est une fréquence intermédiaire entre la fréquence du mode BF orienté selon la polarisation  $x$  et celle du mode HF orienté selon  $y$ :  $\omega_{x,y} = \mp\gamma_p \pm \alpha\gamma_a$ , ainsi  $\omega_{int} = (\omega_x + \omega_y)/2$ .

Les paramètres du modèle sont fixés de la manière suivante:  $\kappa = 300 \text{ ns}^{-1}$ ,  $\gamma_p = 6.28 \text{ rad/ns}$ ,  $\gamma_a = -0.2 \text{ ns}^{-1}$ ,  $\gamma_s = 50 \text{ ns}^{-1}$ ,  $\gamma_e = 0.55 \text{ ns}^{-1}$ ,  $\alpha = 3$ . Avec ces paramètres, la courbe puissance-courant du VCSEL en mode solitaire exhibe un basculement de polarisation de type II (voir Figure 4.4.1, Page 54 dans la version anglaise). En choisissant convenablement le courant d'injection nous montrons que, sous injection optique orthogonale, le modèle décrit par les équations de taux (B.3.1)-(B.3.4) reproduit qualitativement les résultats expérimentaux présentés à la Section B.3.1.

Nous procédons d'une manière similaire à l'expérience réalisée à la Section B.3.1. Le courant d'injection est d'abord fixé de telle sorte que le VCSEL en régime solitaire opère en deçà de la limite inférieure de la zone de bistabilité de polarisation du VCSEL ( $\mu=1.15$ , voir Figure 4.4.1, Page 54 dans la

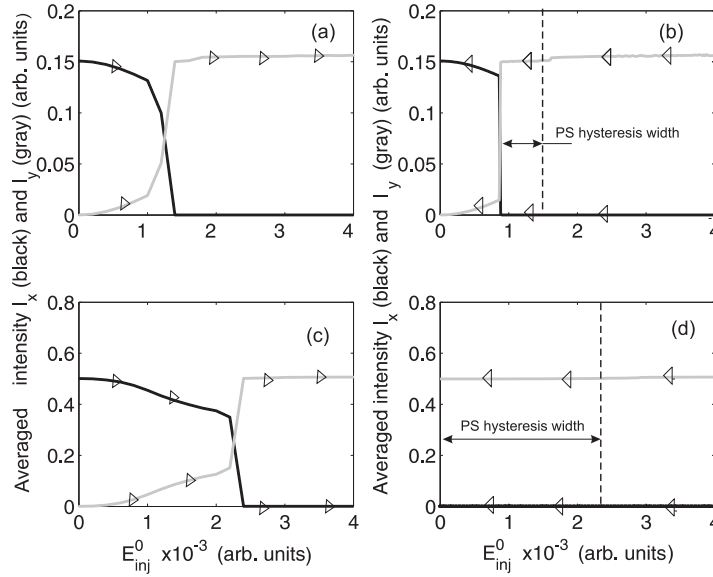


**Figure B.3.3:** Evolution de la puissance de sortie des modes basse fréquence BF ( $x$ -polarisation horizontale en noir) et haute fréquence HF ( $y$ -polarisation verticale en gris) du VCSEL lorsqu'on varie l'amplitude du champ injecté  $E_{inj}^0$  pour deux valeurs distinctes du courant d'injection: 1)  $\mu = 1.15$  en augmentant  $E_{inj}^0$  (a) puis en diminuant  $E_{inj}^0$  (b); 2)  $\mu = 1.5$  en augmentant  $E_{inj}^0$  (c) puis en diminuant  $E_{inj}^0$  (d). Le detuning est fixé à  $\Delta\omega = 3 \text{ rad}\cdot\text{ns}^{-1}$ .

version anglaise). Dans ces conditions, en augmentant l'intensité du champ injecté  $E_{inj}^0$ , un basculement de polarisation du mode BF vers le mode HF est obtenu [Figure B.3.3(a)]. Si, ensuite, nous diminuons  $E_{inj}^0$ , le VCSEL bascule du mode HF vers le mode BF pour un  $E_{inj}^0$  beaucoup plus faible, laissant ainsi apparaître un zone de bistabilité de polarisation induite par injection optique [Figure B.3.3(b)]. Ce résultat s'accorde qualitativement à ce qui a été observé expérimentalement aux Figures B.3.2(a) et (b). Nous fixons maintenant le courant d'injection  $\mu$  de telle sorte que le VCSEL en régime solitaire opère à l'intérieur de la zone solitaire ( $\mu=1.5$ , voir Figure 4.4.1, Page 54 dans la version anglaise). Les simulations numériques montrent qu'un basculement polarisation du mode BF vers le mode HF est obtenu en augmentant progressivement  $E_{inj}^0$  [Figure B.3.3(c)]. Si ensuite nous diminuons  $E_{inj}^0$  [Figure B.3.3(d)], le VCSEL continue à émettre dans le mode HF même si l'on supprime complètement l'injection optique; ce qui est en accord qualitatif avec le résultat expérimental montré à la Figure B.3.2(d).

### B.3.3 Bistabilité de polarisation induite par variation du detuning: *résultats théoriques*

Dans les Sections B.3.1 et B.3.2 la bistabilité de polarisation est induite en variant la puissance injectée tout en fixant le désaccord en fréquence (*detuning*) entre les lasers maître et esclave. Dans cette partie, nous étudions théoriquement la bistabilité de polarisation induite par variation du detuning pour une puissance d'injection fixe. Cette étude a été motivée par les travaux expérimentaux élaborés par Hong *et al* dans la configuration d'injection orthogonale [132].

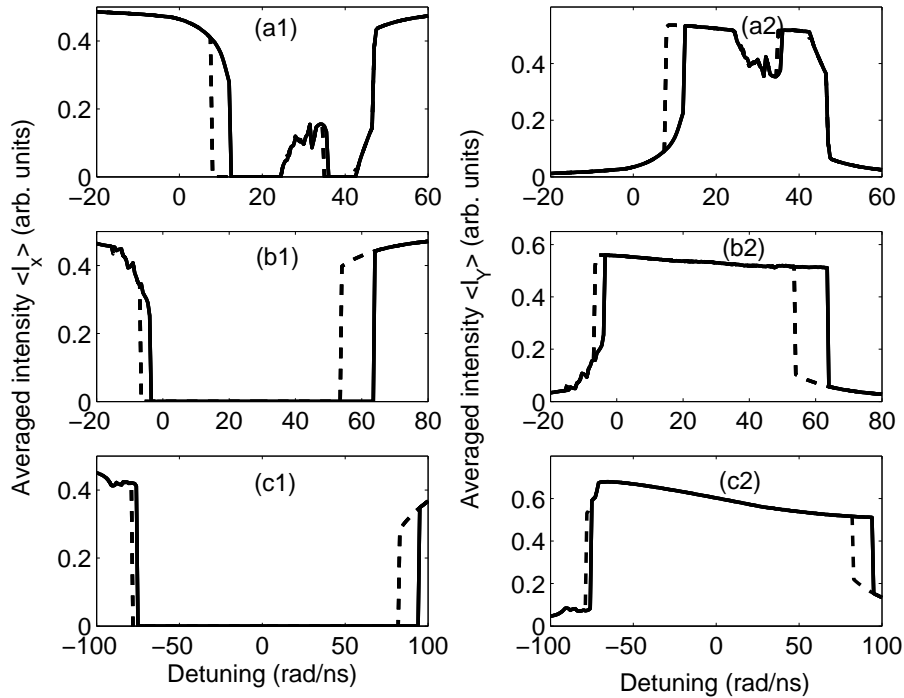


**Figure B.3.4:** Influence de la puissance injectée sur la largeur de l'hystérèse de basculement de polarisation. L'évolution de la puissance moyenne est analysée dans la direction de polarisation horizontale (*x-mode BF*) et verticale (*y-mode HF*). Le désaccord entre la fréquence du VCSEL et celle du laser maître,  $\Delta\omega$ , est balayé d'abord dans le sens des valeurs négatives vers les valeurs positives (trait plein) ainsi que dans le sens contraire (traits en pointillés). Les niveaux des puissances injectées sont les suivants : (a1), (a2):  $P_{inj}/I_0 = 0.05$ , (b1), (b2):  $P_{inj}/I_0 = 0.15$ , (c1), (c2):  $P_{inj}/I_0 = 1.5$ . Avec  $P_{inj} = |E_{inj}^0|^2$  et  $I_0 = |E_x^0|^2 + |E_y^0|^2$ .  $E_x^0$  et  $E_y^0$  étant, respectivement, les amplitudes des champs électriques dans les modes orthogonaux du VCSEL en régime solitaire.

Hong *et al.* [132] ont observé expérimentalement deux points de basculement lorsque le detuning est varié tout en fixant la puissance injectée: pour des detunings croissants, un premier basculement de polarisation est réalisé du mode BF vers le mode HF (point de basculement BF, *PB BF*) et un deuxième, situé dans la zone des larges detunings, est réalisé du mode HF vers le mode BF (point de basculement HF, *PB HF*). Ces résultats expérimentaux montrent, qu'en balayant le detuning, une large zone de bistabilité de polarisation est associée au *PB BF* tandis que le *PB HF* est réalisé quasiment sans hystérèse. Nous complétons ces résultats par une investigation théorique des phénomènes de bistabilité de basculement de polarisation induits par une variation du Detuning. Comme dans l'expérience de Hong *et al.* [132], le schéma d'injection orthogonale est adopté. A cet effet, nous utilisons les équations de taux du modèle SFM étendu à l'injection optique [voir Eqs.(B.3.1)-(B.3.4)]. Le résultat des simulations numériques est présenté à la Figure B.3.4. Nous adoptons trois niveaux de puissance différents. Pour une puissance d'injection relativement faible [Figure B.3.4(a1),(a2),  $P_{inj}/I_0 = 0.15\%$ ], en accord avec les résultats expérimentaux rapportés dans [132], on montre qu'en balayant le detuning, seul le point de basculement *PB BF* fait apparaître un hystérésis. Pour des niveaux élevés de puissance injectée, nous montrons que l'hystérèse de basculement de polarisation est maintenant associée tant au point de basculement *PB BF* qu'à *PB HF*.

Nous avons entrepris d'autres simulations numériques qui montrent que la largeur de l'hystérèse associée à la bistabilité de polarisation dépend de manière très significative non seulement du niveau de puissance injectée mais aussi des paramètres caractéristiques du VCSEL tels le facteur de Henry ( $\alpha$ ) ou le taux de relaxation de l'état de spin des porteurs ( $\gamma_s$ ).

## B.4 Etude expérimentale de dynamiques non-linéaires qui accompagnent le basculement de polarisation d'un VCSEL soumis à injection optique orthogonale

Les lasers à semi-conducteurs soumis à injection optique peuvent exhiber des dynamiques non-linéaires complexes. En fonction des paramètres d'injection, c'est-à-dire puissance injectée et detuning, le laser injecté peut se verrouiller sur la fréquence du laser maître [110, 111]. A part le régime de verrouillage en fréquence, d'autres dynamiques plus complexes tels le mélange d'ondes, le régime périodique ou encore la route de doublement de période vers le régime chaotique ont été observées [11, 16]. Les études théoriques et expérimentales antérieures ont concerné surtout l'injection optique dans les lasers émettant par le côté [12, 16, 137, 143]. Citons, en particulier, les travaux de Simpson

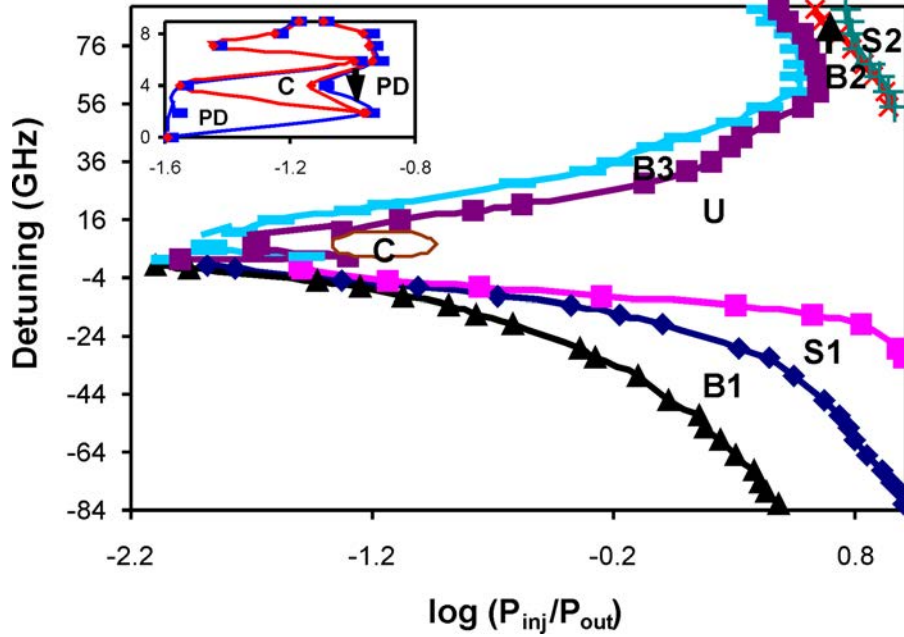


**Figure B.4.1:** Cartographie des dynamiques non-linéaires du VCSEL<sub>2</sub> soumis à injection optique orthogonale. Les zones de dynamiques non-linéaires qualitativement différentes sont représentées lorsqu'on balaye la puissance injectée  $P_{inj}$  pour une gamme relativement large de detuning ( $\Delta\nu = \nu_{ML} - \nu_{SL}$ ). B1, B2, B3: régions de bistabilité de polarisation; S1-S2: région de régime stable de verrouillage; U: zone de régime périodique non-verrouillé; C: zone de dynamiques chaotiques. La figure insérée montre la dynamique de doublement de période (PD) dans le voisinage de la région d'instabilités chaotiques C. Le puissance injectée a été normalisée par rapport à  $P_{out}$  (puissance de sortie du VCSEL en régime solitaire). Le courant d'injection a été fixé à 2.105 mA et la température a été maintenue à 20°C.

et al. [16] qui ont réalisé une cartographie détaillée des dynamiques non-linéaires du laser dans le plan de paramètres d'injection.

En ce qui concerne les VCSELs, les études antérieures sur les dynamiques non-linéaires ont été menées dans la configuration où le faisceau injecté est polarisé parallèlement au mode dominant du VCSEL en régime solitaire [121]. Ces études ont montré que les VCSELs sous injection peuvent exhiber des dynamiques non-linéaires similaires à celles observées dans le cas des lasers émettant par le côté. Toutefois, l'injection parallèle ne permet pas de mettre en évidence la dynamique de polarisation du VCSEL du fait que le faisceau injecté a la même polarisation que celle du mode dominant du VCSEL en régime solitaire.

Nous avons réalisé une étude expérimentale de la dynamique du VCSEL soumis à injection optique orthogonale. Le banc expérimental est le même que celui présenté à la Figure B.3.1. Le courant d'injection est fixé à 2.105 mA de telle sorte que le VCSEL en régime solitaire opère dans le mode fondamental basse fréquence de polarisation linéaire horizontale, en deçà de la zone de bistabilité de polarisation de la courbe puissance-courant.

La Figure B.4.1 représente une cartographie détaillée de la dynamique du VCSEL soumis à injection optique orthogonale dans le plan des paramètres d'injection: detuning  $\Delta\nu = \nu_{ML} - \nu_{SL}$  et puissance injectée normalisée en échelle logarithmique  $[\log(P_{inj}/P_0)]$ . La puissance injectée est balayée pour une gamme relativement large de valeurs du detuning. Tout changement qualitatif dans la dynamique du VCSEL soumis à injection optique est détecté et repéré par une couleur spécifique dans la cartographie.

Dans la gamme des detunings négatifs, en augmentant progressivement la puissance injectée  $P_{inj}$ , on observe un basculement du mode fondamental de polarisation linéaire horizontal vers la polarisation verticale (courbe en bleu foncé). Soulignons le fait que ce basculement de polarisation s'accompagne d'un verrouillage du VCSEL à la fréquence du laser maître. En augmentant d'avantage  $P_{inj}$ , le régime de verrouillage est déstabilisé par l'excitation d'un régime périodique à la fréquence proche de celle des oscillations de relaxation du laser esclave. L'excitation de ce régime est repéré par la courbe en rose (cette courbe correspond, dans le jargon de la dynamique des systèmes non-linéaires, à une bifurcation de Hopf). Les courbes, respectivement, en bleu foncé et en rose délimitent ainsi une large zone de verrouillage (nommé S1 sur la Figure B.4.1) qui s'étend sur une gamme de puissance injectée de plus en plus large à mesure qu'on évolue vers des detunings négatifs plus élevés. En diminuant la puissance injectée après que le basculement de polarisation ait eu lieu, on remarque que le VCSEL retrouve sa polarisation de départ (horizontale) pour une valeur de puissance injectée plus petite que celle qu'il a fallu pour entraîner le basculement dans le sens croissant des puissances injectées. Par conséquent, une large zone de bistabilité de polarisation induite par injection optique est observée (voir la région nommée B1 qui est délimitée par les courbes, respectivement, en noir et en bleu foncé sur la Figure B.4.1). Nous avons remarqué que les régions B1 et S1 s'étendent jusqu'au detuning de 2 GHz qui représente la birefringence du VCSEL, c'est-à-dire le désaccord en fréquence entre les modes fondamentaux orthogonaux du VCSEL.

En opérant dans la gamme des detunings positifs supérieurs à 2 GHz, une augmentation progressive de la puissance injectée conduit au basculement de polarisation du mode horizontal vers le mode vertical (voir la courbe marquée en violet sur la Figure B.4.1). Contrairement à ce qui est observé pour les detunings négatifs, le basculement entre les modes fondamentaux n'est pas accompagné par un verrouillage du VCSEL au laser maître. En effet,

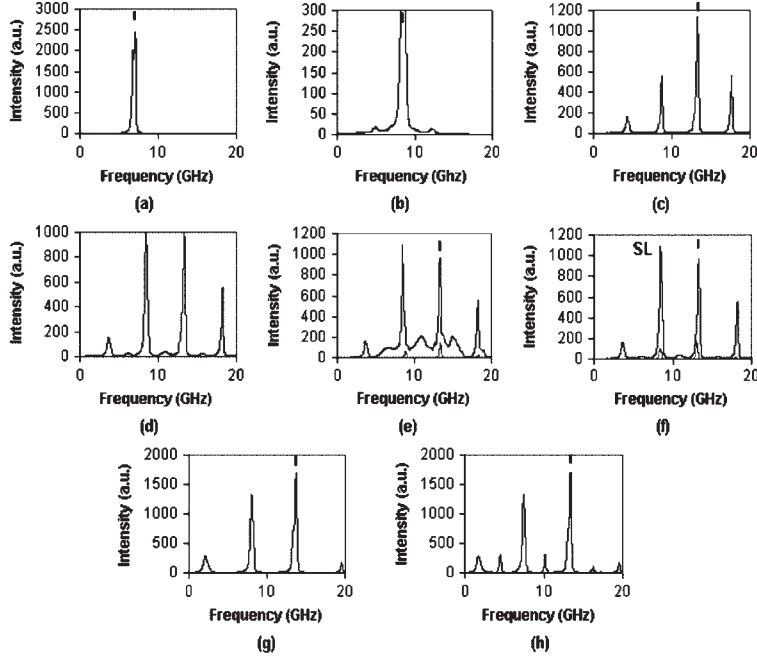


**Figure B.4.2:** Spectres optiques montrant l'évolution de la dynamique du VCSEL soumis à injection optique lorsqu'on augmente la puissance injectée  $P_{inj}$  pour un detuning fixé à  $\Delta\nu = 2$  GHz: (a)  $P = 13.2 \mu W$ ; (b)  $23.6 \mu W$ ; (c)  $36.6 \mu W$ ; (d)  $47.8 \mu W$ ; (e)  $80.3 \mu W$ ; (f)  $136.6 \mu W$ ; (g)  $204 \mu W$ ; (h)  $351 \mu W$ . Le spectre d'intensité faible sur les Figures (e)-(f) correspond à la dynamique dans le mode de polarisation horizontale. Le trait vertical indique la position de la fréquence du laser maître ML.

le VCSEL bascule vers un régime périodique non verrouillé dans le mode de polarisation verticale. Toutefois, pour des detunings positifs suffisamment larges, nous avons observé que le basculement de polarisation entre les modes fondamentaux peut être suivi par un régime de verrouillage du mode transverse de premier ordre à la fréquence du laser maître (l'entrée dans ce régime, nommé S2, est repérée par la courbe en vert foncé sur la Figure B.4.1). A ce régime de verrouillage particulier est également associé une région de bistabilité entre le mode transverse fondamental et le mode transverse de premier ordre (nommée B2 sur la Figure B.4.1).

Nous avons mis en évidence une zone de dynamiques non-linéaires complexes autour de la valeur critique de detuning de 2 GHz. En effet, dans un gamme restreinte de detuning autour de 2 GHz, nous avons remarqué que les dynamiques de basculement de polarisation et de verrouillage peuvent s'accompagner d'un régime de doublement de période vers le chaos optique. Nos résultats montrent, en particulier, que la présence de ces dynamiques non-linéaires complexes a un effet relativement important sur la puissance

injectée nécessaire pour induire le basculement de polarisation.

Nous montrons à la Figure B.4.2 un scénario de basculement de polarisation pour un detuning de  $\Delta\nu = 2$  GHz. Les spectres optiques ont été enregistrés pour plusieurs niveaux de puissance injectée. La Figure B.4.2(a) montre une dynamique dans laquelle le VCSEL est verrouillé sur la fréquence du laser maître après que le basculement de polarisation soit déjà réalisé. En augmentant progressivement la puissance optique injectée, nous mettons en évidence une dynamique périodique à la fréquence des oscillations de relaxation du VCSEL [Figure B.4.2(b)] (ceci se traduit par l'apparition des deux raies latérales de parts et d'autres de la raie à la fréquence du laser maître) ainsi que de ses harmoniques [Figure B.4.2(c)]. Au fur et à mesure qu'on augmente la puissance injectée, le VCSEL exhibe un doublement de période [Figure B.4.2(d)] qui, ensuite, conduit à un régime complexe de dynamique chaotique caractérisé par l'apparition d'un spectre relativement très large et qui met en compétition les deux modes fondamentaux orthogonaux du VCSEL [Figure B.4.2(e)]. Pour des niveaux de puissance plus élevés, la sortie du régime chaotique s'accompagne d'un doublement inverse de période [Figures B.4.2(f)-(g)]. Pour une puissance injectée encore plus élevée, nous avons observé un deuxième régime de doublement de période [Figure B.4.2(h)]. A part le doublement de période vers le chaos optique, nous avons également noté une région de detunings positifs dans laquelle on observe d'autres dynamiques complexes dont le mélange d'ondes et la résonance sous-harmonique.

Nous avons élaboré une autre cartographie détaillée du basculement de polarisation ainsi que des dynamiques non linéaires y associées [voir Figure B.4.3]. Cette dernière complète nos résultats présentés à la Figure B.4.1. Nous nous sommes intéressés particulièrement aux dynamiques périodiques qui accompagnent le basculement de polarisation avec verrouillage du  $VCSEL_1$ <sup>2</sup> à la fréquence du laser maître. Nos observations révèlent également un régime particulier de basculement de polarisation entre un régime périodique dans les deux modes fondamentaux de polarisations linéaires orthogonales et un régime périodique uniquement dans le mode injecté du VCSEL.

La cartographie montrée à la la Figure B.4.3 a été obtenue en fixant le courant d'injection de telle sorte que le VCSEL, libre d'injection optique, émet une lumière polarisée horizontalement. Le VCSEL étant ensuite soumis à une injection optique orthogonale, nous augmentons la puissance d'injection optique pour un detuning fixe entre les lasers maître et esclave.

---

<sup>2</sup>Cette étude a été réalisée en utilisant le composant  $VCSEL_1$ . Le composant  $VCSEL_2$  était endommagé à ce stade de nos expériences. Bien que les deux composants aient des caractéristiques puissance courant différentes leur comportement qualitatif sous injection optique est similaire



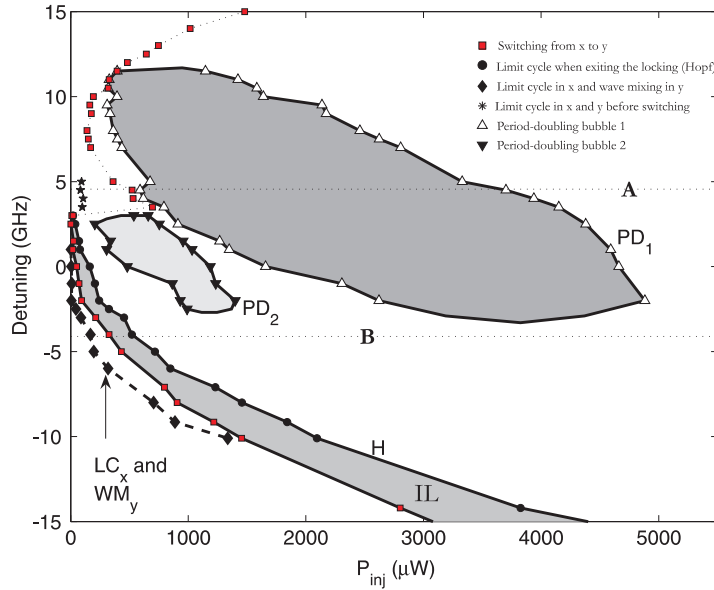


**Figure B.4.3:** *Cartographie détaillée de dynamiques non linéaires du VCSEL soumis à injection optique de polarisation orthogonale. La puissance injectée  $P_{inj}$  est variée pour un désaccord en fréquence (detuning) fixe. Plusieurs zone de dynamiques qualitativement différentes sont observées : zone de verrouillage du VCSEL à la fréquence du laser maître (IL), deux régions de dynamiques de doublement de période délimitées respectivement par  $PD_1$  and  $PD_2$ . Dynamiques périodiques précédant le régime de verrouillage (courbe marqué par des losanges d'une part et des étoiles d'autre part). Le courant d'injection est fixé à 1.175 mA et la température à 20°C. Avec ces conditions, le VCSEL en régime solitaire émet dans le mode fondamental basse fréquence selon la direction de polarisation horizontale (x).*

En procédant ainsi pour plusieurs valeurs de detuning, on enregistre chaque point de bifurcation, c'est-à-dire, le point de changement qualitatif dans la dynamique du VCSEL injecté. Les points de bifurcation correspondant au basculement de polarisation sont indiqués par des carrés en rouge. Le régime de verrouillage du VCSEL sur le laser maître s'étend sur la zone hachurée appelée IL (*injection locking*). Cette dernière se situe essentiellement dans la gamme des detunings négatifs. Elle est délimitée à gauche par la courbe de basculement de polarisation et à droite par la bifurcation de Hopf, qui coïncide avec la déstabilisation du régime de verrouillage via l'excitation d'un régime périodique à la fréquence des oscillations de relaxation du VCSEL. Nous notons également la présence de deux zones distinctes caractérisées par un régime de doublement de période. Les frontières de ces deux zones sont marquées  $PD_1$  et  $PD_2$  respectivement. Nous insistons sur le fait que

la présence de ces dynamiques de doublement de période a un impact significatif sur la courbe de basculement de polarisation. En effet, dans le voisinage de  $PD_1$  et  $PD_2$ , la courbe de basculement de polarisation exhibe une forme particulière en “S”, qui met en évidence une interaction entre dynamiques non-linéaires et basculement de polarisation induits par injection optique. Ci-après, nous analysons plus en détail deux zones de dynamiques périodiques qui accompagnent le basculement de polarisation.

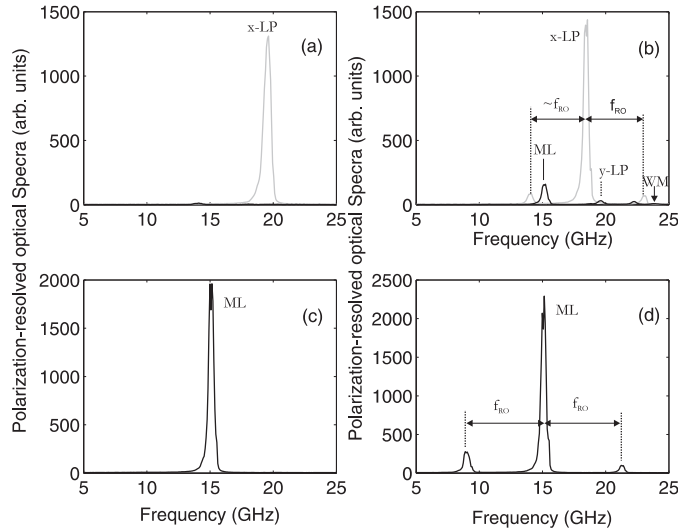


**Figure B.4.4:** Spectres d’intensité optique montrant l’évolution de la dynamique du VCSEL pour un désaccord en fréquence de  $\Delta\nu = -4.1$  GHz, en augmentant la puissance injectée (a)  $P_{inj} = 19 \mu W$ ; (b)  $88 \mu W$ , excitation d’un cycle limite dans le mode non injecté (polarisé horizontalement) et mélange d’onde dans le mode injecté (polarisé verticalement), (c)  $114 \mu W$ , régime de verrouillage du VCSEL sur la fréquence du laser maître; (d)  $236 \mu W$ , excitation d’un cycle limite après déstabilisation du régime de verrouillage. Les courbes noirs (gris) représentent la dynamique dans le mode de polarisation verticale (horizontale).

A la Figure B.4.4 nous décrivons un scénario de dynamique pour lequel le basculement de polarisation suivi du verrouillage du VCSEL sur le laser maître est précédé par l’excitation d’un régime périodique dans les deux modes fondamentaux de polarisations linéaires et orthogonales. A cette fin, nous analysons l’évolution du spectre d’intensité optique lorsque nous varions la puissance injectée  $P_{inj}$  pour un désaccord en fréquence  $\Delta\nu$  fixe (dans ce cas précis  $\Delta\nu = -4.1$  GHz, voir la ligne en pointillés marquée par “B” sur la Figure B.4.3). Pour une puissance injectée faible [voir Figure B.4.4(a)], le VCSEL émet dans le mode polarisé horizontalement. Au fur et à mesure que

nous augmentons la puissance d'injection, nous observons que la fréquence du VCSEL évolue progressivement vers celle du laser maître. Cependant, nos résultats mettent en évidence un point de bifurcation particulier qui correspond à l'excitation simultanée d'un régime périodique à la fréquence des oscillations de relaxation du VCSEL dans le mode non injecté (mode horizontal), et un régime de mélange d'ondes dans le mode injecté du VCSEL (mode vertical) [voir Figure B.4.4(b)]. L'excitation de ce régime est marquée par des losanges dans la Figure B.4.3. En augmentant progressivement la puissance injectée, nous réalisons un basculement de polarisation suivi du verrouillage du VCSEL à la fréquence du laser maître [voir Figure B.4.4(c)]. Ce régime est ensuite déstabilisé par l'excitation d'un régime périodique qui apparaît uniquement dans le mode vertical et à la fréquence des oscillations de relaxation ( $f_{RO}$ ) [voir Figure B.4.4(d)].

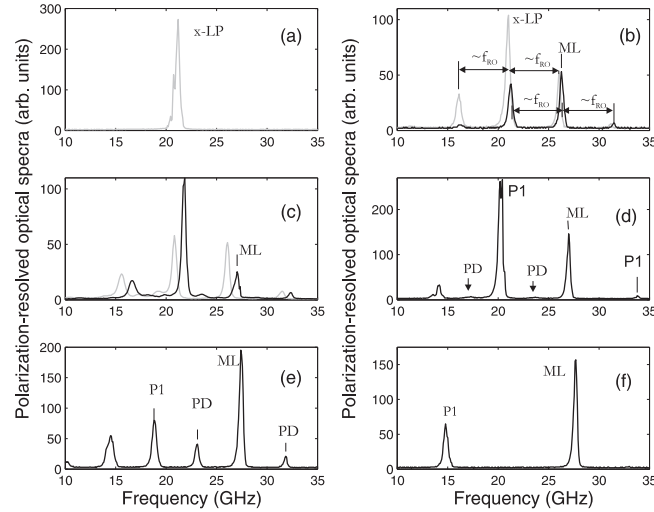


**Figure B.4.5:** Spectres expérimentaux d'intensité optique montrant un scénario de basculement de polarisation impliquant un passage du système d'une dynamique périodique (cycle limite) dans les deux modes de polarisations orthogonales vers une dynamique périodique uniquement dans le mode injecté pour un désaccord en fréquence de  $\Delta\nu = 4.4$  GHz. La puissance injectée  $P_{inj}$  est augmentée progressivement: (a)  $P_{inj} = 3 \mu W$ ; (b)  $83 \mu W$ ; (c)  $185 \mu W$ ; (d)  $265 \mu W$ ; (e)  $558 \mu W$ ; (f)  $3454 \mu W$ .  $P_1$  correspond au régime de cycle limite de période une fois celle des oscillations de relaxation (period-one limit cycle) tandis que PD indique la présence d'un attracteur de doublement de période (period doubling). Le traits noirs (gris) représentent la dynamique dans le mode de polarisation verticale (horizontale).

Nous focalisons ensuite notre attention sur un scénario de basculement

de polarisation qui est observé dans une gamme étroite de désaccord en fréquence localisée à l'extérieure mais tout en restant proche de la zone de verrouillage. Un échantillon de ce régime est présenté à la Figure B.4.5 pour un désaccord en fréquence  $\Delta\nu = 4.4$  GHz. Pour une puissance injectée faible, le VCSEL émet principalement dans le mode de polarisation horizontale [voir Figure B.4.5(a)]. En augmentant la puissance injectée  $P_{inj}$ , un régime périodique apparaît simultanément dans le mode non injecté (de polarisation horizontale) et dans le mode injecté (de polarisation verticale) [voir Figure B.4.5(b)]. Cependant, contrairement à ce que nous avons observé dans le scénario de la Figure B.4.4, les régimes périodiques dans les deux modes de polarisations orthogonales apparaissent à la fréquence des oscillations de relaxation  $f_{RO} \approx 5.1$  GHz. Par ailleurs, avant basculement de polarisation, le régime périodique est déstabilisé. Ceci se manifeste par l'apparition d'un spectre optique plus ou moins large [voir Figure B.4.5(c)], indiquant l'effet d'un attracteur de doublement de période situé dans le voisinage du point de basculement. En augmentant davantage la puissance injectée, le VCSEL bascule vers un régime périodique uniquement dans le mode de polarisation verticale [voir Figure B.4.5(d)]. Ensuite cette dynamique exhibe un régime de doublement de période bien établi [voir Figure B.4.5(e)] qui correspond, en fait, à la zone délimitée par la courbe  $PD_1$  à la Figure B.4.5. Pour un niveau de puissance d'injection beaucoup plus élevée, un régime de doublement de période inverse est observé et conduit à un régime périodique simple dont la fréquence est beaucoup plus grande que celle des oscillations de relaxations ("*enhanced relaxation oscillation frequency*") [Figure B.4.5(f)].

## B.5 Etude théorique du VCSEL soumis à injection optique orthogonale: analyse des bifurcations associées à la dynamique de basculement

Des études théoriques basées sur l'analyse de bifurcations ont été antérieurement entreprises, dans le but d'élucider la complexité des dynamiques non-linéaires induites par injection optique dans les lasers à semi-conducteurs [145, 151, 152]. En utilisant des méthodes modernes de continuation des équations de taux du laser à semi-conducteurs soumis à injection optique, une cartographie de dynamiques non-linéaires a été réalisée dans le plan des paramètres d'injection [152]. Ces travaux ont eu le mérite de montrer que les dynamiques non-linéaires ainsi que les différentes bifurcations qui y sont associés sont globalement liées entre-elles [152].

Un des volets théoriques de nos travaux de thèse a concerné l'étude de la dynamique du VCSEL dans la configuration d'injection orthogonale. Ici l'objectif est de pouvoir apporter une interprétation cohérente de plusieurs

phénomènes que nous avons mis en évidence expérimentalement. A cet effet, nous avons réalisé des simulations numériques moyennant aussi bien les méthodes classiques d'intégration que les méthodes modernes de continuation des équations différentielles de taux du laser injecté. Ainsi, nous pouvons simuler les phénomènes dont la détection expérimentale est limitée, sinon impossible. C'est le cas, par exemple, des bifurcations de dynamiques instables qui ne peuvent pas être détectées expérimentalement mais qui, cependant, participent à l'organisation globale de la dynamique du laser VCSEL sous injection optique [152]. A cette fin, nous avons eu recours aux méthodes modernes de continuation d'équations différentielles. Ces méthodes permettent de détecter et de continuer les différentes bifurcations qui ont lieu sur les solutions tant stables qu'instables. Par bifurcation, nous entendons, l'apparition d'un changement qualitatif de la dynamique lorsqu'on varie un ou plusieurs paramètres du système.

Nous révélons l'existence de bifurcations (Hopf et tore) qui jouent un rôle très important dans l'organisation globale des dynamiques non-linéaires qui accompagnent le basculement de polarisation du VCSEL soumis à injection optique. Nous montrons que nos résultats théoriques sont en accord avec nos observations expérimentales et qu'ils sont génériques aux modèles théoriques simulant le VCSEL sous injection optique (SFM et modèle dit à deux modes).

### B.5.1 Dynamiques non-linéaires accompagnant le basculement de polarisation: *scénarios*

Nous utilisons le modèle SFM décrit par les Eqs. (B.3.1)-(B.3.4). Les paramètres suivants ont été utilisés:  $\kappa = 300 \text{ ns}^{-1}$ ,  $\gamma_p = 30 \text{ rad/ns}$ ,  $\gamma_a = 0.5 \text{ ns}^{-1}$ ,  $\gamma_s = 50 \text{ ns}^{-1}$ ,  $\gamma_e = 1 \text{ ns}^{-1}$ . Le paramètre  $\alpha$  a été modifié en vue d'analyser son influence sur la dynamique globale du VCSEL soumis à injection.

#### B.5.1.1 Dynamiques nonlinéaires accompagnant le basculement de polarisation: modèle SFM

En utilisant les méthodes numériques classiques pour l'intégration des Eqs. - (B.3.1)-(B.3.4) pour une valeur de  $\alpha=3$ , nous mettons en évidence quelques scénarios typiques de basculement de polarisation du VCSEL. La force d'injection  $E_{inj}$  est balayée pour différentes valeurs de detuning  $\Delta\omega$ . Nous montrons que selon la valeur du detuning, le basculement de polarisation peut s'accompagner de dynamiques non-linéaires plus ou moins complexes.

Les Figures B.5.1(a1)-(a2) représente un scénario de basculement de polarisation dans la gamme de detuning relativement larges ( $\Delta\omega = 72 \text{ rad.ns}^{-1}$ ). Dans ce cas, le basculement de polarisation se fait de manière assez abrupte et n'implique pas de dynamiques complexes. Notons qu'une zone d'hystérèse

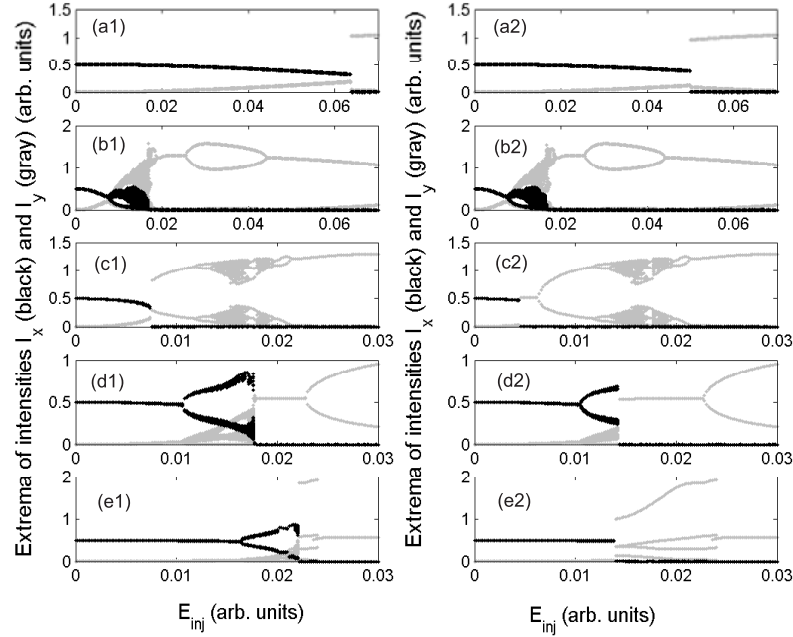


**Figure B.5.1:** Diagrammes de bifurcations montrant l'évolution des maxima et minima des intensités du champ optique du mode fondamental basse fréquence (polarisation  $x$ , noir) et du mode fondamental haute fréquence (polarisation  $y$ , gris) pour les valeurs de detuning suivantes: (a)  $\Delta\omega = 72$ ; (b) 30; (c) 23; (d) 10; and (e)  $-2.2 \text{ rad.ns}^{-1}$ . Colonne de figures à gauche: forces  $E_{inj}$  croissantes; Colonne de figures à droite: forces  $E_{inj}$  décroissantes. Le facteur de Henry  $\alpha = 3$ .

est associé au basculement du mode BF ( $x$ ) (très légèrement modulé en amplitude) vers le mode HF ( $y$ ) en régime périodique à la fréquence proche du detuning.

En fixant le detuning à une valeur assez élevée tout en restant en dehors du régime de verrouillage de VCSEL [Figures B.5.1(b1)-(b2) pour  $\Delta\omega = 30 \text{ rad.ns}^{-1}$ ], le basculement de polarisation du mode  $x$  vers le mode  $y$  s'accompagne de dynamiques non-linéaires complexes. Une analyse détaillée de ce scénario révèle l'excitation des dynamiques périodiques apparaissant dans les deux modes orthogonaux. En fait, en accord avec nos observations expérimentales de la Figure B.4.5, nous notons qu'il s'agit d'une dynamique intéressante montrant un basculement de polarisation d'un régime périodique dans les modes injecté ( $y$ ) et non-injecté ( $x$ ) vers un régime dans le mode non injecté uniquement. Par ailleurs, nous avons remarqué que les oscillations de relaxation du VCSEL  $y$  jouent un rôle important. En utilisant la méthode de continuation, les résultats de nos simulations ont montré que ce régime

particulier implique deux bifurcations de tore successives.

Un autre scénario intéressant est représenté aux Figures B.5.1(c1)-(c2) pour  $\Delta\omega = 23 \text{ rad.ns}^{-1}$ . Dans ce cas, et en accord avec nos investigations expérimentales, nous montrons que le basculement de polarisation peut s'accompagner d'une dynamique de doublement de période vers le chaos optique. En augmentant progressivement  $E_{inj}$ , le VCSEL bascule d'un régime quasi stationnaire du mode BF polarisé selon  $x$  vers un régime périodique dans le mode HF polarisé selon  $y$ . Ce régime est ensuite déstabilisé via une route de doublement de période qui, comme nous le montrons dans la Section B.5.1.2, est due à la présence d'un attracteur chaotique dans la gamme des paramètres d'injection considérée. En diminuant  $E_{inj}$ , nous observons une zone de verrouillage du VCSEL à la fréquence du laser maître qui traduit l'existence d'une bistabilité entre un état stationnaire non-verrouillé dans le mode  $x$  et un état de verrouillage du mode  $y$  sur le laser maître.

Les Figures B.5.1(d1)-(d2), obtenues pour un detuning de  $\Delta\omega = 10 \text{ rad.ns}^{-1}$ , représentent un scénario montrant les dynamiques non-linéaires qui apparaissent sur une route de basculement de polarisation suivie de verrouillage du VCSEL sur le laser maître. Ce résultat montre qu'en augmentant progressivement  $E_{inj}$  avant le basculement de polarisation, le système passe par une bifurcation particulière correspond à l'excitation de dynamiques périodiques dans les deux modes orthogonaux. Une analyse détaillée montre que cette nouvelle bifurcation correspond à l'excitation d'une dynamique périodique dans le mode non injecté  $x$  à une fréquence proche de celle des oscillations de relaxation. D'autre part, le mode injecté  $y$  présente une dynamique de type mélange d'ondes (entre la fréquence du mode non verrouillé  $y$  et celle du laser maître). Nous montrons que le régime périodique est ensuite déstabilisé via un basculement de polarisation qui se traduit par l'extinction du mode  $x$  suivi d'un verrouillage du mode  $y$  à la fréquence du laser maître. Pour des valeurs de  $E_{inj}$  beaucoup plus grandes, le régime de verrouillage est à son tour déstabilisé vers un régime périodique via la bifurcation dite de Hopf (voir Section B.5.1.2).

Un scénario presque similaire à celui de la Figure B.5.1(d1)-(d2) est montré à la Figure B.5.1(e1)-(e2) pour un detuning de  $\Delta\omega = -2.2 \text{ rad.ns}^{-1}$ . La différence entre les deux réside dans le fait que dans ce dernier cas, le VCSEL bascule d'une dynamique périodique dans les modes  $x$  et  $y$  vers un régime périodique uniquement dans le mode injecté  $y$ . En fait, nos résultats révèlent que dans ce cas le VCSEL exhibe un régime périodique quasi pulsé qui précède le verrouillage par injection optique.

### B.5.1.2 Cartographie théorique de bifurcations associées à la dynamique de basculement de polarisation

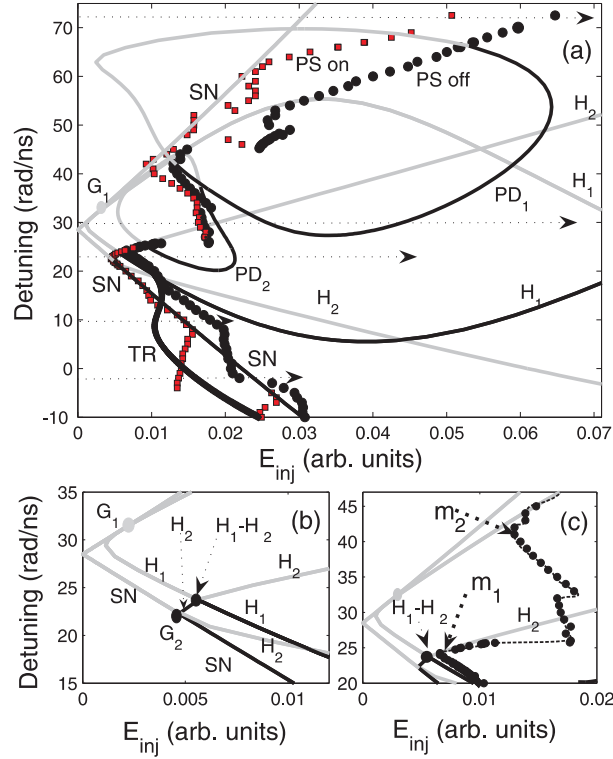


**Figure B.5.2:** *Diagramme de bifurcation dans le plan des paramètres d'injection ( $E_{inj}, \Delta\omega$ ) (a). Le traits en pointillés horizontaux indiquent les scénarios de basculement de polarisation décrite à la Figure. B.5.1. Zoom sur les points de bifurcation de co-dimension deux (b); et de la forme en serpent dans la courbe de basculement de polarisation, qui comporte deux minima indiqués par les flèches en traits pointillés gras (c). Noir (gris) représente la courbe de bifurcation supercritique (souscritique). Les courbes (TR; 'PS on'; 'PS off') et (TR; 'PS on') ont été respectivement supprimées dans les panneaux (b) and (c) pour ses raisons de clarté.*

Nous faisons ici usage des techniques numériques dites de continuation dans le but de compléter nos résultats théoriques résumés dans la Section B.5.1.1. A la Figure B.5.2(a) nous décrivons l'évolution globale de la dynamique du VCSEL soumis à injection optique orthogonale. Les différentes courbes de bifurcations y sont présentées dans le plan des paramètres d'injection ( $\Delta\omega$  et  $E_{inj}$ ). Pour chaque bifurcation, la partie en noir correspond aux transitions apparaissant sur les solutions stables du système.



Les parties en gris représentent les transitions sur les solutions instables. La nomenclature des différentes bifurcations est conforme à celle des systèmes dynamiques non linéaires dont fait partie le laser sous injection optique. Les parties stables de la bifurcation du point de selle (saddle-node,  $SN$ ) et de la bifurcation de Hopf (plus précisément la bifurcation nommée  $H_1$ ) délimitent la zone de verrouillage du VCSEL au laser maître. Une deuxième bifurcation de Hopf ( $H_2$ ) limite la partie supérieure de la zone de verrouillage en dessous du point de co-dimension deux  $G_1$  (point de tangence entre  $SN$  et  $H_1$ ). Ce résultat contraste avec ce qui avait été précédemment rapporté dans le cas d'un laser émettant par le côté soumis à injection optique [152], dans quel cas la zone de verrouillage s'étend jusqu'à  $G_1$ . Nos résultats montrent également que  $H_2$  participe à l'organisation générale du mécanisme de basculement de polarisation [observer, dans le voisinage de  $H_2$ , le changement dans l'évolution de la courbe de basculement du mode  $x$  vers le mode  $y$  représentée par les points ronds en noir sur la Figure B.5.2(a)]. Par ailleurs, nous montrons que le point correspondant à la puissance minimum de basculement est exactement localisé sur  $H_2$ .

En plus de  $H_2$ , nous mettons en évidence la présence de deux bulles ( $PD_1$  et  $PD_2$ ) qui signalent la présence de dynamiques de doublements successifs de période (*period doubling*,  $PD$ ) conduisant au chaos. En accord qualitatif avec nos résultats expérimentaux (voir Figure B.4.3), nous montrons que la présence des bulles de dynamique chaotique peut affecter de manière considérable le basculement de polarisation. En particulier, la présence de  $PD_1$  et  $PD_2$  explique l'existence de deux minima dans la courbe de basculement de polarisation [respectivement nommés  $m_1$  et  $m_2$  dans la Figure B.5.2(c)].

La cartographie à Figure B.5.2(a) révèle une autre bifurcation intéressante. Il s'agit d'une bifurcation de tore (nommée TR) qui coïncide avec l'excitation, d'une part, d'une dynamique périodique à la fréquence des oscillations de relaxation dans le mode non-injecté  $x$  et d'une dynamique de type mélange d'ondes dans le mode injecté  $y$ , d'autre part [voir aussi Figure B.5.1(c)]. Nous soulignons le fait que ce résultat corrobore nos observations expérimentales présentées aux Figures B.4.3 et B.4.4.

En plus du modèle SFM, nous avons également élaboré une autre étude de bifurcations basée sur un modèle alternatif dit à deux modes (*two-mode model*) [146]. Les résultats issus de cette étude confirment ceux obtenus moyennant le modèle SFM, démontrant ainsi que nos observations sont génériques aux systèmes VCSEL à deux modes fondamentaux de polarisations orthogonales. Nous révélons l'existence de deux nouvelles bifurcations de tore qui expliquent l'excitation d'un régime périodique dans les deux modes de polarisations orthogonales, en accord qualitatif avec les résultats expérimentaux de la Figure B.4.3 et B.4.5.

## B.6 Analyse de la compétition des modes transverses dans un VCSEL soumis à injection optique orthogonale

Dans l'introduction à la Section B.1 nous avons mentionné le fait que le VCSEL est typiquement caractérisé par un seul mode fondamental mais qu'il peut exhiber des modes transverses multiples. L'excitation des modes transverses d'ordre supérieur dans le VCSEL en régime solitaire dépend fortement de la structure ainsi que des conditions de fonctionnement (courant d'injection et température par exemple) [29]. Les études antérieures sur des VCSELS multimodes ont révélé que l'injection optique peut considérablement modifier la dynamique des modes transverses [124]. Dans cette Section, nous analysons expérimentalement et théoriquement l'effet de l'injection optique orthogonale sur la compétition des modes transverses. Nous soulignons le fait que notre étude s'intéresse au cas d'un VCSEL qui, en régime solitaire, émet uniquement dans le mode fondamental, c'est-à-dire loin du seuil du mode fondamental d'ordre supérieur. Il s'agit d'une extension du résultat expérimental de la Figure B.4.1 qui révèle l'excitation du mode transverse de premier ordre induite par injection optique.

Notre étude expérimentale des dynamiques de polarisation a été étendue à l'investigation du problème de compétition entre le mode fondamental et le mode transverse de premier ordre. Un des résultats obtenus est présenté à Figure B.6.1 sous la forme d'une cartographie de la dynamique du VCSEL dans le plan des paramètres d'injection [désaccord entre la fréquence du laser maître et celle du VCSEL ( $\Delta\nu$ , *detuning*) et puissance injectée ( $P_{inj}$ )]. Plusieurs régimes qualitativement différents y sont répertoriés. Les triangles désignent la frontière de basculement de polarisation du mode fondamental ( $LP_{01}$ ) du VCSEL; les losanges indiquent la frontière de la zone de verrouillage du mode transverse de premier ordre ( $LP_{11}$ ) à la fréquence du laser maître lorsqu'on augmente  $P_{inj}$  et pour un *detuning* fixe. Par ailleurs, lorsque qu'on diminue  $P_{inj}$  en partant de la zone de verrouillage du mode  $LP_{11}$  (en gris clair), le déverrouillage du mode  $LP_{11}$  met en évidence un phénomène d'hystérésis (zone hachurée en gris foncé). Quant à la frontière formée des points circulaires elle indique l'excitation d'une compétition progressive entre les modes transverse fondamental ( $LP_{01}$ ) et transverse de premier ordre ( $LP_{11}$ ) (ceci après basculement de polarisation).

La Figure B.6.1 révèle un autre résultat intéressant. En effet, la courbe de basculement entre les modes fondamentaux (marquée par des triangles) comportent deux minima locaux de puissance injectée nécessaire pour induire le basculement de polarisation. Le premier minimum est détecté pour un *detuning* proche de la birefringence du VCSEL, c'est-à-dire le désaccord en fréquence entre les deux modes fondamentaux du VCSEL libre d'injection

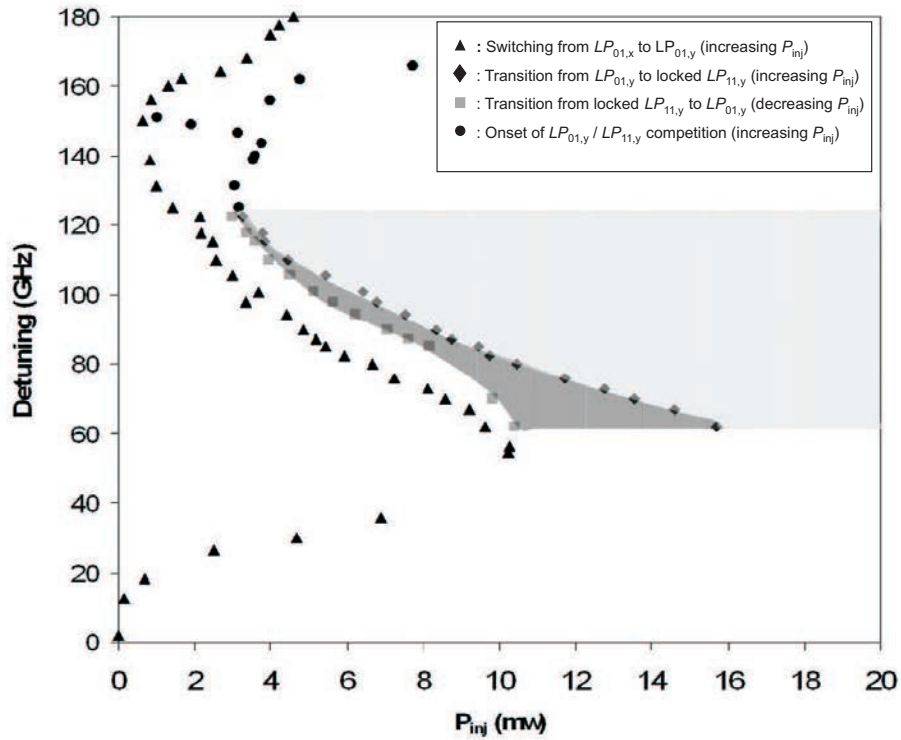


**Figure B.6.1:** Cartographie expérimentale du basculement de polarisation et de la compétition des modes transverse du VCSEL<sub>2</sub> dans le plan des paramètres d'injection optique ( $Detuning = \Delta\nu = \nu_{ML} - \nu_{SL}$  et puissance injectée  $P_{inj}$ ). Le courant d'injection est fixé à 2.105 mA et la température est maintenue à 20°C.

optique. D'autre part, le deuxième minimum est obtenu pour un detuning proche du désaccord en fréquence entre le mode transverse de premier ordre et le mode fondamental du VCSEL. L'existence de ce deuxième minimum est le résultat d'une dynamique de compétition entre le mode transverse fondamental ( $LP_{01}$ ) et le mode transverse de premier ordre ( $LP_{11}$ ).

Dans le but de mieux comprendre cette dynamique de compétition entre les modes transverses fondamental et de premier ordre, nous avons également menée une étude théorique basée sur un modèle SFM étendu qui tient compte des effets spatio-temporels du VCSEL [163]. En accord qualitatif avec nos observations expérimentales, nos résultats numériques montrent l'existence de deux minima locaux de la courbe de basculement de polarisation entre les modes transverses fondamentaux. Par ailleurs, nos simulations suggèrent que la position du second minimum est fonction du coefficient des pertes relatives entre les modes transverses fondamental et de premier ordre.

## B.7 Influence de la dynamique de polarisation sur la synchronisation du chaos optique dans les VCSELS en couplage unidirectionnel

La synchronisation est un concept générique à un grand nombre de systèmes non-linéaires rencontrés dans la nature, la biologie, la physique et dans des disciplines spécialisées telles les neurosciences [168]. La première observation scientifique du phénomène de synchronisation remonte à Huygens qui, en observant le mouvement des deux horloges à pendules, remarqua que ces dernières pouvaient ajuster leurs rythmes et osciller en synchronisme, suite à un faible couplage en elles à travers une poutre ou support [100]. Les études sur la synchronisation ont connu un essor majeur suite au développement des oscillateurs électroniques [169].

Mis à part les études sur la synchronisation des oscillateurs, il a été démontré que le concept de synchronisation peut être étendue aux systèmes non-linéaires chaotiques [177]. La recherche sur ce sujet attire beaucoup d'intérêt à cause de son application dans des schémas de communications par chaos. Bon nombre des travaux se sont focalisés sur la synchronisation du chaos optique dans les systèmes lasers à cause de leurs avantages tels la possibilité de générer un régime chaotique large bande, intéressant pour la sécurité d'une liaison sécurisée de transmission des données [15, 182]. La plupart des travaux sur la synchronisation du chaos ont concerné les lasers à semi-conducteurs émettant par le côté [184, 186, 187, 189, 190, 191, 192, 193]. Cependant les travaux sur la synchronisation du chaos dans les VCSELS demeurent rares [195, 167, 156] et l'effet des leurs propriétés uniques de polarisation sur la synchronisation reste explorer. Cette question est analysée

dans la présente partie de notre thèse.

Nous avons réalisé l'étude théorique de la synchronisation du chaos dans deux VCSELS en couplage unidirectionnel (configuration maître-esclave). Nous nous intéressons au schéma dit à boucle ouverte dans lequel seul le VCSEL maître comporte une rétro-action optique isotrope au moyen duquel le chaos est généré. L'effet de la dynamique de polarisation sur la qualité de la synchronisation du chaos est analysé dans deux schémas différents de couplage entre les lasers maître et esclave: le premier schéma concerne une injection optique dite isotrope et le second une injection optique orthogonale.

### B.7.1 Effet de la dynamique de compétition de modes sur la synchronisation de deux VCSEL couplés: *injection unidirectionnelle isotrope*

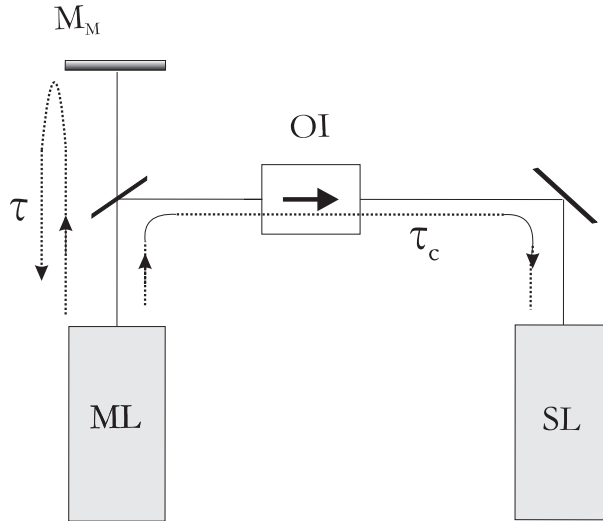


**Figure B.7.1:** Schéma type de couplage unidirectionnel pour la réalisation de la synchronisation par injection optique isotrope. *ML*: laser maître; *SL*: laser esclave;  $M_M$ : miroir de la cavité externe de *ML*; *OI*: isolateur optique;  $\tau$ : délai de feedback optique;  $\tau_c$ : temps de parcours entre les lasers maître et esclave. Il s'agit du schéma dit à boucle ouverte car seul le laser maître comporte une cavité externe de feedback pour la génération du chaos optique.

Dans cette Section, nous mettons en évidence l'effet de compétition des modes transverses fondamentaux sur la qualité de la synchronisation entre deux VCSELS couplés via une injection optique isotrope (voir Figure B.7.1). Dans ce cas particulier, les deux modes fondamentaux de polarisations orthogonales sont injectés dans le VCSEL esclave de manière isotrope, c'est à dire avec des taux d'injection identiques.

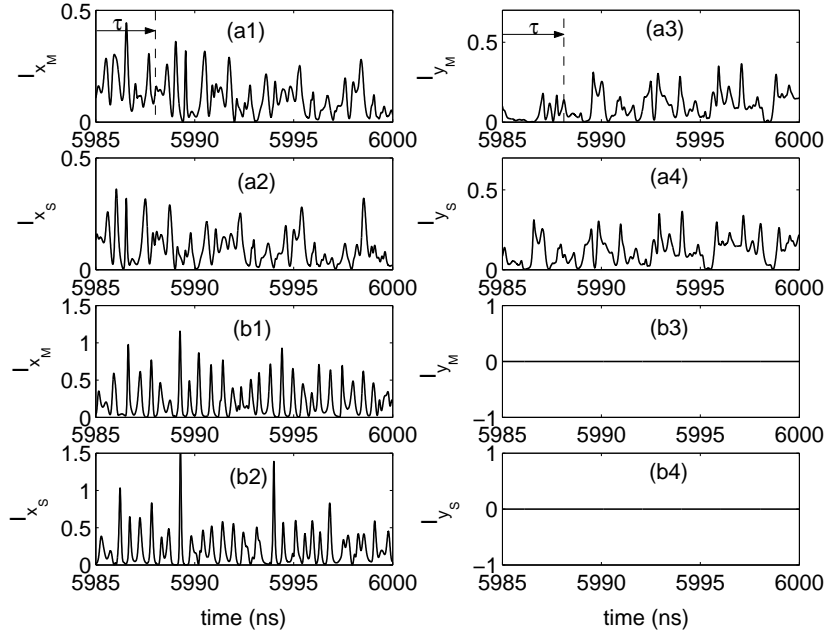


**Figure B.7.2:** Traces temporelles des intensités optiques dans les deux modes fondamentaux de polarisations orthogonales ( $x$  et  $y$ ). Deux cas sont analysés pour un taux d'injection  $\eta = f = 6 \text{ ns}^{-1}$ . Cas 1: Le VCSEL maître exhibe un régime chaotique dans les deux modes (a1-a2) qui sont synchronisés anticipativement à ceux du VCSEL esclave avec un délai  $\tau$  (comparer a1 avec a2 et a3 avec a4); Cas 2: Le VCSEL maître exhibe un régime chaotique seulement dans un seul mode (b1-b3), dans ce dernier cas, une dégradation de la synchronisation est observée (comparer b1 avec b2).

En vue d'évaluer l'effet de la compétition des modes sur la synchronisation des VCSELS couplés, nous avons modélisé le schéma de couplage montré à la Figure B.7.1 moyennant un modèle SFM convenablement modifié [pour détails, voir les Eqs. (8.2.1)- (8.2.8) à la page 159 de la version anglaise]. Les paramètres du modèle sont d'abord choisis tels que les VCSELS fonctionnent dans leur zone de bistabilité de polarisation. Ainsi, selon les conditions initiales, le VCSEL peut exhiber soit un régime chaotique dans les deux modes orthogonaux [voir Figure B.7.2(a1)-(a2)] ou soit dans un seul mode seulement [voir Figure B.7.2(b1)-(b2)]. Nos résultats, commentés à la Figure B.7.2, montrent qu'une très bonne synchronisation anticipative<sup>3</sup> a lieu

<sup>3</sup>Dans la synchronisation anticipative, le laser esclave se synchronise au laser maître avec un temps d'avance égale au délai  $\tau$  dans la boucle de rétro-action optique du maître. Sans nuire à la généralité du cas étudié, on suppose un couplage instantané entre les lasers maître et esclave: temps de parcours  $\tau_C = 0$ .

lorsque les deux modes exhibent simultanément un régime chaotique [Figure B.7.2(a1-a4)]. Par contre, dans un régime chaotique où un seul mode fondamental est émis, on observe une forte dégradation de la qualité de la synchronisation [Figure B.7.2(b1-b4)].

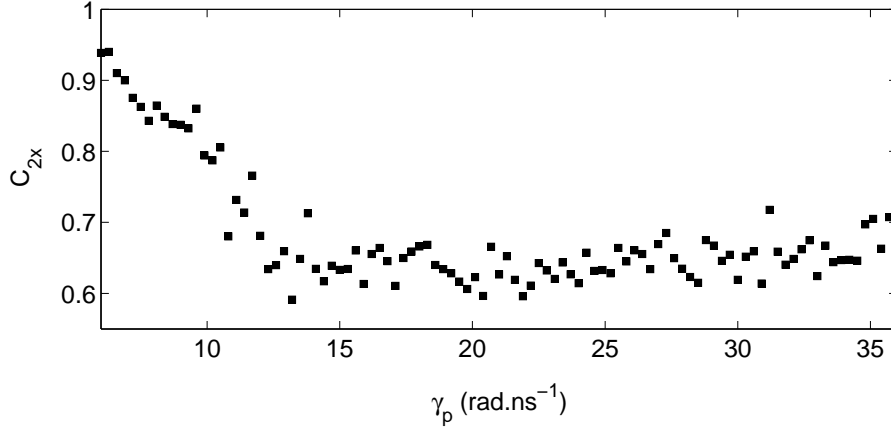


**Figure B.7.3:** Evolution de qualité de la synchronisation anticipative [mesurée via le coefficient de corrélation  $C_{2x}$  défini à la page 159, eq. (8.2.12)] lorsqu'on varie la birefringence  $\gamma_p$  du VCSEL. La dégradation de la qualité de la synchronisation coïncide avec le passage du système d'un régime chaotique dans les deux modes de polarisations orthogonales vers un régime chaotique dans un seul mode.

Par ailleurs, l'effet de la compétition des modes transverses fondamentaux du VCSEL sur la qualité de la synchronisation peut être mis en évidence en jouant sur le paramètre de birefringence  $\gamma_p$  du VCSEL. En effet, comme le montre la Figure B.7.4, en modifiant la birefringence du VCSEL, nous sommes à mesure de faire passer le système d'un régime chaotique dans les deux modes fondamentaux vers un régime chaotique dans un seul mode. En effet, la transition entre les deux régimes correspond bien à un changement relativement abrupt de la qualité de synchronisation.

### B.7.2 Effet de la dynamique de compétition de modes sur la synchronisation de deux VCSEL couplés: *injection unidirectionnelle orthogonale*

Dans cette Section, nous étudions l'effet de la dynamique de compétition des modes transverses fondamentaux sur la synchronisation des deux VCSELs couplés par une injection orthogonale schématisée à la Figure B.7.4. A cet effet, nous modélisons cette configuration moyennant un modèle étendu développé sur base du modèle SFM [pour détails, voir les Eqs. (8.3.1)- (8.3.8)]

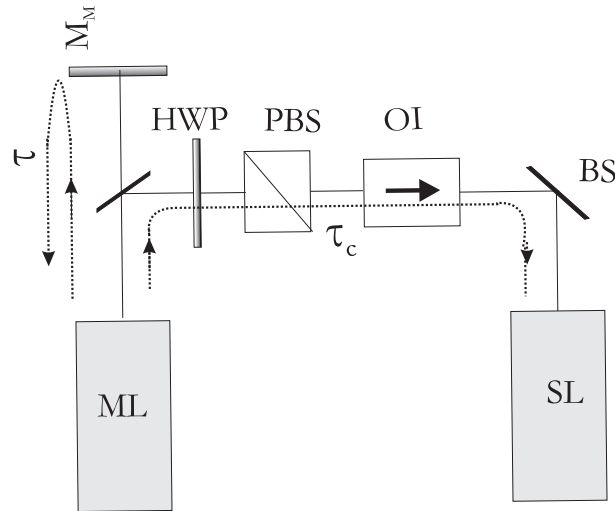


**Figure B.7.4:** Schéma de principe d'un couplage unidirectionnel entre deux VCSELS par injection orthogonale. Le chaos dans le VCSEL maître (ML) est généré grâce à la rétroaction optique isotrope dans la cavité externe constituée par le miroir  $M_M$ . Le chaos peut apparaître dans les deux modes fondamentaux de polarisation orthogonales ( $x$  et  $y$ ). Le plan de polarisation de ML subit d'abord une rotation de  $90^\circ$  moyennant une lame demi-onde (HWP). Le mode de ML dont la polarisation est parallèle à celle du mode dominant du VCSEL esclave (SL), libre d'injection optique, est ensuite sélectionnée au moyen d'un séparateur de faisceaux polarisant (PBS). L'isolateur optique (OI) assure le couplage unidirectionnel entre ML et SL

aux Pages 164 et 165 de la version anglaise]. Les paramètres du modèle sont choisis pour simuler les conditions des travaux expérimentaux antérieurs réalisés en utilisant le même schéma de couplage [167].

La synchronisation entre les VCSELS maître et esclave couplés selon le schéma de la Figure B.7.4 a fait l'objet d'une étude numérique détaillée. Nous avons, notamment, analysé l'évolution de la qualité de synchronisation en variant les paramètres d'injection [puissance injectée et désaccord entre les fréquences des VCSELS maître et esclave (detuning)]. La Figure B.7.5 met en évidence deux régions qualitativement différentes nommées respectivement *region I* et *region II* [voir Figure B.7.5(a)]. Dans la région II, le VCSEL esclave exhibe un régime chaotique dans les deux modes de polarisations orthogonales ( $x$  et  $y$ ). Dans la région I le VCSEL fonctionne dans un régime chaotique dans un seul mode, après basculement vers la polarisation de ML (mode  $y$ ). Nos résultats [voir Figure B.7.5(c)] révèlent que dans la région II la compétition entre les modes orthogonaux de SL contribue à l'amélioration



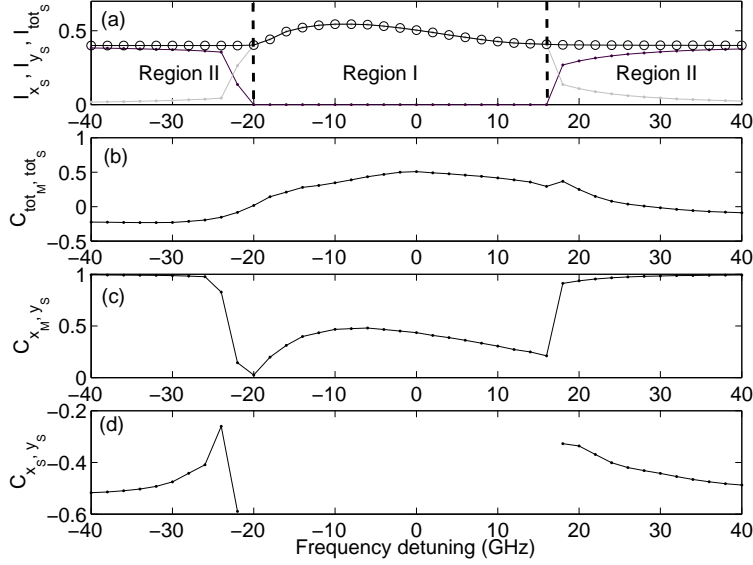


**Figure B.7.5:** Evolution des l'intensité moyenne optiques totale (ligne marqué par des cercles) ainsi que des intensités moyennes dans les mode  $x$  (gris)  $y$  (noir) (a); du coefficient de corrélation isochrone entre les intensités totales de ML et de SL,  $C_{tot_M, tot_S}$  (b); du coefficient de corrélation isochrone entre les intensités du mode  $x$  de ML et celle du mode  $y$  de SL,  $C_{x_M, y_S}$  (c); du coefficient de corrélation isochrone entre l'intensité du mode  $x$  de SL et celle du mode  $y$  de SL,  $C_{x_S, y_S}$  (d) lorsque le detuning est balayé pour une taux d'injection fixe de 100 GHz. Les paramètres du modèle décrit aux pages 164-165 sont:  $\gamma_{a_M} = 0.1$ ,  $\gamma_{p_M} = 6$  rad/ns,  $\mu_M = 1.2$  and  $\gamma_{a_S} = -0.1$ ,  $\gamma_{p_S} = 8.5$  rad/ns,  $\mu_S = 1.4$ .

de la qualité de synchronisation isochrone<sup>4</sup> entre le mode  $x$  de ML et le mode injecté ( $y$ ) de SL ( $C_{x_M, y_S} \approx 1$ ). Cependant dans la région I, on note une forte dégradation de la qualité de synchronisation isochrone. Par ailleurs, nous montrons que dans la région II le coefficient de corrélation entre les modes de SL est négatif. Ce dernier résultat, qui indique une certaine anticorrelation entre les modes  $x$  et  $y$  du VCSEL esclave, est en accord avec les observations expérimentales rapportées par Hong *et al.* [167].

La figure B.7.6 décrit l'évolution globale de la qualité de synchronisation sous forme d'une cartographie du coefficient de corrélation isochrone ( $C_{x_M, y_S}$ ) dans le plan des paramètres d'injection. Cette figure corrobore ce qui est décrit par le cas particulier montré à la Figure B.7.5. Elle révèle égale-

<sup>4</sup>Dans la synchronisation isochrone, le laser esclave se synchronise instantanément au laser maître. Sans nuire à la généralité du cas étudié, on suppose que le temps de parcours entre le maître et l'esclave  $\tau_C = 0$ .

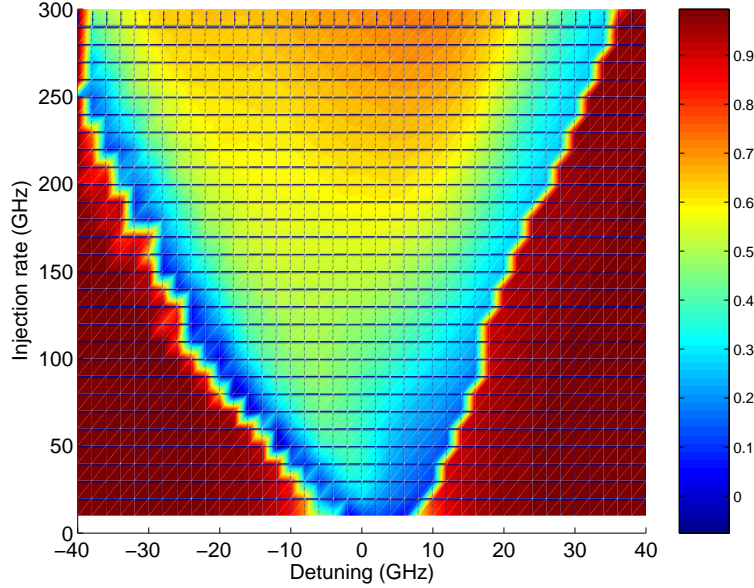


**Figure B.7.6:** *Cartographie du coefficient de corrélation isochrone  $C_{x_M, y_S}$  entre l'intensité du mode  $x$  de SL et celle du mode  $y$  de SL dans le plan des paramètres d'injection (detuning, taux d'injection). Les paramètres internes du modèle sont les mêmes que ceux indiqués à la Figure B.7.5.*

ment une relative augmentation du coefficient de corrélation dans la région I au fur et à mesure que l'on évolue vers des taux d'injection élevés. En évoluant vers les taux d'injection élevés, on remarque également un élargissement de la zone I au détriment de la zone II.

## B.8 Conclusions

Nos investigations ont concerné le contrôle de la bistabilité et du basculement de polarisation, les dynamiques non-linéaires et la compétition des modes transverses dans un VCSEL soumis à injection optique orthogonale. Nous avons également étudié l'effet de la dynamique de polarisation sur la synchronisation du chaos dans deux VCSELS couplés. Nous résumons ci-après les résultats de nos investigations:

Nous avons montré qu'en fonction des paramètres d'injection, c'est-à-dire la puissance injectée et le detuning, le basculement de polarisation est réalisé avec ou sans verrouillage du VCSEL sur la fréquence du laser maître et s'accompagne d'une bistabilité de polarisation. Le contrôle du bascule-

ment de polarisation, en variant la puissance injectée pour un detuning fixe, montre que le régime de verrouillage est observé pour des detunings négatifs par rapport à la birefringence du VCSEL. Par ailleurs, en variant le detuning pour une puissance injectée fixe, nous avons théoriquement montré que les paramètres tels que le facteur de Henry  $\alpha$  et le taux de relaxation de retournement des spins  $\gamma_s$  affectent de manière significative la largeur de la zone de bistabilité de polarisation.

Nos résultats théoriques et expérimentaux ont révélé que le basculement de polarisation peut s'accompagner de dynamiques non-linéaires complexes:

- Nous avons observé une gamme de detunings négatifs dans laquelle la route vers le basculement de polarisation avec verrouillage est précédé de l'excitation des dynamiques périodiques dans les deux modes de polarisations orthogonales. Dans ce cas, le mode non-injecté exhibe une dynamique périodique à une fréquence proche de celle des oscillations de relaxation tandis que le mode injecté exhibe une dynamique de type mélange d'ondes. Notre étude théorique montre que l'excitation de ces dynamiques est associé à une bifurcation de torse ( $TR_1$ ).
- Dans une gamme des detunings positifs au delà mais suffisamment proche de la zone de verrouillage par injection du VCSEL, nous avons rapporté expérimentalement et théoriquement le basculement d'un régime périodique dans les deux modes fondamentaux vers un régime périodique dans le mode injecté, avec une fréquence proche de celle des oscillations de relaxation. Nos résultats théoriques révèlent que ce type de dynamique de basculement de polarisation nécessite deux bifurcations de tore successives  $TR_2$  et  $TR_3$ .
- Nous avons expérimentalement et théoriquement identifié une gamme de detuning dans laquelle le basculement polarisation avec verrouillage par injection du VCSEL peut s'accompagner d'une dynamique très riche. Il s'agit, notamment, d'une route de doublement de période vers un régime de chaos optique. Nous avons mis en évidence deux régions distinctes de doublement de période qui affecte de manière significative la puissance nécessaire pour réaliser le basculement de polarisation. Dans la gamme de detuning concernée, la courbe de basculement de polarisation exhibe une forme en serpent dans le plan des paramètres d'injection optique.
- Nos travaux théoriques sur les bifurcations associées aux dynamiques non-linéaires qui accompagnent le basculement de polarisation ont mis en évidence une nouvelle bifurcation de Hopf que nous avons nommée  $H_2$  pour la distinguer de celle rapportée dans le cas des lasers à semi-conducteurs émettant par le côté. Nous ont montré que  $H_2$  délimite la

region de verouillage par injection optique en dessous du point dit de co-dimension deux  $G_1$ . Par ailleurs, nos résultats révèlent que  $H_2$  (mais aussi  $TR_1$ ,  $TR_2$  et  $TR_3$ ) sont génériques aux modèles à deux modes utilisés pour décrire la dynamique de basculement de polarisation dans les VCSELS.

Nous nous sommes également intéressés à l'étude expérimentale et théorique de la compétition des modes transverses dans un VCSEL soumis à injection optique orthogonale. Nos résultats ont révélé l'existence de deux minima de puissance nécessaire pour induire le basculement entre les deux modes fondamentaux de polarisations orthogonales. D'une part, le premier minimum est observé pour un detuning égal à la birefringence du VCSEL (désaccord en fréquence entre les modes fondamentaux orthogonaux). D'autre part, le second minimum est repéré pour un detuning proche du désaccord en fréquence entre le mode transverse fondamental et le mode transverse de premier ordre. Nos résultats numériques ont révélés que la position de ce second minimum peut être contrôlée via le taux de pertes relatives entre les modes transverses fondamental et de premier ordre. Nous avons mis en évidence une région relativement large de detuning pour laquelle le mode transverse de premier ordre est verrouillé à la fréquence du laser maître. Par ailleurs, ce régime de verrouillage affecte significativement la dynamique de basculement entre les modes fondamentaux de polarisations orthogonales.

Finalement nous avons théoriquement étudié l'influence de la dynamique de polarisation du VCSEL sur la qualité de la synchronisation de deux VCSELS en couplage unidirectionnel, ce dans deux configurations d'injection différentes: injection isotrope et injection orthogonale. Dans les deux cas, nos résultats ont montré que la la qualité de la synchronisation est considérablement amélioré lorsque le VCSEL injecté exhibe un régime chaotique dans les deux modes transverses fondamentaux de polarisations orthogonales.

Nos résultats contribuent au contrôle des dynamiques de polarisation d'un VCSEL, crucial pour les applications telles les réseaux modernes de commutation tout optique utilisant des VCSELS. Par ailleurs, nos travaux sur la synchronisation du chaos sont intéressants dans le cadre du développement récent des liaisons de communication sécurisée basées sur la synchronisation du chaos optique.

# Bibliography

- [1] R. N. Hall, G. E. Fenner, J. O. Kingsley, T. J. Soltys, and R. O. Carlson, “Coherent light emission from GaAs junctions,” *Phys. Rev. Lett.* **9**, 366 (1962).
- [2] A. Einstein, “Zur quantentheorie der strahlung,” *Physikalische Zeitschrift* **18**, 121 (1917).
- [3] N. G. Basow and A. M. Proshorow, “3-level gas oscillator,” *Zur. Eksp. Tior. Fiz.* **27**, 431 (1954).
- [4] J. P. Gordon, H. Zeiger, and C. H. Townes, “Molecular microwave oscillator and new hyperfine structure in the microwave spectrum of  $NH_3$ ,” *Phys. Rev.* **95**, 282 (1954).
- [5] N. Takeuchi, “Development of pseudo-random modulation CW lidar and its application to field measurements,” *Research Rep. from the Nat. Institute for Environ. Studies, Japan* **122**, (1989).
- [6] M. Jacquemet, N. Picqué, G. Guelachvili, A. Garnache, I. Sagnes, M. Strassner, and C. Symonds, “Continuous-wave 1.55  $\mu\text{m}$  diode-pumped surface-emitting semiconductor laser for broadband multiplex spectroscopy,” *Opt. Lett.* **32**, 1387 (2007).
- [7] D. Weidmann, A. A. Kosterev, F. K. Tittel, N. Ryan, and D. McDonald, “Application of a widely electrically tunable diode laser to chemical gas sensing with quartz-enhanced photoacoustic spectroscopy,” *Opt. Lett.* **29**, 1837 (2004).
- [8] G. Ferrari and I. Carusotto, “Cavity-enhanced single-frequency synthesis via difference-frequency generation of mode-locked pulse trains,” *J. Opt. Soc. Am. B* **22**, 2115 (2005).
- [9] R.S. Fyath, S.A. Ali, and M.S. Alam, “Four-operand parallel optical computing using shadow-casting technique,” *Opt. and Laser Technol.* **37**, 251 (2005).

- [10] K. Iga, H. Li, *Vertical-Cavity Surface-Emitting Laser Devices*, Springer Series in Photonics, Springer verlag, (2002).
- [11] J. Sacher, D. Baums, P. Panknin, W. Elsässer, and E. O. Göbel, “Intensity instabilities of semiconductor lasers under current modulation, external light injection, and delayed feedback,” *Phys. Rev. A* **45**, 1893 (1992).
- [12] S. Wieczorek, T. B. Simpson, B. Krauskopf, and D. Lenstra, “Global quantitative predictions of complex laser dynamics,” *Phys. Rev. E* **65**, 045207 (2002).
- [13] S. C. Chan, S. K. Hwang, and J. M. Liu, “Radio-over-fiber AM-to-FM upconversion using an optically injected semiconductor laser,” *Opt. Lett.* **31**, 2254 (2006).
- [14] H. S. Moon, E. B. Kim, S. E. Park, and C. Y. Park, “Selection and amplification of modes of an optical frequency comb using a femtosecond laser injection-locking technique,” *Appl. Phys. Lett.* **89**, 181110 (2006).
- [15] A. Argyris, D. Syvridis, L. Larger, V. Annovazzi-Lodi, P. Colet, I. Fischer, J. G. Ojalvo, C. R. Mirasso, L. Pesquera, and K. A. Shore, “Chaos-based communications at high bit rates using commercial fibre-optic links,” *Nature* **438**, 343 (2005).
- [16] T. B. Simpson, J. M. Liu, K. F. Huang, and K. Tai, “Nonlinear dynamics induced by external optical injection in semiconductor lasers,” *Quantum Semiclass. Opt.* **9**, 765 (1997).
- [17] J. M. Liu, *Photonic devices*, Cambridge University Press (2005).
- [18] W. W. Chow, S. W. Koch, and M. Sargent III, *Semiconductor-laser physics*, Springer Series in Photonics, Springer verlag, (1994).
- [19] H. Soda, K. Iga, C. Kitahara, and Y. Suematsu, “GaInAsP/InP Surface Emitting Injection Lasers,” *Jpn. J. Appl. Phys.* **18**, 2329 (1979).
- [20] K. Iga, S. Ishikawa, S. Ohkouchi, and T. Nishimura, “Room-temperature pulsed oscillation of GaAlAs/GaAs surface emitting injection laser,” *Appl. Phys. Lett.* **45**, 348 (1984).
- [21] K. Iga, S. Kinoshita, and F. Koyama, “Microcavity GaAs/GaAs surface-emitting laser with  $I_{th} = 6$  mA,” *Electron. Lett.* **23**, 134 (1987).
- [22] J. L. Jewell, Y. H. Lee, S. Walker, A. Scherer, J. P. Harbison, L. T. Florez, and S. L. McCall, “Low-threshold electrically pumped vertical-cavity surface-emitting microlasers,” *Electron. Lett.* **25**, 1123 (1989).

- 
- [23] Y. H. Lee, J. L. Jewell, A. Scherer, S. L. McCall, J. P. Harbison, and L. T. Florez, "Room-temperature continuous-wave vertical-cavity single-quantum-well microlaser diodes," *Electron. Lett.* **25**, 1377 (1989).
- [24] K. D. Choquette, R. P. Schneider, Jr., M. H. Crawford, K. M. Geib, and J.J. Figiel, "Continuous wave operation of 640-660 nm selectively oxidised AlGaInP vertical-cavity lasers," *Electron. Lett.* **31**, 1145 (1995).
- [25] G.M. Yang, M.H. MacDougla, and P.D. Dapkus, "Ultralow threshold current vertical-cavity surface-emitting lasers obtained with selective oxidation," *Electron. Lett.* **31**, 886 (1995).
- [26] Y. Hayashi, T. Mukaiharu, N. Hatori, N. Ohnoki, A. Matsutani, F. Koyama, and K. Iga, "Lasing characteristics of low-threshold oxide confinement InGaAs-GaAlAs vertical-cavity surface-emitting lasers," *IEEE Photon. Technol. Lett.* **7**, 1234 (1995).
- [27] K. Iga, "Surface-emitting laser-its birth and generation of new optoelectronics field," *IEEE J. Sel. Top. Quantum Electron.* **6**, 1201 (2000).
- [28] C. J. Chang-Hasnain, M. Orenstein, A. Von Lehmen, L. T. Florez, J. P. Harbison, and N. G. Stoffel, "Transverse mode characteristics of vertical cavity surface-emitting lasers," *Appl. Phys. Lett.* **57**, 218 (1990).
- [29] C. J. Chang-Hasnain, J. P. Harbison, G. Hasnain, A. C. Von Lehmen, L. T. Florez, and N. G. Stoffel, "Dynamic, polarization, and transverse mode characteristics of vertical cavity surface emitting lasers," *IEEE J. Quantum Electron.* **27**, 1402 (1991).
- [30] C. H. Chong and J. Sarma, "Lasing mode selection in vertical-cavity surface-emitting laser diodes," *IEEE Photon. Technol. Lett.* **5**, 761 (1993).
- [31] A. Valle, J. Sarma, and K. A. Shore, "Spatial hole burning effects on the dynamics of vertical-cavity surface-emitting laser diodes," *IEEE J. Quantum Electron.* **31**, 1423 (1995).
- [32] A. Valle, L. Pesquera, and K. A. Shore, "Polarization Behavior of Birefringent Multitransverse Mode Vertical-Cavity Surface-Emitting Lasers," *IEEE Photon. Technol. Lett.* **9**, 557 (1997).
- [33] R. A. Morgan, G. D. Guth, M. W. Focht, M. T. Asom, K. Kojima, L. E. Rogers, and S. E. Callis, "Transverse mode control of vertical-cavity top-surface-emitting lasers," *IEEE Photon. Technol. Lett.* **4**, 374 (1993).
- [34] H. Martinsson, J. A. Vukusic, and A. Larsson, "Single-mode power dependence on surface relief size formode-stabilized oxide-confined vertical-cavity surface-emitting lasers," *IEEE Photon. Technol. Lett.* **12**, 1129 (2000).

- [35] C. Carlsson, C. A. Barrios, E. R. Messmer, A. Lovqvist, J. Halonen, J. Vukusic, M. Ghisoni, S. Lourduodoss, and A. Larsson, "Performance characteristics of buried heterostructure VCSELs using semi-insulating GaInP:Fe regrowth," *IEEE J. Quantum Electron.* **37**, 945 (2001).
- [36] K. D. Choquette, R. P. Schneider, K. L. Lear, and R. E. Leibenguth, "Gain-dependent polarization properties of vertical-cavity lasers," *IEEE J. Select. Topics Quantum Electron.* **1**, 661 (1995).
- [37] J. J. Kim, K. H. Kim, M. H. Lee, H. S. Lee, E. H. Lee, K. Kwon, J. Roh, and B. S. Yoo, "2.5-Gb/s Hybrid single-mode and multimode fiber transmission of 1.5- $\mu$ m wavelength VCSEL," *IEEE Photon. Technol. Lett.* **19**, 297 (2007).
- [38] M.Y.W. Chia, B. Luo, M.L. Yee, and E.J.Z. Hao, "Radio over multimode fibre transmission for wireless LAN using vertical-cavity surface-emitting lasers," *Electron. Lett.* **39**, 1143 (2003).
- [39] J. K. Kash, F. E. Doany, L. Schares, C. L. Schow, C. Schuster, D. M. Kuchta, P. Pepeljugoski, J. M. Trehwella, C. W. Baks, R. A. John, J. L. Shan, Y. H. Kwark, R. A. Budd, P. Chiniwalla, F. R. Libsch, J. Rosner, C. K. Tsang, C. S. Patel, J. D. Schaub, D. Kucharski, D. Guckenberger, S. Hedge, H. Nyikal, R. Dangel, F. Horst, B. J. Offrein, C. K. Lin, A. Tandon, G. R. Trott, M. Nystrom, D. Bour, M. R. Tan, and D. W. Dolfi, "Chip-to-chip optical interconnects," *Opt. Fiber Commun. Conf., Anaheim, CA (USA)*, 2006, Paper OFA3.
- [40] K. D. Choquette, M. J. Hafich, M. H. Crawford, K. M. Geib, and J. J. Hindi, "Improved performance of selectively oxidized visible VCSELs," *LEOS 12th Annual Meeting* **2**, 395 (1999).
- [41] M. S. Wu, E. C. Vail, G. S. Li, W. Yuen, and C. J. Chang-Hasnain, "Tunable micromachined vertical cavity surface emitting laser," *Electron. Lett.*, **31**, 1671 (1995).
- [42] H. Kawaguchi, Y. Yamayoshi, and K. Tamura, "All-optical format conversion using an ultrafast polarization bistable vertical-cavity surface-emitting laser," in *Proc. CLEO*, 379 (2000).
- [43] A. K. J. van Doorn, M. P. van Exter, and J. P. Woerdman, "Elasto-optic anisotropy and polarization orientation of vertical-cavity surface-emitting semiconductor lasers," *Appl. Phys. Lett.* **69**, 1041 (1996).
- [44] M. P. van Exter, A. K. J. van Doorn, and J. P. Woerdman, "Electro-optic effect and birefringence in semiconductor vertical-cavity lasers," *Phys. Rev. A* **56**, 845 (1995).



- 
- [45] B. Ryvkin, K. Panajotov, A. Georgievski, J. Danckaert, M. Peeters, G. Verschaffelt, H. Thienpont, and I. Veretennicoff, "Effect of photon-energy-dependent loss and gain mechanisms on polarization switching in vertical-cavity surface-emitting lasers," *J. Opt. Soc. Amer. B* **16**, 2106 (1999).
- [46] K. Panajotov, B. Ryvkin, J. Dackaert, M. Peeters, H. Thienpont, and I. Veretennicoff, "Polarization switching in VCSELs due to thermal lensing," *IEEE Photon. Technol. Lett.* **10**, 6 (1998).
- [47] A. Valle, K. A. Shore, and L. Pesquera, "Polarization selection of birefringent vertical-cavity surface-emitting lasers," *IEEE J. Lightw. Technol.* **14**, 2062 (1996).
- [48] M. San Miguel, Q. Feng, and J. V. Moloney, "Light polarization dynamics in surface-emitting semiconductor lasers," *Phys. Rev. A* **52**, 1728 (1995).
- [49] D. Vakhshoori, "Symmetry considerations in vertical-cavity surface-emitting lasers: Prediction of removal of polarization isotropicity on (001) substrates," *Appl. Phys. Lett.* **65**, 259 (1994).
- [50] A. Chavez-Pirson, H. Ando, H. Saito, and H. Kanbe, "Polarization properties of a vertical cavity surface emitting laser using a fractional layer superlattice gain medium," *Appl. Phys. Lett.* **62**, 3082 (1993).
- [51] K. D. Choquette, and R. E. Leibenguth, "Control of vertical-cavity laser polarization with anisotropic transverse cavity geometries," *IEEE Photon. Technol. Lett.* **6**, 40 (1994).
- [52] T. Mukaiharu, N. Ohnoki, Y. Hayashi, N. Hatori, F. Koyama, and K. Iga, "Polarization control of vertical-cavity surface emitting lasers using a birefringent metal/dielectric polarizer loaded on top distributed Bragg reflector," *IEEE J. Sel. Top. Quantum Electron.* **1**, 667 (1995).
- [53] H. Y. Chu, B. S. Yoo, M. S. Park, and H. H. Park, "Polarization characteristics of index-guided surface-emitting lasers with tilted pillar structure," *IEEE Photon. Technol. Lett.* **9**, 1066 (1997).
- [54] T. Yoshikawa, H. Kosaka, K. Kurihara, M. Kajita, Y. Sugimoto, and K. Kasahara, "Complete polarization control of 8x8 vertical-cavity surface-emitting laser matrix arrays," *Appl. Phys. Lett.* **66**, 908 (1995).
- [55] T. H. Russell and T. D. Milster, "Polarization switching control in vertical-cavity surface-emitting lasers," *Appl. Phys. Lett.* **70**, 2520 (1997).
- [56] A. Valle, L. Pesquera, and K. A. Shore, "Polarization selection and sensitivity of external cavity vertical-cavity surface-emitting laser diodes," *IEEE Photon. Technol. Lett.* **10**, 639 (1998).

- [57] M. Sciamanna, K. Panajotov, H. Thienpont, I. Veretennicoff, P. Mégret, and M. Blondel, "Optical feedback induces polarization mode hopping in vertical-cavity surface-emitting lasers," *Opt. Lett.* **28**, 1543 (2003).
- [58] M. Arizaleta Arteaga, M. López-Amo, H. Thienpont, and K. Panajotov, "Role of external cavity reflectivity for achieving polarization control and stabilization of vertical cavity surface emitting laser," *Appl. Phys. Lett.* **90**, 1031117 (2007).
- [59] J. Martín-Regalado, M. San Miguel, and N. B. Abraham, "Polarization switching in quantum-well vertical-cavity surface-emitting lasers," *Opt. Lett.* **21**, 351 (1996).
- [60] J. Martin-Regalado, F. Prati, M. San Miguel, and N. B. Abraham, "Polarization properties of vertical-cavity surface-emitting lasers," *IEEE J. Quantum Electron.* **33**, 765 (1997).
- [61] M. Sciamanna, "Nonlinear dynamics and polarization properties of externally driven semiconductor lasers," PhD thesis, Mons Engineering Faculty (Belgium), 2004.
- [62] M. Sondermann, T. Ackemann, S. Balle, J. Mulet, and K. Panajotov, "Experimental and theoretical investigations on elliptically polarized dynamical transition states in the polarization switching of vertical-cavity surface-emitting lasers," *Opt. Commun.* **235**, 421 (2004).
- [63] P. Besnard, M.-L. Chares, G. Stephan, and F. Robert, "Switching between polarized modes of a vertical-cavity surface-emitting laser by isotropic optical feedback," *J. Opt. Soc. Am. B* **16**, 1059 (1999).
- [64] M. Sondermann, M. Weinkath, T. Ackemann, J. Mulet, and S. Balle, "Two-frequency emission and polarization dynamics at lasing threshold in vertical-cavity surface-emitting lasers," *Phys. Rev. A* **68**, 033822 (2003).
- [65] F. Prati and P. Caccia, "Effects of gain saturation on polarization switching in vertical-cavity surface-emitting lasers," *Phys. Rev. A* **66**, 063811 (2002).
- [66] T. Erneux, J. Danckaert, K. Panajotov, and I. Veretennicoff, "Two-variable reduction of the San Miguel-Feng-Moloney model for vertical-cavity surface-emitting lasers," *Phys. Rev. A* **59**, 4660 (1999).
- [67] T. Ackemann and M. Sondermann, "Characteristics of polarization switching from the low to the high frequency mode in vertical-cavity surface-emitting lasers," *Appl. Phys. Lett.* **78**, 3574 (2001).
- [68] Y. C. Chen, H. G. Winful, and J. M. Liu, "Subharmonic bifurcations and irregular pulsing behavior of modulated semiconductor lasers," *Appl. Phys. Lett.* **47**, 208 (1985).

- 
- [69] M. Tang and S. Wang, "Simulation studies of bifurcation and chaos in semiconductor lasers," *Appl. Phys. Lett.* **48**, 900 (1986).
- [70] R. S. Tucker, "High-speed modulation of semiconductor lasers," *IEEE J. Lightw. Technol.* **3**, 1180 (1985).
- [71] H. F. Liu and W. F. Ngai, "Nonlinear Dynamics of a Directly Modulated 1.55  $\mu\text{m}$  InGaAsP Distributed Feedback Semiconductor Laser," *IEEE J. Quantum Electron.* **29**, 1668 (1993).
- [72] S. Tarucha and K. Otsuka, "Response of semiconductor laser to deep sinusoidal injection current modulation," *IEEE J. Quantum Electron.* **17**, 810 (1981).
- [73] C. H. Lee, T. H. Yoon, and S. Y. Shin, "Period doubling and chaos in a directly modulated laser diode," *Appl. Phys. Lett.* **46**, 95 (1985).
- [74] O. Buccafusca, J. L. A. Chilla, J. J. Rocca, S. Feld, C. Wilmsen, V. Morozov, and R. Leibenguth, "Transverse mode dynamics in vertical cavity surface emitting lasers excited by fast electrical pulses," *Appl. Phys. Lett.* **68**, 590 (1996).
- [75] A. Valle, "Selection and Modulation of high-order transverse modes in vertical-cavity surface-emitting lasers," *IEEE J. Quantum Electron.* **34**, 1924 (1998).
- [76] A. Valle, L. Pesquera, S.I. Turovets, and J.M. López, "Nonlinear dynamics of current-modulated vertical-cavity surface-emitting lasers," *Opt. Commun.* **208**, 173 (2002).
- [77] A. Valle, M. Sciamanna, and K. Panajotov, "Nonlinear dynamics of the polarization of multitransverse mode vertical-cavity surface-emitting lasers under current modulation," *Phys. Rev. E* **76**, 046206 (2007).
- [78] M. Sciamanna, A. Valle, P. Mégret, M. Blondel, and K. Panajotov, "Nonlinear polarization dynamics in directly modulated vertical-cavity surface-emitting lasers," *Phys. Rev. E* **68**, 016207 (2003).
- [79] C. Masoller, M. S. Torre, and K. A. Shore, "Polarization dynamics of current-modulated vertical-cavity surface-emitting lasers," *IEEE J. Quantum Electron.* **43**, 1074 (2007).
- [80] R. Lang and K. Kobayashi, "External optical feedback effects on semiconductor injection lasers," *IEEE J. Quantum Electron.* **16**, 347 (1980).
- [81] D. Lenstra, B. Verbeek, and A. Den Boef, "Coherence collapse in single-mode semiconductor lasers due to optical feedback," *IEEE J. Quantum Electron.* **21**, 670 (1985).

- [82] R. W. Tkach and A. R. Chraplyvy, "Regimes of feedback effects in 1.5- $\mu\text{m}$  distributed feedback lasers," *IEEE J. Lightw. Technol.* **4**, 1655 (1986).
- [83] L. Goldberg, H. F. Taylor, A. Dandridge, J. F. Weller, and R. O. Miles, "Spectral characteristics of semiconductor lasers with optical feedback," *IEEE J. Quantum Electron.* **18**, 555 (1982).
- [84] T. Heil, A. Uchida, P. Davis, and T. Aida, "TE-TM dynamics in a semiconductor laser subject to polarization-rotated optical feedback," *Phys. Rev. A* **68**, 03381 (2003).
- [85] W. A. van der Graaf, L. Pesquera, and D. Lenstra, "Stability of a diode laser with phase-conjugate feedback," *Opt. Lett.* **23**, 256 (1998).
- [86] A. P. A. Fischer, K. O. Andersen, M. Yousefi, S. Stolte, and D. Lenstra, "Experimental and theoretical study of filtered optical feedback in a semiconductor laser," *IEEE J. Quantum Electron.* **36**, 375 (2000).
- [87] C. Risch and C. Voumard, "Self-pulsation in the output intensity and spectrum of GaAs-AlGaAs cw diode lasers coupled to a frequency-selective external optical cavity," *J. Appl. Phys.* **48**, 2083 (1977).
- [88] I. Fischer, G. H. M. van Tartwijk, A. M. Levine, W. Elsässer, and E. Göbel, and D. Lenstra, "Fast pulsing and chaotic itinerancy with a drift in the coherence collapse of Semiconductor Lasers," *Phys. Rev. Lett.* **76**, 220 (1996).
- [89] A. A. Tager and K. Petermann, "High-Frequency oscillations and self-mode locking in short external-cavity laser diodes," *IEEE J. Quantum Electron.* **30**, 1553 (1994).
- [90] T. Heil, I. Fischer, and W. Elsässer, "Dynamics of semiconductor lasers subject to delayed optical feedback: the short cavity regime," *Phys. Rev. Lett.* **87**, 243901 (2001).
- [91] A. Tabaka, K. Panajotov, I. Veretennicoff, and M. Sciamanna, "Bifurcation study of regular pulse packages in laser diodes subject to optical feedback," *Phys. Rev. E* **70**, 036211 (2004).
- [92] M. Sciamanna, A. Tabaka, H. Thienpont, and K. Panajotov, "Intensity behavior underlying pulse packages in semiconductor lasers that are subject to optical feedback," *J. Opt. Soc. Am. B* **22**, 777 (2005).
- [93] P. Besnard, F. Robert, M. L. Charès, and G. M. Stéphan, "Theoretical modeling of vertical-cavity surface-emitting lasers with polarized optical feedback," *Phys. Rev. A* **56**, 3191 (1997).

- 
- [94] C. Masoller and N. B. Abraham, "Low-frequency fluctuations in vertical-cavity surface-emitting semiconductor lasers with optical feedback," *Phys. Rev. A* **59**, 3021 (1999).
- [95] M. Sciamanna, C. Masoller, N. B. Abraham, F. Rogister, P. Mégret, and M. Blondel, "Different regimes of low-frequency fluctuations in vertical-cavity surface-emitting lasers," *J. Opt. Soc. Am. B* **20**, 37 (2003).
- [96] M. Giudici and S. Balle, "Polarization dynamics in vertical-cavity surface-emitting lasers with optical feedback: experiment and model," *J. Opt. Soc. Am. B* **16**, 2114 (1999).
- [97] M. Sciamanna, T. Erneux, F. Rogister, O. Deparis, P. Mégret, and M. Blondel, "Bifurcation bridges between external-cavity modes lead to polarization self-modulation in vertical-cavity surface-emitting lasers," *Phys. Rev. A* **65**, 041801(R) (2003).
- [98] M. Sciamanna, T. Erneux, F. Rogister, O. Deparis, P. Mégret, and M. Blondel, "Dynamics of vertical-cavity surface-emitting lasers in the short external cavity regime: Pulse packages and polarization mode competition," *Phys. Rev. A* **73**, 013810 (2006).
- [99] Y. Hong, P. S. Spencer, and K. A. Shore, "Suppression of polarization switching in vertical-cavity surface-emitting lasers by use of optical feedback," *Opt. Lett.* **29**, 2151 (2004).
- [100] C. Huygens, *Horologonium Oscillatorium*. Paris (France), 1673.
- [101] R. Adler, "A study of locking phenomena in oscillators," *Proc. IRE* **54**, 351 (1946).
- [102] H. L. Stover and W. H. Steier, "Locking of laser oscillators by light injection," *Appl. Phys. Lett.* **8**, 91 (1966).
- [103] C. J. Buczek and R. J. Freiberg, "Hybrid injection locking of higher power CO<sub>2</sub> lasers," *IEEE J. Quantum Electron.* **8**, 641 (1972).
- [104] J. I. Nishizawa and K. Ishida, "Injection-induced modulation of laser light by the interaction of laser diodes," *IEEE J. Quantum Electron.* **11**, 515 (1975).
- [105] S. Kobayashi and T. Kimura, "Coherence of injection phase-locked AlGaAs semiconductor laser," *Electron. Lett.* **16**, 668 (1980).
- [106] S. Kobayashi, J. Yamada, S. Machida, and T. Kimura, "Single-mode operation of 500 Mbit/s modulated AlGaAs semiconductor laser by injection locking," *Electron. Lett.* **16**, 746 (1980).

- [107] S. Kobayashi and T. Kimura, "Injection Locking in AlGaAs Semiconductor Laser," *IEEE J. Quantum Electron.* **17**, 681 (1981).
- [108] R. Lang, "Injection Locking Properties of a Semiconductor Laser," *IEEE J. Quantum Electron.* **17**, 976 (1982).
- [109] C. H. Henry, N. A. Olsson, and N. K. Dutta, "Locking Range and Stability of Injection Locked 1.54  $\mu\text{m}$  InGaAsP Semiconductor Lasers," *IEEE J. Quantum Electron.* **21**, 1152 (1985).
- [110] S. Kobayashi and T. Kimura, "Injection Locking Characteristics of an AlGaAs Semiconductor Laser," *IEEE J. Quantum Electron.* **16**, 915 (1980).
- [111] N. A. Olsson, H. Temkin, R. A. Logan, L. F. Johnson, G. J. Dolan, J. P. Van der Ziel, and J. C. Campbell, "Chirp-free transmission over 82.5 km of single mode fibers at 2 Gbit/s with injection locked DFB semiconductor lasers," *IEEE J. Lightw. Technol.* **3**, 63 (1985).
- [112] K. Iwashita and K. Nakagawa, "Suppression of Mode Partition Noise by Laser Diode Light Injection," *IEEE J. Quantum Electron.* **18**, 1669 (1982).
- [113] T. B. Simpson, J. M. Liu, and A. Gavrielides, "Bandwidth enhancement and broadband noise reduction in injection-locked semiconductor lasers," *IEEE Photon. Technol. Lett.* **7**, 709 (1998).
- [114] T. B. Simpson and J. M. Liu, and A. Gavrielides, "Enhancement of modulation bandwidth of lasers diodes injection locking," *Photon. Technol. Lett.* **8**, 34 (1996).
- [115] H.F. Chen, J.M. Liu, T.B. Simpson, "Response characteristics of direct current modulation on a bandwidth-enhanced semiconductor laser under strong injection locking," *Opt. Commun.* **173**, 349 (2000).
- [116] X. J. Meng, T. Chau, and M.C. Wu, "Experimental demonstration of modulation bandwidth enhancement in distributed feedback lasers with external light injection," *Electron. Lett.* **34**, 2031 (1998).
- [117] M. Ohtsu, *Highly coherent semiconductor lasers*, Springer Series in Photonics, Artech House, (1992).
- [118] T. Jung, S. Ji-Lin, D. T. K. Tong, S. Murthy, M. C. Wu, T. Tanbun-Ek, W. Wenshen, R. Lodenkamper, R. Davis, L.J. Lembo, and J. C. Brock, "CW injection locking of a mode-locked semiconductor laser as a local oscillator comb for channelizing broad-band signal," *IEEE Trans. Microw. Techn.*, **47**, 1225 (1999)

- [119] P. K. A. Wai, L. Xu, L. F. K. Lui, L. Y. Chan, and C. C. Lee, "All-optical add-drop node for optical packet-switched networks," *Opt. Lett.* **30**, 1515 (2005).
- [120] Z. G. Pan, S. Jiang, and M. Dagenais, "Optical injection induced polarization bistability in vertical-cavity surface-emitting lasers," *Appl. Phys. Lett.* **63**, 2999 (1993).
- [121] Y. Hong, P. S. Spencer, S. Bandyopadhyay, P. Rees, and K. A. Shore, "Polarization-resolved chaos and instabilities in a vertical cavity surface emitting laser subject to optical injection," *Opt. Commun.* **216**, 185 (2003).
- [122] H. Li, T. L. Lucas, J. G. McInerney, M. W. Wright, and R. A. Morgan, "Injection locking dynamics of vertical cavity semiconductor lasers under conventional and phase conjugate injection," *IEEE J. Quantum Electron.* **32**, 227 (1996).
- [123] S. Bandyopadhyay, Y. Hong, P. S. Spencer, and K. A. Shore, "Experimental observation of anti-phase polarisation dynamics in VCSELS," *Opt. Commun.* **202**, 145 (2002).
- [124] Y. Hong, P. S. Spencer, P. Rees, and K. A. Shore, "Optical injection dynamics of two-mode vertical cavity surface-emitting semiconductor lasers," *IEEE J. Quantum Electron.* **38**, 274 (2002).
- [125] D. L. Boiko, G. M. Stephan, and P. Besnard, "Fast polarization switching with memory effect in vertical-cavity surface-emitting laser subject to modulated optical injection," *J. Appl. Phys.* **86**, 4096 (1999).
- [126] H. Kawaguchi and I. S. Hidayat, "Gigahertz all optical flip-flop operation of polarization-bistable vertical-cavity surface-emitting lasers," *Electron. Lett.* **86**, 1150 (1995).
- [127] H. Kawaguchi, "Bistable laser diodes and their applications: state of the art," *IEEE J. Sel. Top. Quantum Electron.* **3**, 1254 (1997).
- [128] M. Okada and K. Nishio, "Bistability and optical switching in a polarization-bistable laser diode," *IEEE J. Quantum Electron.* **32**, 1767 (1996).
- [129] R. Hui, S. Benedetto, and I. Montrosset, "Optical bistability in diode-laser amplifiers and injection-locked laser diodes," *Opt. Lett.* **18**, 287 (1993).
- [130] K. Nonaka, and T. Kurokawa, "Simultaneous time- and wavelength-domain optical demultiplexing of NRZ signals by using a side-injection-light-controlled bistable laser diode," *Electron. Lett.* **31**, 1865 (1995).

- [131] T. Mori, Y. Yamayoshi, and H. Kawaguchi, "Low-switching-energy and high-repetition-frequency all-optical flip-flop operations of a polarization bistable vertical-cavity surface-emitting laser," *Appl. Phys. Lett.* **88**, 101102 (2006).
- [132] Y. Hong, K. A. Shore, A. Larsson, M. Ghisoni, and J. Halonen, "Pure frequency-polarisation bistability in vertical-cavity surface-emitting semiconductor laser subject to optical injection," *Electron. Lett.* **36**, 2019 (2000).
- [133] M. Sciamanna and K. Panajotov, "Two-mode injection locking in vertical-cavity surface-emitting lasers," *Opt. Lett.* **30**, 2309 (2005).
- [134] M. Sciamanna and K. Panajotov, "Route to polarization switching induced by optical injection in vertical-cavity surface-emitting lasers," *Phys. Rev. A* **73**, 023811 (2006).
- [135] Y. Hong, P. S. Spencer, and K. A. Shore, "Power and frequency dependence of hysteresis in optically bistable injection-locked VCSELs," *Electron. Lett.* **37**, 569 (2001).
- [136] Y. Hong, K. A. Shore, A. Larsson, M. Ghisoni, and J. Halonen, "Polarisation switching in a vertical-cavity surface-emitting semiconductor laser by frequency detuning," *IEE Proc. Optoelectron.* **148**, 31 (2001).
- [137] P. M. Varangis, A. Gavrielides, T. Erneux, V. Kovanis, and L. F. Lester, "Frequency entrainment in optically injected semiconductor lasers," *Phys. Rev. Lett.* **78**, 2353 (1997).
- [138] H. Saito, K. Nishi, I. Ogura, S. Sugou, and Y. Sugimoto, "Room-temperature lasing operation of a quantum-dot vertical-cavity surface-emitting laser," *Appl. Phys. Lett.* **69**, 3140 (1996)
- [139] N. Ledentsov, "Long-Wavelength quantum-dot lasers on GaAs substrates: from media to device concepts," *IEEE J. Sel. Top. Quantum Electron.* **8**, 1015 (2002).
- [140] D. Goulding, S. P. Hegarty, O. Rasskazov, S. Melnik, M. Hartnett, G. Greene, J. G. McInerney, D. Rachinskii, and G. Huyet, "Excitability in a quantum dot semiconductor laser with optical injection," *Phys. Rev. Lett.* **98**, 153903 (2007).
- [141] T. B. Simpson, J. M. Liu, A. Gavrielides, V. Kovanis, and P. M. Alsing, "Period-doubling route to chaos in a semiconductor laser subject to optical injection," *Appl. Phys. Lett.* **64**, 3539 (1994)
- [142] L. Goldberg, H.F. Taylor, J.F. Weller, and D.M. Bloom, "Microwave signal generation with injection-locked laser diodes," *Electron. Lett.* **19**, 491 (1983).



- 
- [143] J. M. Liu and T. B. Simpson, "Four-wave mixing and optical modulation in a semiconductor laser," *IEEE J. Quantum Electron.* **30**, 957 (1994)
- [144] T. B. Simpson, "Mapping the nonlinear dynamics of a distributed feedback semiconductor laser subject to external optical injection," *Opt. Commun.* **215**, 135 (2003).
- [145] S.K. Hwang and J.M. Liu, "Dynamical characteristics of an optically injected semiconductor laser," *Opt. Commun.* **183**, 195 (2000).
- [146] B. S. Ryvkin, K. Panajotov, E. A. Avrutin, I. Veretennicoff, and H. Thienpont, "Optical-injection-induced polarization switching in polarization bistable VCSELs," *J. Appl. Phys.* **96**, 6002 (2004).
- [147] S. Wieczorek, T. B. Simpson, B. Krauskopf, and D. Lenstra, "Bifurcation transitions in an optically injected diode laser: theory and experiment," *Opt. Commun.* **215**, 125 (2003).
- [148] V. Kovanis, A. Gavrielides, T. B. Simpson, and J. M. Liu, "Instabilities and chaos in optically injected semiconductor lasers," *Appl. Phys. Lett.* **67**, 2780 (1995).
- [149] S. K. Hwang, J. M. Liu, and J. K. White, "Characteristics of period-one oscillations in semiconductor lasers subject to optical injection," *IEEE J. Select. Top. Quantum Electron.* **10**, 974 (2004).
- [150] A. Gavrielides, V. Kovanis, M. Nizette, T. Erneux, and T. B. Simpson, "Period three limit-cycles in injected semiconductor lasers," *Quantum Semiclass. Opt.* **4**, 20 (2002).
- [151] S. Wieczorek, B. Krauskopf, and D. Lenstra, "Multipulse excitability in a semiconductor laser with optical injection," *Phys. Rev. Lett.* **88**, 063901 (2002).
- [152] S. Wieczorek, B. Krauskopf, and D. Lenstra, "A unifying view of bifurcations in a semiconductor laser subject to optical injection," *Opt. Commun.* **172**, 279 (1999).
- [153] E. Doedel, T. Fairgrieve, B. Sandstede, A. Champneys, Yu. Kuznetsov, and X. Wang, AUTO 97: <http://indy.cs.concordia.ca/auto/main.html>.
- [154] J. Danckaert, B. Nagler, J. Albert, K. Panajotov, I. Veretennicoff, and T. Erneux, "Minimal rate equations describing polarization switching in vertical-cavity surface-emitting lasers," *Opt. Commun.* **201**, 129 (2002).
- [155] K. Panajotov, J. Danckaert, G. Verschaffelt, M. Peeters, B. Nagler, J. Albert, B. Ryvkin, H. Thienpont, and I. Veretennicoff, "Polarization

- behavior of vertical-cavity surface-emitting lasers: Experiments, models and applications,” AIP Conf. Proc. **560**, 403 (2001).
- [156] M. W. Lee, Y. Hong, and K. A. Shore, “Experimental Demonstration of VCSEL-based chaotic optical communications,” IEEE Photon. Technol. Lett. **16**, 2392 (2004).
- [157] H. Kasuya, M. Moria, R. Goto, T. Goto, and K. Yamane, “All optical mode locking of Fabry-Perot laser diode via mutual injection locking between two longitudinal modes,” Appl. Phys. Lett. **75**, 13 (1999).
- [158] P. Schanne, H. J. Heinrich, W. Elsässer, and E. O. Göbel, “Optical bistability and nearly degenerate four-wave mixing in a GaAlAs laser under intermodal injection,” Appl. Phys. Lett. **61**, 2135 (1992).
- [159] Y. Hong, K. A. Shore, J. S. Lawrence, and D. M. Kane, “Wavelength switching by positively detuned side-mode injection in semiconductor lasers,” Appl. Phys. Lett. **76**, 3170 (2000).
- [160] Y. Hong and K. A. Shore, “Locking characteristics of a side-mode injected semiconductor laser,” IEEE J. Quantum Electron. **35**, 1713 (1999).
- [161] Y. Liu, H. K. Liu, and Y. Braiman, “Injection locking of individual broad-area lasers in an integrated high-power diode array,” Appl. Phys. Lett. **81**, 978 (2002).
- [162] J. M. Regalado, S. Balle, M San Miguel, A. Valle, and L. Pesquera, “Polarization and transverse-mode selection in quantum-well vertical-cavity surface-emitting lasers: index- and gain-guided devices,” Quantum Semiclass. Opt. **9**, 713 (1997).
- [163] M. S. Torre, A. Valle, and L. Pesquera, “Polarization and transverse-mode behavior of vertical-cavity surface-emitting lasers under optical injection,” Opt. Quantum Electron. **38**, 445 (2006).
- [164] J. Mulet and S. Balle, “Transverse mode dynamics in vertical-cavity surface-emitting lasers: Spatiotemporal versus modal expansion descriptions,” Phys. Rev. A **66**, 053802 (2002).
- [165] G. H. M. van Tartwijk and D Lenstra, “Semiconductor lasers with optical injection and feedback,” Quantum Semiclass. Opt. **7**, 87 (1997).
- [166] S. Balle, E. Tolkachova, M. San Miguel, J. R. Tredicce, J. M. Regalado, and A. Gahl, “Mechanisms of polarization switching in single-transverse-mode vertical-cavity surface-emitting lasers: thermal shift and nonlinear semiconductor dynamics,” Opt. Lett. **24**, 1121 (1997).

- 
- [167] Y. Hong, M. W. Lee, P. Spencer, and K. A. Shore, "Synchronization of chaos in unidirectionally coupled vertical-cavity surface-emitting semiconductor lasers," *Opt. Lett.*, **29**, 1215 (2004)
- [168] A. Pikovsky, M. Rosenblum, and J. Kurths, *Synchronization: a universal concept of nonlinear sciences*, Cambridge University Press (2003).
- [169] W. H. Eccles, and J. H. Vincent, Patent Spec. **clxiii**, 462 (1920).
- [170] J. Buck and E. Buck, "Mechanism of rhythmic synchronous flashing of fireflies," *Science* **159**, 1319 (1968).
- [171] T. J. Walker, "Acoustic synchrony: two mechanisms in the snowy tree cricket," *Science* **166**, 891 (1969).
- [172] C. S. Peskin, "Mathematical aspects of heart physiology," Institute of Mathematical Sciences, New York (1975).
- [173] C. M. Gray, P. König, A. K. Engel, and W. Singer, "Oscillatory responses in cat visual cortex exhibit inter-columnar synchronization which reflects global stimulus properties," *Nature* **338**, 334 (1989).
- [174] W. A. MacKay, "Synchronized neuronal oscillations and their role in motor processes," *Trends Cogn. Sci.* **1**, 176 (1997).
- [175] V. I. Arnold, "Cardiac arrhythmias and circle mappings," *Chaos* **1**, 20 (1991).
- [176] S. Strogatz, *Nonlinear Dynamics and Chaos: With Applications to Physics, Biology, Chemistry, and Engineering*, Addison-Wesley publishing company, Newyork, U.S.A (2001).
- [177] L. M. Pecora and T. L. Carroll, "Synchronization in chaotic systems," *Phys. Rev. Lett.* **64**, 821 (1990).
- [178] K. M. Cuomo and A. V. Oppenheim, "Circuit implementation of synchronized chaos with applications to communications," *Phys. Rev. Lett.* **71**, 65 (1993).
- [179] T. Sugawara, M. Tachikawa, T. Tsukamoto, and T. Shimizu, "Observation of synchronization in laser chaos," *Phys. Rev. Lett.* **72**, 3502 (1994).
- [180] D. Y. Tang, R. Dykstra, M. W. Hamilton, and N. R. Heckenberg, "Observation of generalized synchronization of chaos in a driven chaotic system," *Phys. Rev. E* **57**, 5247 (1998).
- [181] R. Roy, and K. S. Thornburg, "Experimental observation of chaotic lasers," *Phys. Rev. Lett.* **72**, 2009 (1994).

- [182] G. D. VanWiggeren and R. Roy, "Communication with chaotic lasers," *Science* **279**, 1198 (1994).
- [183] G. D. VanWiggeren and R. Roy, "Optical communication with chaotic waveforms," *Phys. Rev. Lett.* **81**, 3547 (1998).
- [184] C. R. Mirasso, P. Colet, and P. G. Fernandez, "Synchronization of chaotic semiconductor lasers: application to encoded communications," *IEEE Photon. Technol. Lett.* **8**, 299 (1996).
- [185] J. P. Goedgebuer, L. Larger, and H. Porte, "Optical cryptosystem Based on cynchronization of hyperchaos generated by a delayed feedback Tunable Laser Diode," *Phys. Rev. Lett.* **80**, 2249 (1998).
- [186] S. Sivaprakasam and K. A. Shore, "Demonstration of optical synchronization of chaotic external-cavity laser diodes," *Opt. Lett.* **24**, 1200 (1999).
- [187] S. Sivaprakasam and K. A. Shore, "Signal masking for chaotic optical communication using external-cavity diode lasers," *Opt. Lett.* **24**, 466 (1999).
- [188] D. W. Sukow, A. Gavrielides, T. McLachlan, G. Burner, J. Amonette, and John Miller, "Identity synchronization in diode lasers with unidirectional feedback and injection of rotated optical fields," *Phys. Rev. A* **74**, 023812 (2006).
- [189] C. Masoller, "Anticipation in the synchronization of chaotic semiconductor lasers with optical feedback," *Phys. Rev. Lett.* **86**, 2782 (2001).
- [190] Y. Liu, H. F. Chen, J. M. Liu, P. Davis, and T. Aida, "Synchronization of optical-feedback-induced chaos in semiconductor lasers by optical injection," *Phys. Rev. Lett.* **63**, 031802(R) (2001).
- [191] A. Locquet, C. Masoller, and C. R. Mirasso, "Synchronization regimes of optical-feedback-induced chaos in unidirectionally coupled semiconductor lasers," *Phys. Rev. E* **65**, 056205 (2001).
- [192] R. Vicente, T. Pérez, and C. R. Mirasso, "Open- versus closed-loop performance of synchronized chaotic external-cavity semiconductor lasers," *IEEE J. Quantum Electron.* **38**, 1197 (2002).
- [193] Y. Liu, P. Davis, Y. Takiguchi, T. Aida, S. Saito, and J. M. Liu, "Injection locking and synchronization of periodic and chaotic signals in semiconductor lasers," *IEEE J. Quantum Electron.* **39**, 269 (2003).
- [194] J. Ohtsubo, *Semiconductor lasers: stability, instability and chaos*, Springer Verlag, Berlin (2006).

- 
- [195] P. S. Spencer, C. R. Mirasso, P. Colet, and K. A. Shore, "Modeling of optical synchronization of chaotic external-cavity VCSEL's," *IEEE J. Quantum Electron.* **34**, 1673 (1998).
- [196] P. S. Spencer and C. R. Mirasso, "Analysis of optical chaos synchronization in frequency-detuned external-cavity VCSEL's," *IEEE J. Quantum Electron.* **35**, 803 (1999).
- [197] R. Ju, P. S. Spencer, and K. A. Shore, "Polarization-preserved and polarization-rotated synchronization of chaotic vertical-cavity surface-emitting lasers," *IEEE J. Quantum Electron.* **41**, 1641 (2005).
- [198] N. Fujiwara, Y. Takiguchi, and J. Ohtsubo, "Observation of the synchronization of chaos in mutually injected vertical-cavity surface-emitting semiconductor lasers," *Opt. Lett.* **28**, 1677 (2003).
- [199] C. Masoller and N. B. Abraham, "Low-frequency fluctuations in vertical-cavity surface-emitting semiconductor lasers with optical feedback," *Phys. Rev. A* **59**, 3021 (1999).
- [200] A. Locquet, F. Rogister, M. Sciamanna, P. Mégret, and M. Blondel, "Two types of synchronization in unidirectionally coupled chaotic external-cavity semiconductor lasers," *Phys. Rev. E* **64**, 045203(R) (2001).
- [201] A. Locquet, C. Masoller, P. Mégret, and M. Blondel, "Comparison of two types of synchronization of external-cavity semiconductor lasers," *Opt. Lett.* **27**, 31 (2002).
- [202] F. Rogister, A. Locquet, D. Pieroux, M. Sciamanna, O. Deparis, P. Megret, and M. Blondel, "Secure communication scheme using chaotic laser diodes subject to incoherent optical feedback and incoherent optical injection," *Opt. Lett.* **26**, 1486 (2001).
- [203] M. Sciamanna, C. Masoller, F. Rogister, P. Mégret, N. B. Abraham, and M. Blondel, "Fast pulsing dynamics of a vertical-cavity surface-emitting laser operating in the low-frequency fluctuation regime," *Phys. Rev. A* **68**, 015805 (2003).
- [204] M. Sondermann, H. Bohnet, and T. Ackemann, "Low-frequency fluctuations and polarization dynamics in vertical-cavity surface-emitting lasers with isotropic feedback," *Phys. Rev. A* **67**, 021802(R) (2003).
- [205] K. Panajotov, B. Nagler, G. Verschaffelt, A. Georgievski, H. Thienpont, J. Danckaert, and I. Veretennicoff, "Impact of in-plane anisotropic strain on the polarization behavior of vertical-cavity surface-emitting lasers," *Appl. Phys. Lett.* **77**, 1590 (2000).

- [206] M. Sciamanna, K. Panajotov, H. Thienpont, I. Veretennicoff, P. Mégret, and M. Blondel, “Optical feedback induces polarization mode hopping in vertical-cavity surface-emitting lasers,” *Opt. Lett.* **28**, 1543 (2003).
- [207] J. Revuelta, C. R. Mirasso, P. Colet, and L. Pesquera, “Criteria for synchronization of coupled chaotic external-cavity semiconductor lasers,” *IEEE Photon. Technol. Lett.* **14**, 140 (2002).
- [208] T. Ackemann and M. Sondermann, “Characteristics of polarization switching from the low to the high frequency mode in vertical-cavity surface-emitting lasers,” *Appl. Phys. Lett.* **78**, 3574 (2001).

# List of publications

## JOURNAL PUBLICATIONS

- I. Gatare, M. Sciamanna, M. Nizette, and K. Panajotov, “Bifurcation to Polarization Switching and Locking in Vertical-Cavity Surface-Emitting Lasers with Optical Injection,” *Phys. Rev. A* **76**, 031803(R) (2007).
- I. Gatare, M. Sciamanna, A. Locquet, and K. Panajotov, “Influence of polarization mode competition on the synchronization of two unidirectionally coupled vertical-cavity surface-emitting lasers,” *Opt. Lett.*, **32**, 1629 (2007).
- M. Sciamanna, I. Gatare, A. Locquet, and K. Panajotov, “Polarization synchronization in unidirectionally coupled vertical-cavity surface-emitting lasers with orthogonal optical injection,” *Phys. Rev E* **75**, 056203 (2007).
- A. Valle, I. Gatare, K. Panajotov, and M. Sciamanna “Transverse mode switching and locking in vertical-cavity surface-emitting lasers subject to orthogonal optical injection,” *IEEE J. Quantum Electron.* **43**, 322 (2007).
- I. Gatare, K. Panajotov, and M. Sciamanna, “Frequency-induced bistability in vertical-cavity surface-emitting lasers with optical injection,” *Phys. Rev. A*, **75**, 023804 (2007).
- I. Gatare, J. Buesa, H. Thienpont, M. Sciamanna, and K. Panajotov, “Nonlinear dynamics accompanying polarization switching in vertical-cavity surface-emitting lasers with orthogonal optical injection,” *Appl. Phys. Lett.*, **88**, 101106 (2006).
- J. Buesa, I. Gatare, H. Thienpont, K. Panajotov, and M. Sciamanna, “Mapping of the dynamics induced by orthogonal optical injection in vertical-cavity surface-emitting lasers,” *IEEE J. Quantum. Electron.*, **42**, 198 (2006).

- I. Gatare, J. Buesa, H. Thienpont, K. Panajotov, and M. Sciamanna, "Polarization switching bistability and dynamics in vertical-cavity surface-emitting laser under orthogonal optical injection," *Opt. and Quantum Electron.* 42, 429 (2006).

## CONFERENCE PUBLICATIONS

- I. Gatare, M. Sciamanna, M. Nizette, and K. Panajotov, and, "Bifurcation and nonlinear dynamics accompanying polarization switching in a VCSEL subject to orthogonal optical injection," CLEO-EQEC Europe Int. Conference, June 2007, Munich, Germany.
- I. Gatare, M. Sciamanna, A. Locquet, and K. Panajotov "Polarization synchronization in unidirectionally coupled vertical-cavity surface-emitting lasers," PHASE international workshop, 28- 30 March 2007, Metz, France.
- I. Gatare, A. Valle, K. Panajotov, and M. Sciamanna, and, "Mapping of transverse mode locking and switching in VCSELs under orthogonal optical injection," CLEO-EQEC Europe Int. Conference, June 2007, Munich, Germany.
- I. Gatare, M. Sciamanna, M. Nizette, and K. Panajotov "Bifurcations to polarization switching and locking in optically injected VCSELs," PHASE international workshop, 28-30 March 2007, Metz, France.
- M. Sciamanna, I. Gatare, H. Thienpont, and K. Panajotov, "Bifurcation to polarization chaos in VCSELs with orthogonal optical injection," NOLTA 2006, September 2006, Bologna, Italy.
- M. Sciamanna, I. Gatare, H. Thienpont, and K. Panajotov, "Bifurcation to polarization chaos in VCSELs with orthogonal optical injection," NOLTA 2006, September 2006, Bologna, Italy.
- I. Gatare, J. Buesa, H. Thienpont, K. Panajotov, and M. Sciamanna, "Nonlinear dynamics and polarization bistability in optically injected VCSEL," SPIE, Photonics Europe, Strasbourg, April 2006.
- M. Sciamanna, I. Gatare, K. J. Buesa, H. Thienpont, and K. Panajotov, "Nonlinear polarization dynamics of VCSELs with orthogonal optical injection," Rio de la Plata Workshop on noise, chaos and complexity in lasers and nonlinear optics, 5-9 December 2005, Colonia del Sacramento, Uruguay.
- M. Sciamanna, I. Gatare, K. J. Buesa, H. Thienpont, and K. Panajotov "Optical Switching with VCSELs," CLEO Europe 2005, 13-17 June 2005, Munich, Germany.



- 
- I. Gatare, J. Buesa, H. Thienpont, K. Panajotov, and M. Sciamanna, “Polarization switching and dynamics induced by optical injection in VCSEL,” CLEO-EQEC Europe Int. Conference, June 2005, Munich, Germany.
  - I. Gatare, J. Buesa, H. Thienpont, K. Panajotov, and M. Sciamanna, “Experimental study of polarization switching dynamics induced by optical injection in VCSELs”, Proc. PHASE Int. Workshop p. 24, march 2005, Metz, France.
  - M. Triginer, I. Gatare, H. Thienpont, M. Sciamanna, and K. Panajotov, “Experimental mapping of polarization dynamics induced by optical injection in VCSELs”, Proc. of the 2004 Symposium IEEE/LEOS Benelux Chapter, pp.151-154, December 2004, Gent, Belgium.
  - I. Gatare, M. Triginer, H. Thienpont, K. Panajotov, and M. Sciamanna, “Experimental study of polarization switching and polarization mode hopping induced by optical injection in VCSELs,” Proc. of the 2004 Symposium IEEE/LEOS Benelux Chapter, pp.143-144, December 2004, Gent, Belgium.



# Curriculum Vitae

## CONTACT INFORMATION

GATARE GAHANGARA Ignace

- *Ecole Supérieure d'Electricité*  
2, Rue Edouard Belin  
57070 Metz, France.  
E-mail: gatarega\_ign@metz.supelec.fr
- *Vrije Universiteit Brussel*  
Department of Applied Physics and Photonics (TONA)  
2, Pleinlann  
1050 Brussels, Belgium  
E-mail: igatare@vub.tona.ac.be

## EDUCATION

- *Since October 2004*: PhD graduate fellow jointly at the Vrije Universiteit Brussel (VUB), Belgium, SUPELEC and the Université Paul Verlaine Metz, France. My current research interests include the study of polarization switching dynamics induced by optical injection in vertical-cavity surface-emitting lasers (VCSELs) and synchronization of coupled VCSELs.
- *2004*: M.Sc degree in Electrical Engineering from the Mons Engineering Faculty (FPMs/ Belgium) with a “High Distinction Grade”.
- *2001*: Undergraduate degree in applied sciences from the Mons Engineering Faculty (FPMs/ Belgium) with a “Distinction Grade”.

## PROFESSIONAL, TEACHING and OTHER ACTIVITIES

- *2006*: Invited lecturer (July and August) in Electronics at the Kavumu Professional Training Center/ Rwanda in the framework of the “capac-

ity reinforcement” project sponsored by the United Nations International Organization for Migration (IOM) and the Belgian Ministry of Foreign Affairs and Development Cooperation.

- *2003*: Two-month internship in the Research and Development department of *SEE Telecom*, a Belgian telecom equipments provider. My activities involved technical test and specifications of the optical amplifier and the add-drop multiplexer modules for the MANSYS (Metropolitan Access Network System) project.
- *Reviewing*: served as Referee for the IEEE Journal of Quantum Electronics.

## AWARDS

- The Forbat Prize granted by Mis Forbat-Reichmann, wife of late Prof. Nick Forbat, Professor of Fundamental Mechanics at the Mons Engineering Faculty (FPMs), Belgium from 1944 to 1967. This prize was awarded to the “Meritorious Student of year 2004”.
- The faculty Prize for the “Best Master Thesis in Telecommunications (2004)” at the Mons Engineering Faculty (FPMs), Belgium. The prize was granted by SEE Telecom (Signal Engineering and Electronics), a Belgian telecom equipment provider.
- 2007 IEEE LEOS Graduate Student Fellowship Award, received at the 30<sup>th</sup> LEOS Annual Meeting, October, 22<sup>th</sup>, 2007, Florida, USA.